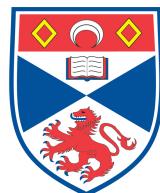


Spin Dynamics of Quantum Spin-Ladders and Chains

Susanne Notbohm



Thesis submitted to the School of Physics and Astronomy
at the University of St Andrews for the degree of Doctor of Philosophy

July 2007

To my parents, Birgit and Manfred Notbohm, who have continually supported and encouraged me and without their support I would not be where I am today.

Abstract

This thesis describes the neutron scattering measurements of magnetic excitations in spin-chains and ladders. The first part discusses an experimental investigation of the copper oxide family $\text{Sr}_{14}\text{Cu}_{24}\text{O}_{41}$ composed of edge-sharing chains and spin-ladders. The study of $\text{La}_4\text{Sr}_{10}\text{Cu}_{24}\text{O}_{41}$ comprises a slightly hole-doped chain and an undoped ladder structure where the chain can be modeled by a ferromagnetic nearest and an antiferromagnetic next-nearest neighbor coupling. The hole effects are apparent in gaps in the dispersion relation and can be described by a charge-density wave agreeing with the commensuration of the dispersion. Investigating the undoped ladder establishes the exchange constants including a cyclic exchange manifested by the two-magnon continuum and the suppression of the $S = 1$ bound mode. An orbital consideration provides an explanation for the exchanges including the different sizes of rung and leg coupling. The excitation spectrum of the doped ladder in $\text{Ca}_{2.5}\text{Sr}_{11.5}\text{Cu}_{24}\text{O}_{41}$ can be described by a direct comparison with the undoped ladder and the differences consisting of a higher energy mode and subgap scattering can be successfully modeled by the charge spectrum of the ladder calculated from the free electron model. The second part of the thesis investigates the alternating chain material $\text{Cu}(\text{NO}_3)_2 \cdot 2.5\text{D}_2\text{O}$ and establishes the gapped one-magnon dispersion, the two-magnon continuum and for the first time the $S = 1$ bound mode. Applying magnetic field drives the system through two critical field transitions, condensation of magnons into the ground state and saturation. The modes beyond saturation can be modeled by spin wave theory and the excitations

at the first critical field follow Luttinger Liquid behavior. Additionally investigated are the temperature effects with the excitations being of a different nature but containing the signature of a strong correlated system. For an outlook the measurements including temperature and field are provided with further theoretical descriptions necessary.

Acknowledgments

Many people have contributed to the work presented in this thesis and I would like to thank them for all their hard work and support. This is really important to me, because without them this thesis would not have been written.

First and foremost I would like to acknowledge my supervisor Alan Tennant. I can truly say that without him this thesis would never have been possible. Much of his time was spent answering my questions, providing support and guidance and in the three years I could not find a question he did not know the answer to, believe it or not. In addition to physics related mentoring Alan has also provided me with a lot of insight into future career options and helped me find out the things I like and more importantly the things I dislike doing. He has made the past 3 years very enjoyable, for which I am extraordinarily grateful. I have learned that endless hours in a small cabin in an experimental hall without any windows or contact to the outside world can be fun if you spent these hours with the right people. So thank you, Alan, for your immense support in and out the world of physics.

There are several people from the University of St Andrews I would like to thank, including my second supervisor, Steve Lee. He has made my association with the University of St Andrews possible during the last two years while I was living and working in Berlin. A special acknowledgment goes to Andy Mackenzie who was my initial contact at St Andrews and made a PhD a possibility for me. Continuously helping with

my situation of living in Berlin and making sure I am informed of all the deadlines and necessary paperwork at St Andrews was Mary Rodger. This was a wonderful help which I could really rely on any time. My fellow PhD students especially David Heron who I spent a majority of my time with during my first year in the Physics building and at our coffee breaks at the Gateway. And also David Bolton for being the great office mate he was.

I have been lucky to spend the last two years at the research laboratory (HMI) in Berlin surrounded by some excellent people. First, there is Bella Lake who accompanied me through all my experiments. She was one of the people sharing my cabin experience and also a great resource in answering my questions and providing guidance in the analysis and the final writing process. Marie Haltod who is the real heart of the structural research department at HMI and has always been there for me when I needed an ear to listen to. Also, I would like to mention some of the people at the Hahn-Meitner-Institut who I have been fortunate enough to meet and work with for the last two years including my friend Cornelia Rohland who has been wonderfully supportive, Robert Wimpory, Kirrily Rule, Phil Bentley, Thomas Hauß, and Silvia Dante.

A special thanks goes to the Ames Laboratory where I grew the copper nitrate crystals. I am very grateful to Paul Canfield, Paul Kögeler and John Fielden for all their help and support during my stay there. A special thanks to Paul Canfield who not only made the growth possible, but was also the one who recommended me to St Andrews in the first place.

I am very grateful to the staff at both the Rutherford Appleton Laboratory in London and the Hahn-Meitner-Institut in Berlin where these experiments were performed. In particular, Toby Perring, Christ Frost, and Mark Telling at the Rutherford Laboratory and Manfred Reehuis at HMI. Additionally I would like to acknowledge the theorists

that supported the experimental studies presented in this thesis: Götz Uhrig and Kai Schmidt for the spin-ladder material, Fabian Essler for the doped ladder and the copper nitrate material and Hans-Jürgen Mikeska for the copper nitrate material.

Also, I would like to thank all my friends and my family without whose constant support this work would never been possible. To name a few: my sister Sylvia and her husband Harald Weimer, the entire Krogmeier family (Dale, Becky, Andrea, and Nic), Carie Hoover, Sally Bell, Bryony Stocking and countless others.

Finally a very significant acknowledgment goes to my fiancé, Tyler Krogmeier, for his unwavering support throughout the past three years. Without him I could not have done this thesis!

Declaration

I, Susanne Notbohm, hereby certify that this thesis, which is approximately 40000 words in length, has been written by me and is the record of work carried out by me and has not been submitted in any previous application for a higher degree.

Susanne Notbohm

September 18, 2007

I was admitted as a research student in September 2004 and as a candidate for the degree of Doctor of Philosophy in September 2004; the higher study for which this is a record was carried out in the University of St Andrews between 2004 and 2007.

Susanne Notbohm

September 18, 2007

I hereby certify that the candidate has fulfilled the conditions for the Resolution and Regulations appropriate for the degree of Doctor of Philosophy in the University of St Andrews and that the candidate is qualified to submit this thesis in application for this degree.

Stephen L. Lee

September 18, 2007

Copyright Declaration

In submitting this thesis to the University of St Andrews I understand that I am giving permission for it to be made available for use in accordance with the regulations of the University Library for the time being in force, subject to any copyright vested in the work not being affected thereby. I understand that the title and abstract will be published, and that a copy of the work may be made and is supplied to any bona fide library or research worker, that my thesis will be electronically accessible for personal or research use, and that the library has the right to migrate my thesis into new electronic forms as required to ensure continued access to the thesis. I have obtained any third-party copyright permissions that may be required in order to allow such access and migration.

Susanne Notbohm

September 18, 2007

Contents

1	Introduction	1
2	Background to Magnetism	5
2.1	Origin of Magnetism	5
2.1.1	Magnetic Moments	5
2.1.2	Magnetic Interactions	6
2.1.3	Orbital Consideration in Cuprates	7
2.1.4	Magnetic Ordering	12
2.2	Theories of Magnetism	13
2.2.1	Spin Wave Theory	13
2.2.2	Antiferromagnetic Spin Chain	16
2.2.3	Spin-Ladder	19
3	Neutron Scattering Theory	23
3.1	Introduction	23
3.2	Scattering Cross-Section	24
3.3	Interaction Potentials	27
3.3.1	Nuclear Scattering	27
3.3.2	Magnetic Scattering	29
3.4	Spallation Source	31

3.5	Time-of-Flight Spectrometer	32
3.5.1	Direct Geometry	32
3.5.2	Indirect Geometry	34
4	Study of the Doped Edge-Sharing Cuprate Chain	37
4.1	Motivation	37
4.2	Background	38
4.3	Experimental Details	41
4.4	Measurement and Results	42
4.4.1	Background Subtraction	42
4.4.2	Dispersion Relation	44
4.5	Analysis	45
4.5.1	Fitting Without Holes	45
4.5.2	Fitting With Holes	46
4.5.3	Ground State	48
4.5.4	Energy Treatment of Hole Hopping	50
4.6	Discussion	53
4.7	Conclusion	59
5	One- and Two-Magnon Spectra of the Ideal Cuprate Ladder	61
5.1	Introduction	61
5.2	Background	62
5.3	Magnetic Features of $\text{La}_4\text{Sr}_{10}\text{Cu}_{24}\text{O}_{41}$	64
5.4	Experimental Details	66
5.5	Measurements and Results	67
5.5.1	Rung Modulation	67
5.5.2	Background Subtraction	70
5.5.3	One- and Two-Magnon Dispersion	71

5.6	Analysis	73
5.6.1	Hamiltonian and Fitting	73
5.6.2	Comparison to Theory	76
5.6.3	Cyclic Exchange	77
5.6.4	Electronic Hamiltonian	80
5.7	Discussion	81
5.8	Conclusion	84
6	Investigation of a Cuprate Ladder under Low Carrier Doping	87
6.1	Motivation	87
6.2	Background	88
6.3	Experimental Details	90
6.4	Measurements and Results	90
6.4.1	Background Subtraction	90
6.4.2	One-Magnon Dispersion	93
6.4.3	Two-Magnon Dispersion	96
6.5	Analysis	97
6.5.1	Charge Scattering	97
6.5.2	Independent Electron Model (IEM)	97
6.5.3	IEM Applied to the Ladder	99
6.5.4	Comparison to Data	102
6.5.5	Parity Breaking	103
6.6	Discussion	105
6.7	Conclusion	109
7	Magnetic Field Effects on the Quantum Magnet Copper Nitrate	111
7.1	Motivation	111
7.2	Background	113

7.3	Crystal Growth	116
7.3.1	Solution Growth Method	116
7.3.2	Production of Crystals	117
7.3.3	Distillation Process	118
7.4	Magnetic Properties	119
7.5	Experimental Details	121
7.6	Zero Field	122
7.6.1	Background Subtraction	122
7.6.2	Dispersion Relation	124
7.6.3	One-Magnon Scattering	126
7.6.4	Dimer Structure Factor	129
7.6.5	Two-Magnon Scattering	132
7.7	Magnetic Field	136
7.7.1	Overview	136
7.7.2	Determination of the Critical Fields	139
7.7.3	Excitation Spectrum above Saturation	140
7.7.4	Investigation of the Critical Field Regime	142
7.8	Conclusion	145
8	Temperature Effects of Copper Nitrate	147
8.1	Motivation	147
8.2	Temperature Effects without Applied Field	148
8.2.1	Theory Background	148
8.2.2	One-Magnon	149
8.2.3	Two-Magnon	154
8.2.4	Intraband Scattering	158
8.3	Outlook: Field Dependence	160

8.4 Conclusion	166
9 Conclusion	169
A Parity conservation	171
A.1 Hamiltonian	171
A.2 Plaquette	172
A.3 Hamiltonian H_{leg}	174
A.4 Structure factor	175
A.4.1 One-magnon	176
A.4.2 Two-magnon	179
A.5 Other Hamiltonian	179
B Band Structure Calculation	181
B.1 Calculation of the Dispersion Relation	181
B.2 Calculation of Fermi wavevector	184
C Parity Breaking for Hole Doping	187
D High Field Excitations in Copper Nitrate	191
D.1 Dispersion Relations	191
D.2 Intensity Distribution	195

Chapter 1

Introduction

This thesis mainly focuses on the investigation of the spin dynamics of ideal quasi one-dimensional (1D) systems. Two different groups of materials are studied causing the experimental section of this thesis to be divided into two parts: The study of magnetism in cuprates upon hole-doping and the interplay of quantum and thermal effects in copper nitrate. The similarity of the two groups of materials is their quasi 1D character presenting the simplest case and providing the possibility of an accessible theoretical description. The common goal consists of the measurement of the excitation spectrum and the allocation of a physical picture. In both groups a complete experimental and complementary theoretical description has not been available so far, but this thesis provides a detailed experimental investigation. While some theoretical work exists and is used for comparison, this investigation serves as a guideline for the development of advanced theories necessary to describe all features of the data. However, the development of those theories is beyond the scope of this thesis leading to a qualitative description of the data where theory is not available. The systems presenting the study of magnetism in cuprates upon hole doping are the spin-ladder materials $\text{La}_4\text{Sr}_{10}\text{Cu}_{24}\text{O}_{41}$ and $\text{Ca}_{2.5}\text{Sr}_{11.5}\text{Cu}_{24}\text{O}_{41}$ allowing a measurement of the effects of hole doping in a 1D chain and a spin-ladder (system consisting of two coupled antiferromagnetic spin 1/2 chains). The interplay of quantum and thermal effects in copper nitrate is performed on the dimerized alternating chain material $\text{Cu}(\text{NO}_3)_2 \cdot 2.5\text{D}_2\text{O}$ for the investigation of

temperature effects while tuning the system into criticality by magnetic field.

This thesis begins with a brief theoretical review provided in Chapters 2 and 3. Chapter 2 concentrates on the background to magnetism, focusing on the magnetic phenomena relevant for this thesis, including the magnetic moment, magnetic ordering and the exchange interactions between moments including some necessary orbital considerations. Additionally an introduction to spin-wave theory, the excitation spectrum of a low-dimensional antiferromagnetic chain, and the characteristics of spin-ladder systems is provided. The neutron scattering theory explaining the scattering processes is outlined in Chapter 3, along with the basic experimental set-up at a neutron spallation source and the description of the spectrometer types used in this thesis.

The first set of neutron scattering experiments is introduced in Chapter 4 also starting the investigation of the magnetism in cuprates upon hole-doping, which continues through to Chapters 5 and 6. The system of focus in Chapter 4 is the chain substructure of the spin-ladder material $\text{La}_4\text{Sr}_{10}\text{Cu}_{24}\text{O}_{41}$ consisting of a slightly hole-doped edge-sharing 1D spin-1/2 chain. In contradiction to the well-understood corner-sharing chain, the edge-sharing structure has been the subject of controversy in the exact determination of the coupling constants. Our neutron results establish for the first time the coupling of the chain as being composed of a very strong ferromagnetic nearest neighbor coupling of $J_{NN} = -24.0 \pm 1.2 \text{ meV}$ and an antiferromagnetic next-nearest neighbor coupling of $J_{NNN} = 2.7 \pm 0.3 \text{ meV}$. The holes are predicted to enter the chain in the form of a charge density wave resulting in small gaps throughout the dispersion relation where the wavevector of the gaps provide an indication of the location of the holes and the size of the gap the periodic potential caused by them.

Chapter 5 continues the study of $\text{La}_4\text{Sr}_{10}\text{Cu}_{24}\text{O}_{41}$ with the investigation of the spin-ladder substructure. Determined by previous investigations of this system and con-

firmed by the study of Chapter 4, the holes are located on the chain leaving the ladder hole-free and realizing a Mott-Hubbard Insulator (MHI) regime. This study provides a starting point for the investigation of the doped ladder via a direct comparison between the two ladder systems (doped and undoped). The key feature of the analysis is the separation between one- and two-magnon scattering processes due to an antiphase rung intensity modulation. This allows an extraction of the dispersion relation and by using the continuous unitary transformation (CUT) method the coupling constants can be fitted to be $J_{leg} = 186$ meV, $J_{rung} = 124$ meV along the leg and the rung of the ladder respectively, as well as a cyclic exchange of $J_{cyc} = 31$ meV. Additionally the two-magnon continuum scattering has been observed for the first time providing access to the important strong quantum fluctuations. A complete theoretical description by the CUT method could model the excitation spectrum of the one- and the two-magnon scattering. This ensured the correctness of the coupling constants and confirmed the existence of the cyclic exchange in these ladder compounds, a subject of dispute for over a decade.

In the next Chapter, Chapter 6, the doped version of the cuprate ladder, $\text{Ca}_{2.5}\text{Sr}_{11.5}\text{Cu}_{24}\text{O}_{41}$, is studied. Due to the weak doping of this system the material embodies an intermediate regime between a MHI and a conventional conductor. The analysis has been performed in analog to the undoped version and extra scattering is observed at high energies as well as subgap scattering. In addition to the scattering of the MHI, the scattering of an Independent Electron Model (IEM) is also considered. A hybridization between the spin and the charge scattering suggests the subgap scattering may occur due to slow moving holes resulting in the formation of a new mode starting at two incommensurate wavevectors and the high energy mode being accessible through fast moving holes along the ladder. This chapter concludes the regime of hole doped materials.

The following two chapters discuss the interplay of quantum and thermal effects in copper nitrate. Chapter 7 provides an introduction to the material including the crystal growth and the determination of the coupling constants. Copper nitrate realizes a dimerized chain with dominant dimer coupling $J = 0.443$ meV, an alternation parameter $\alpha = 0.227$ and additionally very weak ferromagnetic interchain couplings of $J_{a_{\text{inter}}} = 0.006$ meV and $J_{c_{\text{inter}}} = 0.0018$ meV along the a and the c direction respectively, and is characterized by a gap to both the one-magnon dispersion and the two-magnon continuum. Using these coupling constants the one- and the two-magnon scattering can be simulated accurately with the 1D perturbation approach. Applying magnetic field the system can be driven through two phase transitions due to the Zeeman splitting causing magnons to condense into the ground state and changing the statistics of the system. Above the second phase transition (saturation) the excitations can be modeled by spin wave theory, while at the first transition the system behaves according to a Luttinger Liquid.

Chapter 8 continues the study of copper nitrate with an investigation of the temperature effects of the system and additionally the interplay between the magnetic field and the temperature. The treatment of temperature is theoretically challenging and this study provides a clean investigation of an ideal system embodying the simplest case. Using temperature the ground state can also be populated by magnons similar to the field measurement but with the one-magnon gap remaining intact leading to a different statistics of the system as compared to the magnetic field case. The second and last part of the chapter combines the temperature and the magnetic field following the changes of the system and providing an experimental study for the interplay between thermal and quantum effects.

A conclusion of this thesis is provided in chapter 9 summarizing the new findings of the experimental studies and outlining further work.

Chapter 2

Background to Magnetism

2.1 Origin of Magnetism

2.1.1 Magnetic Moments

The fundamental object in magnetism is the magnetic moment of the electron with its interactions giving rise to cooperative magnetic phenomena such as paramagnetism or ferromagnetism. The atomic moment arises from summing the individual electronic moments depending on the orbital angular momentum \mathbf{L} and the intrinsic spin angular momentum \mathbf{S} each obtained by a vector sum due to quantization. The occupancy of the available electronic states within an atom is determined by Hund's rules [1] identifying the filling of the states leading to the determination of \mathbf{L} , \mathbf{S} and the total atomic angular momentum \mathbf{J} . While in filled electronic shells the angular momentum sums up to zero, transition or rare earth metals possess an incomplete shell resulting in a net magnetic moment. In this thesis the interest is in the transition metal ion Cu^{2+} with an incomplete 3d shell leading to a total spin angular momentum of $\mathbf{S} = 1/2$ and a total orbital momentum that is quenched. The quenching can be illustrated as follows: For an ion not experiencing quenching the orbitals are degenerate leading to orbital transformation without any energy cost, e.g. from a $d_{x^2-y^2}$ into a d_{xy} orbital. If, however, this transformation is subject to an energy cost due to e.g. the surrounding ions, the orbital

is stationary and the expectation value of the components of the angular momentum are essentially zero, i.e. quenched. Since all materials discussed in this thesis are based on Cu²⁺ the total angular momentum is $\mathbf{J}=\mathbf{S}$ with \mathbf{S} being used through the thesis.

2.1.2 Magnetic Interactions

The dominant interactions between magnetic atoms in solids are exchange interactions resulting from electrostatic interactions. These arise from the requirement of an antisymmetric wavefunction as a consequence of the Pauli exclusion principle for electrons being fermions. The total wavefunction of two electrons, composed of the product of the spatial and the spin wavefunctions, must be antisymmetric giving rise to two different possibilities of combining the spin and the spatial part. The first one consists of a symmetric spatial and an antisymmetric spin wavefunction while the second one presents the opposite with an antisymmetric spatial and a symmetric spin version. Including a Coulomb interaction between the electrons lifts the degeneracy between the two possibilities resulting in an energy difference between the symmetric and the antisymmetric spatial wavefunctions. This energy difference is expressed as a magnetic interaction between electrons known as the exchange interaction. Heisenberg [2] proposed the effective magnetic interaction for neighboring spins S_i and S_j to be:

$$H = J \mathbf{S}_i \cdot \mathbf{S}_j \quad (2.1)$$

A negative value of J favors the symmetric spin wavefunction known as ferromagnetic exchange due to the spin alignment. Antiferromagnetic exchange is obtained for the antisymmetric spin wavefunction presented by a positive value of J . Generalizing to a many-body system is complex but in many cases can be approximated by the sum of the two spin interactions to be:

$$H = \sum_{\langle i,j \rangle} J_{ij} \mathbf{S}_i \cdot \mathbf{S}_j \quad (2.2)$$

where J_{ij} presents the exchange between the i^{th} and j^{th} spin being summed over distinct pairs of spins i, j .

The exchange interactions are divided into two groups: the direct and the indirect exchange. Direct exchange where electrons on two neighboring magnetic atoms interact without any intermediate ion is often ferromagnetic from electrostatic Coulomb repulsion favoring the antisymmetric spatial wavefunction. The indirect exchange also called superexchange is defined as an exchange between non-neighboring magnetic ions mediated by a diamagnetic ion between them. In Anderson's superexchange [3] the magnetic ions, usually a transition metal, can couple antiferromagnetically resulting in a lowering of the energy of the system by allowing the electrons of the non-magnetic and magnetic ions to delocalize over the system described further in the next section.

2.1.3 Orbital Consideration in Cuprates

All materials discussed in this thesis consist of copper oxide compounds, also called cuprates, and to develop an understanding of the exchanges present in these systems, the orbital configurations of the cuprate compounds have to be considered. Oxygen consists of 8 electrons leading to a $1s^22s^22p^4$ configuration with two single electrons in the p-shell demanded by Hund's rule, and resulting in a complete 2p shell for the O^{2-} ion ($1s^22s^22p^6$) considered in the copper oxide compounds. A p-shell atom consists of three p-orbitals appearing like dumbbells as displayed in Figure 2.1 (a).

The transition metal Cu is made up of 29 electrons forming an $[\text{Ar}]4s^13d^{10}$ leading to one unpaired electron in the d-shell for the Cu^{2+} ion ($[\text{Ar}]3d^9$). The d-shell consists of five 3d orbitals as illustrated in Figure 2.1 (b). Since the copper oxide compounds are planar in all systems considered in this thesis, the only overlap to be considered arises between the $\text{Cu}3d_{x^2-y^2}$ and the $\text{O}2p_x$ and $\text{O}2p_y$ orbitals with the exchange cou-

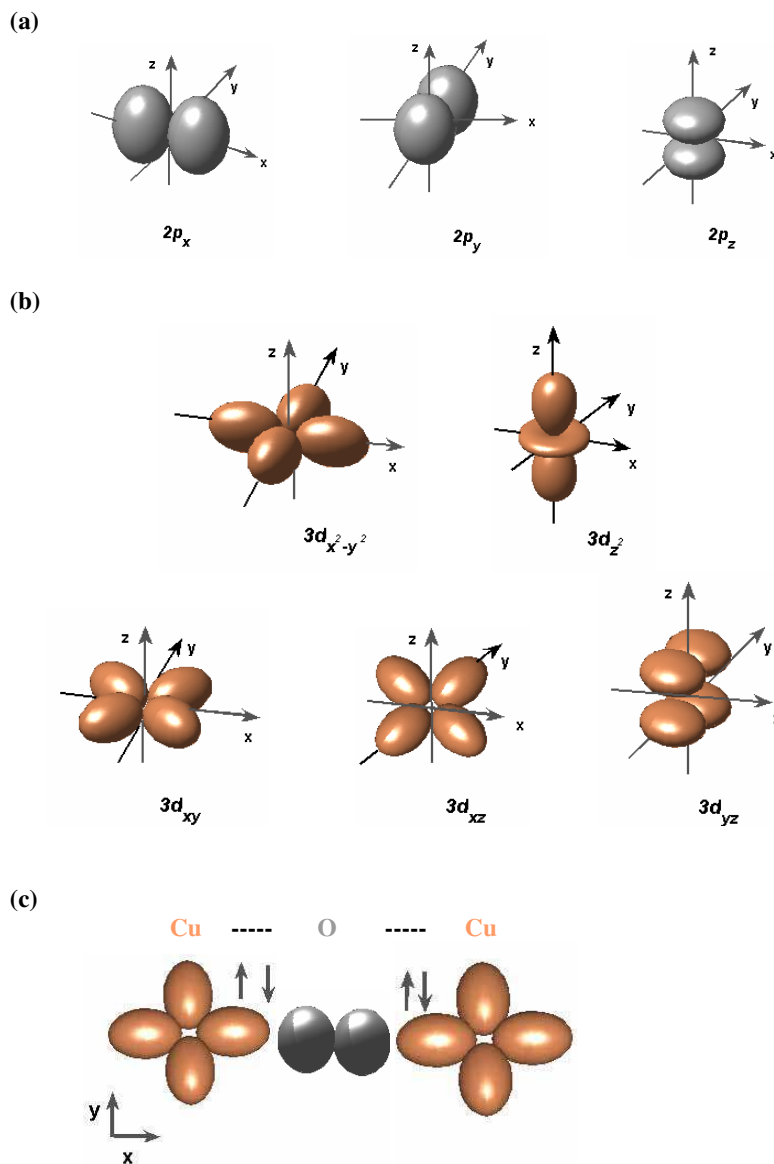


Figure 2.1: Orbital arrangement for (a) the three different 2p orbitals occurring for O. (b) displays the five possible 3Cu d orbitals. (c) Anderson's superexchange pathway for planar copper oxide compound.

plings strongly depending on the hopping matrices. Several hopping pathways have to be considered in these copper oxide compounds. First the hopping between two different $3d_{x^2-y^2}$ copper orbitals, t_{dd} , usually ferromagnetic due to the Coulomb energy maximizing the separation between the electrons achieved by an antisymmetric spatial wavefunction. This interaction is referred to as direct exchange. A similar situation is

found for the exchange between different O2p orbitals with associated hopping defined as t_{pp} and also ferromagnetic. The last coupling considered in this thesis is a Cu-O-Cu bond with the magnitude strongly depending on the bond angle. Anderson's superexchange can occur if the single spin of the two Cu²⁺ ions and the delocalized spins of the two electrons in the O²⁻ couple antiferromagnetically resulting in a lowering of the energy of the system. This coupling is shown in Figure 2.1 (c) strongest for a 180° bond angle and will weaken with the reduction of the bond angle until reaching a suppression at a bond angle of 90° according to the Goodenough-Kanamori-Anderson rules [4, 5, 6]. The hopping matrix for this exchange is referred to as t_{pd} hopping.

The strength of the superexchange process strongly depends on the onsite Coulomb potential U and the hopping energy t between different sites. The one-band Hubbard model [7] can capture the physics of a fermion system with a short-range repulsive interaction U given by:

$$H = - \sum_{i,j,\sigma} t_{ij} c_{i,\sigma}^\dagger c_{j,\sigma} + U \sum_i n_{i,\uparrow} n_{i,\downarrow} \quad (2.3)$$

where t_{ij} is the hopping energy from site i to site j , U the onsite Coulomb potential, $c_{i,\sigma}^\dagger$ ($c_{i,\sigma}$) are the creation (annihilation) operators at site i with spin σ and $n_{i,\sigma} = c_{i,\sigma}^\dagger c_{i,\sigma}$ is the number operator.

In the case of half filling ($U \gg t$, and n particles in n sites) the problem can be simplified by applying Dirac's formalism using perturbation theory [8]. This approach starts at the infinite U limit with each site being occupied by one particle; a Coulomb energy U is paid each time two particles occupy the same site and each particle has a probability t_{ij} of hopping from site i to site j . The resulting Hamiltonian does not explicitly depend on the spin resulting from the treatment of particle distinguishability in this approach and is provided by [8]:

$$H = \sum_n (-1)^{n+1} J_n P'_n \quad (2.4)$$

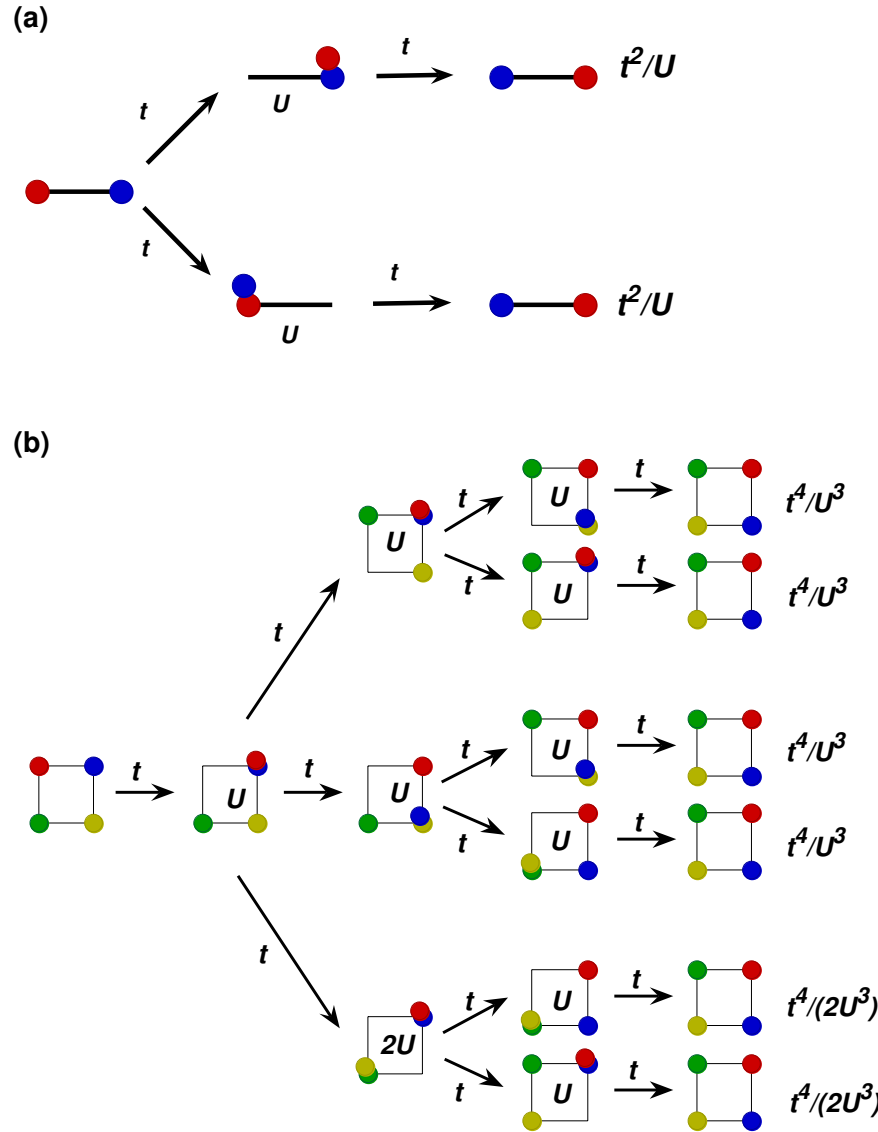


Figure 2.2: Possible permutation for (a) a two particle system and (b) a four particle system representing the cyclic exchange [9].

where P'_n is the permutation operator of the n particles given by $P'_n = (P_n + P_n^{-1})$ with P_n^{-1} being the reversed permutation which can be simplified for a two-particle process as $P_2 = P'_2$. J_n presents the exchange coefficient of n particles, i.e the sum of energies resulting in distinct permutation states. The possible permutations for a two-particle system are illustrated in Figure 2.2 (a) with the initial situation consisting of each particle occupying a different site with particle 1 (red) located at site i and particle 2 (blue) at site j . The two distinct pathways for the possible permutations are displayed in the

figure with the first hopping consisting of an energy cost of t/U and the second permutation of only t due to the empty site i resulting in a total energy cost of t^2/U for each permutation. The total exchange energy for a two-particle process is therefore: $\tilde{J}_2 = 2t^2/U$. The particle exchange Hamiltonian can be related to the spin Hamiltonian using the two-spin permutation operator [8] and by redefining the zero of the energy the constant can be omitted:

$$P_2 = \frac{1}{2}(1 + \sigma_i \cdot \sigma_j) = \frac{1}{2} + 2\mathbf{S}_i \cdot \mathbf{S}_j \quad (2.5)$$

where σ_i are the Pauli matrices and \mathbf{S}_i the spin operator (using $\sigma_i = 2\mathbf{S}_i$). This consideration leads to the spin Hamiltonian of:

$$H = \tilde{J}_2 P_2 = 2\tilde{J}_2 \mathbf{S}_i \cdot \mathbf{S}_j = J \mathbf{S}_i \cdot \mathbf{S}_j \quad (2.6)$$

with J presenting the spin exchange constant determined as $J = 4t^2/U$ for a two-spin interaction process.

An analog consideration can be carried out for a four particle cyclic permutation with the possible processes displayed in Figure 2.2 (b) [9]. There are 16 possible permutations involving an energy cost of t^4/U^3 (the 4 displayed in the figure and an additional 12 possibilities arising from the different choice of starting particles) where a clockwise permutation direction is chosen. In addition another 8 permutations exist with an energy cost of $t^4/(2U^3)$ due to a double occupancy during the first permutation resulting in a total energy of $\tilde{J}_4 = 20t^4/U^3$. The relationship to the spin operator only including the four operator terms characteristic of the cyclic exchange process is provided by [8]:

$$\begin{aligned} P_4 &\propto \frac{1}{2}[(\sigma_i \cdot \sigma_j)(\sigma_k \cdot \sigma_l) + (\sigma_j \cdot \sigma_k)(\sigma_l \cdot \sigma_i) - (\sigma_i \cdot \sigma_k)(\sigma_j \cdot \sigma_l)] \\ &= 4[(\mathbf{S}_i \cdot \mathbf{S}_j)(\mathbf{S}_k \cdot \mathbf{S}_l) + (\mathbf{S}_j \cdot \mathbf{S}_k)(\mathbf{S}_l \cdot \mathbf{S}_i) - (\mathbf{S}_i \cdot \mathbf{S}_k)(\mathbf{S}_j \cdot \mathbf{S}_l)] \end{aligned}$$

resulting in a total spin exchange energy coupling of $J=80t^4/U^3$ for a four spin operator cyclic exchange [9].

2.1.4 Magnetic Ordering

Without any exchange interactions the individual magnetic moments would be disordered at any temperature in the absence of magnetic field. Including exchange interactions produces non-vanishing moments below a critical temperature T_c leading to magnetic order. However, the exchange interactions in magnetic compounds can be rather complex exhibiting several different exchanges between ions. Additionally to the exchanges between neighboring ions, couplings between next-nearest ions have to be taken into account, although usually expected to be weaker due to a greater distance between the ions. The exact contribution of couplings strongly depends on the symmetry of the compound.

Magnetic structures important for this thesis include ferromagnetism consisting of a spontaneous magnetization with all magnetic moments aligned in the same direction, and the more common case of antiferromagnetism pictured as two interpenetrating sublattices. Within each sublattice the moments have the same magnitude and direction but the net moments of the two sublattices are opposite leading to a zero total moment.

The critical temperature T_c below which magnetic ordering occurs is known as the Curie temperature in ferromagnets and Neel temperature (often written as T_N) in antiferromagnets. By approaching the critical temperature from lower values the spontaneous magnetization (or in the case of the antiferromagnetism the magnetization of the sublattice) drops continuously to zero and just below T_c the magnetization can be described by a power law of $M(T) \sim (T_c - T)^\beta$ with $\beta = 1/8$ for the two-dimensional Ising model, and $\beta \sim 1/3$ for most three-dimensional systems [10].

Some structural arrangements cause competition between exchange interactions suppressing magnetic long-range order. These occur due to frustration effects where it is impossible to satisfy the different exchange interactions simultaneously and those appear in triangular and Kagome lattices causing the order to vanish completely or to develop only at very low temperatures.

2.2 Theories of Magnetism

2.2.1 Spin Wave Theory

An important theory describing the ferromagnet representing the simplest structure in magnetism was introduced as that of spin waves by Bloch [11]. In addition to modeling the low-lying excitations it is able to explain the deviation in spontaneous magnetization from its saturation value by an amount of $T^{3/2}$, a result known as Bloch's law [11].

For the ferromagnet the ground state is composed of all spins being aligned in the same direction (z direction) and an excitation can be created by reducing the spin z component at an individual site also defined as a spin deviation [12] presented by a spin flip in the case of $S = 1/2$. This causes an excitation of $\Delta S^z = 1$ which obey Boson commutation relations (due to the integer spin value). Spin deviations operators are conventionally introduced that create and annihilate a spin deviation. The common approach to spin waves follows the method first introduced by Holstein and Primakoff [12] where the Hamiltonian is rewritten in terms of spin deviation operators and a linear approximation is adopted for simplicity keeping only terms up to second order in the Hamiltonian. In the next step the Fourier transform of the spin deviation operators is imposed resulting in a second order but non-diagonal Hamiltonian. Diagonalizing this Hamiltonian leads to the normal modes of the magnetic system. The resulting excita-

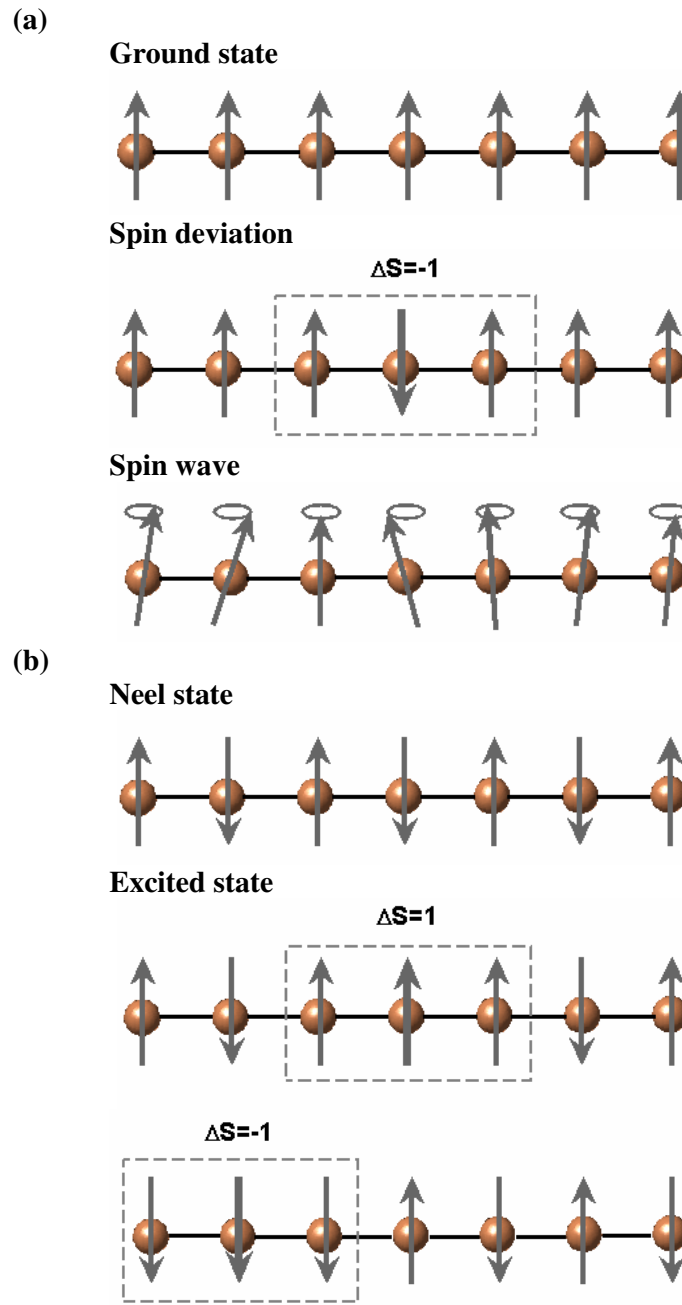


Figure 2.3: (a) Ferromagnet. Upper part: the ground state with all spins aligned in one direction. Middle part: spin deviation with one spin flipped in the opposite direction. Lower part: superposition of spin deviation (middle part) spread over the system resulting in the formation of a spin wave. (b) Antiferromagnet. Upper part: Neel state with alternating direction of spins. Lower parts: excited states with spin deviations on either sublattice. Normal mode excitation created as superposition (not shown).

tions are dispersive in reciprocal lattice wavevector \mathbf{Q} with well defined energies due to the non-vanishing transverse components and are also called spin waves. Neutrons

serve as an ideal probe to detect these spin waves and confirmed the Q^2 dependence for the spin wave excitation energy in ferromagnets (e.g. [13]). Figure 2.3 (a) illustrates the physical picture of the spin wave for a ferromagnetic system. The top part of Figure 2.3 (a) represents the ground state of a ferromagnetic spin-1/2 system with all spins aligned in the same direction, while the middle part introduces a spin deviation presented by one reversed spin. The last part shows the spin wave excitation as a superposition of the spin deviations introduced in the middle plot with it being spread over the system resulting in the observed dispersion.

Spin wave theory can also describe the excitations in an antiferromagnet, although this case is more complex because the Neel state is not the exact ground state and slight modifications have to be made to cover the existence of the two sublattices of the antiferromagnet. Since all spins are aligned in one direction on each sublattice the spin wave theory can be implemented the same way as for the ferromagnet but with two sets of spin deviation operators, one for each sublattice. The spin wave is presented as a superposition of states with a spin deviation on either lattice illustrated in Figure 2.3 (b). The top plot shows the Neel state of an antiferromagnet (in this case for simplicity 1D), while the other two plots present a spin deviation on either sublattice with the normal mode excitations obtained by a superposition of these states. Theory predicts, in contrast to the ferromagnetic case, the spin wave excitation energy to be linear in \mathbf{Q} at $Q=\pi$.

In Chapter 7 spin wave theory is used to calculate the excitations in the dimerized chain copper nitrate after reaching the second critical field transition (saturation) with all spins aligned in one direction.

2.2.2 Antiferromagnetic Spin Chain

While spin wave theory predicts fairly well the observed behavior in 3D systems, discrepancies in the excitation spectrum arise in low-dimensional systems where quantum effects dominate the behavior such as the 1D antiferromagnetic Heisenberg spin-1/2 chain. One of the key aspects of spin wave theory is the linear approximation with the excitations being formed as a superposition of single spin deviations only valid if two spin deviations have a greater energy than a single spin deviation justifying the approach of linear superposition for the excitations.

This situation applies to the case described in the previous section of the ferromagnets with the ground state consisting of all spins aligned in one direction and an excitation being composed of a single spin flip. This spin flip costs a finite energy allocated by the coupling constants leading to a higher energy cost for two spin deviations pictured as two single spin flips compared to only one spin deviation validating the use of spin wave theory. The spin-1/2 antiferromagnetic Heisenberg chain is an example of a low-dimensional antiferromagnet failing to develop long-range order and to express the excitations as a superposition of single spin deviations leading to the failure of spin wave theory.

The failure of spin wave theory will be explained for the case of the doubly degenerate Ising chain with the ground state composed as a superposition of the two Neel states as shown in Figure 2.4 (a). This can then be generalized to the more complex Heisenberg chain. The top part of Figure 2.4 (b) shows the excitation as expected from spin wave theory with one single spin deviation presented as a spin flip costing an energy of the coupling constant J and creating an excitation of $\Delta S = 1$. Due to the dimensionality of the chain the same situation can be reached by a state with several consecutive spins reversed, illustrated by the remaining plots of Figure 2.4 (b) with three and five spins

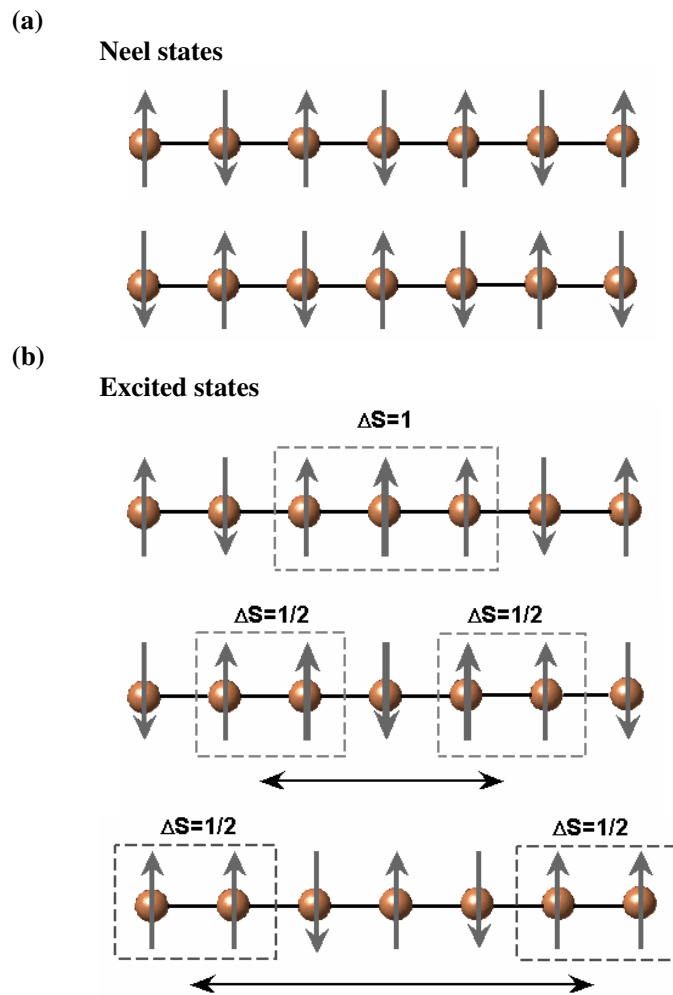


Figure 2.4: Spin-1/2 antiferromagnetic chain. (a) Doubly degenerate Neel states of the ground state for the Ising chain. (b) Possible excited states with all possessing the same energy J and spin-1. States are degenerate and thus have to be combined and diagonalized to find the eigenstates.

respectively reversed also leading to a $\Delta S = 1$ state with an energy J . These states are degenerate and have to be taken into account for the formation of an excitation explaining the failure of the spin-wave approach. Alternatively the excitations can be thought of as spin-1/2 domain walls (indicated by the dashed boxes) enclosing a different sized region of the sublattice. Including a small transverse field or coupling the domain walls can move through the system creating a dispersion relation associated with these moving domain walls which are also called solitons. Due to the condition of the change in spin number by unity in the neutron scattering process the solitons are created in pairs

with their total momentum and energy obtained as a sum from the individual wavevector and energy of each soliton. Because of the range of possibilities for the wavevector indicated by the black arrow in Figure 2.4 (b) and for the corresponding energy, the excitation is observed as a gapped continuum with the gap provided by J (still finite cost of spin flipping) and the width of the continuum by the size of the introduced transverse field [14].

Similar is true for the isotropic case of the Heisenberg chain with its excitations being spinons ($S = 1/2$ particles) in analog to the domain walls in the Ising chain but confined to half the Brillouin zone [15]. Again they are created as pairs resulting in the existence of a continuum lacking the spin gap due to strong quantum fluctuations and formation of a Luttinger Liquid. The upper and lower boundaries of the continuum are given by:

$$E^- = \pi J |\sin(\mathbf{Q} \cdot \mathbf{a})|$$

and

$$E^+ = 2\pi J |\sin(\mathbf{Q} \cdot \mathbf{a}/2)|$$

where \mathbf{a} is the lattice vector in the direction of the chain. The upper boundary E^+ can be viewed as two spinons each moving with momentum $\mathbf{Q}/2$, while the lower boundary represents one spinon with zero momentum and the other spinon with momentum of \mathbf{Q} [16]. The resulting excitation spectrum is provided in Figure 2.5. The spinons are fractional particles possessing a spin moment $S = 1/2$ and can be viewed as twists in the chain with two interpenetrating twists ensembling the pair creation of the spinons. Any small interchain coupling experienced in most real one-dimensional system will often cause long-range order and lift the degeneracy of the first excited states. Considering a coupling in the direction perpendicular to the chain would lead to a lower energy for the top part of Figure 2.4 (b) compared to the middle one due to the smaller number of reversed spins. Increasing the number of reversed spins causes a greater energy for an

excitation due to the coupling to the neighboring chains. In this case the lowest lying excitation is best described by a single spin flip also defined as a $S = 1$ magnon.

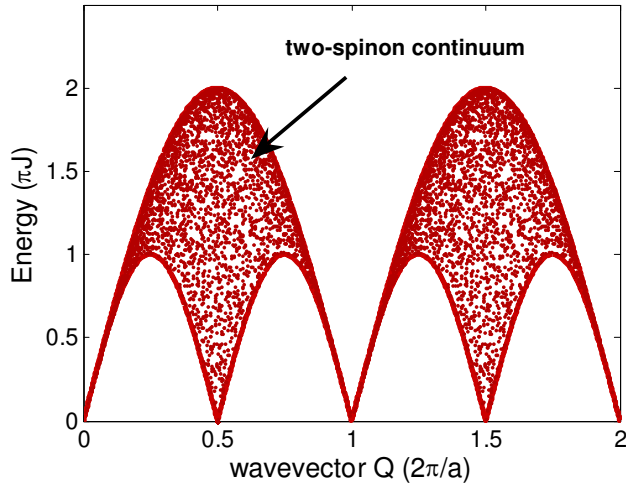


Figure 2.5: Excitations of the spin-1/2 Heisenberg antiferromagnetic chain in form of a two-spinon continuum.

2.2.3 Spin-Ladder

A spin ladder is a system defined as coupled spin-1/2 chains with the rungs being formed by neighboring spins of opposite chains as shown in Figure 2.6. This feature makes the spin-ladder an example of a quasi one-dimensional system providing a bridge between one- and two-dimensional materials [17]. Figure 2.6 (a) displays a two-leg ladder with two chains being coupled together while part (b) represents a three-leg ladder consisting of three combined chains. A comparison will illustrate the difference between even and odd leg ladders.

The most common structure is the two-leg ladder with its characteristics being extendable to even n -leg ladders and with the most important feature consisting of a spin gap in the excitation spectrum. The existence of the spin gap can be understood when focusing on the ‘strong coupling’ limit composed of a much larger rung coupling J_{rung}

compared to the leg coupling J_{leg} . This leads to the formation of spin singlets consisting of two spins forming an $S = 0$ state on each rung of the ladder, which is then weakly coupled to the singlets on neighboring rungs. An excitation is formed by breaking one of the singlets and promoting it into a triplet, two spins forming an $S = 1$ state, costing an energy of the order of the rung coupling and leading to an energy gap from the ground to the first excited state of the size of J_{rung} . For the opposite limit with a much stronger leg coupling the system can be viewed as isolated chains experiencing no spin gap in the excitation spectrum (e.g. [16]). Including a nonzero rung coupling features the instant appearance of the spin gap [18] with the gap found to be of the order of $J_{leg}/2$ in the isotropic limit [19, 20] which is the limit suggested to appear in most real systems due to the geometry of the ladder with equal distances of the rung and the leg.

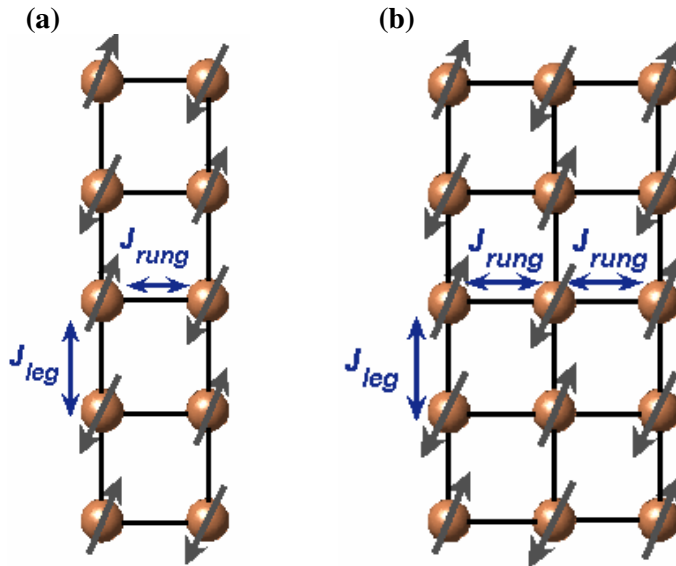


Figure 2.6: Spin ladder layout: (a) two-leg ladder with ground state consisting of spin singlets on each rung creating a gap in the excitation spectrum. (b) three-leg ladder presenting an odd leg ladder leading to a single spin chain and no gap in the excitation spectrum.

This result of the spin gap appearance can be generalized to any even n -leg ladder due to the singlet formation on the rungs and therefore resulting from an $S = 0$ ground state with an $S = 1$ first excited state. This spin gap decreases with increasing n re-

covering the gapless 2D plane necessary for $n \rightarrow \infty$ [21]. The situation is different for odd n -leg ladders consisting of a doubly degenerate ground state resulting from the two possible spin values of $S = \pm 1/2$ for each rung. This degree of freedom can be mapped onto a spin-1/2 chain [17] resulting in the gap-less excitation spectrum for the n -odd-leg ladder exhibiting the same low energy properties like the spin-1/2 Heisenberg chain with spinons as excitations [22, 23].

Hole-doping breaks the rung singlets costing an energy of rung coupling J_{rung} per singlet breaking. t - J calculations performed by Dagotto *et al* [19] showed to be energetically favorable to have two holes sharing one rung. A feature easily understood in the strong coupling limit with J_{rung} much larger than J_{leg} , as a rung sharing decreases the energy cost from two holes breaking two singlets to only one singlet breaking saving an energy cost of the order of J_{rung} .

References

- [1] F. Hund, *Line Spectra and Periodicity of the Elements*, Springer, Berlin (1927).
- [2] W. Heisenberg, *Z. Physik* **49**, 619 (1929).
- [3] P. W. Anderson, *Phys. Rev.* **79**, 350 (1929).
- [4] J. B. Goodenough, *Phys. Rev.* **100**, 564 (1955).
- [5] J. Kanamori, *J. Phys. Chem. Solids* **10**, 87 (1959).
- [6] P. W. Anderson, *Solid State Phys.* **14**, 99 (1963).
- [7] J. Hubbard, *Proc. Roy. Soc. London A* **272** (1963).
- [8] P. A. M. Dirac, *The Principles of Quantum Mechanics*, Clarendon Press, Oxford (1958).
- [9] A. M. Toader, *Ring Exchange in solid ^3He and La_2CuO_4* , PhD thesis, University of Liverpool (2005).
- [10] N. W. Ashcroft, and N. D. Mermin, *Solid State Physics*, Cornell University (1976).

- [11] F. Bloch, *Z. Phyisk* **61**, 206 (1930).
- [12] T. Holstein, and H. Primakoff, *Phys. Rev.* **58**, 1098 (1940).
- [13] R. N. Sinclair, and B. N. Brockhouse, *Phys. Rev.* **120**, 1638 (1960).
- [14] N. Ishimura, and H. Shiba, *Prog. Theor. Phys.* **63**, 743 (1980).
- [15] L. D. Faddeev, and L. A. Takhtajan, *Phys. Lett.* **85A**, 375 (1981).
- [16] D. A. Tennant, T. G. Perring, R. A. Cowley, and S. E. Nagler, *Phys. Rev. Lett.* **70**, 4003 (1993).
- [17] E. Dagotto, *Report on Progress in Physics* **62**, 1525 (1999).
- [18] T. Barnes, E. Dagotto, J. Riera, and E. S. Swanson, *Phys. Rev. B* **47**, 3196 (1993).
- [19] E. Dagotto, J. Riera, and D. J. Scalapino, *Phys. Rev. B* **45**, 5744 (1992).
- [20] R. M. Noack, S. R. White, and D. J. Scalapino, *Phys. Rev. Lett.* **73**, 882 (1994).
- [21] S. Chakravarty, B. I. Halperin, and D. R. Nelson, *Phys. Rev. B* **39**, 2344 (1989).
- [22] T. M. Rice, S. Gopalan, and M. Sigrist, *Europhys. Lett.* **23**, 445 (1993).
- [23] S. Gopalan, T.M. Rice, and M. Sigrist, *Phys. Rev. B* **49**, 8901 (1994).

Chapter 3

Neutron Scattering Theory

3.1 Introduction

Due to its characteristics the neutron serves as a powerful tool for exploring many important features in condensed matter systems; a subject covered in depth by many authors including Squires [1] and Lovesey [2]. The provision of neutrons can be achieved by either using a nuclear reactor or a spallation source where the latter is the method used in this thesis and its principles will be discussed in greater detail in a later section.

The neutrons produced using either one of these methods typically have an energy corresponding to the order of a typical excitation in a condensed matter system and changes in the neutron energy during an inelastic scattering process will provide information on the interatomic forces and the dynamics of these systems. The de Broglie wavelength determined by the particle mass of 1,0087 amu of the neutron is comparable to the interatomic spacing in solids giving rise to interference effects that offer insight into the structure of the scattering system.

The additional properties of the neutron include a zero charge and a spin value of 1/2 allowing an interaction with solids in two distinct ways. The first one is based on the zero charge of the neutron facilitating scattering from the nucleus via the nuclear

force. The second possibility of scattering is ensured by the magnetic moment of the neutron resulting in an interaction with the unpaired electrons of the atoms found in the system. While elastic neutron scattering provides information about the atomic structure due to the nuclear scattering and also about the magnetic structure due to the magnetic scattering, inelastic scattering provides insight into the lattice vibrations and magnetic excitations respectively.

In the next section, 3.2, the important concept of the cross-section, expressing the likeliness of a scattering event, is introduced, while section 3.3 studies the cross-section for the two interaction possibilities expressed via a nuclear and magnetic potential. The last section introduces the method of neutron scattering measurement for the time-of-flight method at a spallation source and provides a detailed explanation of the spectrometers used for the experiments described in the thesis.

3.2 Scattering Cross-Section

The fundamental quantity of any type of scattering process, and giving account for the number of scattering events, is the cross-section. The experimental arrangement for a neutron scattering experiment is presented in Figure 3.1 (a). An incident neutron with wavevector \mathbf{k} and energy E gets scattered by the sample obtaining a new state with wavevector \mathbf{k}' and energy E' while changing the sample state from state $|\lambda\rangle$ to $|\lambda'\rangle$ during this scattering process. A detector with an area A placed a distance R away from the sample collects the neutrons scattered into the solid angle with final energies between E' and $E'+\Delta E'$ and therefore measures the neutron intensity according to:

$$I = \Phi \left(\frac{d^2\sigma}{d\Omega dE'} \right) \Delta\Omega \Delta E'$$

with Φ being the incident flux and the quantity $d^2\sigma/d\Omega dE'$ the partial differential cross-section defined as number of neutrons scattered per second into the solid angle $\Delta\Omega$ with energies between E' and $E'+\Delta E'$, divided by the flux, solid angle and range of scattered energy.

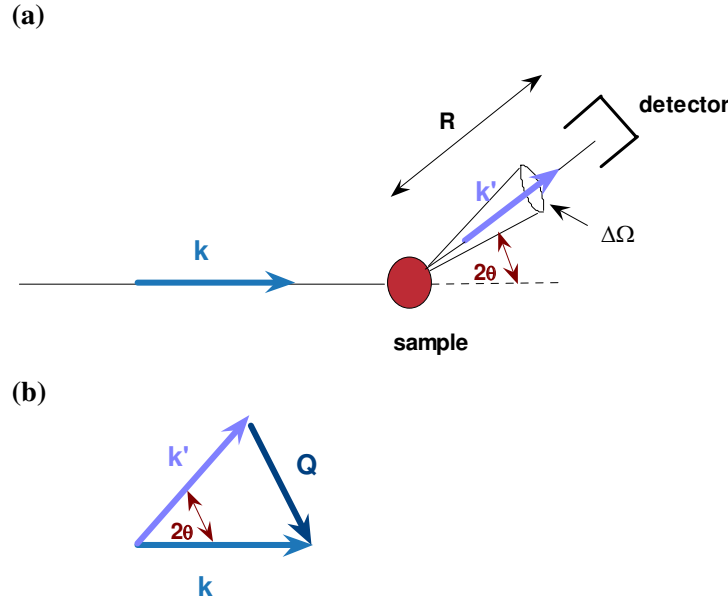


Figure 3.1: Schematic view of the scattering process. (a) Neutron scattering arrangement where incoming neutrons with wavevector \mathbf{k} are scattered by the sample. A detector, a distance R away from the sample and forming an angle of 2θ with the incident beam direction, detects only the scattered neutrons with a wavevector \mathbf{k}' . (b) Scattering triangle presenting the relation between the incoming and scattered wavevectors \mathbf{k} and \mathbf{k}' and the wavevector transfer \mathbf{Q} .

Since all the experiments performed for this thesis are inelastic experiments, the partial differential cross-section has to be introduced describing the most general case including the analyzing of the neutron energy. This is in contradiction to elastic experiments counting all neutrons and the differential cross-section $d\sigma/d\Omega$ is sufficient. The inelastic scattering experiments measure the partial differential cross-section directly and can be compared to predictions from theory.

Important for finding both the partial and the differential cross-section is an expres-

sion for the number of transitions from the initial state defined by \mathbf{k} for the neutron and λ for the system, to the final state given by \mathbf{k}' , λ' . While this transition is correct for the nuclear scattering, the change in spin state from σ to σ' also has to be taken into account in the case of the magnetic scattering. In this section a general expression for the cross-section valid for both scattering processes assuming the interaction of the neutron with the system via a potential V is provided. This expression is proportional to the number of transitions or rate $W_{\Lambda \rightarrow \Lambda'}$ of the system changing from the initial state $|\Lambda\rangle$ defined by \mathbf{k} , λ and σ to the final state $|\Lambda'\rangle$ by \mathbf{k}' , λ' and σ' enforced through the potential V and can be obtained from Fermi's Golden Rule given by:

$$W_{\Lambda \rightarrow \Lambda'} = \frac{2\pi}{\hbar} \rho_{\mathbf{k}'} |\langle \Lambda | V | \Lambda' \rangle|^2 \quad (3.1)$$

where $\rho_{\mathbf{k}'}$ is the density of states at final wavevector k' and energy E' . Fermi's Golden Rule is based on first order perturbation theory requiring weak scattering making a modification of the nuclear interaction potential into a pseudo-potential (discussed in the next section) necessary. For the determination of the density of states the concept of the ‘box normalization’ is adopted allowing only neutron states with a de Broglie wavefunction periodic in a box of volume V . The matrix element of equation 3.1 can be evaluated by expressing the neutron wavefunction as a plane wave according to $|\mathbf{k}\rangle = 1/V e^{i\mathbf{k} \cdot \mathbf{r}}$.

Using the definition of the differential cross-section representing the sum of all processes involving a change in neutron state from \mathbf{k} to \mathbf{k}' and from scattering system λ to λ' with the rate $W_{\Lambda \rightarrow \Lambda'}$, the differential cross-section can be calculated directly. Allowing also inelastic scattering an expression for the partial differential cross-section can be found including the energy conservation [1]:

$$\left(\frac{d^2\sigma}{d\Omega dE'} \right) = \frac{\mathbf{k}'}{\mathbf{k}} \left(\frac{m}{2\pi\hbar^2} \right) \sum_{\lambda' \sigma'} \sum_{\lambda \sigma} \rho(\sigma) \rho(\lambda) |\langle \mathbf{k}', \sigma', \lambda' | V | \mathbf{k}, \sigma, \lambda \rangle|^2 \delta(E_\lambda - E_{\lambda'} + \hbar\omega) \quad (3.2)$$

where the initial and final energy of the neutron, E and E' respectively, are related by $\hbar\omega = E - E' = \frac{\hbar^2}{2m} (k^2 - k'^2)$ and E_λ and $E_{\lambda'}$ are the initial and final energies of the scattering system.

3.3 Interaction Potentials

As mentioned in the previous section the neutron interaction with condensed matter can occur in two different ways. First, the neutron can be scattered by the strong nuclear potential of the nuclei due to a deep penetration depth into the material because of its zero charge. Second, due to the neutron's magnetic dipole moment it can be scattered by any magnetic moment present in the system. The discussion of the nuclear scattering is presented first.

3.3.1 Nuclear Scattering

To evaluate the partial differential cross-section a functional form for the potential $V(\mathbf{r})$ has to be found by considering the scattering of a single fixed nucleus [1]. These results can then be generalized to a j^{th} nucleus to take following form of the potential:

$$V_j(r) = \frac{2\pi\hbar}{m} b_j \delta(\mathbf{r} - \mathbf{R}_j) \quad (3.3)$$

illustrating the interaction between a neutron with position \mathbf{r} and the j^{th} nucleus at position \mathbf{R} where the quantity b_j is the bound scattering length of the j^{th} nucleus depending mainly on the particular nucleus. This form of the potential consisting of a delta function for each nucleus is known as the Fermi pseudo-potential and validates the use of Fermi's Golden rule based on a small potential for the first order approximation. It can be used due to the short-ranged nuclear force existing over the size of the nucleus which is ~ 10000 smaller than the typical de Broglie wavelength resulting in approximately isotropic scattering.

Using this form of the potential in equation 3.2 and expressing the energy delta function as a Fourier transform with respect to time and summing over all nuclei the partial differential cross-section can be obtained. Due to the fact that the system usually contains a large number of nuclei, small discrepancies from the average scattering length b_j occur leading to a division of the cross-section into two parts: a coherent part depending on the average value of b_j and an incoherent part presenting the deviation from the average.

$$\frac{d^2\sigma}{d\Omega dE'} = \left(\frac{d^2\sigma}{d\Omega dE'} \right)_{coh} + \left(\frac{d^2\sigma}{d\Omega dE'} \right)_{inc} = \frac{\mathbf{k}'}{\mathbf{k}} \frac{N}{4\pi} (\sigma_{coh} S(\mathbf{Q}, \omega) + \sigma_{inc} S_i(\mathbf{Q}, \omega)) \quad (3.4)$$

where

$$S(\mathbf{Q}, \omega) = \frac{1}{2\pi\hbar N} \sum_{j,j'} \int_{-\infty}^{\infty} \langle \exp(-i\mathbf{Q} \cdot \mathbf{R}_{j'}(0)) \exp(i\mathbf{Q} \cdot \mathbf{R}_j(t)) \rangle e^{-i\omega t} dt \quad (3.5)$$

and

$$S_i(\mathbf{Q}, \omega) = \frac{1}{2\pi\hbar N} \sum_j \int_{-\infty}^{\infty} \langle \exp(-i\mathbf{Q} \cdot \mathbf{R}_j(0)) \exp(i\mathbf{Q} \cdot \mathbf{R}_j(t)) \rangle e^{-i\omega t} dt \quad (3.6)$$

\mathbf{Q} presents the wavevector transfer illustrated in Figure 3.1 (b) and is given by:

$$\mathbf{Q} = \mathbf{k} - \mathbf{k}'$$

and the quantities σ_{coh} and σ_{inc} are the coherent and incoherent cross-sections respectively with σ_{coh} only depending on the average scattering length and σ_{inc} presenting the deviation from the average:

$$\sigma_{coh} = 4\pi \bar{b}^2 \text{ and } \sigma_{inc} = 4\pi(\bar{b}^2 - \bar{b}^2)$$

$S(\mathbf{Q}, \omega)$ is a correlation function and depends on the correlation of the *same* nucleus at different times and of *different* nuclei at different times giving rise to interference effects and therefore providing information on the structure of the system and its lattice excitations. $S_i(\mathbf{Q}, \omega)$ is called the self-correlation function and depends on the correlation between the positions of the same nucleus at different times and does not give rise to interference effects. For all experiments carried out in this thesis the incoher-

ent scattering presented by $S_i(\mathbf{Q}, \omega)$ results in an isotropic background in wavevector with its functional form deduced from fitting the data with a suitable background and a delta-function in energy modeled by a Gaussian due to experimental resolution.

3.3.2 Magnetic Scattering

The second possible interaction emerges from the magnetic dipole moment μ_n of the neutron and causes an interaction with ions possessing a net magnetic moment with an intensity comparable to the nuclear scattering. The magnetic dipole of the neutron is given by:

$$\mu_n = -\gamma \mu_N \sigma$$

where $\mu_N = e\hbar/2m_p$ is the nuclear magneton with m_p being the mass of the proton and e its charge. The gyromagnetic ratio is $\gamma = 1.913$ and σ the Pauli spin operator for the neutron with possible eigenvalues of ± 1 . The electrons in the system possessing both a spin and an orbital angular momentum produce a field given by the Biot-Savart law:

$$\mathbf{B}_i = -\frac{\mu_0}{4\pi} 2\mu_B \left(\nabla \times \left(\frac{\mathbf{s}_i \times \mathbf{R}_i}{R^3} \right) + \frac{\mathbf{l}_i \times \mathbf{R}_i}{R^3} \right) \quad (3.7)$$

\mathbf{B}_i is the magnetic field produced by the i^{th} electron a distance \mathbf{R} away, \mathbf{s}_i and \mathbf{l}_i are the spin and orbital angular momenta of the i^{th} electron and μ_B is the Bohr magneton defined as $e\hbar/2m_e$.

The scattering of the neutrons by the nuclear field can be ignored, because this field generated by the nuclear moments is about 2000 times smaller compared to the field produced by the angular moments. The first part of the bracket in equation 3.7 arises from the spin angular momentum while the second part occurs due to the angular momentum. The total field created by an ion is found by summing equation 3.7 over all its electrons leading to the change from \mathbf{s}_i to the total spin momentum \mathbf{S} and also from \mathbf{l}_i to the total angular momentum \mathbf{L} . Our case is simplified due to the fact that the materials

studied in this thesis, $\text{La}_4\text{Sr}_{10}\text{Cu}_{24}\text{O}_{41}$, $\text{Sr}_{2.5}\text{Ca}_{11.5}\text{Cu}_{24}\text{O}_{41}$ and $\text{Cu}(\text{NO}_3)_2 \cdot 2.5\text{D}_2\text{O}$, all possess $\mathbf{L} = 0$ due to orbital quenching and a total spin $\mathbf{S} = 1/2$ making only the spin consideration necessary.

The magnetic interaction potential needed for calculating the cross-section in equation 3.2 of a neutron with the j^{th} electron is given by:

$$V = \mu_n \cdot \mathbf{B}_j$$

where \mathbf{B}_j is the magnetic field generated by the total spin \mathbf{S}_j (and in the general case the total \mathbf{L}_j) of the j^{th} electron. Inserting this magnetic potential in equation 3.2 and after some lengthy algebra [1, 2] an expression for the cross-section for a compound only possessing one type of magnetic ion (in our case Cu^{2+}) and only a spin angular moment can be found:

$$\frac{d^2\sigma}{d\Omega dE'} = (\gamma r_0)^2 N \frac{k'}{k} \left(\frac{g}{2} F(\mathbf{Q}) \right)^2 \exp(-2W(\mathbf{Q})) \sum_{\alpha\beta} (\delta_{\alpha\beta} - \hat{Q}_\alpha \hat{Q}_\beta) S^{\alpha\beta}(\mathbf{Q}, \omega) \quad (3.8)$$

where $(\gamma r_0) = 5.29 \text{ fm}$ is constant, g is the Landé factor for the magnetic ion and $F(\mathbf{Q})$ is its magnetic form factor given by the Fourier transform of the density of unpaired electrons of a single magnetic atom and is rapidly falling off with \mathbf{Q} . The exponent $\exp(-2W(\mathbf{Q}))$ is called the Debye-Waller factor which can be neglected in most cases, as it falls less rapidly with \mathbf{Q} than the form factor. The main difference between the magnetic and nuclear cross-sections is in the geometrical term $(\delta_{\alpha\beta} - \hat{Q}_\alpha \hat{Q}_\beta)$ arising as a consequence of the neutron-electron interaction potential meaning that the neutron only couples to components of the magnetic moment perpendicular to the scattering vector \mathbf{Q} . $S^{\alpha\beta}(\mathbf{Q}, \omega)$ is the Fourier transform of the dynamical spin correlation function and is given by:

$$S^{\alpha\beta}(\mathbf{Q}, \omega) = \frac{1}{2\pi N} \sum_{i,j} \exp(i\mathbf{Q} \cdot (\mathbf{R}_i - \mathbf{R}_j)) \int_{-\infty}^{\infty} \exp(i\omega t) \langle S_i^\alpha S_j^\beta(t) \rangle dt \quad (3.9)$$

where $S_j^\beta(t)$ is the time dependent operator for the β -component of the spin of the j^{th} magnetic ion.

A further simplification is achieved because the magnetism in $\text{La}_4\text{Sr}_{10}\text{Cu}_{24}\text{O}_{41}$, $\text{Sr}_{2.5}\text{Ca}_{11.5}\text{Cu}_{24}\text{O}_{41}$ and $\text{Cu}(\text{NO}_3)_2 \cdot 2.5\text{D}_2\text{O}$ can be approximated by a Heisenberg Hamiltonian where the total z component is conserved resulting in a vanishing of the dynamical correlation function $S^{\alpha\beta}(\mathbf{Q}, \omega)$ if $\alpha \neq \beta$ and in the relation $S^{zz}(\mathbf{Q}, \omega) = S^{xx}(\mathbf{Q}, \omega) = S^{yy}(\mathbf{Q}, \omega)$. This last expression is not valid when applying magnetic field as is the case in Chapter 7 requiring some modification. For zero field and zero temperature measurements the dynamical correlation function $S^{\alpha\beta}(\mathbf{Q}, \omega)$ can now be expressed as [1]:

$$S^{\alpha\alpha}(\mathbf{Q}, \omega) = \sum_{\lambda, \lambda'} \left| \langle \lambda' | S_{\mathbf{Q}}^\alpha | \lambda \rangle \right|^2 \delta(\hbar\omega - E_{\lambda'} + E_\lambda) \quad (3.10)$$

where λ and λ' are the ground and the first excited states respectively and $S_{\mathbf{Q}}^\alpha$ is given by the Fourier transform of the spin angular operator :

$$S_{\mathbf{Q}}^\alpha = \frac{1}{\sqrt{N}} \sum_j S_j^\alpha \exp(i\mathbf{Q} \cdot \mathbf{R}_j) \quad (3.11)$$

3.4 Spallation Source

As mentioned in the introduction section the neutron experiments presented in this thesis were undertaken at a spallation source, i. e. at ISIS, Rutherford Appleton Laboratory. For the spallation process a heavy metal target (in our case tantalum) is bombarded with a pulse of highly energetic protons from an accelerator (synchrotron) and the protons hitting the nucleus in the target material trigger an intranuclear cascade. During this process the nucleus is placed in a highly excited state and evaporates nucleons (mainly neutrons) to release the excess energy. Some nucleons will leave the target and are used for experiments, while others trigger further nuclear reactions [4].

3.5 Time-of-Flight Spectrometer

The neutron scattering experiments presented in this thesis are performed on time-of-flight spectrometers allowing an accurate measurement of the cross-section and a comparison to theoretical models where applicable. All measurements were performed on a spallation source allowing a large range of incoming energies and wavevector transfers providing an assessment of the magnetism involved in the system. Two different types of geometries are possible with the time-of-flight method: First the direct geometry method selecting a fixed incoming energy and second the indirect geometry allowing a range of incoming energies and fixing the final energy. Both are used in this thesis with the direct geometry set-up in Chapters 4, 5 and 6 and the indirect geometry in Chapters 7 and 8. The direct geometry is introduced first.

3.5.1 Direct Geometry

In the direct geometry an experimental arrangement is chosen to measure the final energy and the wavevector transfer by selecting a single incoming energy [3, 4].

The correlation function $S(\mathbf{Q}, \omega)$ depends on two quantities (compare to equation 3.9, the energy transfer $\hbar\omega$ and momentum transfer \mathbf{Q}) which can be related considering the scattering triangle in Figure 3.2:

$$\begin{aligned}\mathbf{Q}^2 &= \mathbf{k}^2 + \mathbf{k}'^2 - 2\mathbf{k}\mathbf{k}' \cos(2\theta) \\ \frac{\hbar^2\mathbf{Q}^2}{2m} &= E_i + E_f - 2\sqrt{E_i E_f} \cos(2\theta)\end{aligned}$$

Expressing in terms of the initial energy E_i by using $E_i = \hbar\omega - E_f$:

$$\frac{\hbar^2\mathbf{Q}^2}{2m} = 2E_i - \hbar\omega - 2\cos(2\theta)E_i\sqrt{(E_i - \hbar\omega)} \quad (3.12)$$

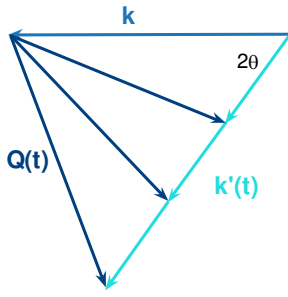


Figure 3.2: Scattering triangle: relating the incoming wavevector \mathbf{k} and the outgoing wave vector \mathbf{k}' with the wavevector transfer \mathbf{Q} .

The components involved in direct geometry instrumentations are illustrated in Figure 3.3 [3]. During the spallation a burst of very fast, high energy neutrons are produced. Moderators are used to slow down these neutrons resulting in energies able to measure the magnetic excitations. An example is H_2O at room temperature which uses the high scattering cross-section of hydrogen for moderation. One of the main advantages of a spallation source is the large flux of high energy neutrons. To prevent a loss of these high energy neutrons during the moderation process the beam is under-moderated leading to a split into two components: a Maxwellian component caused by the moderation and an epithermal component consisting of a high energy flux due to weakly moderated neutrons. The next stage of the neutron path is the background chopper consisting of a rotating block of steel reducing background scattering arising from γ -rays during the collision of the proton beam with the target and also from fast neutrons thermalizing within the spectrometer. Most of this background is significantly reduced by closing the beam by the background chopper upon the proton beam hitting the target capturing the majority of the γ -rays and some ultra-fast neutrons. The actual monochromation and initial energy selection of the incoming neutrons is performed by the Fermi chopper consisting of an aluminum drum with alternating sheets of a highly absorbing material such as boron and sheets of aluminum transparent to neutrons. The rotation velocity and phasing of the chopper determines the desired initial energy E_i and wavevector k_i establishing the flux and the resolution of the neutron beam. The

background arising from air scattering is reduced by creating an evacuated sample environment and beam tubes. The final energy of the neutrons can be calculated by the velocity of the scattered neutrons determined by the time-of-flight method measuring the time between the interaction with the sample and the arrival at the detectors.

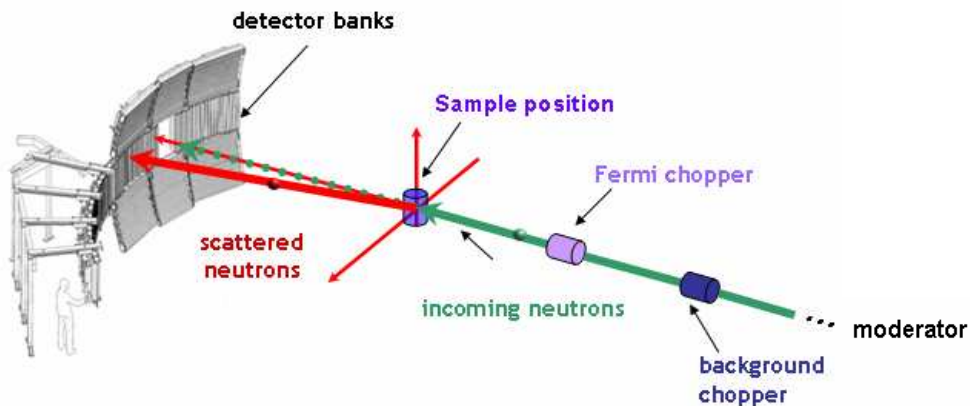
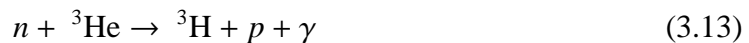


Figure 3.3: Diagram for the direct geometry. After being cooled by the moderator the neutrons hit the background chopper eliminating γ -rays and ultra-fast neutrons. The initial energy is selected by the velocity of the rotating and phasing of the neutron transparent blades of the Fermi chopper before hitting the sample. The scattered neutrons are detected by large detector banks.

The direct geometry spectrometer used in this thesis is made up of ^3He detector banks counting the neutrons detected according to following reaction:



The advantage of the helium detectors is their high efficiency for low energy neutrons covering the range selected for most inelastic experiments and also their low efficiency for γ -rays and very high energy neutrons [4].

3.5.2 Indirect Geometry

In the indirect geometry the scattered neutrons are energy-analyzed choosing a final energy in contrast to the direct geometry with its initial energy selection. The incom-

ing neutrons cover a range of energies chosen via two disk choppers, in analogy to the Fermi chopper in the direct geometry, and after the scattering process an analyzer crystal determines the final energy of the neutrons. Only the neutrons with the energy and wavelength satisfying the Bragg condition according to equation 3.14 are directed towards the detector banks. The experimental arrangement is shown in Figure 3.4.

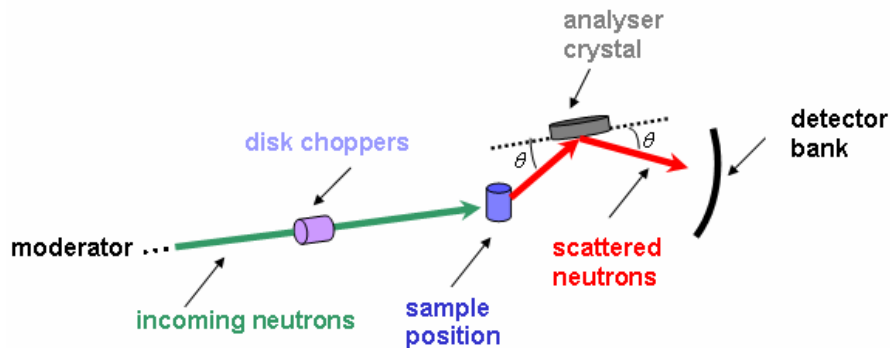


Figure 3.4: Arrangement for an indirect spectrometer for inelastic neutron scattering measurements. The incoming neutron beam after being cooled by the moderator consists of neutrons with a range of initial energies limited by two disk choppers. After being scattered by the sample the final energy of the neutrons is selected by an analyzer crystal with the detected neutrons fulfilling the Bragg condition of the analyzer.

The analyzer crystal selects the final energy of the neutrons according to the Bragg condition:

$$\lambda = 2d \sin(\theta) \quad (3.14)$$

leading to a final energy of:

$$E_f = \frac{p^2}{2m} = \frac{h^2}{2m\lambda} = \frac{\pi^2 \hbar^2}{2d^2 \sin^2(\theta)} \quad (3.15)$$

where d is the spacing of the analyzer crystal. With the condition of the scattering triangle of Figure 3.2 the energy transfer $\hbar\omega$ and momentum transfer \mathbf{Q} can be related for the calculation of the correlation function $S(\mathbf{Q}, \omega)$ and the initial energy E_i can be calculated from the time-of-flight method.

For the experiments presented in this thesis an instrument using a moderator of liquid hydrogen cooled to 25K was chosen creating a large flux of long-wavelength cold neutrons providing the fairly low energies needed for the study of Cu(NO₃)₂ · 2.5D₂O [5]. The two disk choppers are used to define a range of initial neutron energies incident upon the sample. This white beam of neutrons gets scattered by the sample with a final energy selection by the analyzer crystal. Typically the analyzer crystal consists of graphite and is cooled to reduce background contributions from thermal diffuse scattering. ³He detectors are also used for the detection of the neutrons on the instrument. The advantage of the indirect geometry compared to the direct geometry is the good resolution and its limitation is the less flexible initial energy range.

References

- [1] G. L.Squires, *Introduction to the Theory of Thermal Neutron Scattering*, Dover, New York, (1996).
- [2] S. W. Lovesey, *Theory of Neutron Scattering from Condensed Matter*, Oxford University Press, Oxford, (1987).
- [3] R. S. Eccleston, R. Osborn, and R. I. Bewley, *The HET mini-manual*, RAL report RAL-94-117, (1999).
- [4] G. Kadar, and L. Rosta, *Lecture Notes to Neutron Scattering Introductory Course*, Prosperitas Press, Budapest, (2003).
- [5] M. T. F. Telling, and K. H. Anderson, *The OSIRIS User Guide*, ISIS Facility, Rutherford Appleton Laboratory, (2005).

Chapter 4

Study of the Doped Edge-Sharing Cuprate Chain

4.1 Motivation

Copper oxide chains have received a lot of attention in connection with the physics of high- T_c cuprates. These chain materials can be divided into two categories according to their structure: The first concerns the corner-sharing Cu-O chains consisting of CuO_4 units coupled through 180° Cu-O-Cu bonds leading to the connection of the corners of neighboring units. These chains have been studied extensively due to their closeness to high- T_c cuprates identified as the 2D version of this chain type and are now well modeled by experiment and theory. The edge-sharing Cu-O chain is the second possible structure with the CuO_4 units sharing their edges leading to a 90° Cu-O-Cu bond coupling [1]. The different bond angle for the edge-sharing chain changes the electronic and magnetic properties of the system compared to the corner-sharing chain and until now these properties are not well understood.

The spin-ladder compound $(\text{Sr}, \text{Ca}, \text{La})_{14}\text{Cu}_{24}\text{O}_{41}$ embodies one system of choice consisting of the edge-sharing chains and additionally Cu_2O_3 ladder layers. The advantage of this system is the determination of the hole-doping level by varying the composition through a change of the La to the Sr/Ca content. Although consisting of

two different structures, the majority of the holes reside on the more electronegative chains [2] allowing a study of a slightly doped chain - in our case $\text{La}_4\text{Sr}_{10}\text{Cu}_{24}\text{O}_{41}$ with a hole content of $\sim 20\%$ and determination of the effects due to hole-doping. This investigation should help to answer the interesting question of the nature of the hole with its integration into the chain, i.e. as a static hole or as a charge density wave (CDW) strongly depending on the coupling within the chain consisting of the nearest and next-nearest neighbor couplings, the hopping of the hole, and the electrostatic energy between neighboring hole sites. It should be possible to describe the exact hole hopping and electrostatic energy with the help of the three-band Hubbard model providing a great insight into the question of hole behavior upon doping.

The discovery of superconductivity in the $(\text{Sr}, \text{Ca}, \text{La})_{14}\text{Cu}_{24}\text{O}_{41}$ family has caused additional interest although only observed for the special hole-doping conditions of $\text{Sr}_{0.4}\text{Ca}_{13.6}\text{Cu}_{24}\text{O}_{41}$ and of $\text{Sr}_{2.5}\text{Ca}_{11.5}\text{Cu}_{24}\text{O}_{41}$ and under pressure [3, 4]. Ca doping causes the holes to be transferred from the chain to the ladder system [5, 6, 7] explaining the great interest in the study of the ladder materials due to their similarity to the superconductivity in 2D cuprate systems. It is believed that the interplay between chains and ladders plays an important role in the understanding of the mechanism for the superconductivity in the ladder systems.

4.2 Background

The compounds of the $(\text{Sr}, \text{Ca}, \text{La})_{14}\text{Cu}_{24}\text{O}_{41}$ families are composed of two substructures consisting of chains and ladders which share a supercell with lattice parameters $a = 11.36 \text{ \AA}$, $b = 12.92 \text{ \AA}$ and $c_{\text{super}} = 27.45 \text{ \AA}$. The two substructures can be distinguished by their c parameter, as 10 chain segments compared to 7 ladder segments occupy the supercell leading to different parameters along the c direction: $c_{\text{chain}} = 3.92 \text{ \AA}$

and $c_{\text{ladder}}=2.75 \text{ \AA}$ [8, 9]. The chain crystal structure of $\text{La}_4\text{Sr}_{10}\text{Cu}_{24}\text{O}_{41}$ [9] is shown in Figure 4.1 and consists of chains staggered in the c direction in contradiction to the chain structure of the parent compound $\text{Sr}_{14}\text{Cu}_{24}\text{O}_{41}$ composed of neighboring chains shifted only marginally in the c direction.

The ladder excitation spectrum consist of a gap of ~ 27 meV [10] facilitating a separation between the chain and the ladder spectra according to their different energy and wavevector contributions. The formal valence of Cu for our composition is 2.08 resulting in approximately two holes per formula unit in the system, i.e. one hole per five chain spins. The holes are attracted to the more electronegative chains [2] leaving the ladder for our composition hole-free [11] and thus leading to a slightly doped chain material.

A very important feature for the edge-sharing chain crucial for the coupling within the chain is the bond angle between neighboring Cu-O-Cu bonds. According to the Goodenough- Kanamori- Anderson rules [12, 13, 14] the nearest-neighbor (NN) spin interaction J_{NN} (compare Figure 4.1) changes from antiferromagnetic (AFM) to ferromagnetic (FM) for the angle of the Cu-O-Cu bond approaching 90° . This transition results from a reduction of the AFM Anderson's superexchange interaction (compare Section 2.2) due to the orthogonality of the bond. The bond angle for the undoped compound is determined to be $\theta \sim 91^\circ$ [1] giving rise to the expectation of a FM NN coupling and additionally a weaker AFM NNN exchange through the Cu-O-O-Cu bonds [1].

Susceptibility and resistivity measurements on $\text{La}_{6-y}\text{Sr}_y\text{Ca}_8\text{Cu}_{24}\text{O}_{41}$ reveal that the undoped sample ($y=0$) and the slightly doped sample $\text{La}_4\text{Sr}_2\text{Ca}_8\text{Cu}_{24}\text{O}_{41}$, equivalent in valence to our compound, share the same chain characteristics. The susceptibility and resistivity data for both y -values can be described with a model consisting of a FM NN intrachain coupling ($J_{NN} = -21 \pm 2$ meV for $y=0$ and $J_{NN} = -20 \pm 2$ meV for $y=2$) and

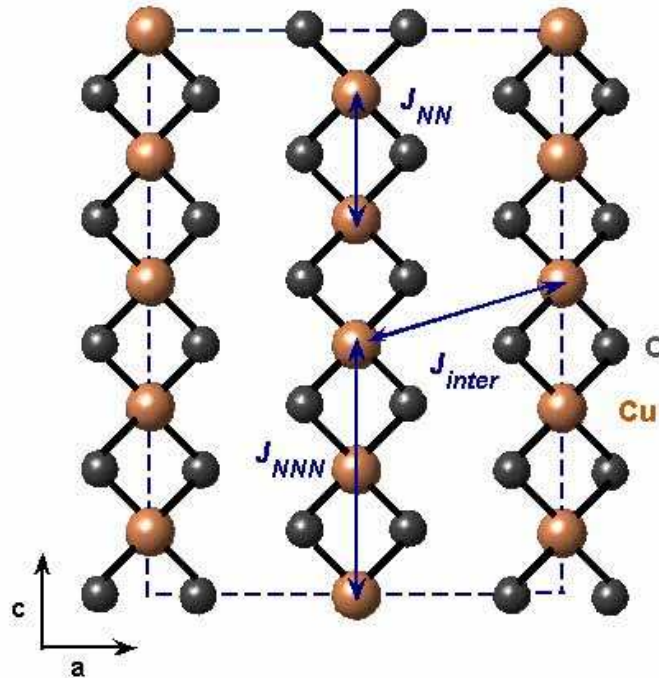


Figure 4.1: Arrangement of the chain structure of the undoped version of $\text{La}_4\text{Sr}_{10}\text{Cu}_{24}\text{O}_{41}$ in the $a^*\text{-}c^*$ plane. The big spheres represent the copper ions and the small spheres the oxygen. The blue dashed lines indicates the unit cell in the (010) plane for the a axis and half the unit cell in the c axis.

an AFM interchain coupling ($J' = 36 \pm 4$ meV). A crossover to a negligible interchain coupling is found for higher doping of $y=4$ [2]. The effect of substituting Sr^{2+} for Ca^{2+} does not change the overall valence, but causes the chain and the ladder layers to move further apart due to a greater ionic radius of Sr compared to Ca [5] and important when studying the hole transfer with doping. Theoretical calculations for $\text{La}_6\text{Ca}_8\text{Cu}_{24}\text{O}_{41}$ based on a three-band Hubbard model find a FM NN coupling of $J_{NN} = -21.5$ meV and an AFM NNN coupling of $J_{NNN} = 7.8$ meV [1]. In contradiction inelastic neutron scattering measurements on $\text{La}_5\text{Ca}_9\text{Cu}_{24}\text{O}_{41}$ performed by Matsuda *et al* [15] claim opposite coupling including a weak AFM NN coupling of $J_{NN} = 0.20$ meV, a weak FM NNN coupling of $J_{NNN} = -0.18$ meV and the strongest coupling consisting of an AFM NN interchain coupling $J_{inter} = 0.68$ meV and a NNN interchain coupling half this size.

4.3 Experimental Details

Single crystals of $\text{La}_4\text{Sr}_{10}\text{Cu}_{24}\text{O}_{41}$ were grown at the Leibniz-Institute for Solid State and Material Research, Dresden using the ‘Traveling Solvent Floating Zone’-method in a four mirror optical furnace and 9 bar oxygen pressure. For the melt a solvent disk of 30% mol (Sr, La)O and 70% mol CuO with a Sr/La ratio equal to the feed rods are used. The feed rods are cylindrical polycrystalline rods prepared by cold pressing and sintering of the powder mixture. The cooling rate was 0.8-2 mm/h yielding single crystals which have an elliptical cross-section with the short axis about 4 mm and the long axis about 5 mm and are about 50 mm long [16].

The inelastic neutron measurements on $\text{La}_4\text{Sr}_{10}\text{Cu}_{24}\text{O}_{41}$ were performed on the MAPS spectrometer at ISIS, Rutherford Appleton Laboratory, U.K. presenting a spectrometer with a direct geometry as introduced in Section 3.5.1. Three single crystals of total mass of ~ 15 g were co-aligned using the Four-Circle diffractometer E5 at the Hahn-Meitner-Institute, Berlin. The samples were orientated with the $(0, k, l)$ reciprocal plane horizontal and the c direction (chain direction) perpendicular to the incident neutron beam k_i resulting in an accurate alignment of the three crystals with a mosaic spread of 0.5° in the b^*-c^* plane and 1° in the a^*-c^* plane. The reciprocal lattice vectors a^* , b^* and c^* are given by $a^* = 2\pi(b \times c)/(a \cdot (b \times c))$, $b^* = 2\pi(c \times a)/(b \cdot (c \times a))$ and $c^* = 2\pi(a \times b)/(c \cdot (a \times b))$ defining the wavevector transfer along these axis to be Q_a (in units of $2\pi/a$), Q_b (in units of $2\pi/b$) and Q_c (in units of $2\pi/c$) respectively, a notation used throughout this thesis. Data were collected for incident energies $E_i = 30$, 50, and 100 meV monochromated with a Fermi chopper frequency of 300 Hz at a base temperature of $T = 10$ K. Additionally a high temperature run of $T = 150$ K was performed at incident energy of $E_i = 100$ meV to identify the magnetic signal versus phonon scattering.

4.4 Measurement and Results

4.4.1 Background Subtraction

A suitable background subtraction is of great importance due to the expected weak magnetic signal of the chain and also because of interference effects with the ladder

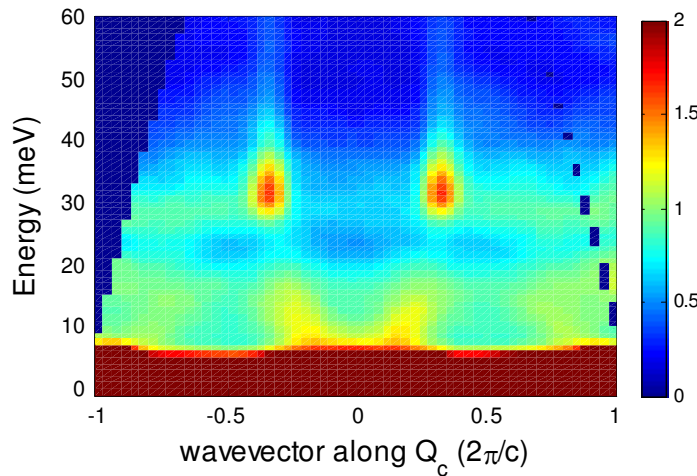


Figure 4.2: Color plot along the chain wavevector Q_c without any background subtraction.

signal at certain wavevectors. Figure 4.2 displays the data without any background subtraction revealing the less intense magnetic excitation spectrum dominated by incoherent scattering. The chain signal can be identified starting at $Q_c=0,\pm 1$ and becoming apparent above the incoherent line revealing the features of a dispersion relation, while the intense, sharp signal appearing at $E \sim 30$ meV and wavevectors of $Q_c = -0.4$ and $Q_c = 0.4$ results from ladder scattering indicated by the gap and the wavevector. The non-magnetic background can be taken around $Q_c=0$ due to the prediction of the sum rule [17] confirming the vanishing of the correlation function at this wavevector. The periodicity of the chain lattice allows this sum rule to also hold at $Q_c = \pm 1$ (in units of $2\pi/c$, a notation used throughout this thesis) leading to a background obtained by interpolating rods around $Q_c=0\pm 0.05$ and $Q_c=1\pm 0.05$ consisting of regions characterized by the zero magnetic signal.

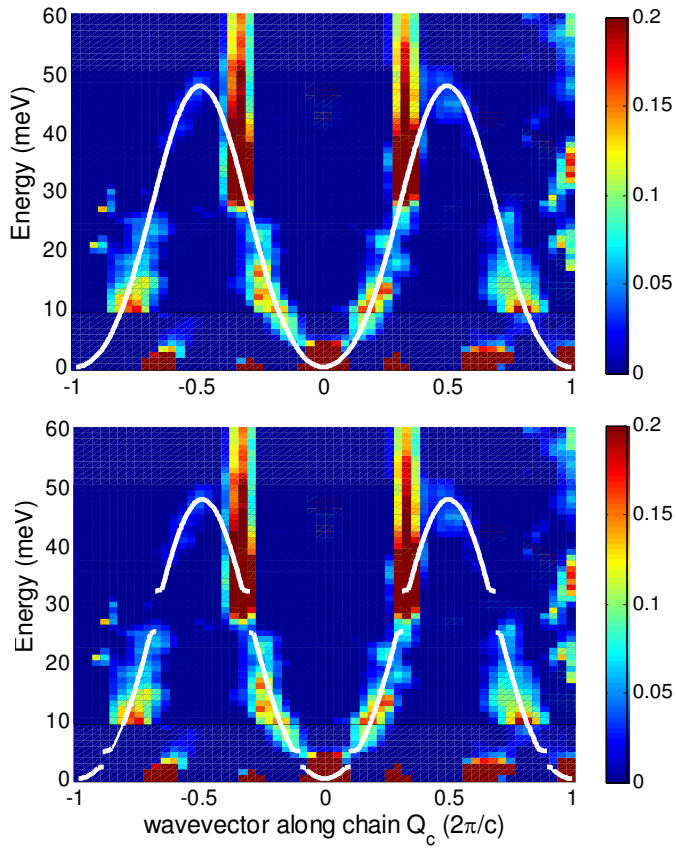


Figure 4.3: Color plot of the background subtracted data along the chain direction Q_c . The upper part is the theoretical obtained dispersion curve for the undoped chain, while the lower part describes the dispersion as expected for the presence of holes.

The resulting background subtracted data is displayed in Figure 4.3 revealing the dispersion of the chain in the c direction. The high-intensity streaks starting at $E \sim 30$ meV originate from ladder scattering and are ignored for the analysis of the chain. The white curve in the top part of the figure is the fitted dispersion for an undoped chain while the curve in the bottom part of the figure displays the dispersion including the presence of the holes; both curves will be discussed in detail in a later section.

For the determination of the dimensionality of the chain the dependence of the wavevector perpendicular to the chain (along the a direction) Q_a has to be investigated using a narrow integration region along Q_c necessary to ensure a correct assessment of

the Q_a relation. Unfortunately missing detectors made a thorough analysis impossible, but estimates from the data lead to the conclusion of a very small dispersion in the a direction with a maximal antiferromagnetic coupling of ~ 2 meV in good agreement with the data obtained by Matsuda [15].

4.4.2 Dispersion Relation

Using the background subtracted data enables an extraction of the chain dispersion relation along Q_c by taking constant energy cuts. A typical cut is shown in Figure 4.4 performed for an energy of $E = 8 \pm 1$ meV and integrated over the perpendicular Q_a direction to maximize the extracted intensity valid due to the negligible dispersion along this direction.

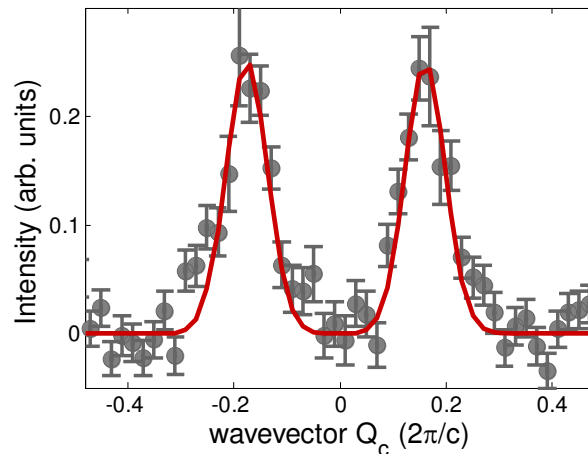


Figure 4.4: Typical cut along the Q_c wavevector direction for an energy of $E = 8 \pm 1$ meV. The solid line through the data presents two fitted Gaussians used for determination of the peak position.

The solid red line presents two least square Gaussians fitted through the data determining the peak positions at wavevectors $Q_c = -0.172$ and 0.165 . Repeating this procedure for several energies the experimental dispersion relation as shown in Figure 4.5 is obtained with the light red data points derived from an initial energy of $E_i = 50$ meV and

the dark red points from an initial energy of $E_i = 100$ meV. The gray curve is the fitted theoretical dispersion relation obtained for an undoped chain discussed in the following section.

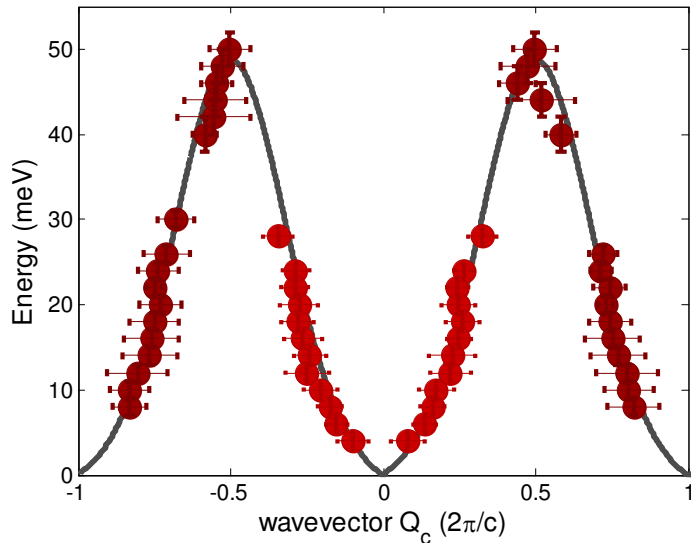


Figure 4.5: Experimental data points for the chain dispersion relation. Gray curve indicates the theoretical determined dispersion curve for an undoped chain.

4.5 Analysis

4.5.1 Fitting Without Holes

In this first stage of the analysis the chain is treated as a pure 1D chain ignoring the existence of holes. This approach is valid due to the low hole density in the system allowing a perturbative treatment of the holes. A first investigation of the dispersion relation along the c direction leads to the conclusion of a dominant FM chain coupling J_{NN} supported by the energy minimum at $Q_c = 0$ (compare Figure 4.5). However, using a pure FM exchange does not capture all of the features of the experimentally obtained data resulting in a necessary modification of the dispersion by introducing a NNN coupling J_{NNN} . The NNN coupling can be added perturbatively due to the

dominance of the FM exchange supported by an overall good description of the data using only a pure FM coupling. This leads to the following dispersion relation along the c direction:

$$\omega_{chain} = -J_{NN}(1 - \cos(Q_c \cdot c)) - J_{NNN}(1 - \cos(2Q_c \cdot c)) \quad (4.1)$$

where a negative J presents a FM exchange coupling and a positive J the AFM counterpart. The second term in the dispersion relation presents the NNN coupling indicated by the spin separation of $2c$ (compare Figure 4.1). By fitting equation 4.1 to the experimentally extracted data points of Figure 4.5 a FM NN coupling of $J_{NN} = -24.0 \pm 1.2$ meV and an AFM NNN exchange of $J_{NNN} = 2.7 \pm 0.3$ meV can be extracted. The good agreement between this theoretically calculated dispersion and the data is presented in the top part of Figure 4.3 and in Figure 4.5 with the dispersion of equation 4.1 and the fitted exchange couplings included as the white and gray curve respectively. As mentioned in the previous section, the upper boundary of the interchain coupling can be estimated as $J_{inter} \sim 2$ meV [15] which is very weak compared to the strong FM intrachain coupling J_{NN} leading to a 1D treatment of the system. From these considerations the resulting minimal spin Hamiltonian can be written as:

$$H = \sum_i (J_{NN} \mathbf{S}_i \cdot \mathbf{S}_{i+1} + J_{NNN} \mathbf{S}_i \cdot \mathbf{S}_{i+2}) \quad (4.2)$$

4.5.2 Fitting With Holes

The next stage of the analysis focuses on the effects of the presence of the holes in the chain by identifying the differences between the dispersion of the pure 1D chain as obtained in the previous section and the data. Figures 4.3 and 4.5 illustrate the overall good agreement between the dispersion for the undoped chain and the data with the only discrepancy presented by the gaps in the dispersion visible at wavevectors $Q_c = 0.1, 0.3, 0.7$ and 0.9 . Because the dispersion for the undoped chain is continuous,

the gaps must result from the presence of holes in the chain with the wavevector of the gaps strongly depending on the doping level. Confirmation between the wavevector of the gaps and the doping is provided by considering the transformation of the dispersion into the reduced Brillouin zone (BZ) scheme illustrated in Figure 4.6 with the gray curve presenting the chain dispersion as obtained for the undoped case over one reciprocal unit cell of size $2\pi/c$. The doping of $\text{La}_4\text{Sr}_{10}\text{Cu}_{24}\text{O}_{41}$ consists of one hole per five lattice sites leading to an effective unit cell of $5c$ for the doped chain compared to c in the undoped case.

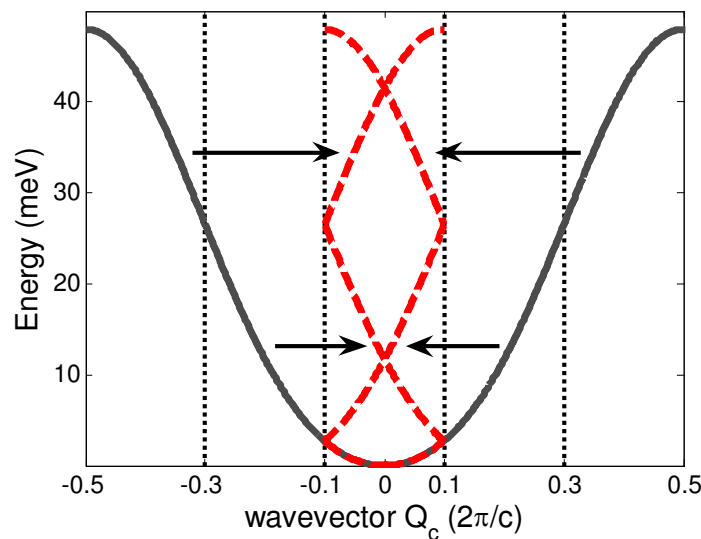


Figure 4.6: Dispersion relation (gray curve) folded into 1st BZ (dashed lines at -0.1 and 0.1) indicated by black arrows. The resulting folded dispersion curve is shown by the red dashed curve.

This determines the width of the BZ to be $2\pi/5c$ for the doped version indicated by the dashed vertical lines in Figure 4.6 and identifies the characteristic hole wavevectors at $Q_c = \pm 0.1, \pm 0.3, \pm 0.5$ and also $Q_c = \pm 0.7, \pm 0.9$ for the extended zone. The focus in the reduced scheme is on the 1st BZ centered symmetrically around $Q_c = 0$ where the dispersion relation has been folded back into indicated by the black arrows in the figure and resulting in the red dashed curve. The presence of the holes in the chain introduces a periodic potential at the characteristic wavevectors where the effect of this

potential is to introduce energy gaps at the characteristic hole wavevectors. By translating this approach into the reduced BZ scheme these gaps appear at the boundary of the 1st BZ at energies corresponding to the characteristic hole wavevectors. Transforming this gapped curve into the experimentally observed zone ($2\pi/c < Q_c < 2\pi/c$) results in the white curve of the lower part of Figure 4.3 and by comparing with the data a very good agreement between experiment and theoretical approach is apparent. A thorough identification of the size of the gaps should provide an indication of the potential but for an accurate determination of the gaps a higher statistic data set is necessary. Our approach of associating a periodic potential with the holes translated into gaps in the dispersion relation is valid due to the perturbative treatment of the holes. This is comparable to the tight-binding model of an electron in a solid with the size of the gap being a direct measure of the potential. The difference in our case is the projection of the hole potential onto the magnetic scattering assuming a modulation in the coupling constants due to the presence of the holes.

4.5.3 Ground State

After determining the coupling constants the consistency of the ground state, i.e. the spin arrangement of the system is of great importance. In analog to the previous section the undoped chain is considered first with its results being generalized to the doped version. The dispersion relation for the undoped chain can be thought of as a superposition of a FM component consisting of $-J_{NN}(1 - \cos(Q_c \cdot c))$ and an AFM component presented by $-J_{NNN}(1 - \cos(2Q_c \cdot c))$. Depending on the ratio of the coupling constants several possibilities of the spin arrangement of the ground state are possible. Knowing that the NNN coupling is AFM determines the condition of the ratio for keeping an overall FM ground state. The key characteristics of the FM spin arrangement is the dispersion minimum at $Q_c = 0$ and by including an AFM contribution a shift to an

incommensurate wavevector will occur upon a certain value of J_{NNN} due to the dispersion maximum at $Q_c = 0$ for an AFM contribution. The condition for keeping an overall ferromagnetic ground state is:

$$\frac{d\omega}{dQ_c} = -|J_{NN}|Q_c \sin(Q_c \cdot c) + |J_{NNN}|2Q_c \sin(2Q_c \cdot c) = 0 \quad (4.3)$$

with the minimum at $Q_c = 0$ and where the property of the FM coupling consisting of $J_{NN} = -|J_{NN}|$ and for the AFM coupling of $J_{NNN} = |J_{NNN}|$ have been used. The solution for a stable FM spin arrangement is found for $|J_{NNN}| \leq |J_{NN}|/4$ with higher values of $|J_{NNN}|$ leading to an incommensurate wavevector dependence. Our chain parameters of $J_{NN} = -24$ meV and $J_{NNN} = 2.7$ meV fulfill this condition leading to an overall FM spin arrangement confirmed by the commensurate wavevector dependence of our data and also seen by Matsuda *et al* [15].

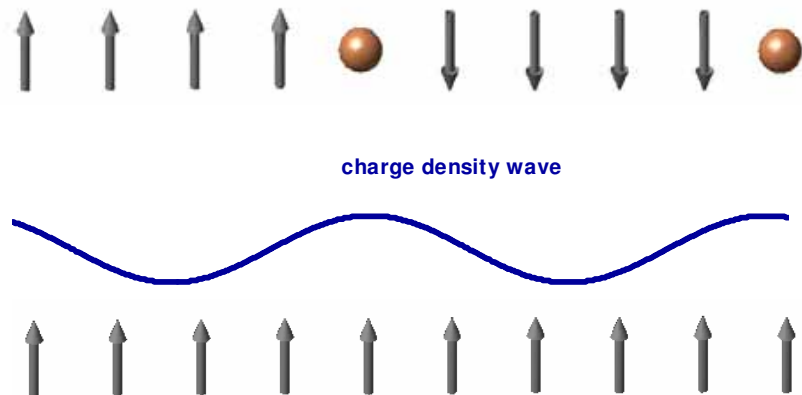


Figure 4.7: Possible hole integration. Upper part: Static hole with an AFM exchange through the hole. Lower part: Hole included in the chain as CDW with a maximum for the hole probability at every 5th lattice site.

After considering the undoped case and determining the condition for an overall FM ground state, the doped version of the chain is investigated. Crucial for the behavior of the spin arrangement is the nature of the hole and from the determination of the coupling constants with a FM NN and an AFM NNN coupling two contrary possibilities

for the hole integration into the chain and resulting ground state are possible, both are displayed in Figure 4.7. The upper part of Figure 4.7 assumes static holes spread evenly throughout the chain to minimize the Coulomb repulsion resulting in a hole located at every 5th lattice site and enclosing a four spin unit. The dominant exchange in this unit is the FM NN coupling leading to an arrangement with all spins pointing in the same direction in their four-spin unit as indicated in the figure. However, the presence of the hole will suppress the FM NN coupling between units allowing only the AFM NNN coupling resulting in reversed spin directions of neighboring units. This arrangement would lead to a shift to an incommensurate wavevector in the dispersion relation with the same reasoning as presented in the discussion of the undoped chain earlier. Since this shift is not observed in our data or by Matsuda *et al* [15], the possibility of the hole entering the chain as a static hole can be ruled out. The second possibility for the holes to be included into the chain is illustrated in the lower part of Figure 4.7 with the hole presented as a charge density wave (CDW) with the highest probability of the hole location every 5th site in analog to the static case. This allows a spin arrangement of an overall FM ground state associated with a commensurate wavevector in agreement with our and Matsuda's [15] findings which leads to the conclusion of the hole entering the chain as a CDW.

4.5.4 Energy Treatment of Hole Hopping

This section includes a more general approach for the treatment of the nature of the hole by investigating the energy cost of hole hopping for both a FM and an AFM coupling between neighboring four-spin units.

Including the hole statically allows an evaluation of the energy cost for the hole hopping performed for both configurations. For simplicity only the NN coupling is considered valid due to the dominance of this coupling. The first configuration present-

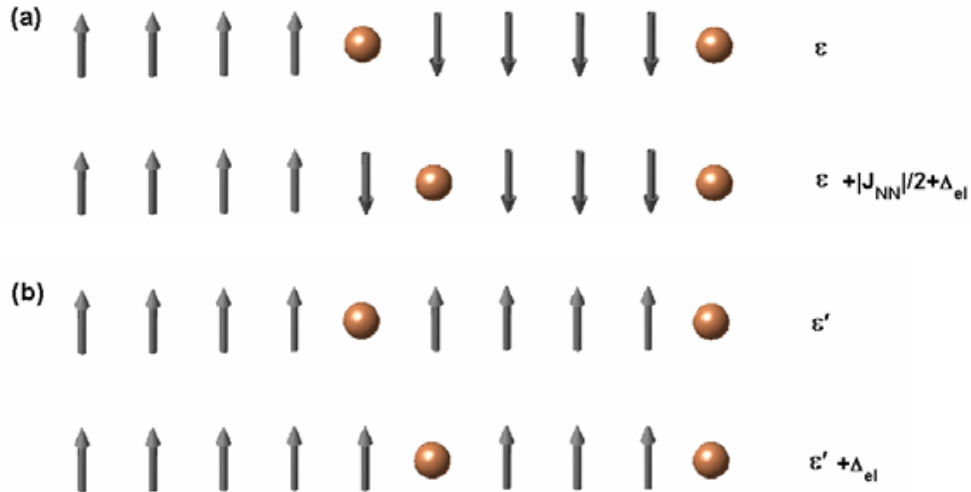


Figure 4.8: Energy cost for hole hopping for (a) the AFM coupling through the hole and (b) the FM coupling through the hole leading to a CDW behavior.

ing the AFM coupling through the hole is illustrated in the top part of Figure 4.8 (a), while the second one consisting of the FM coupling is shown in the top part of Figure 4.8 (b). Comparing the two arrangements reveals the AFM coupling through the hole being energetically favorable as established by Eccleston *et al* in $\text{Sr}_{14}\text{Cu}_{24}\text{O}_{41}$ where a weak AFM coupling of ~ 10 meV through a static hole is seen [18] and also confirmed by our AFM NNN coupling. These considerations lead to a lower ground state energy for the AFM option ($\epsilon < \epsilon'$). However, including a hole in the chain will introduce a hopping matrix element influencing the ground state energy differently for both configurations illustrated by the energy cost of a hole hopping from position i to $i + 1$ as presented in the lower part of Figure 4.8 (a) and (b). The energy cost of the hole hopping for the AFM arrangement is $|J_{NN}|/2 + \Delta_{el}$. For an explanation consider the spin arrangement in the lower part of Figure 4.8 (a). Moving the hole from position i to $i + 1$ breaks the unit to the right of the original hole position costing an energy of $|J_{NN}|/4$. The singled-out spin is added to the neighboring unit with an energy cost of $|J_{NN}|/4$ due its AFM alignment resulting in a total energy cost of $|J_{NN}|/2$ for the spin configuration. Additional to the spin the energy cost associated with the hole movement has

to be considered where the energy of a hole hopping from position i to $i + 1$ is defined by Δ_{el} . This results in a total energy cost for the hole hopping in the AFM arrangement of $|J_{NN}|/2 + \Delta_{el}$ higher than the ground state energy ϵ . In the FM case as displayed in the lower part of Figure 4.8 (b) the energy cost of breaking a unit is equalized by the energy gain of adding the spin FM to the neighboring unit leading to a total energy cost of only Δ_{el} higher than the ground state energy ϵ' . Very important for the energy comparison between the FM and the AFM hole coupling is the size of Δ_{el} providing a measurement for the probability of the hole hopping. This can be estimated by calculating the Coulomb difference for the hole hopping from i to $i + 1$ for a large chain with 10000 sites where the Coulomb energy strongly depends on the dielectric constant ϵ_τ . Calculating the energy for free space (without including ϵ_τ) for our chain material finds an energy of $U \sim -104$ meV where $\Delta_{el} = \frac{1}{\epsilon_\tau} U$ and since ϵ_τ can take values of 7-100 [19], Δ_{el} is of the order of a few meV and smaller than the dominant FM NN exchange leading to the occurrence of hole hopping. The resulting ground state can be formed by an admixture of states with different hole positions as sketched by the two states in part (a) or in part (b). However mixing the states for a FM coupling through the hole as presented in part (b) can have a lower ground state energy than the AFM counterpart (part (a)) if ϵ' is quite close in size to ϵ leading to a smaller difference in the ground state energies than the additional energy cost of $|J_{NN}|/2$ occurring for the AFM hole coupling. This is the case in our compound since the energy difference between the ground states must be small compared to $|J_{NN}|/2$ due to the lack of an incommensurate wavevector shift and confirmed by the small AFM NNN coupling. The low value of Δ_{el} confirms the likeliness of hole hopping leading to a CDW behavior rather than a static hole configuration.

4.6 Discussion

Our data of the edge-sharing chain system embodied by $\text{La}_4\text{Sr}_{10}\text{Cu}_{24}\text{O}_{41}$ confirms the different behavior between the edge-sharing and the corner-sharing chains. While the corner-sharing chains are dominated by a strong AFM NN coupling in the order of a couple of 100 meV (e.g. ~ 200 meV as found in the corner-sharing chains Sr_2CuO_3 and SrCuO_3 [20] due to strong superexchange), the edge-sharing chains experience a much weaker FM NN coupling and an even weaker AFM NNN coupling as predicted by bond-angle considerations [1] and consistent with our results of $J_{NN} = -24.0 \pm 1.2$ meV and $J_{NNN} = 2.7 \pm 0.3$ meV.

Comparing our results with the previous measurements of the same doping level performed by Carter *et al* [2] for $\text{La}_4\text{Sr}_2\text{Ca}_8\text{Cu}_{24}\text{O}_{41}$ find an agreement in the FM coupling between our $J_{NN} = -24.0 \pm 1.2$ meV and Carter's $J = -20 \pm 2$ meV, but differences are established in the NNN and the interchain coupling. While our AFM NNN coupling of $J_{NNN} = 2.7 \pm 0.3$ meV is introduced for the first time in these chain materials, a strong interchain coupling of $J = 36 \pm 4$ meV is established by Carter in contrast to our very weak, negligible interchain coupling. An explanation confirming this weak interchain coupling, the dominant FM NN and the weaker AFM NNN coupling is provided considering the orbital arrangement of the edge-sharing chain as displayed in Figure 4.9.

Because of the location of the chains in the a^*-c^* plane, the consideration of the planar Cu-O bonds presented by the $3d_{x^2-y^2}$ orbital for the Cu^{2+} ion and the p_x and p_y orbitals for the O^{2-} ion are sufficient as introduced in Section 2.1.3. The $\text{Cu}3d_{x^2-y^2}$ is illustrated by the copper color orbitals in Figure 4.9, while the $\text{O}2p_x$ and the $\text{O}2p_y$ are indicated by the light and dark gray orbitals respectively. The total NN coupling can be obtained by a sum of a FM and an AFM contribution. The FM coupling can

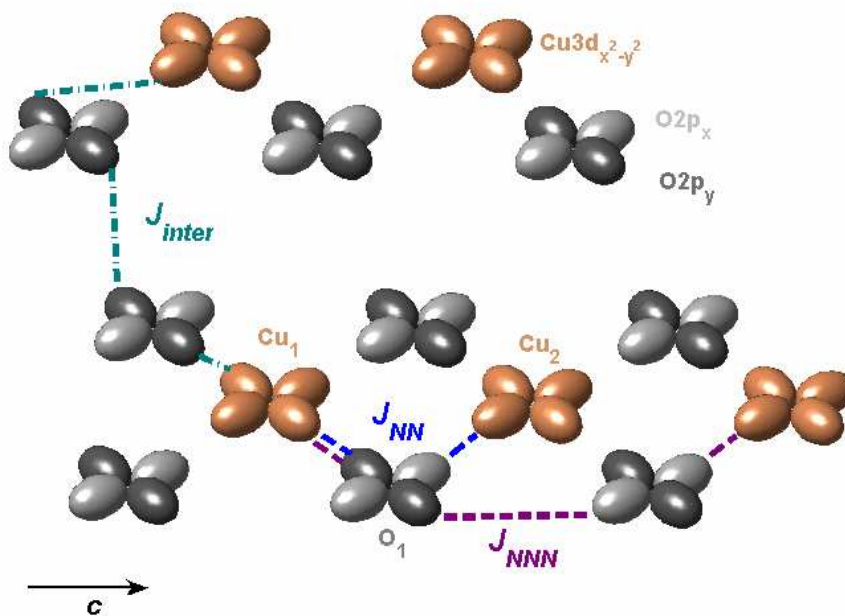


Figure 4.9: Orbital arrangement for the edge-sharing chain. Included are the possible exchange paths for the Anderson's superexchange for the case of the NN coupling J_{NN} indicated by the blue dashed line, for the NNN coupling J_{NNN} by the purple dashed line and the interchain coupling J_{inter} by the cyan dashed-dotted line.

be derived from two mechanisms: The first one occurs from Hund's rule coupling between oxygen sites and the second one from a direct exchange between the copper and the oxygen orbitals [1]. For the Hund's rule coupling a hybridization between the $3d_{x^2-y^2}$ of the Cu_1 site (compare Figure 4.9) and the $2p_y$ orbital of the O_1 and also between the neighboring $3d_{x^2-y^2}$ of the Cu_2 site with $2p_x$ orbital of the same oxygen O_1 site (compare Figure 4.9) is possible with Hund's rule demanding the spins in the different $O2p$ orbitals to align FM. The direct exchange arises from an overlap between the Cu_1 orbital with the $2p_x$ of the O_1 orbital due to the large size of oxygen causing a FM alignment to minimize Coulomb repulsion. The AFM contribution occurs through Anderson's superexchange process due to a possible hybridization between the $Cu3d$ and $O2p$ orbitals. For this contribution to occur the $Cu-O-Cu$ bond has to be considered with a possible pathway presented in Figure 4.9 by the blue dashed line. Shown is a strong overlap between the $3d_{x^2-y^2}$ orbital of the Cu_1 ion with the $2p_y$ orbital of the O_1

ion and the neighboring Cu ion overlaps with the $2p_x$ orbital of the same O ion (O_1), but a pathway from the $2p_x$ orbital to the orthogonal $2p_y$ orbital necessary for the AFM coupling to occur is not possible due to the orthogonality of the O orbitals. A direct path between the $3d_{x^2-y^2}$ of the Cu orbital along the y axis and the $2p_x$ of the O orbital is negligible due to the bond angle of approximately 90° ($\theta=91^\circ$) suppressing the AFM superexchange almost entirely leading to an overall FM NN coupling mediated through the direct exchange and the Hund's rule coupling considerably contributing to this FM exchange. The NNN coupling can occur due to a superexchange coupling facilitated through a Cu-O-O-Cu bond as shown by the purple dashed lines in Figure 4.9. The overlap between the two O_2p orbitals is possible due to the existence of a common O_2p orbital (seen better for an orbital rotation of 45°) enabling a weak AFM NNN exchange J_{NNN} possible through the hybridization between the Cu3d and O_2p orbitals. A similar pathway is accessible for the interchain coupling J_{inter} indicated by the cyan dashed-dotted curve in Figure 4.9, but this coupling is expected weaker than J_{NNN} due to the larger separation between the two O_2p orbitals, a feature also presented in Figure 4.1. These orbital considerations define the upper boundary for the interchain coupling to be smaller than J_{NNN} explaining the non-dispersive behavior along the a direction as seen in our data and also found by Matsuda [15].

Our findings for the coupling constants are consistent with the three-band Hubbard model calculations performed for the hole-free chain compound $La_6Ca_8Cu_{24}O_{41}$ based on orbital consideration [1]. The following couplings for the chain have been extracted from these calculations: a FM NN of $J_{NN} \sim -21.5$ meV, an AFM NNN of $J_{NNN} = 7.8$ meV and a FM interchain coupling of $J_{inter} \sim -3$ meV. While the FM NN is in very good agreement with our results, the NNN coupling is smaller in our compound possibly resulting from the hole doping. The interchain coupling strongly depends on the distance of the neighboring chains and is consistent with the estimate of the inter-

chain coupling in our compound.

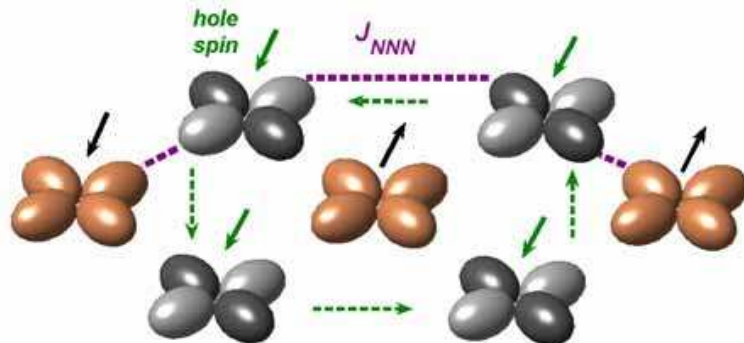


Figure 4.10: Formation of a Zhang-Rice singlet. The hole is located on the oxygen site (green arrow) and can form a non-magnetic singlet with the hole spin on the copper site. An AFM NNN coupling is possible through the Cu-O-O-Cu path indicated by the purple dashed line.

Very important for the energy treatment of the hole hopping leading to the CDW behavior rather than a static hole configuration as introduced in Section 4.5.4, is the weak AFM coupling of ~ 10 meV through a static hole as found from $\text{Sr}_{14}\text{Cu}_{24}\text{O}_{41}$ [18]. This coupling is the result of including a hole into the chain causing the formation of a Zhang-Rice singlet [21] as illustrated in Figure 4.10. It is energetically favorable for the hole to sit on the oxygen site indicated by the green arrows and due to the symmetric arrangement of the oxygen around the copper site, a hole hopping probability is evident shown by the dashed green arrows. The hole on the oxygen site can form a singlet with the hole on the copper site causing a non-magnetic unit and referred to as Zhang-Rice singlet [21]. An AFM coupling between the two spins on the neighboring copper sites is possible due to a superexchange pathway through a Cu-O-O-Cu bond indicated by the purple dashed line in the figure. The double pathway causes this coupling to be rather weak, but stronger than our determined AFM NNN J_{NNN} due to the intermediate non-magnetic unit.

A comparison with the inelastic neutron scattering (INS) results of Matsuda *et al* [15] studying the similar composition $\text{La}_5\text{Sr}_9\text{Cu}_{24}\text{O}_{41}$, consisting of a lower doping

level with only one hole per unit chain, reveals nominal differences in the exchange constants. Matsuda claims the couplings to consist of a weak AFM NN coupling of $J_{c_1} = 0.2$ meV, a comparable FM NNN of $J_{c_2} = -0.18$ meV and the strongest exchange to be a AFM NN interchain coupling of $J_{inter} = 0.68$ meV with its NNN counterpart being half this size, all in strong contradiction to our results. The intrachain couplings J_{c_1} and J_{c_2} are determined by a fitted dispersion through only a few experimentally extracted data points along the chain direction [15], similar to the procedure introduced in this chapter but lacking the high density of the extracted points in our analysis. Only a very limited region from $Q_c = 0$ to 0.1 is chosen resulting in a very unreliable fitting and precluding an exact determination of the coupling constants. However, comparing Matsuda's limited data along this direction with our data for the same range reveals an agreement and also confirms the commensuration of the system and therefore the interpretation of the spin arrangement. The determination of the interchain coupling is performed over a wider range in the a direction resulting in a reliable determination of the interchain exchanges justifying the 1D character of the chain.

Remarkable is the large FM exchange of $J_{NN} = -24$ meV found in our chain compound resulting from the strong FM coupling between O2p orbitals based on Hund's rule, the direct exchange contribution and the bond angle of approximately 90° ($\theta = 91^\circ$) suppressing any AFM contribution due to Anderson's superexchange. A FM coupling of this size has not been seen before and was not considered to be possible explaining the difficulty in the determination of the coupling constants in our chain structure. Our results should also help clarify the discussion about the exchanges in other edge-sharing chain materials such as the similar structure material Li_2CuO_2 with the situation similar to our chain material prior to this investigation consisting of two diverse views about the exchange constants. While some experimental results in Li_2CuO_2 [22, 23] claim a weak AFM NN, a weak FM NNN and a dominant interchain coupling, other experi-

mental and theoretical findings [1, 24] indicate a fairly large FM NN ($J_{NN} = -11 \pm 2$ meV and -10 meV respectively), and a weaker AFM NNN ($J_{NNN} \sim 10$ meV and 6.2 meV) exchange. The latter possibility has been doubted before due to the large FM exchange, but is consistent with our results in the chain structure of $\text{La}_4\text{Sr}_{10}\text{Cu}_{24}\text{O}_{41}$ with the lower FM coupling resulting from a slightly higher bond angle of $\theta = 94^\circ$ in Li_2CuO_2 (compare to $\theta = 91^\circ$ in $\text{La}_4\text{Sr}_{10}\text{Cu}_{24}\text{O}_{41}$) enabling a small AFM contribution from Anderson's superexchange. This comparison and our findings provide a strong indication for a strong and dominant FM exchange coupling also being present in Li_2CuO_2 .

Drawing a comparison between the results for our compound and other doping levels could help forming an understanding for the chain dynamics in the superconducting materials $\text{Sr}_{0.4}\text{Ca}_{13.6}\text{Cu}_{24}\text{O}_{41}$ and $\text{Sr}_{2.5}\text{Ca}_{11.5}\text{Cu}_{24}\text{O}_{41}$ being responsible for the hole reservoir for the ladder structures. The only chain compositions understood so far are $\text{Sr}_{14}\text{Cu}_{24}\text{O}_{41}$ consisting of 6 holes in the system nearly all identified on the chain [18] and now $\text{La}_4\text{Sr}_{10}\text{Cu}_{24}\text{O}_{41}$. The exchange in $\text{Sr}_{14}\text{Cu}_{24}\text{O}_{41}$ is dominated by an AFM coupling $J_1 \sim 11.4$ meV between two spins coupled through a Zhang-Rice singlet and a weaker FM exchange of $J_2 \sim -1$ meV between spins coupled through two Zhang-Rice singlets. While in $\text{Sr}_{14}\text{Cu}_{24}\text{O}_{41}$ the holes are static and bound into the system, the holes in our chain behave according to a CDW leading to a spread over several sites. Nominally the two superconducting materials have the same valence as $\text{Sr}_{14}\text{Cu}_{24}\text{O}_{41}$, but inserting Ca causes holes to migrate from the chain to the ladder structure with the exact amount unknown resulting in a chain composition with doping level between the two known cases. Having established these limiting cases should help the investigation of the chain structure in the superconducting compounds providing insight into the interesting question of the hole reservoir in these compounds.

4.7 Conclusion

In this chapter the magnetic excitations of the chain substructure in $\text{La}_4\text{Sr}_{10}\text{Cu}_{24}\text{O}_{41}$ have been studied by INS. The dispersion relation along the chain direction could be modeled with a 1D dispersion including a dominant FM NN coupling and a much weaker AFM NNN exchange. The two holes per unit chain are established to enter the chain as a CDW leaving gaps in the dispersion at characteristic doping-level specific wavevectors presenting for the first time a successful modeling of a doped cuprate system. For future experimental work a high statistics measurement would be of great use to link the size of the gap to the potential introduced by the presence of the holes. This experimental work on $\text{La}_4\text{Sr}_{10}\text{Cu}_{24}\text{O}_{41}$ successfully established for the first time the very strong FM coupling also claimed by orbital considerations based on three-band Hubbard calculations.

References

- [1] Y. Mizuno, T. Tohyama, S. Maekawa, T. Osafune, N. Motoyama, H. Eisaki, and S. Uchida, *Phys. Rev. B* **57**, 5326 (1998).
- [2] S. A. Carter, B. Batlogg, R. J. Cava, J. J. Krajewski, W. F. Peck Jr., and T.M. Rice, *Phys. Rev. Lett.* **77**, 1378 (1996).
- [3] M. Uehara, T. Nagata, J. Akimitsu, H. Takahashi, N. Môri, and K. Kinoshita, *J. Phys. Soc. Jpn.* **65**, 2764 (1996).
- [4] T. Nagata, M. Uehara, J. Goto, N. Komiya, J. Akimitsu, N. Motoyama, H. Eisaki, S. Uchida, H. Takahashi, T. Nakanishi, and N. Môri, *Physica C* **282-287**, 153 (1997).
- [5] T. Osafune, N. Motoyama, H. Eisaki, and S. Uchida, *Phys. Rev. Lett.* **78**, 1980 (1997).
- [6] Y. Mizuno, T. Tohyama, and S. Maekawa, *J. Phys. Soc. Jpn.* **66**, 937 (1997).
- [7] N. Nücker et al., *Phys. Rev. B* **62**, 14384 (2000).
- [8] E. M. McCarron III, M. A. Subramanian, J. R. Calabrese, and L. Harlow, *Mater. Res. Bull.* **23**, 1355 (1988).

- [9] T. Siegrist, L. F. Schneemeyer, S. A. Sunshine, J. V. Waszczak, and R. S. Roth, *Mater. Res. Bull.* **23**, 1492 (1988).
- [10] S. Notbohm, P. Ribeiro, B. Lake, D. A. Tennant, K. P. Schmidt, G. S. Uhrig, C. Hess, R. Klingeler, G. Behr, B. Büchner, M. Reehuis, R. I. Bewley, C. D. Frost, P. Manuel, and R. S. Eccleston, *Phys. Rev. Lett.* **98**, 027403 (2007).
- [11] C. Hess, C. Baumann, U. Ammerahl, B. Büchner, F. Heidrich-Meisner, W. Brenig, and A. Revcolevschi, *Phys. Rev. B* **64**, 184305 (2001).
- [12] J. B. Goodenough, *Phys. Rev.* **100**, 564 (1955).
- [13] J. Kanamori, *J. Phys. Chem. Solids* **10**, 87 (1959).
- [14] P. W. Anderson, *Solid State Phys.* **14**, 99 (1963).
- [15] M. Matsuda, K. Kakurai, J. E. Lorenzo, L. P. Regnault, A. Hiess, and G. Shirane, *Phys. Rev. B* **68**, 060406(R) (2003).
- [16] A. Revcolevschi, U. Ammerahl, and G. Dhaleine, *J. Crystal Growth* **198**, 593 (1999).
- [17] P.-C. Hohenberg, and W. F. Brinkman, *Phys. Rev. B* **10**, 128 (1974).
- [18] R. S. Eccleston, M. Azuma, and M. Takano, *Phys. Rev. B* **53**, R14721 (1996).
- [19] N. F. Mott, *J. Phys. Cond. Mat.* **5**, 3487 (1993).
- [20] N. Motoyama, H. Eisaki, and S. Uchida, *Phys. Rev. Lett.* **76**, 3212 (1996).
- [21] F. C. Zhang, and T. M. Rice, *Phys. Rev. B* **37**, 3759 (1988).
- [22] T. Matsuda, A. Zheludev, A. Bush, M. Markina, and A. Vasiliev, *Phys. Rev. Lett.* **92**, 177201 (2004).
- [23] M. Boehm, S. Coad, B. Roessli, A. Zheludev, M. Zolliker, P. Böni, D. McK. Paul, H. Eisaki, N. Motoyama, and S. Uchida, *Europhys. Lett.* **43**, 77 (1998).
- [24] S.-L. Drechsler, J. Målek, J. Richter, A. S. Moskvin, A.A. Gippius, and H. Rosner, *Phys. Rev. Lett.* **94**, 039705 (2005).

Chapter 5

One- and Two-Magnon Spectra of the Ideal Cuprate Ladder

5.1 Introduction

This chapter completes the study of $\text{La}_4\text{Sr}_{10}\text{Cu}_{24}\text{O}_{41}$ with the investigation of the ladder substructures embodying the ideal case of an undoped two-leg spin-ladder as introduced in Section 2.2.3. The main motivation for the study of the undoped ladder is in its quasi one-dimensional character adding a second dimension due to its rung coupling and opening the possibility of a comparison with exact theoretical calculations. Understanding the spin-ladder should help to clarify 2D cuprate systems where a comparison with theory has been difficult due to the complexity of the systems. However, in the case of the spin-ladder systems accurate and non-perturbative theories can be applied due to the quasi one-dimensional character providing the opportunity of an exact theoretical description [1]. A connection between the spin-ladder system and high- T_c cuprate superconductors can be made because the similar building structure of both systems consist of layered copper oxide plaquettes. The rungs of the ladder cause spin pairing believed to be of great importance for charge pairing upon hole-doping giving rise to superconductivity [2, 3]. Experimental and theoretical considerations have also shown that the ladders share several characteristic features with the 2D high- T_c superconductors such as a pseudogap, non-Fermi liquid behavior [4, 5] and similar

coupling constants. Recently the newer concept of stripe theory has been introduced describing the excitation spectrum of high- T_c cuprate superconductors. In this theory the superconductors are thought to charge order in the cuprate layers forming alternating regions of hole-rich stripes and hole-poor spin-ladders with the superconductivity being achieved by pairs of holes moving across the ladder from stripe to stripe [6]. As mentioned in the previous chapter the advantage of the $(\text{La}, \text{Sr}, \text{Ca})_{14}\text{Cu}_{24}\text{O}_{41}$ family is the possibility of hole-doping by varying the ratio of the La to the Sr/Ca content. A version of the doped ladder compound is studied in the next chapter with the detailed investigation of the undoped ladder performed in this chapter serving as a direct comparison and the differences in the excitation spectra can be linked to the presence of the holes.

5.2 Background

A large variety of experiments on the spin-ladder compounds $(\text{La}, \text{Ca}, \text{Sr})_{14}\text{Cu}_{24}\text{O}_{41}$ exist due to their significance to 2D cuprate systems in addition to the discovery of superconductivity in the compounds with the special doping condition of $\text{Sr}_{0.4}\text{Ca}_{13.6}\text{Cu}_{24}\text{O}_{41}$ and $\text{Sr}_{2.5}\text{Ca}_{11.5}\text{Cu}_{24}\text{O}_{41}$ when measured under pressure [7, 8]. Despite the amount of studies, including a diversity of experimental techniques, a discrepancy in the determination of the exact coupling constants and the energy gap has survived giving rise to our experimental study on $\text{La}_4\text{Sr}_{10}\text{Cu}_{24}\text{O}_{41}$ including for the first time an exact description by theory confirming our results. While there is an agreement of the existence of the spin gap, the size varies between 28-56 meV among different techniques [9, 10, 11]. First INS experiments performed on $\text{Sr}_{14}\text{Cu}_{24}\text{O}_{41}$ reveal coupling constants of $J_{leg} = 130$ meV, $J_{rung} = 72$ meV and an energy gap of 32.5 ± 0.1 meV. These findings determine the ratio of leg to rung coupling to be much larger than 1 in contradiction to geometrical considerations suggesting a ratio of 1 due to the same distance of neigh-

boring Cu²⁺ ions on legs and rungs. This discrepancy caused great interest in the theory community leading to the introduction of the cyclic exchange J_{cyc} describing the four-spin exchange interaction around the plaquettes (compare with Figure 5.1 and Section 2.1.3).

An INS investigation by Matsuda *et al* [12] on a single crystal of La₆Ca₈Cu₂₄O₄₁ with the undoped ladder substructures reveals coupling constants of $J_{leg} = 106$ meV and $J_{rung} = 53$ meV without including the cyclic exchange and obtained by fitting a dispersion relation calculated by the Lanczos method for ladders with 12 rungs (24 spins). Including the cyclic exchange into the calculation causes the ratio of the coupling constants to shift to: $J_{leg} = J_{rung} = 110$ meV and $J_{cyc} = 16.3$ meV. While the discussion of the coupling constants seemed to be resolved with the introduction of the cyclic exchange recent measurements using light scattering techniques find different sized leg and rung couplings despite including the cyclic exchange [13, 14]. A comparison between the experimental data of optical conductivity measurements on La_{5.2}Ca_{8.8}Cu₂₄O₄₁ and the theory based on a density-matrix renormalization find exchange parameters of: $J_{rung} \sim 118 - 136$ meV, $J_{leg}/J_{rung} = 1.25 - 1.35$ (leading to $J_{leg} \sim 147 - 184$ meV) and $J_{cyc}/J_{rung} \sim 0.2 - 0.27$ ($J_{cyc} \sim 23.6 - 36.7$ meV). Raman measurements on Sr₁₄Cu₂₄O₄₁ extract coupling constants in agreement with the optical conductivity of $J_{leg} = 174 \pm 16$ meV, $J_{rung} = 142 \pm 20$ meV and $J_{cyc} = 30 \pm 5$ meV [14]. Motivated to clarify the actual coupling constants, a first complete study of the magnetic excitation spectrum consisting of the one and two-magnon excitations of the Mott-Hubbard insulating phase of La₄Sr₁₀Cu₂₄O₄₁ is performed [15]. A clear difference in rung versus leg coupling is established and an explanation for the difference is provided by considering the orbital arrangement in the ladder (compare discussion section).

5.3 Magnetic Features of $\text{La}_4\text{Sr}_{10}\text{Cu}_{24}\text{O}_{41}$

As already mentioned in the previous chapter $\text{La}_4\text{Sr}_{10}\text{Cu}_{24}\text{O}_{41}$ consists of CuO_2 chains and Cu_2O_3 ladders sharing a supercell and distinguishable due to their different c parameter with 10 chain sites and 7 ladder rungs occupying this supercell leading to lattice parameter for the ladder structure of: $a = 11.375 \text{ \AA}$, $b = 12.902 \text{ \AA}$ and $c_{\text{ladder}} = 3.915 \text{ \AA}$ [16, 17]. X-ray absorption spectroscopy performed on the $\text{La}_x(\text{Sr}, \text{Ca})_{14-x}\text{Cu}_{24}\text{O}_{41}$ family for different x values which varies the doping levels, show the predominant location of the holes on the chains [18] leaving the ladders essentially undoped [19, 20]. This is confirmed by the absence of magnon-hole scattering in the heat conductivity measurements of $\text{Ca}_9\text{La}_5\text{Cu}_{24}\text{O}_{41}$ [21, 22] leading to the conclusion that $\text{La}_4\text{Sr}_{10}\text{Cu}_{24}\text{O}_{41}$ is in fact an ideal spin-ladder system consistent with the results established for the chain measurements in the previous chapter with 2 holes residing on the chain in exact agreement with the formal valence of Cu (2.08) in our compound.

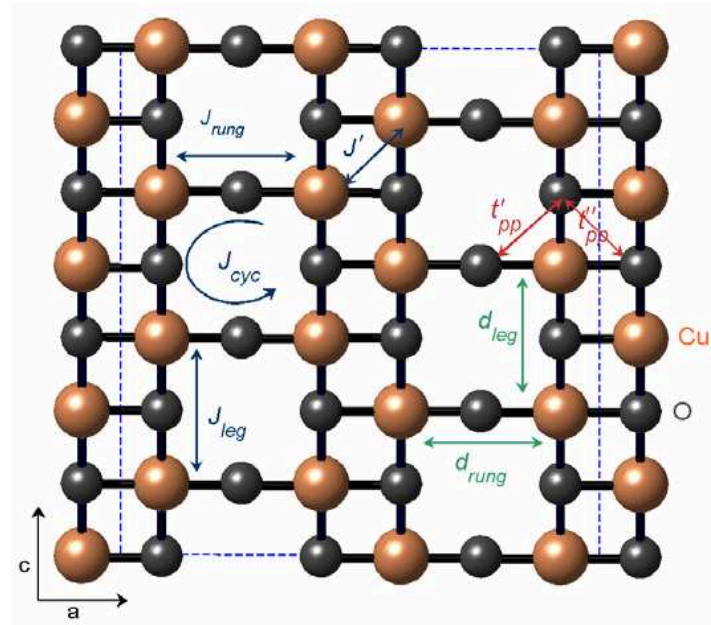


Figure 5.1: Arrangement of the ladder planes in $\text{La}_4\text{Sr}_{10}\text{Cu}_{24}\text{O}_{41}$ with the big copper-colored spheres presenting the copper and the small grey spheres the oxygen atoms. The blue dashed rectangle displays the unit cell in the $(0, k, 0)$ crystallographic plane for the a axis and half of the unit cell in the c axis.

Figure 5.1 illustrates the ladder structure of $\text{La}_4\text{Sr}_{10}\text{Cu}_{24}\text{O}_{41}$. The spin 1/2 Cu^{2+} ions are connected through 180° Cu-O-Cu bonds along the a (rung) and c (leg) direction leading to strong AFM intraladder coupling arising from strong superexchange effects. J_{leg} describes the coupling along the c direction and J_{rung} along the rung in the a direction, also necessary to take into account is the cyclic exchange J_{cyc} connecting the four spins in each plaquette (compare figure). Neighboring ladders are connected through 90° Cu-O-Cu bonds causing frustration resulting in weak FM interladder coupling labeled by J' [3, 11, 12, 23]. The ladders are stacked in the b direction with alternating layers of chains giving rise to a negligible coupling in this direction [16, 17].

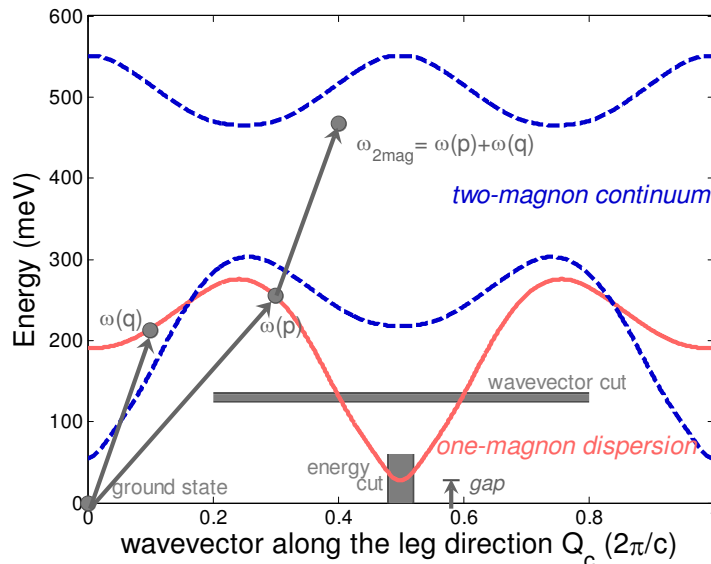


Figure 5.2: $S = 1$ excitation spectrum. A gap exists from the $S = 0$ ground state to the $S = 1$ magnon band (solid red curve) presenting the energy cost of promoting a rung singlet into a triplet. The two-magnon continuum can be constructed via the scattering of the two magnons illustrated by the arrows (blue dashed curves).

The expected $S = 1$ excitation spectrum of the spin-ladder accessible to neutrons is displayed in Figure 5.2. The strongest scattering effect arises from the scattering of the neutron with the sample creating a spin-1 excitation, also called a magnon, shown as the red curve in the figure. The energy gap in the dispersion (seen at $Q_c = 0.5$) is

explained by the formation of a spin singlet on the rungs.

During the neutron scattering process this singlet gets excited into a triplet $S = 1$ state with the energy cost of the size of the gap. The leg coupling linking the rungs gives rise to the possible existence of double excited dimers forming a $S = 0$ state and therefore mixing into the ground state. A two-magnon excitation can be created by a neutron scattering off this vacuum fluctuation exciting both dimers to form a $S = 1$ state. The two-magnon process can be visualized by the interference of two magnons with the conservation of energy and momentum up to a lattice vector during the scattering. The energy of this new state $\omega_{k_1, k_2}(k)$ can be obtained by the addition of the energies of the two single magnons involved in the scattering as $\omega_{\text{mag}}(k_1) + \omega_{\text{mag}}(k_2)$ where $k = k_1 + k_2$ is the total wavevector. This vector addition presented as the gray arrows in Figure 5.2 results in the formation of a continuum illustrated by the two blue dashed lines indicating the boundaries of the two-magnon continuum.

5.4 Experimental Details

The INS measurements were performed with the same samples used for the chain measurements as described in the previous chapter. The MAPS time-of-flight spectrometer was also well matched for the ladder. The same experimental arrangement as for the chain measurements was chosen with the three crystals co-aligned in the $(0, k, l)$ reciprocal plane and the incident wavevector k_i perpendicular to the c direction. The three crystals had a mosaic spread determined by MAPS operated as a Laue camera of 0.4° in the b^*-c^* plane and 5.5° in the a^*-c^* plane. Data were collected for a base temperature of $T = 10$ K and for several initial energies, a low energy run with $E_i = 75.55$ meV, an initial energy of $E_i = 363.7$ meV and a high energy run of $E_i = 606.2$ meV with the combination of these runs providing a suitable energy range to measure the com-

plete excitation spectrum. The low energy data set used a Fermi chopper frequency of 300 Hz, while the other two energies a frequency of 600 Hz. The magnetic cross-section was normalized using incoherent nuclear scattering from a vanadium standard. Long counting times, the large sample mass and the large wavevector energy coverage provided by MAPS made a measurement of the two-magnon scattering in a ladder possible for the first time.

5.5 Measurements and Results

5.5.1 Rung Modulation

One very important feature of the spin-ladder is the separation of the excitation spectrum into contributions mainly due to one-magnon and two-magnon scattering resulting from an antiphase intensity contribution as a function of wavevector along the rung of the ladder. This feature turns out to be very useful for the analysis especially for the background subtraction of the data. The antiphase intensity modulation occurs because of parity conservation during the scattering process based on a connection between even (odd)-magnon with even (odd)-magnon scattering but no coupling between the channels [1]. The separation into different channels can be understood when considering the case of a plaquette on the ladder. A brief outline is provided in this section with a more detailed calculation given in Appendix A. A plaquette consists of two rungs (dimers) coupled by the leg, cyclic and diagonal exchanges. The eigenstates of the dimer are the singlet $S = 0$ ground state and the triplet $S = 1$ excited state. Considering the case of the rung exchange being much larger than the other exchange constants, the eigenstates of the plaquette can simply be formed as the product of the dimer states for both rungs leading to different contributions including a pure singlet contribution with total spin $S = 0$ (no excited dimer), a total $S = 1$ spin state (one excited dimer), and

finally two excited dimers creating a total spin state of $S = 0, 1, 2$. An increase in leg, cyclic or other exchanges causes these two dimer basis states to mix and form states of definite spin and symmetry according to the Clebsch-Gordon series. The new ground state consists of a combination of the two possible $S = 0$ states, the first contribution arising from two singlets forming the plaquette (no excited dimer) and the second from the two excited dimer contribution. Important is the observation that states with one excited dimer do not mix into the ground state leading to the separation of the one- and two-magnon scattering. The one-magnon excitation arises from the interference of a neutron with the pure singlet part of the ground state while the two-magnon occurs from scattering off the double excited contribution. In both cases the structure factor can be decomposed into a product of wavevector along the rung direction and wavevector along the leg direction of the ladder [24]. The structure factor for the one-magnon scattering is proportional to the matrix element of applying the spin transition operator onto the pure singlet part of the ground state:

$$S(\mathbf{Q}, \omega) \propto \left| \langle \rho\sigma | S_{\mathbf{Q}}^{\alpha} | \rho\rho \rangle \right|^2 \quad (5.1)$$

with $|\rho\rho\rangle$ presenting the pure singlet contribution (no excited dimer), $|\rho\sigma\rangle$ consisting of the $S = 1$ contribution with one excited dimer and $S_{\mathbf{Q}}$ being the spin creation operator as introduced in Section 3.3.2:

$$S_{\mathbf{Q}}^{\alpha} = \sum_j \exp(-i\mathbf{Q} \cdot \mathbf{R}_j) S_j^{\alpha} \quad (5.2)$$

The evaluation of equation 5.1 established the structure factor for the one-magnon scattering being proportional to $(1 - \cos(Q_a \cdot a))$. For the two-magnon structure factor the matrix element between the double excited part of the ground state $|\sigma\sigma\rangle_0$ and the $S = 1$ state with two excited dimers $|\sigma\sigma\rangle_1$ has to be considered:

$$S(\mathbf{Q}, \omega) \propto \left| {}_1 \langle \sigma\sigma | S_{\mathbf{Q}}^{\alpha} | \sigma\sigma \rangle_0 \right|^2 \quad (5.3)$$

leading to a rung modulation according to $(1 + \cos(Q_a \cdot a))$ resulting in the antiphase rung wavevector (Q_a) modulation for the one-magnon as compared to the two-magnon scattering.

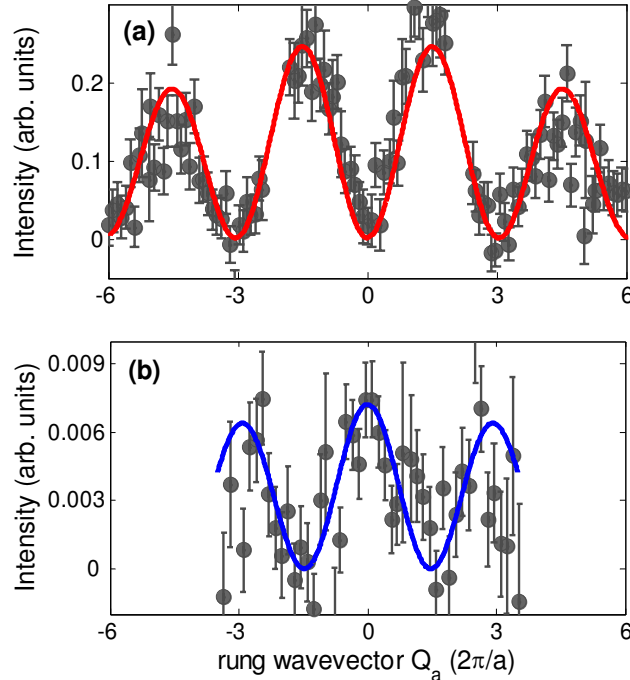


Figure 5.3: Cut along the rung wavevector displaying the intensity modulation: (a) For the one-magnon with a cut performed for $E = 30 \pm 5$ meV and $Q_c = 0.5 \pm 0.05$ and the solid line presenting the one-magnon fit according to $(1 - \cos(Q_a \cdot a))$. (b) For the two-magnon scattering with a cut for $E = 300 \pm 10$ meV and $Q_c = 0.25 \pm 0.05$ and the solid line displaying the antiphase $(1 + \cos(Q_a \cdot a))$ modulation.

Figure 5.3 shows the measured modulation for both the one-magnon (part (a)) and the two-magnon contribution (part(b)). The one-magnon data are obtained by taking a constant energy cut of $E = 30 \pm 5$ meV for a leg wavevector of $Q_c = 0.5 \pm 0.05$ containing an expected high intensity region for the one-magnon signal and a vanishing two-magnon signal (compare with Figure 5.2). The red solid line is the fitted $(1 - \cos(Q_a \cdot a))$ including the anisotropic form factor of copper [25] explaining the intensity drop off for increasing $|Q_a|$. Figure 5.3 (b) illustrates the two-magnon modulation with the solid blue line presenting the fitted $(1 + \cos(Q_a \cdot a))$. Extracting the two-magnon modulation

is more difficult due to the intense one-magnon and weak two-magnon signal arising from the scattering off the vacuum fluctuations. The best region for a strong two-magnon signal necessary to extract the modulation is found by performing an energy cut of $E = 300 \pm 10$ meV for a constant leg wavevector $Q_c = 0.25 \pm 0.05$ as shown in part (b). Summarizing Figure 5.3 verifies the antiphase modulation predicted by the evaluation of the structure factor for each contribution in the case of the plaquette.

5.5.2 Background Subtraction

One valuable advantage of the antiphase rung modulation is its application to the subtraction of the non-magnetic background which mostly results from the incoherent scattering processes. Choosing a rung wavevector region Q_a facilitates the extraction of the scattering mainly due to either one- or two-magnon resulting in the possibility of performing a separate background subtraction for either contribution.

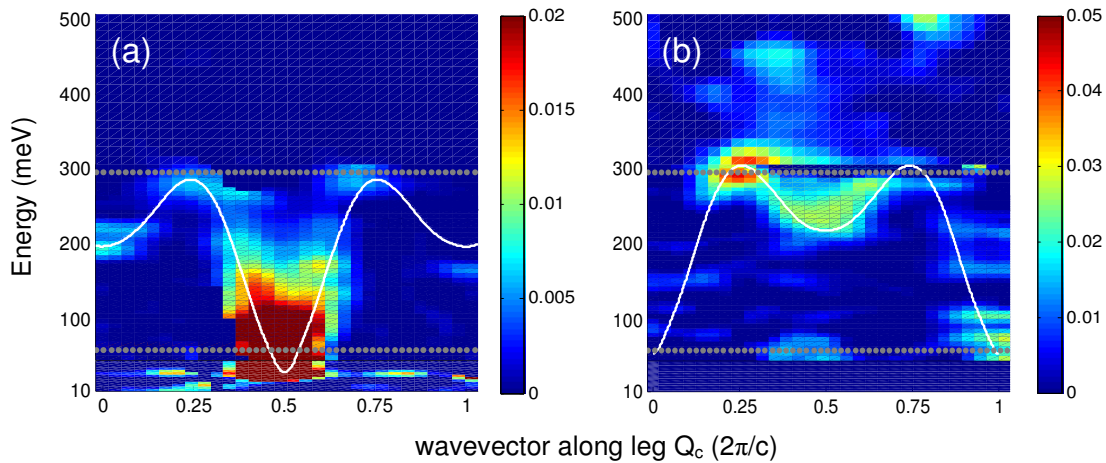


Figure 5.4: Measured data with non-magnetic background subtracted: (a) one-magnon and (b) two-magnon. Data are composed of all initial energy runs separated by the dotted gray line and also included the calculated dispersion curve for the one-magnon and the lower boundary of the two-magnon continuum as white curves.

The wavevector region of the one-magnon scattering is chosen at the maximum of the associated modulation as presented in Figure 5.3 corresponding to $1 < Q_a < 2$. For

the two-magnon scattering two regions consisting of $0 < Q_a < 0.5$ and $2.65 < Q_a < 3.35$ are added to increase the statistics with the form-factor corrected data used for the addition.

Choosing these regions enables the separate background subtraction and these characteristic wavevector regions are used throughout the analysis to distinguish between the one- and the two-magnon signal. The one-magnon nonmagnetic background is determined by an interpolation of the intensities above and below the one-magnon dispersion (see Figure 5.2). The non-magnetic background for the two-magnon signal is deduced from scattering at $Q_c = 0 \pm 0.05, \pm 1 \pm 0.05$ and $\pm 2 \pm 0.05$ presenting the regions of vanishing magnetic two-magnon signal with the background subtracted signal shown in Figure 5.4 (b). Figure 5.4 also includes the fitted dispersion curve (white curve) for both the one- and the two-magnon scattering which will be discussed in great detail in the following section.

5.5.3 One- and Two-Magnon Dispersion

Using the background subtracted data allows an extraction of the dispersion curve of the one- and the two-magnon signal by performing constant energy and wavevector cuts. These experimentally extracted data points are used to fit a theoretical dispersion curve and to determine the coupling constants of the ladder structure discussed in the next section.

The extraction of the data points for the identification of the dispersion is performed separately for the one- and the two-magnon signal by using the characteristic Q_a contributions. Both constant energy and wavevector cuts along the leg direction Q_c indicated by the horizontal and vertical slice respectively in Figure 5.2 are performed with the constant energy cuts yielding better results for the steep part of the dispersion and the

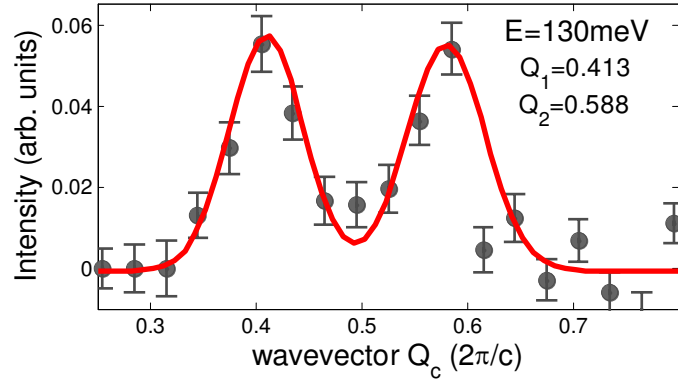


Figure 5.5: Typical cut through the one-magnon signal along Q_c for an energy of $E = 130 \pm 10 \text{ meV}$. The solid line presents two fitted Gaussians for the determination of the peak position.

constant Q_c cuts for the narrow regimes around $Q_c = 0, 0.25, 0.75$ and 1 . A sample constant energy cut is displayed in Figure 5.5. Least square fitted Gaussians included as the red curve in the figure are used to determine the peak position. The energy cut of $E = 130 \pm 10 \text{ meV}$ in Figure 5.5 gives rise to two peak positions at $Q_1 = 0.413$ and $Q_2 = 0.588$ and are presented in Figure 5.6 along with the data from all other constant energy and wavevector cuts where an extraction of a peak position is possible.

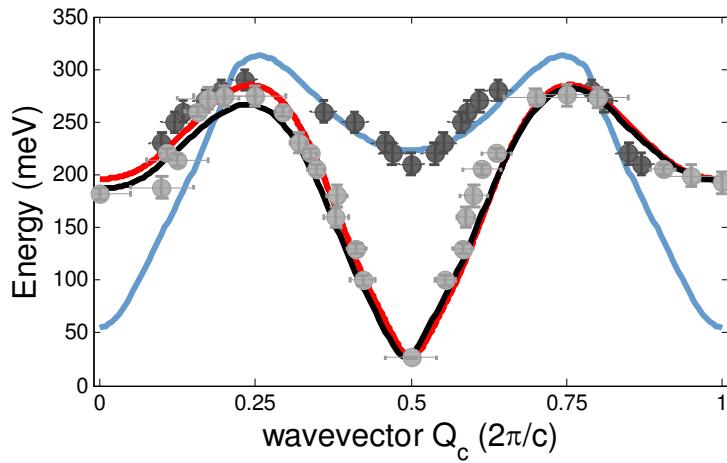


Figure 5.6: Experimental data points for the dispersion relation. The light gray points are the one-magnon and the dark gray points are the two-magnon scattering. Also included are the theoretical curves with the red (without interladder coupling) and black (with interladder coupling) curves illustrating the one-magnon dispersion and the blue curve the lower boundary of two-magnon dispersion.

Figure 5.6 summarizes the determination of the dispersion relation for both the one- and the two-magnon scattering. The experimental extracted one-magnon data points are indicated as the light gray points in the figure and the red curve is the corresponding theoretical fitted one-magnon dispersion relation. The black curve also presents the one-magnon dispersion with the same coupling constants but additionally including an interladder coupling of $J' = -36$ meV. The dark gray data points and the blue curve present the lower boundary of the two-magnon continuum. The exact fitting of the curves will be discussed in the following section.

5.6 Analysis

5.6.1 Hamiltonian and Fitting

The minimal model necessary to describe the magnetic properties of the ladders consists of an antiferromagnetic Heisenberg Hamiltonian plus a cyclic four spin exchange term H_{cyc} [14]:

$$H = J_{rung} \sum_i \mathbf{S}_{i,1} \cdot \mathbf{S}_{i,2} + J_{leg} \sum_{i,l} \mathbf{S}_{i,l} \cdot \mathbf{S}_{i+1,l} + H_{cyc} \quad (5.4)$$

where

$$\begin{aligned} H_{cyc} = & J_{cyc} \sum_i (\mathbf{S}_{i,1} \cdot \mathbf{S}_{i+1,1})(\mathbf{S}_{i,2} \cdot \mathbf{S}_{i+1,2}) + (\mathbf{S}_{i,1} \cdot \mathbf{S}_{i,2})(\mathbf{S}_{i+1,1} \cdot \mathbf{S}_{i+1,2}) \\ & - (\mathbf{S}_{i,1} \cdot \mathbf{S}_{i+1,2})(\mathbf{S}_{i+1,1} \cdot \mathbf{S}_{i,2}) \end{aligned} \quad (5.5)$$

The parameter i denotes the rungs and $l = 1, 2$ the legs of the ladder. As mentioned earlier the exchange couplings along the rung and along the leg are denoted by J_{rung} and J_{leg} respectively (compare Figure 5.1). This Hamiltonian is consistent with the interactions for the low-lying modes in a realistic three-band Hubbard model including the O2p and the Cu3d orbitals [26]. These calculations state the importance of only the short range Heisenberg and cyclic exchange while diagonal coupling across the CuO

square plaquette as well as next nearest neighbor interactions are small and negligible.

The continuous unitary transformation (CUT) has been adapted to the specifics of the ladder [1] resulting in a unique theory used for the fitting procedure and the extraction of the coupling constants of the ladder structure in $\text{La}_4\text{Sr}_{10}\text{Cu}_{24}\text{O}_{41}$. The simplified procedure of the CUT starts with non-interacting dimers resulting in a diagonal Hamiltonian matrix and enabling the extraction of the corresponding energy eigenvalues. Including a small interaction between these dimers (leg and/ or cyclic exchange) introduces off-diagonal terms, however iteratively re-grouping these entries enables the diagonalization of the matrix. In the next step a larger interaction can be included featuring a new diagonalization process. This procedure applied to the spin-ladder structure and undertaken by Kai Schmidt and Götz Uhrig allows an evaluation of the energy values for a range of leg wavevectors for both the one-magnon and the two-magnon contributions.

The crucial data points for the fitting process of the dispersion curve are the experimentally determined one-magnon energy gaps at $\omega_{Q_c=0.5}$ and $\omega_{Q_c=0}$ and the dispersion maximum at $\omega_{Q_c=0.25}$ extracted by the procedure described in the previous section. The characteristic gaps from the data are provided at: $\omega_{Q_c=0.5} = 27 \text{ meV}$, $\omega_{Q_c=0.25} = 286 \text{ meV}$ and $\omega_{Q_c=0} = 197 \text{ meV}$ leading to the following coupling constants: $J_{\text{leg}} = 186 \text{ meV}$, $J_{\text{rung}} = 124 \text{ meV}$ and $J_{\text{cyc}} = 31 \text{ meV}$. The computed one-magnon dispersion relation is displayed as the red solid curve in Figure 5.6 and shows excellent agreement with the data. After establishing the coupling constants the lower boundary of the two-magnon continuum can be calculated with the result displayed by the blue curve in Figure 5.6. Additionally the effect of the interladder coupling on the one-magnon dispersion is considered and is illustrated by the black curve using the same coupling constants plus a FM interladder coupling of $J' = -36 \text{ meV}$. A great similarity between the black and the red curves exists with the discrepancy found in the asym-

metry of the energy peaks (compare peaks at $Q_c = 0.25$ and 0.75) and a slight shift of the gap away from $Q_c = 0.5$. However, the resolution of the data is insufficient to distinguish between the two curves and thus our data can only account for an upper boundary of the interladder coupling of $J' = -36$ meV. (For these 90° Cu-O-Cu bonds this is a realistic value see Chapter 4.)

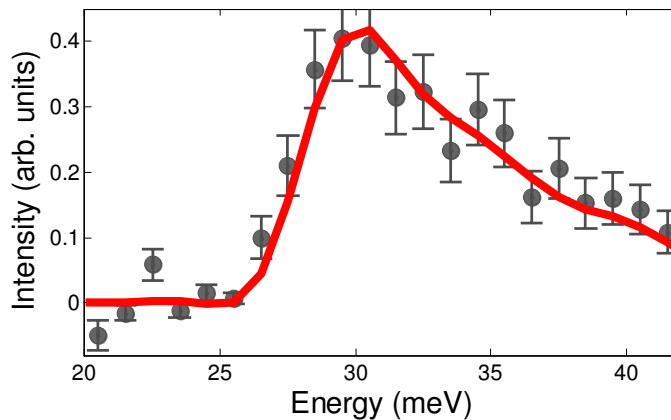


Figure 5.7: Energy cut for $0.48 < Q_c < 0.52$ for the determination of the energy gap of the one-magnon scattering. The solid red curve is the theoretical fitted energy gap.

A very important energy cut of the wavevector $0.48 < Q_c < 0.52$ for the exact determination of the energy gap is displayed in Figure 5.7. This cut displays the excellent comparison between data and theory with the solid red curve describing the theoretical dispersion convolved with the instrumental resolution and the mosaic spread of the crystals. Due to the instrumental resolution the peak position is broadened and asymmetric, with the ‘real’ energy gap found halfway between the energy at the start of the peak and the maximum of the peak. The fitted value is $E_{gap} = 26.4 \pm 0.3$ meV and is lower than found in previous experiments (32.5 ± 0.1 meV found by Eccleston *et al* [11] and 30.5 ± 5 meV by Matsuda *et al* [12]).

5.6.2 Comparison to Theory

The CUT method is also used for the calculation of the neutron structure factor enabling the comparison between the data and theory as displayed in Figure 5.8 with parts (b) and (d) illustrating the calculated one-magnon and two-magnon scattering respectively.

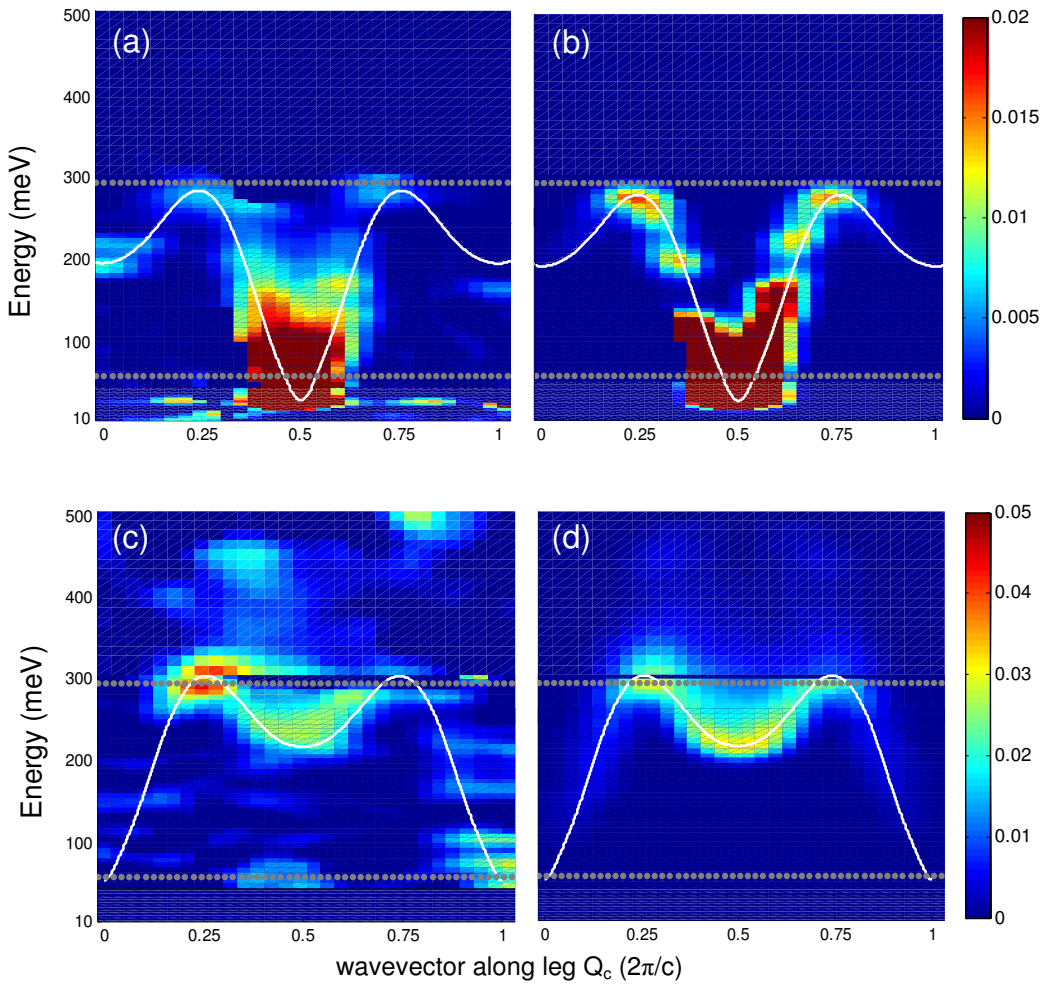


Figure 5.8: (a) Measured one-magnon data with the non-magnetic background subtracted and the white curve representing the theoretically calculated one-magnon dispersion curve. (b) Calculated one-magnon scattering with corrections for detector coverage, crystalline mosaic and instrumental resolution included. (c) Measured two-magnon scattering with non-magnetic background subtracted. The white curve represents the lower boundary of the two-magnon dispersion curve. (d) Calculated two-magnon intensities.

For a direct comparison between the data and the calculation the conditions of the experimental arrangement including the detector coverage, the instrumental resolution and the mosaic spread of the crystals have to be taken into account. While the instrumental resolution can be corrected by a convolution of a Gaussian with its FWHM (full width half maximum) characteristic of the instrument, the mosaic spread is accounted for by performing a Monte Carlo calculation of 500 crystal orientations to simulate the spread observed from the neutron Laue. The agreement between the data and the theory is excellent, although a 15% intensity increase has to be added to the two-magnon simulation for the best match with the data. This discrepancy arises from an uncertainty in the Monte Carlo calculation due to the limited quantity of data points possible for the simulation. Several repeats in the calculation reveal a 15-20% spread for the one-magnon intensities with this spread being of the order of the discrepancy between simulation and data leading to the validation of the calculation. The uneven profile appearing as the slightly patchy intensity distribution rather than the expected smooth distribution (seen in the data in parts (a) and (c)) occurs due to the combination of detector coverage and crystalline mosaic, an effect captured very well in the simulations (compare parts (b) and (d)). Also included in the color plots are the theoretically calculated one-magnon dispersion curve and the lower boundary of the two-magnon dispersion curve (white curves).

5.6.3 Cyclic Exchange

The cyclic exchange plays a key role in the description of the data and is necessary to obtain the level of agreement presented in this study. Recent polarized neutron scattering measurements on La_2CuO_4 also confirm the importance of cyclic exchange in 2D antiferromagnets [27]. Although the cyclic exchange in the ladder was first introduced to the spin interaction Hamiltonian [28] to explain the difference between J_{leg} and J_{rung}

[11] this section will explain the necessity of the cyclic exchange and its effects on the one-magnon dispersion and especially on the lower boundary of the two-magnon continuum. These effects are illustrated in Figure 5.9 with part (a) presenting the one-magnon dispersion and part (b) the lower boundary of the two-magnon continuum. The dashed lines, red for the one-magnon (part (a)) and blue for the two-magnon (part (b)), illustrate the dispersion found for the same J_{rung} and J_{leg} but without including the cyclic exchange ($J_{\text{cyc}} = 0$). The discrepancy between the dashed lines and the data is clearly observed around $\omega_{Q_c=0}$ and $\omega_{Q_c=1}$ for the one-magnon dispersion and around $\omega_{Q_c=0.5}$ for the lower boundary of the two-magnon continuum. Including the cyclic exchange increases the energy at these wavevector regions necessary for an agreement with the data.

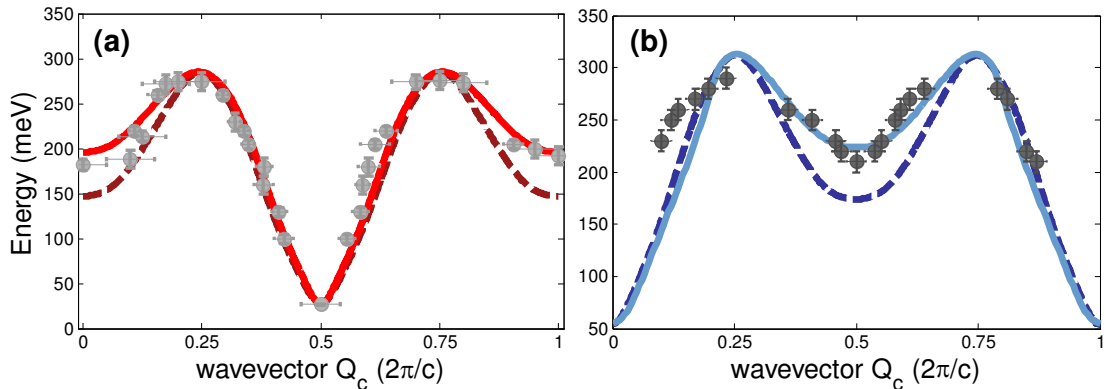


Figure 5.9: Dispersion relation for one- and two-magnon scattering (a) one-magnon with the red curve presenting the fit using the cited coupling constants and the red dashed curve is the same fit without cyclic exchange. (b) Lower boundary of the two-magnon continuum with the blue curve illustrating the fit and the dashed curve obtained without including the cyclic exchange.

Another effect of including the cyclic exchange consists of the frustration in the bound mode. The $S = 1$ bound mode can form in the case of the two-magnon scattering where neighboring magnons can lower their energy by sticking together [24] visible at certain wavevectors and most stable at $Q_c = 0.5$ in the ladder if no cyclic exchange

is present [29]. Investigating the lower boundary of the two-magnon continuum with its onset energy ω_{onset} defined as the energy of the lower boundary of the two-magnon continuum at $Q_c = 0.5$ where it is most sensitive to the binding, will provide further insight into the size of the cyclic exchange.

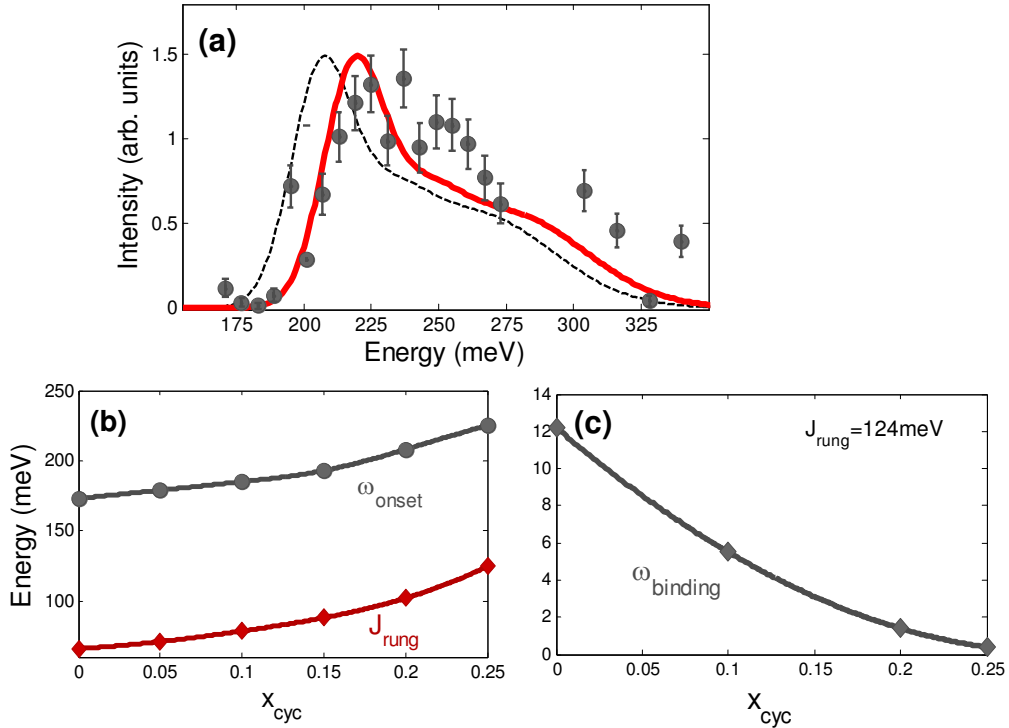


Figure 5.10: Constant wavevector cut for $Q_c = 0.5 \pm 0.1$ for the two-magnon signal with the red solid line presenting the same cut performed through the simulation. The thin dashed line is the effect of absent cyclic exchange for fixed J_{rung} and J_{leg} . (b) Relationship for ω_{onset} describing the two-magnon energy at $Q_c = 0.5$ and J_{rung} w.r.t x_{cyc} with $x_{cyc} = J_{cyc}/J_{rung}$. (c) Frustration of the bound mode with increasing cyclic exchange where $\omega_{binding}$ describes the difference between ω_{onset} and the energy of the bound mode.

Figure 5.10 summarizes the effects of the cyclic exchange on the bound mode. Part (a) illustrates a constant wavevector cut at $Q_c = 0.5 \pm 0.1$ for the two-magnon scattering allowing the determination of the measured onset energy to be $\omega_{onset} = 224 \text{ meV}$. The red curve is the same cut performed for the simulation with the fitted exchange constants displaying the excellent agreement between data and calculation. The black dashed line

indicates the energy of the mode evaluated for the same coupling constants but with no cyclic exchange where the energy difference between the bound mode and ω_{onset} is 12 meV. It is included in the figure to demonstrate that it would be possible to resolve the bound mode if it were present. This along with the lack of the expected double peak structure is a strong indication of the suppression of the bound mode by the existence of the cyclic exchange. Part (b) of the figure displays the strong dependence of the onset energy on the cyclic exchange where x_{cyc} is defined as $x_{cyc} = J_{cyc}/J_{rung}$. To obtain a two-magnon onset of $\omega_{onset} = 224$ meV as determined from the peak position of the constant wavevector cut at $Q_c = 0.5$ in part (a), a $x_{cyc} = 0.25$ is necessary as illustrated by the gray curve. This indicates a rung coupling of $J_{rung} = 124$ meV (red curve) resulting in a cyclic exchange of $J_{cyc} = 31$ meV. The last part of the figure (part (c)) shows the frustration of the bound mode for a fixed $J_{rung} = 124$ meV. For a value of $x_{cyc} = 0.25$ the binding energy vanishes leading to the suppression of the bound mode. Lowering the cyclic exchange with the fixed $J_{rung} = 124$ meV separates the bound mode from the onset energy ω_{onset} with the maximum occurring at a binding of $\omega_{binding} = 12$ meV found without any cyclic exchange and indicated by the black dashed curve in part (a).

5.6.4 Electronic Hamiltonian

Since the undoped ladder $\text{La}_4\text{Sr}_{10}\text{Cu}_{24}\text{O}_{41}$ realizes the Mott-Hubbard insulating (MHI) phase of the ladder a gap between the spin and the electronic part of the Hamiltonian exists allowing a mapping from the spin to the electronic Hamiltonian where the electronic Hamiltonian can be described by the one-band Hubbard model as introduced in equation 2.3 in Section 2.1.3:

$$H = - \sum_{i,j,\sigma} t_{i,j} (c_{i,\sigma}^\dagger c_{j,\sigma} + \text{h. c.}) + U \sum_i n_{i,\uparrow} n_{i,\downarrow} \quad (5.6)$$

with U being the onsite Coulomb potential energy, t the inter-site hopping between neighboring pairs and c the electron annihilation operator. Lower order perturbation theory links the exchange couplings extracted from the spin Hamiltonian (equation 5.4) with the parameters of the electronic Hamiltonian consisting of the hopping along the leg and the rung, t_{leg} and t_{rung} respectively, and the Coulomb energy U according to following relations as introduced in Section 2.1.3:

$$J_{leg} = 4 t_{leg}^2 / U, \quad J_{rung} = 4 t_{rung}^2 / U \quad \text{and} \quad J_{cyc} = 80 t_{leg}^2 t_{rung}^2 / U^3$$

leading to $U = 3.72 \text{ eV}$, $t_{leg} = 0.416 \text{ eV}$ and $t_{rung} = 0.34 \text{ eV}$. These results are consistent with the findings of Yang *et al* [30] performing resonant valence bond (RVB) calculations for $\text{La}_{2-x}\text{Sr}_x\text{CuO}_4$ with: $t = 0.3 \text{ eV}$ and $U = 4 \text{ eV}$. For higher accuracy three-band Hubbard model calculations are necessary, but our extracted parameters are sufficient for the connection between the doped and the undoped ladder. In the case of the doped ladder the spin and the charge scattering cannot be separated anymore and the hopping parameters along with the Coulomb energy are crucial for the connection between the spin and the charge excitation spectrum discussed in greater detail in the next chapter.

5.7 Discussion

While our coupling constants of $J_{leg} = 186 \text{ meV}$, $J_{rung} = 124 \text{ meV}$ and $J_{cyc} = 31 \text{ meV}$ are in good agreement with the results established by light scattering ($J_{rung} \sim 118 - 136 \text{ meV}$, $J_{leg} \sim 147 - 184 \text{ meV}$ and $J_{cyc} \sim 23.6 - 37.6 \text{ meV}$ from optical conductivity [13] and $J_{leg} = 174 \pm 16 \text{ meV}$, $J_{rung} = 142 \pm 20 \text{ meV}$ and $J_{cyc} = 30 \pm 5 \text{ meV}$ from Raman measurements [14]), there exists a discrepancy to earlier INS by Eccleston *et al* and Matsuda *et al*. The main difference occurs in the ratio of the leg to the rung coupling with the results from Matsuda *et al* and theoretical considerations [28] suggesting the ratio to be equal to 1 due to geometrical considerations of the ladder structure (compare Figure 5.1). The

results from our fitting indicate J_{leg} to be 1.56 times stronger than J_{rung} despite being the marginal longer pathway with $d_{leg} = 3.96 \text{ \AA}$ to $d_{rung} = 3.84 \text{ \AA}$ illustrated in Figure 5.1 and suggesting a weaker coupling. However the determination of the exchange couplings depends strongly on the electronic structure supported by the findings in the case of the chain investigation of the previous chapter with the orbital considerations providing the necessary explanation for the dominant FM coupling.

Anderson's superexchange is responsible for the strong AFM coupling in the ladder (for both the rung and the leg) and results from strong hopping effects [31] directly depending on the electrostatic environment [32]. In the ladder structure the exchange arises from two contributions: first the hopping between the Cu3d and O2p orbitals, t_{pd} , and second the hopping between O2p orbitals, t_{pp} , where the total hopping matrix is formed as a difference of the absolute values of the two contributions. If only comparing the t_{pd} hopping the rung coupling should be stronger than the leg coupling due to the smaller Cu-O-Cu separation in the rung. However the t_{pp} hopping strongly depends on the potential around Cu and O mainly determined by the local environment. This environment is characterized by the number of O around the Cu ions and the number of additional Cu²⁺ (or other positive ions) located around the Cu and O ions [32]. In the case of the ladder a differentiation between the hopping matrix of the oxygen along the rung pathway, t'_{pp} , and the leg pathway, t''_{pp} , (compare Figure 5.1) has to be made due to a difference in the local environment. A comparison between the two pathways reveals the potential barrier for the t''_{pp} hopping is increased due to the existence of two neighboring Cu²⁺ ions blocking the hopping of the magnetic Cu hole, while in case of the rung pathway t'_{pp} only one Cu²⁺ neighbor exists leading to a stronger $|t'_{pp}|$ than $|t''_{pp}|$ hopping and therefore for the overall weaker rung coupling.

Calculations based on the hopping matrix elements between Cu3d and O2p and between O2p orbitals including the potential giving rise to the different coupling along the

leg and the rung find exchanges of $J_{leg} = 168$ meV and $J_{rung} = 153$ meV for $\text{Sr}_{14}\text{Cu}_{24}\text{O}_{41}$ [32]. However, the substitution of La will lead to a further enhancement of the leg coupling due to the larger valence of La compared to Sr [32]. These findings are in agreement with band structure calculations suggesting that the effective hopping between nearest neighbor Cu sites along the legs of the ladder is larger by $\sim 35\%$ [33, 34]. Recent quantum chemistry calculations for the ladder structure of SrCu_2O_3 [35] including the cyclic exchange reveal couplings of $J_{leg} = 203$ meV, $J_{rung} = 157$ meV and $J_{cyc} = 34$ meV confirming a ratio larger than 1 (in this case 1.3) consistent with our results. The orbital considerations also explain the strong FM interladder coupling J' with an upper boundary of $J' = -36$ meV. This coupling strongly depends on the geometry of the neighboring ladders forming a 90° Cu-O-Cu bond angle (compare Figure 5.1) leading to a suppressing of the Anderson's AFM superexchange resulting in a total FM coupling due to the direct exchange contribution between neighboring Cu and O and the contribution based on Hund's rule for O2p orbitals for the oxygen. This FM coupling is in analog to the coupling in the edge-sharing chains as discussed in the previous chapter.

While the discussion explains the difference in the couplings along the leg and the rung of the ladder, the discrepancy in the size of the coupling constants between our results and previous INS still exists, although a comparison to the results of light scattering and the calculations based on the electronic structure are consistent with our findings. Both Eccleston *et al* and Matsuda *et al* find couplings considerably smaller with $J_{leg} = 130$ meV and $J_{rung} = 72$ meV and $J_{leg} = J_{rung} = 110$ meV and $J_{cyc} = 16.3$ meV respectively. Considering the experimental arrangement used in both INS experiments reveals a problem in identifying the peak positions of the one-magnon dispersion at $\omega_{Q_c=0.25}$ arising from aligning the sample with k_i along the rung direction Q_a . Choosing this configuration causes the data to be dominated by the dimer modulation ($1-\cos(qa)$)

with the appearance of the peak positions due to the modulation when performing constant wavevector and energy cuts. To avoid this complication in the data treatment the arrangement with k_i perpendicular to a was chosen in our experiment in addition to the advantage of separating the one- and the two-magnon signal due to the antiphase modulation along Q_a . In the previous INS measurements a peak position due to the modulation at a lower energy was misidentified to be the top of the one-magnon dispersion at $Q_c = 0.25$ (compare Figure 5.2) leading to erroneously small coupling constants.

5.8 Conclusion

This investigation on the undoped spin-ladder system $\text{La}_4\text{Sr}_{10}\text{Cu}_{24}\text{O}_{41}$ establishes for the first time measurement of the two-magnon continuum and also provides an accurate theoretical description and comparison of the complete excitation spectrum. Additionally the existence of the cyclic exchange is clarified by examining the effects of the cyclic exchange on the one-magnon dispersion, the lower boundary of the two-magnon continuum and the bound mode. By using the CUT theory to fit the data the exchanges consisting of $J_{leg} = 186 \text{ meV}$, $J_{rung} = 124 \text{ meV}$ and $J_{cyc} = 31 \text{ meV}$ could be extracted with the difference in the ratios between the leg and the rung coupling explained by the electronic structure and the resulting hopping pathways for the oxygen ions. The hopping along the legs is enhanced due to the existence of the neighboring ladder. Importantly a link with the electronic Hamiltonian can be established which is necessary for the comparison between the undoped ladder discussed here and the doped ladder presented in the next chapter. Quantum chemical calculations for our composition would be beneficial for an additional confirmation of the coupling constant and the large difference between the leg and the rung coupling.

References

- [1] K. P. Schmidt, and G. S. Uhrig, *Mod. Phys. Lett. B* **19**, 1179 (2005).
- [2] E. Dagotto, J. Riera, and D. Scalapino, *Phys. Rev. B* **45**, 5744 (1992).
- [3] T. M. Rice, S. Gopalan, and S. Siegrist, *Europhys Lett.* **23**, 445 (1993).
- [4] T. Takahashi, T. Yokoya, A. Ashihara, O. Akaki, H. Fujisawa, A. Chainani, M. Uehara, T. Nagata, J. Akimitsu, and H. Tsunetsugu, *Phys. Rev. B* **56**, 7870 (1997).
- [5] E. Dagotto, *Rep. Prog. Phys.* **62**, 15521 (1999).
- [6] J. M. Tranquada, H. Woo, T. G. Perring, H. Goka, G. D. Gu, G. Xu, M. Fujita, and K. Yamada, *Nature* **429**, 534 (2004).
- [7] M. Uehara, T. Nagata, J. Akimitsu, H. Takahashi, N. Môri, and K. Kinoshita, *J. Phys. Soc. Jpn.* **65**, 2764 (1996).
- [8] T. Nagata, M. Uehara, J. Goto, N. Komiya, J. Akimitsu, N. Motoyama, H. Eisaki, S. Uchida, H. Takahashi, T. Nakanishi, and N. Môri, *Physica C* **282-287**, 153 (1997).
- [9] M. Takigawa, N. Motoyama, H. Eisaki, and S. Uchida, *Phys. Rev. B* **57**, 1124 (1998).
- [10] K. Magishi, S. Matsumoto, Y. Kitaoka, K. Ishida, K. Asayamy, M. Uehara, T. Nagata, and J. Akimitsu, *Phys. Rev. B* **57**, 11533 (1998).
- [11] R. S. Eccleston, M. Azuma, and M. Takano, *Phys. Rev. B* **53**, R14721 (1998).
- [12] M. Matsuda, K. Kasumata, R. S. Eccleston, S. Brehmer, and H.-J. Mikeska, *Phys. Rev. B* **62**, 8903 (2000).
- [13] T. S. Nunner, P. Brune, T. Kopp, M. Windt, and M. Grüninger, *Phys. Rev. B* **66**, R180404 (2002).
- [14] K. P. Schmidt, C. Knetter, M. Grüninger, and G. S. Uhrig *Phys. Rev. Lett.* **90**, 167204 (2003).
- [15] S. Notbohm, P. Ribeiro, B. Lake, D. A. Tennant, K. P. Schmidt, G. S. Uhrig, C. Hess, R. Klingeler, G. Behr, B. Bchner, M. Reehuis, R. I. Bewley, C. D. Frost, P. Manuel, and R. S. Eccleston, *Phys. Rev. Lett.* **98**, 027403 (2007).
- [16] E. M. McCarron III, M. A. Subramanian, J. R. Calabrese, and L. Harlow, *Mater. Res. Bull.* **23**, 1355 (1988).
- [17] T. Siegrist, L. F. Schneemeyer, S. A. Sunshine, J. V. Waszczak, and R. S. Roth, *Mater. Res. Bull.* **23**, 1492 (1988).
- [18] N. Nücker et al., *Phys. Rev. B* **62**, 14384 (2000).

- [19] S. A. Carter, B. Batlogg, R. J. Cava, J. J. Krajewski, W. F. Peck Jr., and T.M. Rice, *Phys. Rev. Lett.* **77**, 1378 (1996).
- [20] D.A. Tennant, R. Bewley, R.S. Eccleston, T. Nagata, and J. Akimitsu, *not published*, (2004).
- [21] C. Hess, C. Baumann, U. Ammerahl, B. Büchner, F. Heidrich-Meisner, W. Brenig, and A. Revcolevschi, *Phys. Rev. B* **64**, 184305 (2001).
- [22] C. Hess, H. ElHaed, Büchner, U. Ammerahl, M. Hücker, and A. Revcolevschi, *Phys. Rev. Lett.* **93**, 027005 (2004).
- [23] S. Gopalan, T. M. Rice, and M. Sigrist, *Phys. Rev. B* **49**, 8901 (1994).
- [24] D. A. Tennant, *Phys. Rev. B* (2003).
- [25] S. Shamoto, M. Sato, J. M. Tranquada, B. J. Sternlieb, and G. Shirane, *Phys. Rev. B* **48**, 13817 (1993).
- [26] E. Müller-Hartmann, and A. Reischl, *Eur. Phys. J. B* **28**, 173 (2001).
- [27] A. M. Toader, J. P. Goff, M. Roger, N. Shannon, R. J. Stewart, and M. Enderle, *Phys. Rev. Lett.* **94**, 197202 (2005).
- [28] S. Brehmer, H.-J. Mikeska, M. Müller, N. Nagaosa, and S. Uchida, *Phys. Rev. B* **60**, 329 (1999).
- [29] K. P. Schmidt, and G. S. Uhrig, *private communications* (2006).
- [30] K.-Y. Yang, C. T. Shih, C. P. Chou, S. M. Huang, T. K. Lee, T. Xiang, and F. C. Zhang, *Phys. Rev. B* **73**, 224513 (2006).
- [31] H. Eskes, and J.H. Jefferson, *Phys. Rev. B* **48**, 9788 (1993).
- [32] Y. Mizuno, T. Tohyama, and S. Maekawa, *Phys. Rev. B* **58**, R14713 (1998).
- [33] M. Arai, and H. Tsunetsugu, *Phys. Rev. B* **56**, R4305 (1998).
- [34] T. F. A Müller, *Phys. Rev B* **57**, R12655 (1998).
- [35] C. J. Calzado, C. de Graaf, E. Bordas, R. Caballol, and J.-P. Malrieu, *Phys. Rev B* **67**, 132409 (2003).

Chapter 6

Investigation of a Cuprate Ladder under Low Carrier Doping

6.1 Motivation

After capturing the features of the MHI phase of the ladder presented in the previous chapter, this investigation focuses on the low carrier doped version of the ladder realized in $\text{Sr}_{2.5}\text{Ca}_{11.5}\text{Cu}_{24}\text{O}_{41}$ with a doping of $\sim 6\%$ in the ladder structure. A main motivation for studying this system is the interplay between the spin and the charge degrees of freedom crucial for developing an understanding of cuprate systems. So far the 1D MHI characterized by a large gap between the spin and the charge spectrum and thus independently treatable is both experimentally and theoretically accessible as shown in the previous chapter [1]. The excitation spectrum of a MHI can be described by a spin excitation spectrum, as the electronic Hamiltonian based on the one-band Hubbard model can be mapped onto a purely magnetic, approximately Heisenberg, spin Hamiltonian as introduced in Section 2.1.3. The other limiting case consisting of a conductor characterized by the gap closure between the spin and the electronic spectrum can be described by a pure electronic Hamiltonian with band structure dominating the excitation spectrum. The intermediate regime of competing charge and spin excitations of a fairly weak doped system realized by our compound has not yet been captured by theory. While theoretical work is in progress [2], for the analysis of the

data a comparison with the two limiting cases (MHI and conductor) is performed to stimulate discussion and extract the features due to hole scattering. Once a theory is established significant progress in the analysis of both weakly doped cuprates as well as high- T_c materials should be provided because in cuprate high- T_c superconductors the coupling between the magnetic spin excitations and the charge mobility of the conduction electrons are proposed to be responsible for the superconductivity [3]. Additional interest in this group of materials has occurred after the discovery of superconductivity in $\text{Sr}_{2.5}\text{Ca}_{11.5}\text{Cu}_{24}\text{O}_{41}$ when pressurized [4, 5].

As well as sharing many features of the 2D high- T_c materials such as pseudo-gap, similar coupling parameters and excitation spectra, the doped ladder material also provides a bridge between the doped Heisenberg chain and the perplexing 2D doped Heisenberg antiferromagnet. The ladder systems are characterized by short-ranged singlet spin pairing on the rungs and excited well-defined spin-1 magnons as discussed in the case of the MHI ladder structure, and upon doping these pairs are believed to provide a mechanism for the formation of hole pairing giving rise to either charge density waves or superconducting states [6, 7, 8, 9, 10]. This chapter presents a measurement of the excitation spectrum of the hole-doped ladder $\text{Sr}_{2.5}\text{Ca}_{11.5}\text{Cu}_{24}\text{O}_{41}$ directly compared with the undoped MHI ladder material $\text{La}_4\text{Sr}_{10}\text{Cu}_{24}\text{O}_{41}$.

6.2 Background

Structurally $\text{Sr}_{2.5}\text{Ca}_{11.5}\text{Cu}_{24}\text{O}_{41}$ consists like the previously discussed $\text{La}_4\text{Sr}_{10}\text{Cu}_{24}\text{O}_{41}$ of two unique subsystems: the edge-sharing CuO_2 chains and the Cu_2O_3 ladder (see previous chapter).

In $\text{Sr}_{14}\text{Cu}_{24}\text{O}_{41}$ the formal valence of 2.25 for Cu^{2+} gives 6 holes per f.u. in the system, with nearly all holes identified by INS to be on the chain [11]. Substituting

Ca^{2+} for Sr^{2+} does not change the overall hole concentration, but results in a closer hybridization of the chain and the ladder subsystems due to the smaller ionic radius of Ca enabling some holes to migrate onto the ladder [12, 13]. While hole migration onto the ladder structure for Ca doping is agreed on among different experimental techniques the resulting amount of holes on the ladder is disputed. NMR measurements find 1.75 holes on the ladder segment [14], optical conductivity measurements claim 2.8 holes on the ladder for $x=11$ and spin echo 3.5 holes for $x=11.5$ [15].

Resistivity measurements for $\text{Sr}_{2.5}\text{Ca}_{11.5}\text{Cu}_{24}\text{O}_{41}$ along the ladder direction reveal a semiconductor behavior for the ladder with nearly linear temperature dependence above $T = 130\text{ K}$ (metallic state), while below $T = 60\text{ K}$ a sharp resistivity increase can be found with decreasing temperature (insulating behavior) indicating hole localization in this regime [4, 16, 17]. Measurements perpendicular to the ladder show a negative temperature coefficient indicative of incoherent charge dynamics (weak coupling) between the ladders [4]. Optical conductivity measurements reveal a pseudo-gap in both the a and c direction [18] with the interpretation of hole pair forming into a CDW state at low temperatures. However, NMR measurements find a small magnetic moment in the c direction suggesting single holes instead of pairs and therefore a CDW-like state below $T = 60\text{ K}$ where charge order is formed by localized single holes [15].

Applying pressure $\text{Sr}_{2.5}\text{Ca}_{11.5}\text{Cu}_{24}\text{O}_{41}$ becomes superconducting at 4.5 GPa [4, 5] with the resistivity changing from the insulating to the superconducting state without an intermediate metallic regime allowing the conclusion of a cross-over from a charge density wave to superconducting state being present in $\text{Sr}_{2.5}\text{Ca}_{11.5}\text{Cu}_{24}\text{O}_{41}$.

6.3 Experimental Details

The single crystals of $\text{Ca}_{2.5}\text{Sr}_{11.5}\text{Cu}_{24}\text{O}_{41}$ were obtained from the group of J. Akimitsu and the INS measurements were preformed in identical fashion to the measurements on $\text{La}_4\text{Sr}_{10}\text{Cu}_{24}\text{O}_{41}$ introduced in the last chapter to allow a direct comparison. The only difference between the two experiments consists of the sample mass of the doped ladder composed of four single crystals and a total mass of 25 g in contrast to the three crystals of 15 g used for the undoped ladder resulting in a higher scattering intensity for the doped system. Additionally a more accurate alignment could be accomplished with a resulting mosaic spread of 0.3° in the b^*-c^* plane and 0.4° in the a^*-c^* plane. The four co-aligned (in the $(0, k, l)$ plane) crystals were investigated on the MAPS spectrometer and data were collected for incident energies $E_i = 50, 100, 360$ and 600 meV and monochromated with a Fermi chopper of 300 Hz and 600 Hz for the high energy run. Measurements were taken at $T = 10 \text{ K}$ and 80 K below and above the charge ordering temperature.

6.4 Measurements and Results

6.4.1 Background Subtraction

The advantage in the study of the doped ladder is its similarity to the undoped case with the only difference in the presences of holes. This similarity allows the analysis to closely follow the one of the undoped ladder discussed in great detail in the previous chapter. One of the key features of this analysis consists of the separation of one- and two-magnon contributions due to the antiphase rung modulation. For a confirmation of this upon hole doping constant energy cuts for the maximum signal for both the one- and the two-magnon scattering are performed as illustrated in Figure 6.1. Part (a) presents a cut for constant energy of $E = 80 \pm 10 \text{ meV}$ and leg wavevector

$Q_c = 0.45 \pm 0.05$ presenting the one-magnon modulation with the red curve illustrating the expected $(1 - \cos(Q_a \cdot a))$ behavior with the anisotropic Copper form factor included. Part (b) shows the two-magnon modulation for a cut at $E = 310 \pm 10$ meV and $Q_c = 0.25 \pm 0.05$ with the blue curve presenting the expected antiphase modulation $(1 + \cos(Q_a \cdot a))$.

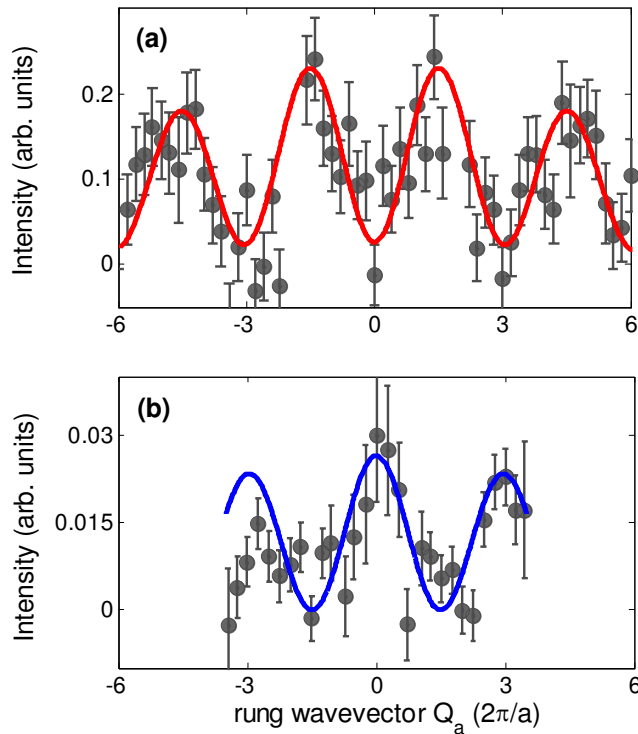


Figure 6.1: Cut along the rung wavevector showing the modulation for: (a) one-magnon scattering with a cut performed for an energy $E = 80 \pm 10$ meV and a leg wavevector $Q_c = 0.45 \pm 0.05$. The red curve is the fitted one-magnon modulation $(1 - \cos(Q_a \cdot a))$. (b) Two-magnon contribution with cut for $E = 310 \pm 10$ meV and $Q_c = 0.25 \pm 0.05$ and included the fitted $(1 + \cos(Q_a \cdot a))$ as blue curve.

After confirming the modulation feature in the doped ladder the background subtraction can be performed in analogy to the undoped case. The background subtracted data for the doped ladder is displayed in Figure 6.2 (b) and (d) with part (a) and (c) illustrating the results for the undoped ladder serving as a direct comparison revealing strong similarities between the spectra, but also profound differences are apparent directly linkable to the presence of holes. (Note that the intensities cannot be directly

compared, as there is a factor of ~ 1.3 difference due to higher mass of the doped ladder).

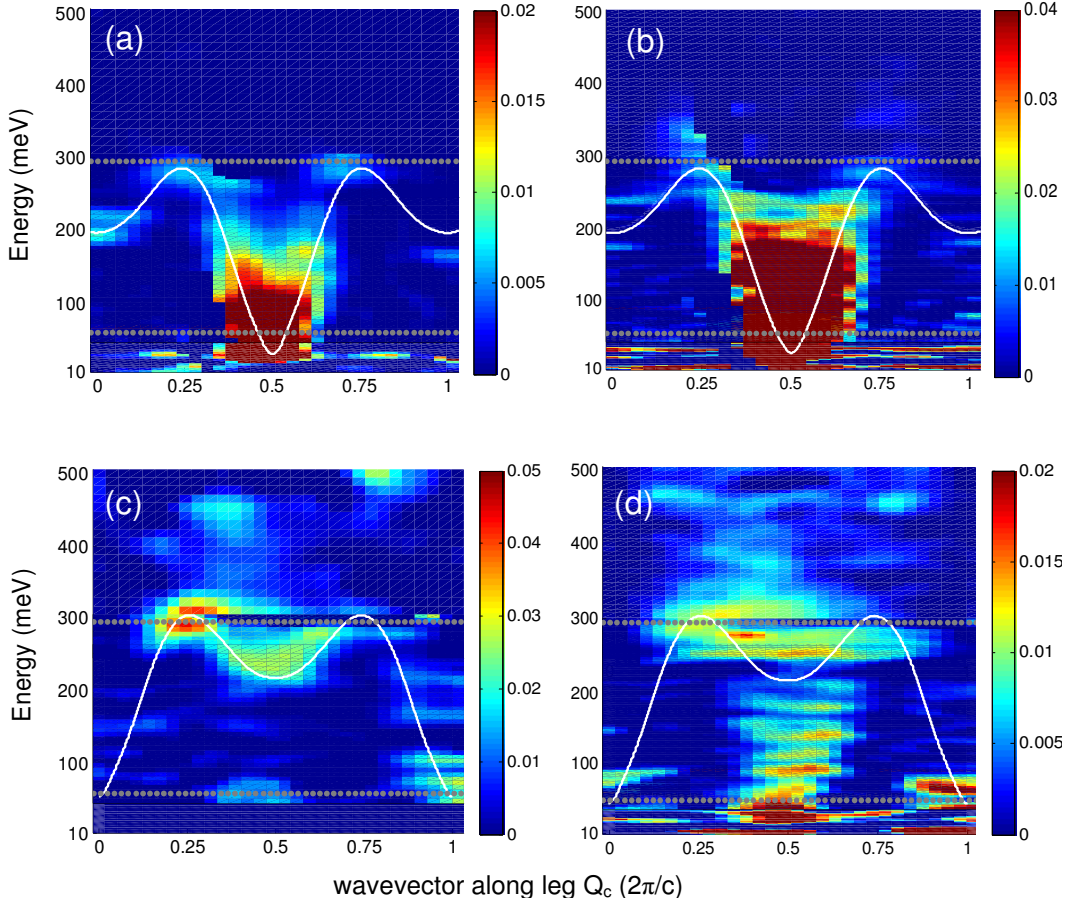


Figure 6.2: (a) Measured one-magnon data with the non-magnetic background subtracted for the *undoped* ladder, the white curve indicates the theoretically calculated one-magnon dispersion curve. (b) Measured one-magnon scattering for *doped* ladder with non-magnetic background subtracted off (same method as for undoped ladder), included is the calculated one-magnon dispersion curve from undoped ladder (white curve). (c) Measured two-magnon data with non-magnetic background subtracted off for *undoped* ladder. The white curve presents the lower boundary of the two-magnon dispersion curve. (d) Measured two-magnon data with non-magnetic background subtracted off for *doped* ladder. Lower boundary of calculated two-magnon scattering for undoped case indicated by white curve

Turning the attention to the one-magnon contribution reveals an extra mode appearing at higher energies around $Q_c = 0.25$ and 0.75 at energies above $E = 300$ meV for the doped ladder (part (b)) not apparent for the undoped case (part (a)). This scattering exceeds the one-magnon dispersion curve included as the white curve suggesting that this

mode results from a different scattering process than the one-particle magnetic scattering, because it exceeds the maximum magnetic energy provided by the superexchange process in the ladder structure. Additionally to this high energy mode subgap scattering can be detected for the doped ladder with a more detailed investigation provided in the next section covering the differences in the dispersion relations.

The discrepancies in the two-magnon spectrum are most profound in the extra scattering located at $Q_c = 0.5$ up to energies of $E \sim 200$ meV and clearly located below the lower boundary of the two-magnon continuum discovered for the undoped case (included as the white curve in parts (c) and (d)). Additionally to this profound difference broadening of the signal can be detected for the doped ladder appearing in an intensity redistribution and smearing of scattering instead of the majority being located at the lower boundary. For a more detailed investigation a comparison of the two-magnon dispersion relation between both cases is provided in a later section.

6.4.2 One-Magnon Dispersion

Figure 6.3 displays the extracted dispersion relations, part (a) and (c) for the undoped and part (b) and (d) for the doped ladder obtained by applying the usual method of fitting least-square Gaussians to constant energy and wavevector cuts giving rise to the energy and wavevector dependencies displayed in the data points of the dispersion curves. The width of the cut is illustrated by the horizontal ‘error bar’ of each point providing a direct measurement of any broadening effects between the ladders.

The direct comparison of the changes in the one-magnon spectrum upon hole doping is presented in the figure by including the theoretically calculated dispersion curve (black curve) to the experimentally extracted data points (red point in parts (b) and (d)). An overall very good agreement is apparent with the differences seen in the additional

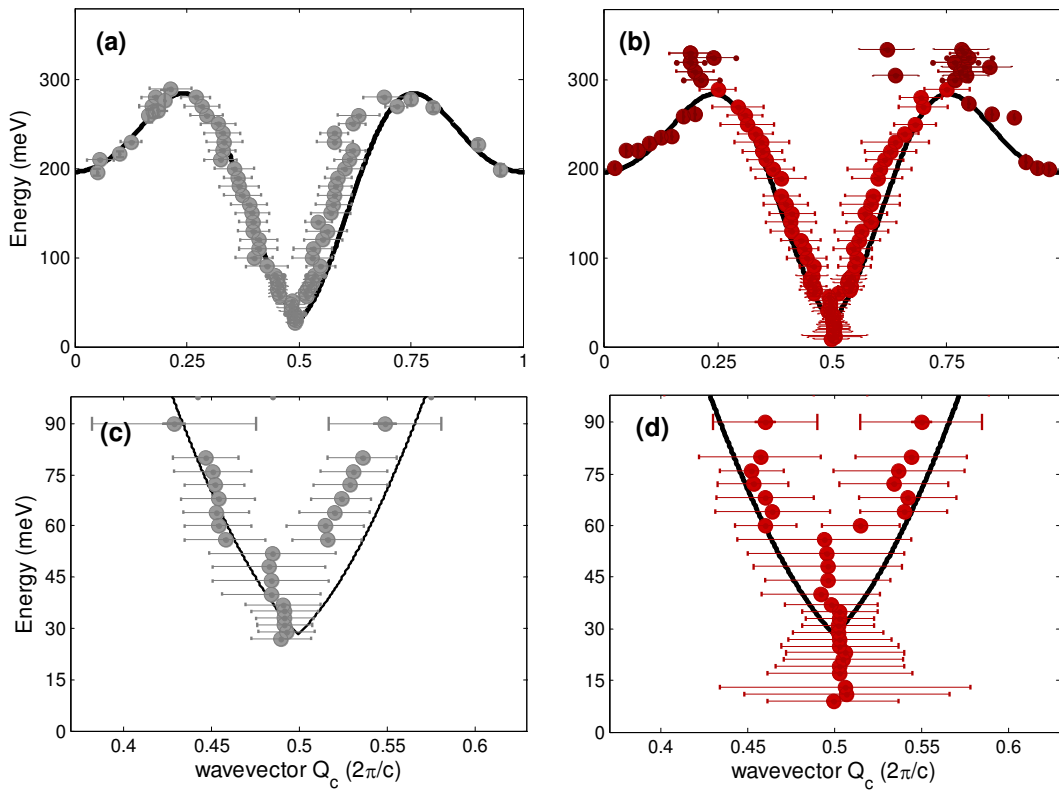


Figure 6.3: One-magnon dispersion. (a) Experimental points for the *undoped* ladder obtained from constant energy cuts with the width of fitted Gaussians included as ‘error bar’. The theoretical one-magnon dispersion is included as the black curve. (b) Experimental points for the *doped* ladder with theoretical calculated one-magnon dispersion for undoped case (black curve). ‘Error bars’ represent the width of fitted Gaussian peaks. (c) Experimental points for gap scattering for the *undoped* case. (d) Experimental points for gap and sub-gap scattering for the *doped* ladder. Broadening of peaks indicates life-time effects.

scattering observed as a new mode starting around $E \sim 300$ meV and the subgap scattering. The light red data is obtained from the $E_i = 360$ meV data run and the dark red data from the $E_i = 600$ meV run. Part (d) provides a closer look at the existence of the subgap scattering for the doped ladder clearly not observed in the undoped case (compare to part (c)). While scattering below the previous determined gap of the undoped ladder is present, a gap of $E \sim 8$ meV can be observed for the subgap scattering in addition to a width increase of the cuts with decreasing energy leading to the conclusion of a possible formation of a mode evolving at two incommensurate wavevectors. A third difference in the spectrum of the doped ladder consists of peak broadening confirmed

by the length of the ‘error bars’ providing a measurement of the width of the fitted Gaussians. While the width of the peaks for the undoped ladder are resolution limited (part (c)), the width of the cuts for the doped ladder are intrinsic (part (d)). This broadening can be explained as a life-time effect due to collisions between the magnons and the holes on the ladder.

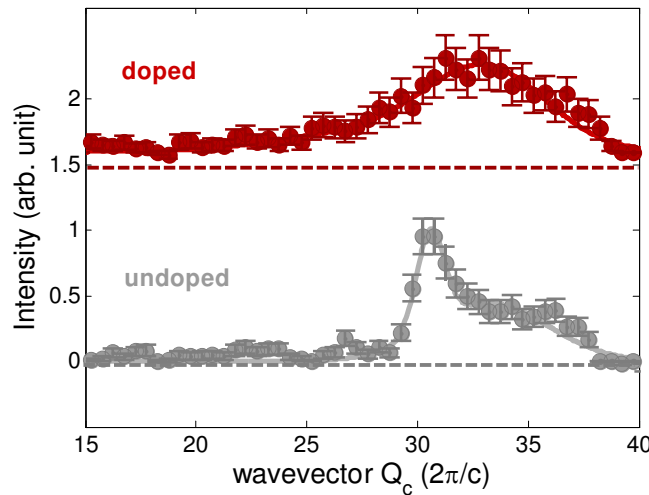


Figure 6.4: Constant one-magnon wavevector cut $0.48 < Q_c < 0.52$ for the gap energy with the gray curve illustrating the undoped and the red curve the doped ladder.

This broadening effect is also apparent in the comparison of the gap energies displayed in Figure 6.4 for a constant one-magnon wavevector cut of $0.48 < Q_c < 0.52$. The gray curve illustrates the gap energy of the undoped case with a sharp (resolution limited) intensity increase and a gap energy of $E_{gap} = 26.4$ meV. The red curve presents the same situation for the doped case with the curve shifted vertically by 1.5 intensity unit for a better comparison revealing intensity surviving below the gap however drastically reduced. The intensity of the doped gap energy is also decreased with a clear broadening and shift in amplitude to higher energies leading to a gap energy of E_{gap} (doped) = 29.8 meV.

6.4.3 Two-Magnon Dispersion

A similar comparison performed for the two-magnon dispersion is displayed in Figure 6.5 with part (a) showing the results for the undoped and part (b) for the doped ladder. Included in both parts is the theoretically calculated lower boundary of the two-magnon continuum obtained from the undoped case and indicated by the black curve. The data points are again extracted by fitting least-square Gaussians with the width demonstrated by the length of the ‘error bars’ just as for the one-magnon treatment. In both cases the darker data points are obtained from an initial energy $E_i = 600$ meV and the lighter data points from the $E_i = 360$ meV.

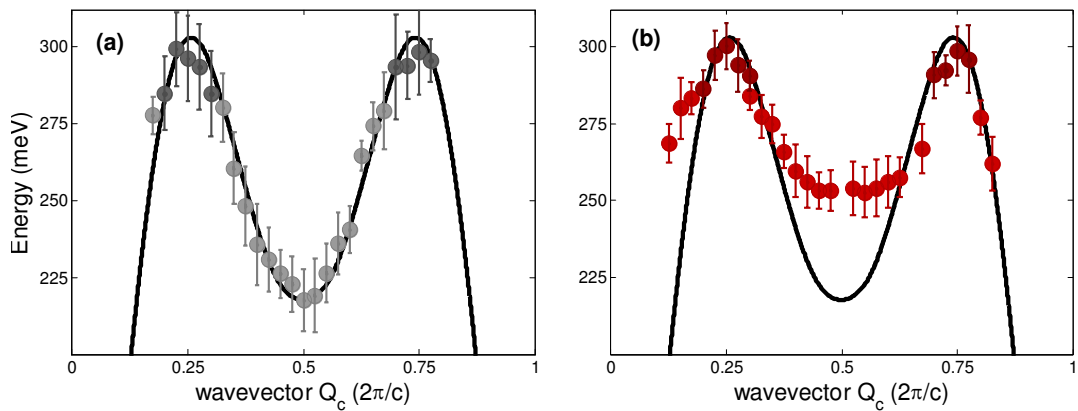


Figure 6.5: Two-magnon dispersion relation: (a) Experimental points for the *undoped* ladder, included is the lower boundary of the two-magnon continuum obtained from the undoped ladder (black curve). (b) Experimental points for the *doped* ladder with lower boundary of two-magnon scattering included for comparison (black curve).

Part (a) shows the excellent agreement between the data and the calculated curve, while part (b) displays the two-magnon signal above the lower boundary of the two-magnon continuum. Agreement between the data points of the doped ladder and the lower boundary of the two-magnon continuum is apparent. The data points around $Q_c = 0.5$ are located at a higher energy than predicted by the theoretical calculated dispersion curve suggesting energy broadening resulting from life-time effects of the

magnons. This is consistent with the broadening effects discovered for the one-magnon signal of the previous section and is characteristic of a disruption of the two-magnon states by defects (in this case holes) [19].

6.5 Analysis

6.5.1 Charge Scattering

The comparison between the one-magnon signal of the undoped and doped ladder reveals an extra mode at higher energies plus subgap scattering. These effects are due to the presence of holes in the ladder. Considering that the doped ladder realizes a system in the regime between a MHI and a conductor, a comparison to the excitation spectrum arising from the metallic phase of the ladder in analogy to the treatment with the MHI phase suggests itself. This comparison provides a possible explanation for the extra features in the doped ladder by proposing a hybridization between spin (magnon) and charge (hole) sector. For the determination of the hole scattering an Independent Electron Model (IEM) describing the charge spectrum of a conventional metal is considered. Due to the rung coupling of the ladder the charge dispersion consists of two bands, an upper and a lower band for $k_{perp} = 0$ and π respectively, with the one-magnon scattering embodied by interband scattering. The lower boundary of the charge spectrum identifying the energies for a possible hybridization can be found by the scattering of states at the Fermi points (intersection of band dispersion with Fermi level) into the lower or upper band.

6.5.2 Independent Electron Model (IEM)

An estimate of the hole scattering is provided when considering the IEM ensembling the case of gap closure between the spin and charge excitation spectrum presented by

the dominance of the electronic Hamiltonian. The electronic Hamiltonian for the ladder can be described by the free electron Hamiltonian H_0 and an interacting part H_{int} .

$$H = H_0 + H_{int} \quad (6.1)$$

The free electron part is introduced in equation 2.3 in Section 2.1.3 and given by:

$$H_0 = -t_{para} \sum_{j,\sigma,l} (c_{j,\sigma,l}^\dagger c_{j+1,\sigma,l} + h.c) - t_{perp} \sum_{j,\sigma} (c_{j,1,\sigma}^\dagger c_{j,2,\sigma} + h.c) \quad (6.2)$$

with $\sigma = \uparrow$ or \downarrow , j is the index along the legs and $l = 1$ or 2 identifying the leg, t describing the hopping parameter along the leg (t_{para}) and along the rung (t_{perp}) and c the annihilation operator. The interaction Hamiltonian for the extended Hubbard model is:

$$H_{int} = U \sum_{j,l} n_{j,l,\uparrow} n_{j,l,\downarrow} + V_{para} \sum_{j,l} n_{j,l} n_{j+1,l} + V_{perp} \sum_{j,l} n_{j,1} n_{j,2} \quad (6.3)$$

where the first term is the on-site Coulomb repulsion with $U = 3.72$ eV as found from the analysis of the undoped ladder, V is the Coulomb potential between the different sites and n the number operator. In the normal Hubbard model the first term is the only potential considered, however in the extended Hubbard model the repulsion of the nearest neighbors along the leg (second term) and along the run (third term) are also taken into account.

For solving the extended Hubbard model the successful approach consists of focusing on the scattering arising from the non-interaction part H_0 presented by the IEM and then turning on the interaction effects U and V . The effects of such interaction have to be treated non-perturbatively because the electron as a quasi-particle is unstable resulting in the formation of coupled charge and spin modes. A field theoretical calculation for the complicated extended Hubbard model has been performed by F. Essler *et al* [20] using Quantum Field Theory covering a metallic U/t parameter space different from our doped ladder regime. However the treatment of the free-electron part will

already provide a good indication of the characteristics of the hole scattering such as incommensurate wavevectors and the boundary scattering.

6.5.3 IEM Applied to the Ladder

Considering only the free electron part and diagonalizing H_0 using a Fourier transformation the Hamiltonian can be re-written (exact calculation in Appendix B) as:

$$H_0 = \sum_{k,\sigma} \epsilon(k) c_\sigma^\dagger(k) c_\sigma(k) + \text{constant} \quad (6.4)$$

where $\epsilon(k) = -2t_{para} \cos(k_{para}) - t_{perp} \cos(k_{perp})$ is the band dispersion illustrated in Figure 6.6 with the two separate bands occurring due to the rung coupling leading to two distinct values of k_{perp} : $k_{perp}=0$ for bonding and $k_{perp}=\pi$ for antibonding. For the calculation of the band dispersion the hopping parameters as found from the analysis of the undoped ladder consisting of $t_{para} = 0.42$ eV and $t_{perp} = 0.34$ eV are used necessary to determine the energy scale of the charge scattering. The effect of doping the ladder is a shift in the Fermi level by δ (in our case $\sim 6\%$, compare Figure 6.6) resulting in incommensurate wavevectors along the leg direction. The corresponding Fermi points can be obtained by the intersection of the doping level with each band as indicated in the figure with the Fermi points for the lower (upper) level labeled with $k_{F,0}^d$ ($k_{F,\pi}^d$) and given by the exact determination presented in Appendix B:

$$k_{F,0}^d = \pi/2(1-\delta) \text{ and } k_{F,\pi}^d = \pi/2(1-\delta) - \lambda$$

with

$$\lambda = \arcsin\left(\frac{t_{perp}}{2t_{para} \cos(\delta\pi/2)}\right)$$

The scattering spectrum for the hole scattering can be obtained by considering the scattering from the ‘hole-filled’ part of the lower band to the ‘hole-free’ part of the

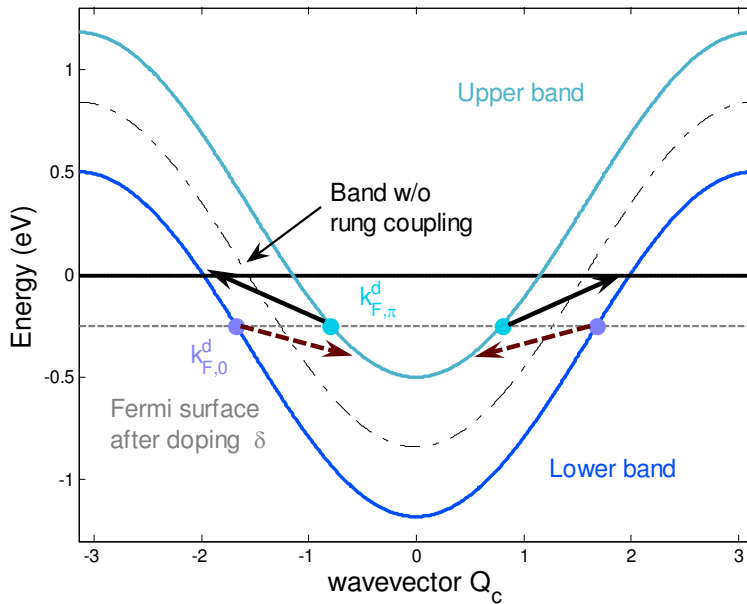


Figure 6.6: Hole scattering as determined from the IEM. Due to the rung coupling the dispersion splits into two bands, a bonding and antibonding configuration. The Fermi points $k_{F,0}^d$ and $k_{F,\pi}^d$ are obtained from the intersection of the doped Fermi level δ with the corresponding bands.

upper band and vice versa. This interband scattering involves a π -shift and is therefore characteristic for the one-magnon channel also including the scattering from the bonding to the antibonding configuration. The intraband scattering presents the two-magnon channel without the requirement of a change in parity. For an explanation of the mode at higher energies and the subgap scattering in the one-magnon channel of our data it is therefore sufficient to focus on the interband scattering. The hole filled part of the lower band consists of the states located above the Fermi level, i.e. $k < -k_{F,0}^d$ or $k > k_{F,0}^d$, and the hole free part of the upper band by states below the Fermi level, $-k_{F,\pi}^d < k < k_{F,\pi}^d$, and vice versa (see Figure 6.6). The calculated complete interband scattering as obtained for the free holes is illustrated in Figure 6.7.

The characteristic of the doped ladder consists of the reduction (almost closure) of the gap between the spin and the charge sector enabling the neutron to also access the charge spectrum at certain wavevectors where a hybridization between the spin and the

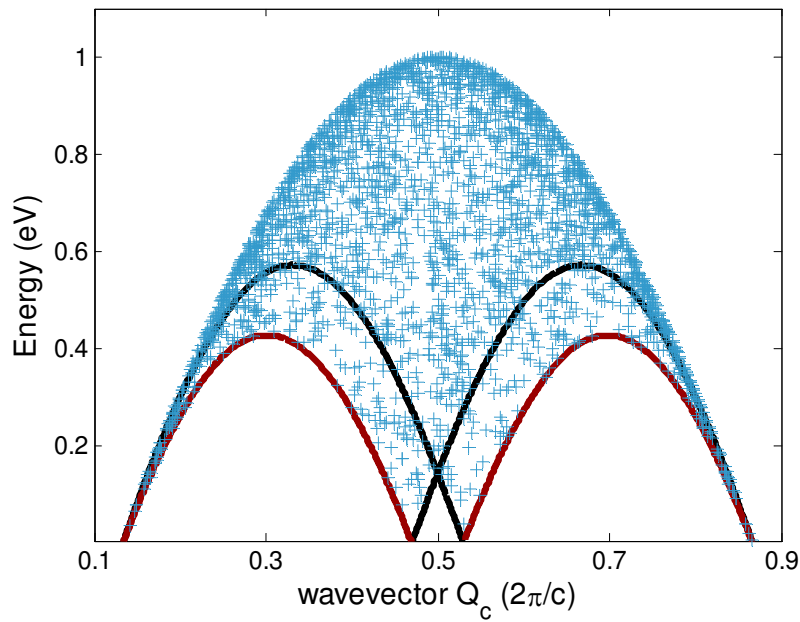


Figure 6.7: Hole scattering from IEM for a metal for the interband scattering (one-magnon channel). Included is the lower boundaries obtained from scattering of points close to the Fermi level (as described in text). These give an indication of accessible wavevectors and energies for a possible hybridization between the spin and hole sector.

charge excitation is possible, i.e. comparable energies between the spin and the charge spectrum possible for the scattering of the lower boundary of the hole interband scattering. This boundary can be obtained by holes located at the Fermi points characterized by the lowest energy cost for the scattering between bands (compare Figure 6.6) and indicated by the arrows in Figure 6.6. The color corresponds to the one of the lower boundary as illustrated in Figure 6.7 with the two colors presenting the two different scattering processes possible between different bands.

The scattering from the upper band, i.e. from the Fermi points of the upper band, $\pm k_{F,\pi}^d$, to the hole free region of the lower band, i.e. region $k < -k_{F,0}^d$ or $k > k_{F,0}^d$, is illustrated by black arrows in Figure 6.6 while the scattering from the Fermi points of the lower band, $\pm k_{F,0}^d$, to the 'hole-free' region of the upper band, $-k_{F,\pi}^d < k < k_{F,\pi}^d$ by the dashed dark red arrows.

6.5.4 Comparison to Data

The comparison between the charge scattering with the one-magnon signal is displayed in Figure 6.8 including the theoretical calculated dispersion curves of the hole scattering (lower boundaries), indicated by the dashed curves, and the spin scattering by the solid curves.

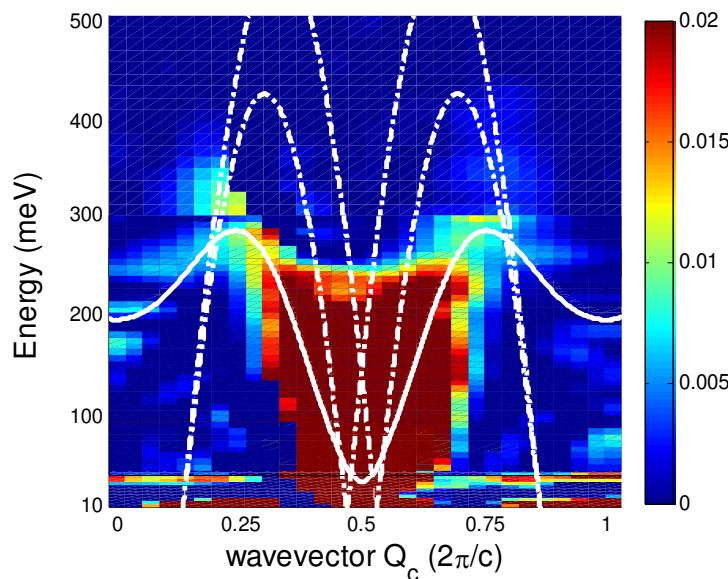


Figure 6.8: One-magnon excitation spectrum including the theoretically calculated spin dispersion curve of the undoped ladder (white solid line) and the lower boundary of the hole scattering (white dashed line).

This comparison suggests the extra mode found at higher energies does indeed follow the lower boundary of the hole scattering resulting in the assumption of hybridization effects between the charge and the spin scattering. For the subgap scattering the IEM predicts a new mode starting at two incommensurate wavevectors both symmetrically displaced around $Q_c = 0.5$, the characteristic wavevector for the gap energy in the undoped case. This finding is in agreement with the width increase for decreasing energies found in the subgap regime of our data shown in Figure 6.3. For confirmation of the incommensuration constant energy cuts performed in the subgap regime should resolve two distinct peaks, but impossible with the insufficient resolution of our

experiment. The separation into two bands and the resulting interband scattering processes give rise to subgap modes starting at incommensurate wavevectors as seen in Figure 6.7. The two inner modes cross at around $E \sim 120$ meV, but a hybridization with the spin scattering occurs already around the gap energy for the spin spectrum (around $E \sim 30$ meV) leading to an increase and a broadening effect of the gap energy consistent with the changes in the gap energy discussed in the previous section and as seen in Figure 6.4.

6.5.5 Parity Breaking

This section focuses on the extra mode of the scattering in the two-magnon channel for the lower energies as seen in Figure 6.2 (d). A direct comparison to the one-magnon signal leads to the prediction of this extra mode scattering being related and the possibility of a shadow scattering is investigated by performing constant energy cuts for both the one- and the two-magnon signal and comparing the fitted width and amplitude between the cuts.

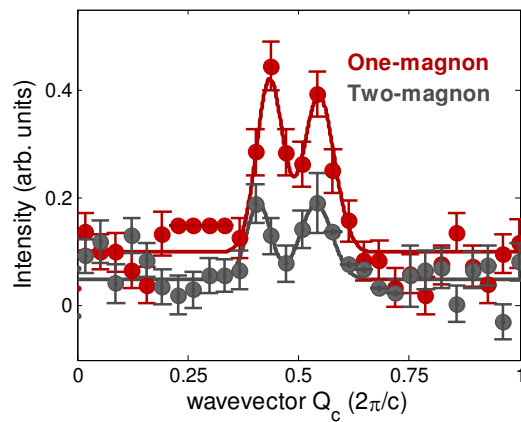


Figure 6.9: Typical constant energy cut through the one-magnon (red) and the two-magnon (gray) signal performed for $90 < E < 110$ meV.

A typical constant energy cut performed at $90 < E < 110$ meV and presenting the comparison is displayed in Figure 6.9 where the red curve presents the one-magnon

and the gray curve the two-magnon results. The figure illustrates the similarity in the behavior between the one- and the two-magnon scattering and by fitting Gaussians throughout the data points the amplitude and the width of the peaks can be extracted. Repeating this procedure for different energies, the product of amplitude and width can be compared presented in Figure 6.10 revealing the same behavior for the two-magnon scattering as the one-magnon with the difference consisting of a constant amplitude factor confirming the idea of shadow scattering. This leads to the conclusion of the left-right mirror symmetry being disturbed and can be understood when treating the holes as being single, localized holes leading to the breaking of a rung singlet at the location of the hole. In Appendix C the calculation for a 5-spin system, two dimers coupled with one single spin, is provided explaining the parity breaking. However the rung modulation for the doped ladder has been confirmed in Section 6.4.1 resulting in the conclusion of a perturbative hole treatment in agreement with the presence of only $\sim 1 - 2$ holes per unit ladder ($\sim 1 - 2$ holes holes per 14 Cu²⁺ spins). This investigation suggests the low energy scattering observed in the two-magnon channel results from single holes independent of the rung wavevector.

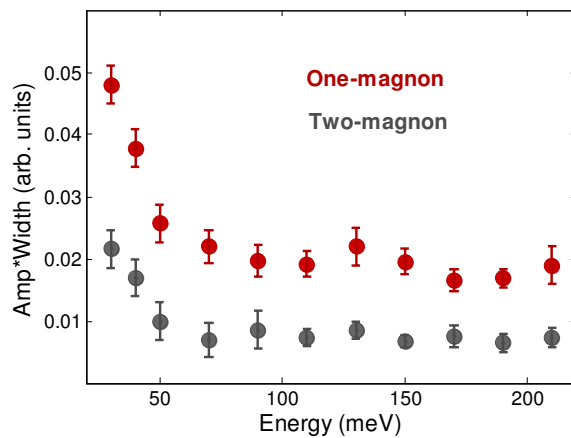


Figure 6.10: Comparison of the product of amplitude and width obtained from constant energy cuts through the one-magnon (red) and the two-magnon (gray) signal.

Figure 6.11 displays the rung wavevector dependence for the one-magnon and the

subgap regime with part (a) presenting a constant energy cut for $E = 30 \pm 10$ meV compared with the fitted one-magnon modulation ($1 - \cos(Q_a \cdot a)$) indicated by the red curve. Part (b) shows the cut performed at a lower energy of $E = 21 \pm 3$ meV through the subgap scattering showing the lack of a modulation agreeing with the finding of localized single holes instead of two holes sharing a rung. For the subgap energy the scattering is due to the hole sector (as discussed in the previous section) and single holes distributed on both legs throughout the ladder will break the parity requirement due to an interruption of the dimer formation of the rungs responsible for the rung modulation. In the case of hole pairing where two holes share a common rung giving rise to a hole dimer a modulation would be apparent along the rung direction. The idea of single holes agrees with NMR studies where a CDW-like state is anticipated from single holes due to unpaired spins around them [15].

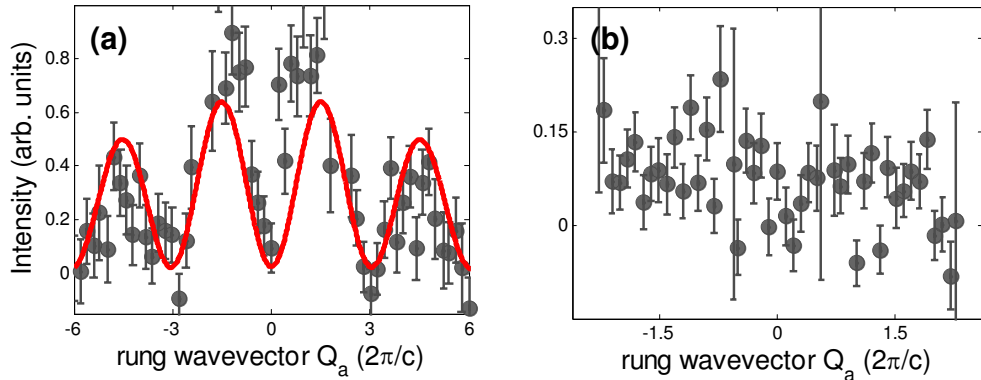


Figure 6.11: Rung modulation: (a) Constant energy cut for $E = 30 \pm 10$ meV along the rung wavevector, the solid line is the fitted $(1 - \cos(Q_a \cdot a))$ modulation for the one-magnon channel. (b) Energy cut performed for $E = 21 \pm 3$ meV displaying the subgap scattering without any modulation.

6.6 Discussion

The work performed on the doped ladder material $\text{Sr}_{2.5}\text{Ca}_{11.5}\text{Cu}_{24}\text{O}_{41}$ reveals some insight into the doped MHI as a system bridging the MHI and a conventional metal. For a

complete explanation of the excitation spectrum it is necessary to consult both the spin and the charge spectrum due to the discovery of new modes at high and low energies allowing a hybridization between the spin and the charge scattering.

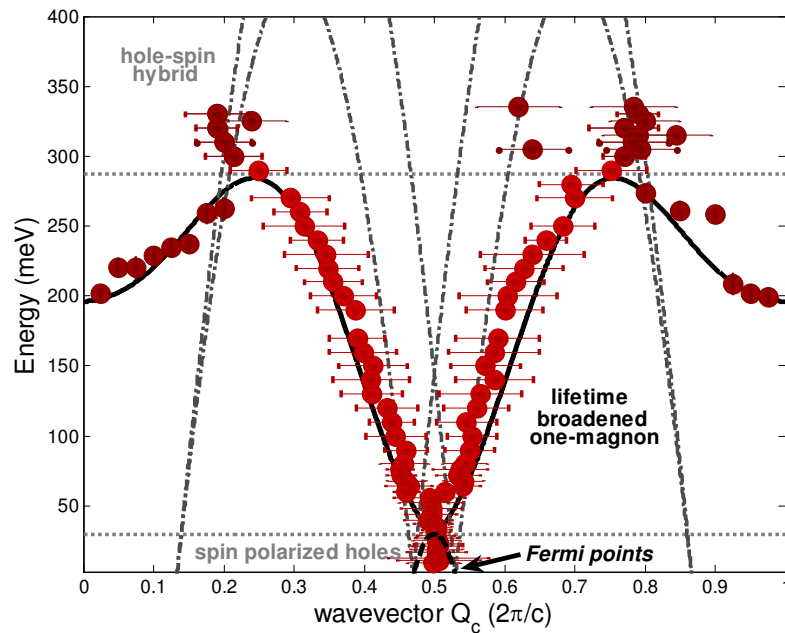


Figure 6.12: Excitation spectrum of the one-magnon channel including the charge scattering. Scattering can be divided into three regimes: The first regime is the subgap scattering characterized by spin polarized holes indicated by the low energy black curve (obtained by hybridization between charge and spin scattering). Second regime consists of the scattering due to spin shown by the lifetime broadened one-magnon dispersion relation. And the third regime is a new mode above 300 meV explained by a hole-spin hybrid.

The analysis for the doped ladder closely follows the one introduced for the undoped case using the key feature of separating the one- and two-magnon contributions due to the antiphase rung modulation. This analysis is only possible due to a direct comparison with the excitation spectrum of the undoped ladder enabling the discovery of hole doping effects. The differences between the doped and the undoped ladder can be successfully explained by considering the charge scattering made accessible to the neutron due to the gap closure between the spin and the charge part for the doped MHI allowing hybridization effects at certain energies, agreeing well with the observed

data. From these considerations a physical picture for the scattering of the doped MHI can be developed. The excitation spectrum of the one-magnon channel can be divided into three different regimes due to different scattering processes and indicated in Figure 6.12 by the horizontal gray dotted lines. The first regime consists of the subgap hole scattering occurring up to energies of about $E \sim 30$ meV (labeled spin polarized holes in Figure 6.12), the second regime is presented by the spin scattering from $E \sim 30$ to 300 meV (lifetime broadened one-magnon) and lastly the high energy hole scattering for a signal above $E \sim 300$ meV (hole-spin hybrid).

The subgap scattering is a feature identified to occur from hole scattering due to its absence in the undoped ladder and its appearance for the considerations of the scattering spectrum in the case of the IEM and thus has to be related to the charge scattering process. During this process the neutron can move the hole along the ladder, but for such low energy transfers involved in this process the holes are slowly moving along the ladder providing a possibility for a pairing mechanism, as predicted by theoretical considerations [6, 7] and the superconducting characteristics when pressurized. This scattering is illustrated by the black dashed curve in Figure 6.12 where hybridization effects with the spin scattering at the spin gap of $E \sim 30$ meV have been included. Due to the slow moving hole the neighboring spins have enough time to create a spin polarization cloud around these holes as illustrated in the upper part of Figure 6.13. These spin clouds can provide a pathway for the coupling of the two holes illustrated in the lower part of Figure 6.13. A hole traveling through the ladder with its polarized spins can attract a hole on the opposite leg if the polarized spins couple antiferromagnetically. Pressuring causes the holes to move closer together providing a possible pathway for Cooper pairing effects and superconductivity to dominate.

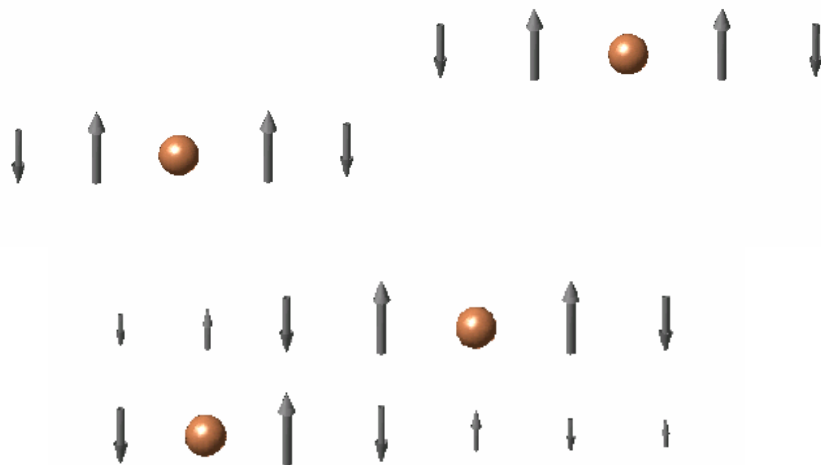


Figure 6.13: Upper part: spin polarization around slow moving holes. Lower part: polarized spins can couple antiferromagnetic and result in a hole pairing process.

The second regime is dominated by the spin spectrum of the ladder characterized by the creation of a magnon in analogy to the undoped ladder and indicated by the good agreement between the one-magnon dispersion curve and the extracted data as found in Figure 6.3. The only difference between the doped and the undoped ladder is a width broadening of the fitted Gaussians due to life-time effects of the magnons before colliding with the localized holes. Additionally some hybridization between the spin and the charge scattering is possible at the steep part of the dispersion (around $Q_c=0.5$) due to the small energy difference between the spin scattering indicated by the dispersion relation and the lower boundary of the charge scattering (compare Figure 6.12) also giving rise to broadening effects.

The third regime consisting of the new mode at high energies is directly related to charge scattering, because the necessary transfer energies are above the maximum energy of the spin scattering determined by the dispersion of the undoped ladder. Energies of the necessary order can be obtained by neutrons moving holes along the ladder provided by the rung hopping t_{perp} determined for the undoped case to be of the order of $E \sim 340$ meV ($t_{rung} = 0.34$ eV, compare with Section 5.6.4). This hopping param-

eter has been used to calculate the lower boundary of the charge scattering enabling hybridization effects with the top of the dispersion at wavevectors around $Q_c = 0.25$ and 0.75 providing very good agreement with the extra mode of scattering obtained for the doped ladder. Because of the rather large energy transfer involved in this type of scattering it will lead to fast moving holes in the ladder.

6.7 Conclusion

This chapter provides an investigation of a doped MHI phase and identification of the hole scattering with a possible explanation on the assumption of hybridization effects between the spin and the charge excitation spectrum. A direct measurement of the hole effects could be undertaken for the doped spin-ladder system $\text{Sr}_{2.5}\text{Ca}_{11.5}\text{Cu}_{24}\text{O}_{41}$ via a direct comparison with the undoped version characterized by a pure spin excitation spectrum. The differences in the two spectra could be explained with reference to the excitation spectrum for the metallic phase of the ladder given by the electronic Hamiltonian with the hopping parameters and the onsite energy obtained from the analysis of the undoped version. The extra effects discovered in our doped ladder follow the charge scattering obtained by a IEM calculation suggesting a spin-charge hybridization. Also suggested by the analysis is the hole integration into the ladder as single, localized holes necessary to explain the symmetry breaking apparent in the lower mode of the two-magnon scattering and the lack of the rung wavevector modulation in the subgap regime of the doped ladder.

References

- [1] S. Notbohm, P. Ribeiro, B. Lake, D. A. Tennant, K. P. Schmidt, G. S. Uhrig, C. Hess, R. Klingeler, G. Behr, B. Büchner, M. Reehuis, R. I. Bewley, C. D. Frost, P. Manuel, and R. S. Eccleston, *Phys. Rev. Lett.* **98**, 027403 (2007).
- [2] G. S. Uhrig, K. P. Schmidt, and A. L. Läuchli, *private communications* (2007).

- [3] A. V. Chubukov, D. Pines, and J. Schmalian, *The Physics of Superconductors* Vol. I, *Conventional and High- T_c Superconductors* **485-590**, Springer, Berlin (2003).
- [4] T. Nagata, M. Uehara, J. Goto, J. Akimitsu, N. Motoyama, H. Eisaki, S. Uchida, H. Takahashi, T. Nakanishi, and N. Môri, *Phys. Rev. Lett.* **81**, 1090 (1998).
- [5] T. Takahashi, T. Yokoya, A. Ashihara, O. Akaki, H. Fujisawa, A. Chainani, M. Uehara, T. Nagata, J. Akimitsu, and H. Tsunetsugu, *Phys. Rev. B* **56**, 7870 (1997).
- [6] E. Dagotto, J. Riera, and D. Scalapino, *Phys. Rev. B* **45**, 5744 (1992).
- [7] T. M. Rice, S. Gopalan, and S. Siegrist, *Europhys Lett.* **23**, 445 (1993).
- [8] S. Gopalan, T. M. Rice, and M. Sigrist, *Phys. Rev. B* **49**, 8901 (1994).
- [9] H. Tsunetsugu, M. Troyer, and T. M. Rice, *Phys. Rev. B* **51**, 16456 (1995).
- [10] M. Troyer, H. Tsunetsugu, and T. M. Rice, *Phys. Rev. B* **53**, 251 (1996).
- [11] R. S. Eccleston, M. Azumu, and M. Takano, *Phys. Rev. B* **53**, R14721 (1998).
- [12] T. Osafune, N. Motoyama, H. Eisaki, and S. Uchida, *Phys. Rev. Lett.* **78**, 1980 (1997).
- [13] Y. Mizuno, T. Tohyama, and S. Maekawa, *J. Phys. Soc. Jpn B* **66**, 937 (1997).
- [14] M. Takigawa, N. Motoyama, H. Eisaki, and S. Uchida, *Phys. Rev. B* **57**, 1124 (1998).
- [15] S. Oshugi, K. Magishi, S. Matsumoto, Y. Kitaoka, T. Nagata, and J. Akimitsu, *Phys. Rev. Lett.* **82**, 4715 (1999).
- [16] N. Motoyama, T. Osafune, T. Kakeshita, H. Eisaki, and S. Uchida, *Phys. Rev. B* **55**, R3386 (1997).
- [17] K. Magishi, S. Matsumoto, Y. Kitaoka, K. Ishida, K. Asayama, M. Uehara, T. Nagata, and J. Akimitsu, *Phys. Rev. B* **57**, 11533 (1998).
- [18] T. Osafune, N. Motoyama, H. Eisaki, S. Uchida, and S. Tajima, *Phys. Rev. Lett.* **82**, 1313 (1999).
- [19] B. D. Gaulin, *private communications* (2006).
- [20] F. H. L. Essler, and R. M. Konik, *Phys. Rev. B* **75**, 144403 (2007).

Chapter 7

Magnetic Field Effects on the Quantum Magnet Copper Nitrate

7.1 Motivation

This chapter starts the second part of the thesis with the investigation of the 1D alternating Heisenberg chain material copper nitrate which serves as a model system to study the effects of quantum and thermal fluctuations due to its dimensionality. In contrast to one-magnon states, higher order excitations have received less attention. However these will provide interesting insight into the interplay between thermal and quantum fluctuations in gapped quantum magnets [1, 2]. Copper nitrate embodies a very attractive system ensuring an energy separation between the different scattering processes due to its alternation parameter α with its value predicted to be in the regime of maximum separation [3]. Its low energy scale also makes it possible to investigate the quantum fluctuation effects by applying magnetic field driving the system through two critical fields affecting the ground state and dynamical characteristics of the system.

Figure 7.1 presents the changes in statistics the system undergoes when applying magnetic field. Without any magnetic field the magnons can be viewed as localized particles, because the band width of the one-magnon branch due to the size of the alternation parameter α is narrow compared to the energy gap resulting from the dimer

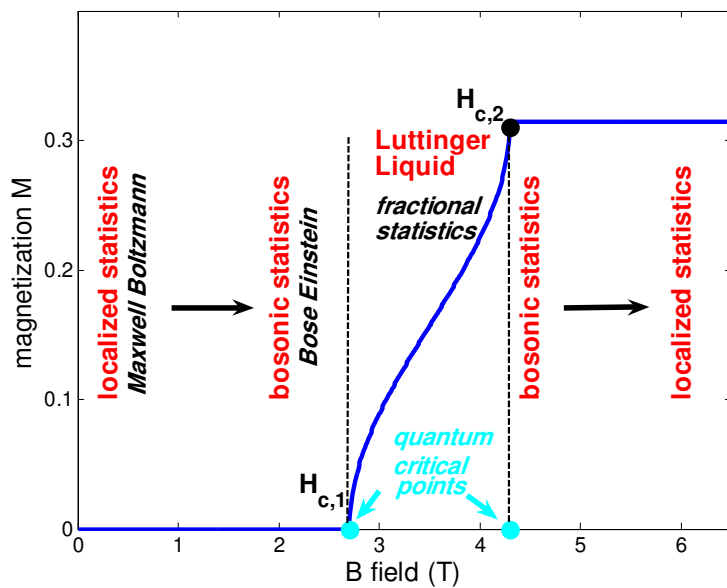


Figure 7.1: Change of the statistics of the system upon applying magnetic field.

coupling. This can be interpreted as the de Broglie wavelength of the magnons being shorter than the inter-magnon distance, i.e. no overlapping of the magnons resulting in the treatment of the magnons as distinguishable particles and Maxwell Boltzmann statistics to hold [4, 5]. Applying a magnetic field to the system will Zeeman split the one-magnon dispersion relation until energy gap closure resulting in a change of statistics from quasi-particles to a quantum mechanical treatment. For a gap smaller than the magnon band width the wavefunctions of the magnons overlap due to the longer wavelengths compared to the spacing leading to indistinguishability of the magnons. Since Maxwell Boltzmann statistic is not valid in this regime the system has to be treated by Bose Einstein statistics. A first critical field $H_{c,1}$ is reached at gap closure causing the formation of a new ground state. This regime is gapless and is characterized by strong quantum fluctuations leading to Luttinger Liquid (LL) type behavior dominated by fractional excitations (e.g. spinons). Increasing the field further will drive the system through a second critical field $H_{c,2}$ reaching saturation. In this last regime all spins are aligned ferromagnetically in the direction of the applied field and the one-magnon

dispersion will follow the cosinusoidal dispersion of a 1D ferromagnet. For higher fields a gap reappears and for a gap size small enough compared to the band width the magnons can be treated by bosonic statistics. At a larger gap the overlap of the magnon wavefunctions is compensated resulting in distinguishable particles allowing the treatment of localized statistics.

The first part of this chapter investigates the system at zero field including the two-magnon excitation spectrum and the bound mode. A theoretical description is available enabling the simulation of the data and a direct comparison. In the second part of the chapter the application of magnetic field is studied with the theoretical description valid for fields smaller than the first critical field $H_{c,1}$ and the magnetic excitation modes above the second critical field $H_{c,2}$ expressed by spin wave theory (the exact calculation is provided in Appendix D). The very interesting region in the vicinity of the two critical fields is investigated experimentally thoroughly including a possible physical picture describing the effects providing the foundation for a detailed theoretical study. The next chapter deals with the temperature effects at zero and also at applied field. For the zero field a theory based on the exact diagonalization is available, while the field data provides an outlook for the interplay between thermal and quantum effects where future theoretical input is necessary.

7.2 Background

The spin-1/2 alternating Heisenberg chain consists of antiferromagnetically coupled spin pairs, dimers, which are themselves coupled by a weaker antiferromagnetic interaction to form the alternating chain as shown in Figure 7.2. The intradimer coupling is labeled by J and the interdimer coupling by αJ resulting in the following Hamiltonian

for the system [1]:

$$H = \sum_{m=1}^{N/2} J \mathbf{S}_{m,-} \cdot \mathbf{S}_{m,+} + \alpha J \mathbf{S}_{m,+} \cdot \mathbf{S}_{m+1,-} \quad (7.1)$$

The index m labels the dimers, the + and - indicate the left and right spin of each dimer, \mathbf{d} is the chain repeat vector and ρ is the intradimer separation.

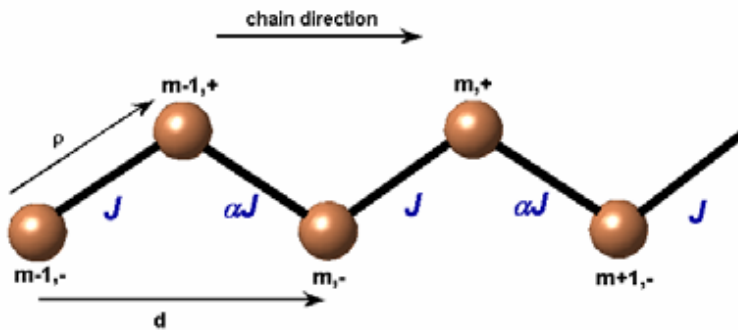


Figure 7.2: Alternating chain layout with the dimer coupling strength provided by J and the intradimer coupling αJ . Each dimer is labeled with an index m and ρ denotes the separation between dimer spins. The chain repeat vector is given by \mathbf{d} .

The $\Delta S = 1$ excitation spectrum for the alternating chain is displayed in Figure 7.3. The one-magnon excitation can be thought of as an excited dimer, the $S = 1$ exciton, traveling along the chain presented as a singlet background. This one-magnon $S = 1$ triplet has an energy gap of $\delta = J - \alpha J/2$ presenting the energy cost to excite a dimer and the dispersion is approximately given by [1]:

$$\omega_{1mag}(\mathbf{Q}) = J - \alpha J/2 \cos(\mathbf{Q} \cdot \mathbf{d}) \quad (7.2)$$

This one-magnon dispersion is displayed by the red solid curve in Figure 7.3. Additionally accessible with INS through vacuum fluctuations is the two-magnon continuum shown by the blue dashed lines in Figure 7.3 with the two-magnon scattering process occurring as described as in Section 5.3. At certain wavevectors the interaction potential between the two magnons is strong causing the formation of a bound mode [3]. In contrast to the spin-ladder material where the bound mode is suppressed it appears

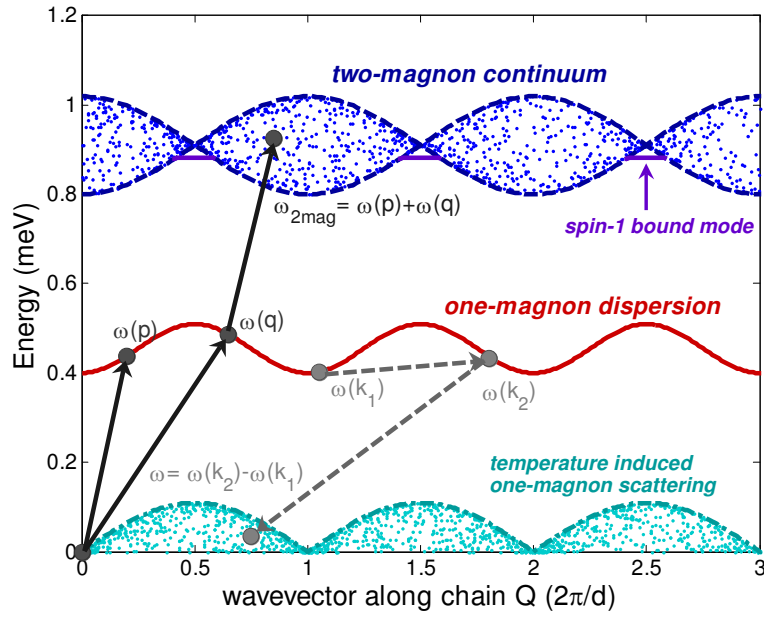


Figure 7.3: The $S = 1$ excitation spectrum for the dimerized chain with a gapped one-magnon dispersion shown by the red solid curve and the also gapped two-magnon continuum by the dashed blue lines. The construction of the two-magnon states is illustrated by the black arrows as an inelastic scattering of two magnons. When applying temperature to the system the one-magnon intraband scattering centered at zero energy occurs shown by the gray dashed arrows and illustrated by the green continuum centered at zero energy.

in copper nitrate at wavevectors below the nodes of the continuum [1] as shown in Figure 7.3.

When applying temperature to the system the one-magnon state gets thermally occupied resulting in the possibility of intraband scattering illustrated by the light gray dashed arrows in the figure. The neutron can transfer energy and momentum to a thermally excited magnon during the scattering process causing a displacement along the dispersion curve resulting in a continuum centered at zero energy shown by the green dashed curves where the effect of this quasi-elastic scattering is similar to the Villain mode found in soliton systems [6].

7.3 Crystal Growth

7.3.1 Solution Growth Method

Due to the weak two-magnon scattering of about 1% of the one-magnon signal a high-quality sample is crucial for a possible resolution of the two-magnon signal. In its original form copper nitrate - $\text{Cu}(\text{NO}_3)_2 \cdot 2.5\text{H}_2\text{O}$ - produces a high incoherent cross-section due to the associated crystal water giving rise to incoherent scattering signal. This can be avoided by replacing hydrogen with deuterium (D) possessing a comparably low incoherent cross-section (compare $\sigma_H^{inc} = 81 \text{ b}$ to $\sigma_D^{inc} = 2.03 \text{ b}$). This substitution is performed by several distillation runs following a procedure similar to the one outlined by Xu [7]. The powder of $\text{Cu}(\text{NO}_3)_2 \cdot 2.5\text{H}_2\text{O}$ is dissolved in high purity heavy water ($> 99.9\%$) and during a vacuum pumping process in a 60°C heat bath most of the regular and heavy water mixture is removed. This procedure is repeated several times reducing the regular water fraction to a minimum and creating a saturated solution during the last distillation run. Cooling this solution facilitates the formation of small ‘seed’ crystals and suspending one seed crystal into the reheated solution causes the seed to act as a nucleation point yielding the growth of a big crystal while slowly cooling the solution. A slow cooling rate is of great importance for a homogeneous growth necessary for the growth of a *single* crystal. Complications of the growth procedure result from the highly hygroscopic nature of copper nitrate due to the existence of a second phase, $\text{Cu}(\text{NO}_3)_2 \cdot 6\text{H}_2\text{O}$, below 26°C . To limit any substitution with hydrogen the whole growth process is preformed in a nitrogen enclosed atmosphere prepared in a glove bag and the final growth products are kept sealed in a hydrogen-free environment. This growth process allowed a growth of an 8 g single crystal with a deuteration level of $< 98\%$ determined by activation measurements.

7.3.2 Production of Crystals

The first step for the growth of the copper nitrate crystals is the generation of seed crystals obtained from a saturated solution. For a saturated solution at 80° C the exact solubility of copper nitrate has to be established with the difficulty in determining the exact amount of crystal water H₂O enclosed in our starting material. Any contact with air below 26° C will increase the crystal water in the material changing the solubility where the solubility is defined as the amount of Cu(NO₃)₂ dissolvable in a 100 g solution. Cost issues recommended the use of H₂O for the determination of the solubility for our starting material and it was determined that 238.8 g Cu(NO₃)₂·2.5H₂O could be dissolved in 50 g H₂O at 80° C corresponding to a solubility of 66.7% in good agreement with the tabulated value of 67.51% [8]. This saturated solution in a sealed glass container is placed into a temperature controlled oil bath at 85° C ensuring a complete dissolution. The liquid is cooled to 35° C, well above the second phase transition temperature, over several hours producing needle-shaped seeds of size ~1 cm×2 mm×1 mm. Choosing one seed and placing the rest back into the solution to avoid any changes in the solubility, a thread is tied around the upper part of the seed and it is placed vertically into the solution. The thread has to be kept outside the solution ensuring the growth of the crystal below it and an easy removal after the completion of the growth process. The new starting temperature with the suspended seed consists of 65° C to avoid any dissolving of the seed, and a cooling rate of 0.5° C per hour until 45° C is achieved necessary for a homogeneous growth. The whole growth process is performed in a nitrogen filled glove bag and resulted in the growth of the 8 g single crystal used in our neutron experiment.

7.3.3 Distillation Process

The aim of the distillation process is the replacement of the crystal water associated with the copper nitrate powder by heavy water and the creation of a saturated solution. For the desired deuteration ratio of at least 98% five distillation runs had to be implemented with the distillation process performed by using a rotation pump with its flask kept at 60° C in a heat bath. The starting solution consists of a saturated heavy water solution and additionally some extra heavy water for the pumping process and replacement of the crystal water ensuring the existence of a solution during the whole distillation process. The saturated solution is prepared using the results mentioned in the previous section consisting of 238.8 g Cu(NO₃)₂·2.5H₂O powder dissolvable in 50 g of H₂O. This ratio has to be corrected due to the higher density of deuterium ($\rho_D = 1.107 \text{ g/mol}$) compared to hydrogen. 238.8 g of the powder material Cu(NO₃)₂ · 2.5H₂O consist of 192.7 g Cu(NO₃)₂ and 46.23 g H₂O resulting in a total of 96.23 g H₂O for a saturated solution equivalent to 106.53 g D₂O establishing the total mass of a saturated heavy water solution at 299.1 g.

The first distillation run is performed with recycled heavy water consisting of a deuteration ratio of at least 80% for which 262.4 g D₂O are mixed to 238.8g Cu(NO₃)₂·2.5H₂O ensuring a deuteration mass ratio of at least 68.0% and an atomic ratio of 65.7%. During the distillation 190.7 g liquid are pumped out of the mixture leaving 310 g of solution. The deuteration ratio does not change significantly during the distillation if at all a slight shift to a higher ratio is possible due to a 1.4° C lower boiling point of H₂O compared to D₂O. For the second run 253.4 g D₂O are added to the remaining solution raising the mass ratio to 89.9% and the atomic ratio to 88.8%; 263.3 g of liquid is pulled during the pumping process. The solution is replenished by 253.4 g of D₂O for the third run creating a mass ratio of 96.9% (atomic ratio of 96.6%) and during the distillation 244.6 g of liquid is removed from the solution. In the second

to last distillation run a mass ratio of 99.0% and an atomic ratio of 98.9% are obtained by mixing 253.2 g D₂O to the solution and during the pumping 259.6 g of liquid is extracted. For the last process 230.0 g D₂O are added and a mass ratio of 99.7% and an atomic ratio of 99.7% are reached. In this last distillation 232.1 g of solution have to be extracted from the mixture to ensure a saturated solution for the growth process and during the actual run 233.7 g of liquid is pulled out. This amount is within the limits of having a saturated solution at 80° leading to the decision to not add more D₂O to limit the air contact of the solution and thus a possible exchange between hydrogen and deuterium. By performing these five distillation runs the target deuteration ratio of >99% is achieved and the growth process as described in the previous section can be started.

7.4 Magnetic Properties

Cu(NO₃)₂·2.5H₂O has a monoclinic symmetry with a space group *I*12/c1 [9, 10]. The deuterated form Cu(NO₃)₂·2.5D₂O has low-temperature (3 K) lattice parameters of $a = 16.1 \text{ \AA}$, $b = 4.9 \text{ \AA}$, $c = 15.8 \text{ \AA}$ and $\beta = 92.9^\circ$. The magnetism of copper nitrate arises from the Cu²⁺ ions coupled through a double Cu-O-O-Cu exchange path explaining the rather weak coupling constants found in the system [1, 11]. The chains are positioned in the a^*-c^* plane with a projection onto this plane shown in Figure 7.4 [12]. The main coupling J is between pairs of spins (e.g. spins 7 and 8, 3 and 4) forming the dimers with a bond length of 5.3 Å illustrated in the Figure 7.4 by the gray solid lines. The next strongest exchange path is between dimers via $J_{[1/2,1/2,1/2]}$ with a bond length of 6.2 Å representing the interdimer coupling αJ shown by the gray dashed lines in the figure. Due to this exchange two different sets of chains exist in the system with one running along [1,-1,1]/2 and the other one along [1,1,1]/2. The repeat distance d in the chain (compare Figure 2) is $d = 11.3 \text{ \AA}$ and the interdimer vector ρ is given by

$\rho = [0.252, 0.027, 0.228]$ from the crystallographic data [10].

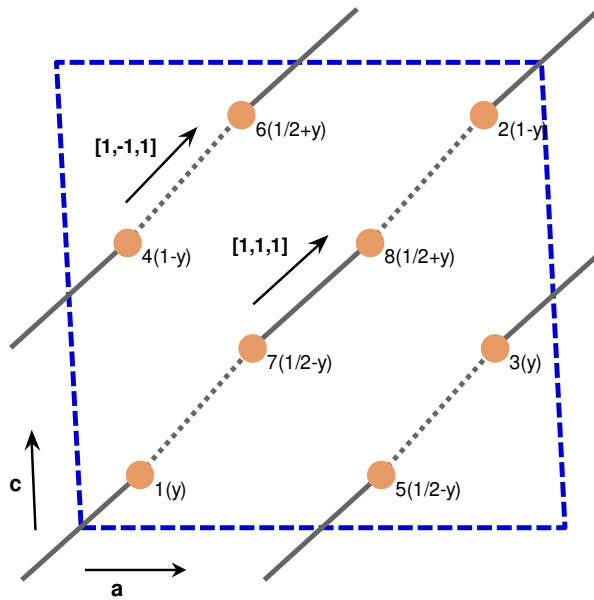


Figure 7.4: Position of the copper ions as projected onto the a^* - c^* plane. Two sets of identical chains exist running in the $[1,1,1]$ and the $[1,-1,1]$ direction.

Magnetization measurements show that a spin-flop ordering is induced in copper nitrate above a first critical field $H_{c,1} \sim 2.7$ T and a second transition to full alignment for $H_{c,2} \sim 4.3$ T [13] with a coupling parameter $\alpha = 0.27$ is found. This is in agreement with the magnetic susceptibility measurements [14] and specific heat measurements confirming the critical field results with $H_{c,1} = 2.8$ and $H_{c,2} = 4.4$ T. The first critical field $H_{c,1}$ can be used to determine the gap energy (using $g = 2.33$) and has been reported as $\Delta = 0.378 \pm 0.007$ meV [13].

These results are in good agreement with the values found from a triple-axis experiment by using perturbation theory of an expansion to $O(a^9)$ determining the coupling constants to be $J = 0.455 \pm 0.002$ meV, $\alpha = 0.277 \pm 0.006$ and $\Delta = 0.379$ meV [1]. These measurements also confirm the existence of the weak two-magnon scattering with its intensity approximately 1% of the one-magnon, but for a comparison with the perturbative model the triple-axis results are insufficient leading to the necessity of

high-resolution time-of-flight measurements on a highly deuterated sample [1].

Previous INS measurements performed by Xu *et al* [11] explored the temperature dependence with zero field and evaluated the coupling constants. Using a dispersion based on first-order perturbation theory and including interdimer coupling in both the a^* and the c^* direction the following coupling constants were obtained: $J = 0.442$ meV, $\alpha = 0.24$, $J_{a_{inter}} = 0.012$ meV and $J_{c_{inter}} = 0.018$ meV. The different value of α compared to previous measurement was explained by the inclusion of the interchain coupling absent in previous analyses. For the temperature treatment Xu *et al* observed an exponentially activated band and damping effects modeled by Lorentzian line broadening.

7.5 Experimental Details

INS measurements were performed on the inverse geometry, time-of-flight spectrometer OSIRIS described in detail in Section 3.5.2. The final energy was chosen by the graphite analyzer to be $E_f = 1.845$ meV. The highly deuterated sample was mounted with the a^*-c^* plane as scattering plane and orientated with the b^* direction along k_i . The two sets of chains provide an equal contribution to the cross-section due to this equal projection onto the a^*-c^* plane. The wavevector transfer $\mathbf{Q} = k_i - k_f$ is projected along the chain direction as presented in Figure 7.4 and the rotation angle φ presents the difference between k_i and the actual inplane chain direction.

The sample was mounted on a dilution stick in a ${}^3\text{He}$ cryostat to ensure a base temperature of $T = 120$ mK more than an order of magnitude smaller than the gap energy (~ 4.4 K) ensuring the ground state to be free of any thermally activated magnons. A first experiment without any magnetic field measurements was performed for base temperature, $T = 2$ K, 4 K and 6 K. In a second experiment the temperature dependence under field was studied where first an overview was established by measuring a range

of 28 different fields between $B = 0\text{ T}$ and 6 T at the base temperature of $T = 120\text{ mK}$ with the aim of an accurate determination of the two critical fields. Afterwards a more throughout measurement with temperature dependence was performed for six fields enclosing the two critical fields ranging from $B = 2.7\text{ T}$, 2.84 T , 3.0 T , 3.5 T , 4.0 T , 4.26 T to 4.4 T and for various temperatures of $T = 0.12\text{ K}$, 0.3 K , 0.5 K , 0.8 K , 2 K and 4 K .

7.6 Zero Field

7.6.1 Background Subtraction

The one-magnon structure factor for the dimerized chain is dominated by the dimer structure factor which is proportional to $(1 - \cos(\mathbf{Q} \cdot \rho))$ (exact expression provided in [1]) providing a vanishing intensity when fulfilling $\mathbf{Q} \cdot \rho = 2\pi n$ (n as an integer). In our experiment this occurs for $Q \sim 2$ (in units of $2\pi/d$) with any remaining scattering due to the incoherent scattering mainly from the 2% hydrogen in the system. The reason for this residual scattering is as follows: The incoming neutron scatters off inelastically with wavevector and energy transfer (\mathbf{Q}, ω) creating a magnon during this process. Afterwards the neutron has a small probability of scattering elastically during an incoherent process changing its wavevector again. The total scattering process is a product of our one-magnon inelastic scattering and the elastic incoherent scattering serving as background. However, the incoherent scattering is independent of the wavevector and appears as a wavevector band underlying the one-magnon signal. Taking a constant wavevector cut around $Q = 2.1$ will give a measurement of the incoherent scattering due to the vanishing of the inelastic scattering. The constant energy cut for the lowest signal appears for $Q = 2.1 \pm 0.05$ and is displayed in Figure 7.5. The red solid line presents a function based on five fitted Gaussians and will be used for the one-magnon background subtraction throughout this thesis. The one-magnon background

subtracted data is illustrated in Figure 7.6.

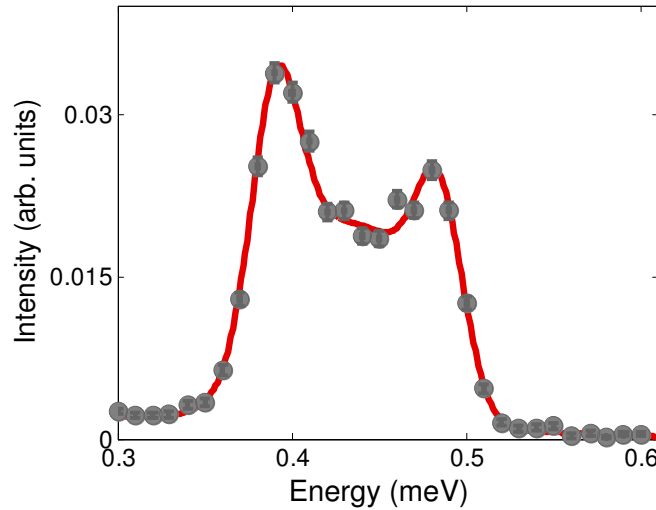


Figure 7.5: Constant wavevector cut at $Q = 2.1 \pm 0.05$ to determine incoherent one-magnon background and the red solid line is 5 fitted Gaussians.

A similar situation should be found for the two-magnon signal also dominated by the dimer structure factor. However a small wavevector dependent background is discovered when taking constant wavevector cuts throughout the experimentally accessible Q range most likely resulting from crystallites in the system. Similar to the one-magnon background treatment a constant wavevector cut is performed at $Q = 2.0 \pm 0.05$ (region with weakest signal) where a single Gaussian with a center $E = 0.876$ and width=0.047 can be fitted through the signal. Taking wavevector cuts all through the two-magnon region confirms this center and width, but an overall quadratic wavevector dependent background has to be included. The two-magnon background subtracted data is shown in Figure 7.6, but the intensity has to be enhanced by a factor of 100 to display it in the same figure as the one-magnon signal.

The intraband scattering is only apparent upon heating allowing the low temperature data ($T = 120$ mK) to serve as a background accounting for the elastic scattering by fitting a Gaussian through a zero energy cut. The background subtracted intraband scat-

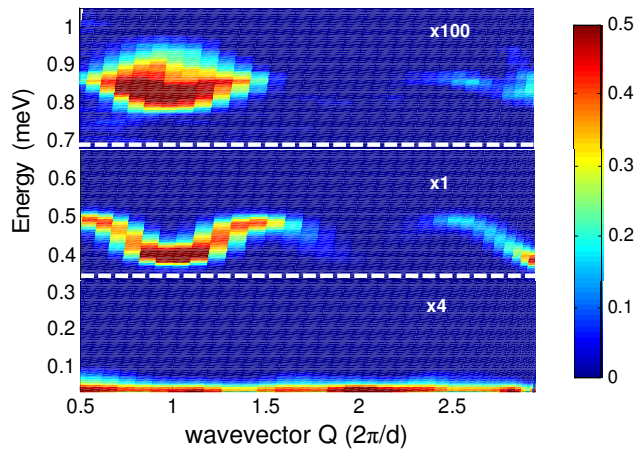


Figure 7.6: Background subtracted complete excitation spectrum with the one-magnon dispersion, the two-magnon continuum (intensity enhanced by a factor of 100) and the intraband scattering at $T = 6\text{ K}$ centered at zero energy (enhanced by a factor of 4).

tering is shown for a temperature of $T = 6\text{ K}$ displaying the effect most pronouncedly in Figure 7.6 where the intensity had to be enhanced a factor of 4 to illustrate it in the same plot as the one- and two-magnon data.

7.6.2 Dispersion Relation

For an exact determination of the coupling constants a dispersion relation for several chain settings each with a different rotation angle φ is considered. Introducing a rotation angle φ only a part of the chain actually contributes to the wavevector transfer Q and thus by choosing different rotation angles different contributions can be viewed leading to an accurate determination of the coupling constants. With the help of the detector angles the parallel and perpendicular contributions of the wavevector transfer for the actual chain position can be calculated. Knowing the perpendicular component the contribution of the interchain dispersion can be corrected and the projection of the actual chain position onto the wavevector transfer Q can be evaluated.

Figure 7.7 displays the measured dispersion for the chain with several rotation angles. In part (a) rotation angle of $\varphi = -4^\circ$ is chosen showing an optimal Q range coverage

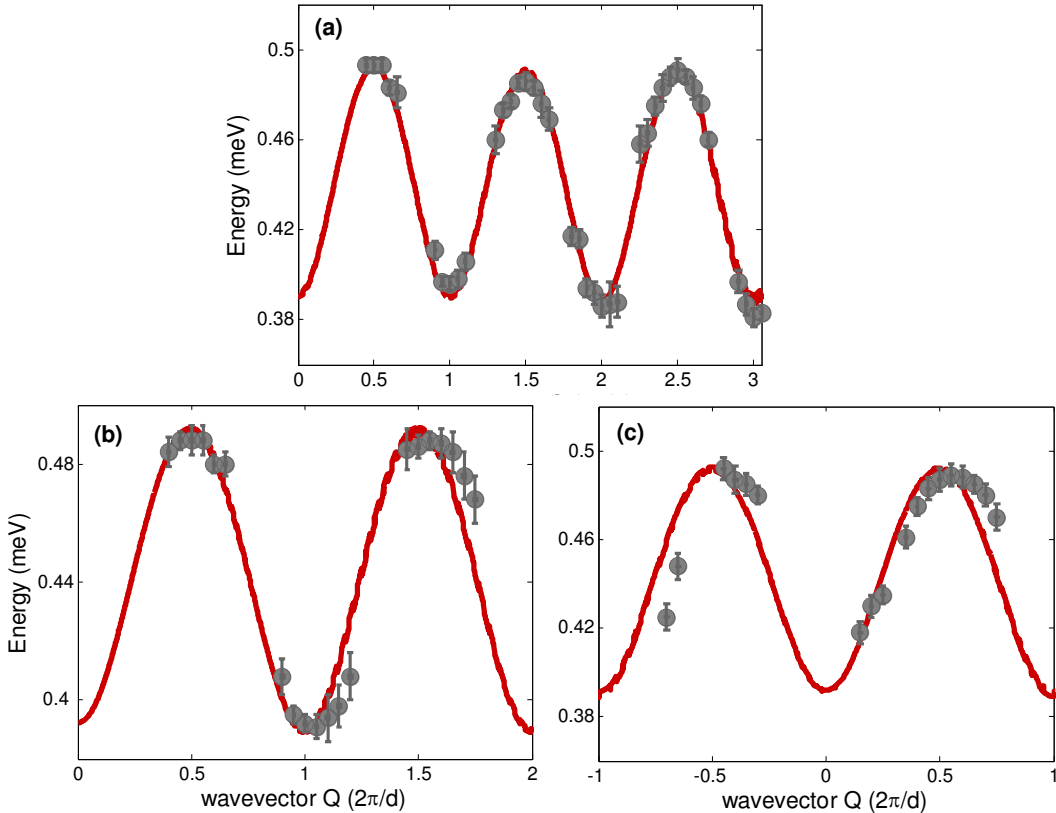


Figure 7.7: Dispersion relation for several different chain orientations: (a) angle $\varphi = -4$ compared to wavevector transfer Q . (b) angle $\varphi = 44$ and (c) $\varphi = 77$.

including all prominent features, and the majority of the experiment is performed with this rotation angle. The two other chain orientations with $\varphi = 44$ illustrated in part (b) and $\varphi = 77$ in part (c) are performed ensuring a very accurate determination of the coupling constants. Using the same dispersion relation as used by Xu [7] and performing a simultaneous fitting of the three different rotation values for φ our data is well described by a dispersion relation form of:

$$\omega(\mathbf{Q}) = J - \frac{1}{2} \sum J \cos(Q \cdot \mathbf{d}) \quad (7.3)$$

with a dominant dimer coupling $J = 0.443 \pm 0.002$ meV, an alternation ratio $\alpha = 0.227 \pm 0.005$ leading to an interdimer coupling of $J_2 = \alpha J = 0.101$ meV along $[1\ 1\ 1]/2$ as discussed in Section 7.4. Additionally weak antiferromagnetic interchain coupling along the a and the c direction is included with $J_{a_{inter}} = 0.006 \pm 0.003$ meV and

$J_{c_{inter}} = 0.0018 \pm 0.0005$ meV where the coupling along the a^* direction follows [1/2 0 0] and the coupling along the c^* direction [0 0 1/2] in reference to Figure 7.4. The solid red line in Figure 7.7 presents the one-magnon dispersion relation as calculated by the coupling constants displaying a very good agreement with our data. The only small discrepancy can be found in part (c) in the two data points around $Q \sim -0.7$ which could result from a crystalline in the sample being in agreement with the Q dependency found in the two-magnon background subtraction.

These values are in good agreement with the coupling constants found by Xu [11], but in our case the alternation parameter is smaller ($\alpha = 0.227$ compared to $\alpha = 0.24$) as well as our interchain couplings. Our fitting procedure is more accurate than the one performed by Xu due to the different rotation angles taken into account and a fairly poor background subtraction by Xu making a precise fitting difficult. Using our coupling values the one-magnon gap can be extracted using the dispersion relation given by equation 7.3 to be $\Delta = 0.388$ meV in very good agreement with the result from Diederix *et al* of $\Delta = 0.378 \pm 0.007$ meV. The small discrepancy of $\sim 2\%$ could result from the anisotropic g -value used by bulk magnetic measurements to determine the gap value.

7.6.3 One-Magnon Scattering

The one-magnon scattering can be calculated by using the dispersion relation in equation 7.3 and extracting the neutron scattering matrix $S^{+-}(\mathbf{Q}) \equiv \left| \langle \Psi_{\lambda'} | S_{\mathbf{Q}}^+ | \Psi_{\lambda} \rangle \right|^2$ based on the 1D perturbation theory [3]. This neutron scattering matrix element is dominated by the dimer structure factor and can be approximated as:

$$S^{+-}(\mathbf{Q}) = (1 - \cos(Q \cdot \rho)) \left[1 + \frac{1}{2} \alpha \cos(Q \cdot \mathbf{d}) \right] \quad (7.4)$$

The leading-order scattering process results from the bare dimer component of the ground state and the $(\alpha/2 \cos Q \cdot \mathbf{d})$ component arises from a two-dimer excitation

in the ground state (vacuum fluctuation). The contribution of the two-dimer excitation only accounts for $\sim 2\%$ of the structure factor [1] making an approximation of the structure factor by the bare dimer contribution sufficient. Since the experimental setup studies the projection of the chain onto the a^*-c^* plane the matrix element can be simplified using $\rho = [0.252, \pm 0.027, 0.228]$ resulting in an expression of the structure factor of $S^{+-} = (1 - \cos(0.252 \cdot Q_h + 0.228 \cdot Q_l))$. The calculation includes the correction for the Cu^{2+} magnetic form factor [15] and also the instrumental line broadening by convolving the theoretical calculations with an estimate of the instrumental resolution and the sample mosaic spread.

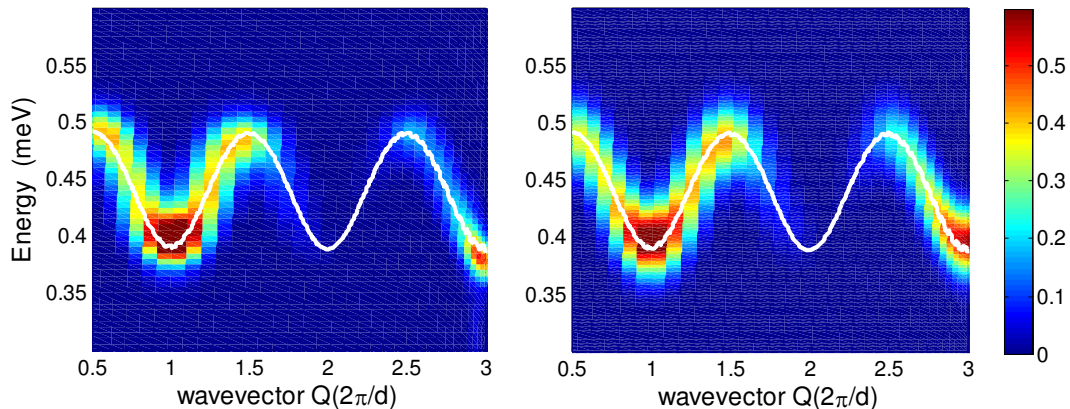


Figure 7.8: Color plot of the one-magnon signal. (a) Measured one-magnon data with non-magnetic background subtracted and included is the calculated dispersion curve (white curve). (b) Calculated one-magnon data from the dispersion curve and the dimer structure factor.

Figure 7.8 displays the comparison between the data and the calculated one-magnon signal. In part (a) the background subtracted one-magnon signal is shown with the theoretically calculated one-magnon dispersion curve illustrated by the white curve. Part (b) presents the simulated one-magnon signal based on the dispersion relation (equation 7.3) with the fitted coupling constants, the structure factor and also including the calculated one-magnon dispersion curve (white curve). Overall a very good agreement is found between the data and the simulated one-magnon signal with the only discrep-

ancy seen in the intensity distribution at higher Q values with an overestimation of the calculation. The intensity vanishes around $Q \sim 2.1$ resulting from the dominance of the dimer structure factor with the exact wavevector depending on the rotation angle φ .

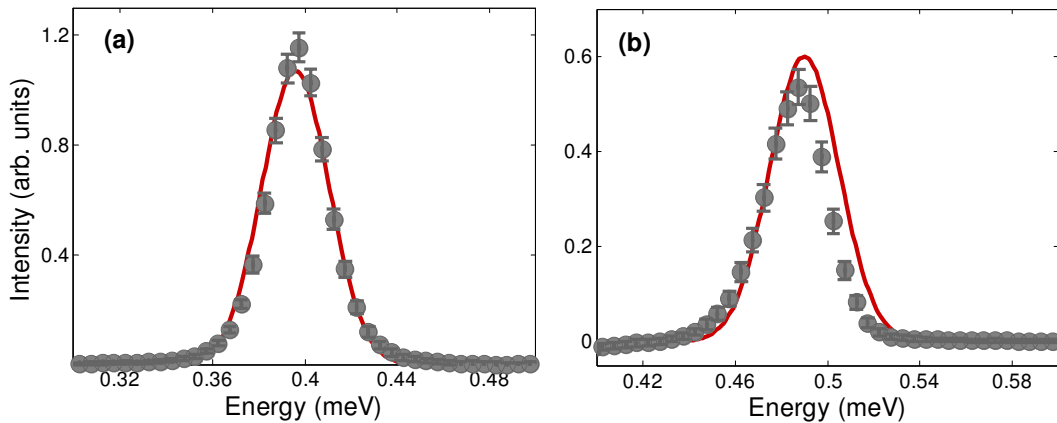


Figure 7.9: Constant wavevector cuts included is the theoretical calculated curve by performing the same cut through the simulated one-magnon signal illustrated by the red curve. (a) for the dispersion minimum at $Q = 1$ and (b) for the dispersion maximum at $Q = 1.5$.

A direct intensity comparison between the background subtracted data and the calculated one-magnon signal is provided by taking constant wavevector cuts around the dispersion minimum at $Q = 1$ and the dispersion maximum at $Q = 1.5$ displayed in Figure 7.9. Figure 7.9 (a) presents a cut performed at $0.95 < Q < 1.05$ shown by the gray data points while the red curve is the calculated one-magnon signal for the same cut describing the data very well. In part (b) the energy maximum of the dispersion is examined by taking a constant wavevector cut for $1.45 < Q < 1.55$ and comparing with the calculated signal (red curve). The calculation overestimates the intensity for this Q vector already and a more pronounced overestimation is apparent for even higher wavevectors as illustrated by the color plot in Figure 7.8. A detailed investigation of the intensity distribution is provided in the next section.

7.6.4 Dimer Structure Factor

The intensity discrepancy between the data and the simulation for higher wavevector values can be explained by a difference between the proposed [10] and the actual position of the dimer. A change in dimer d -spacing will alter the intradimer vector ρ and thus the structure factor dominated by the dimer proportional to $(1 - \cos(Q \cdot \rho))$ with $\rho = [0.252, \pm 0.027, 0.228]$ as identified by Morosin *et al* [10].

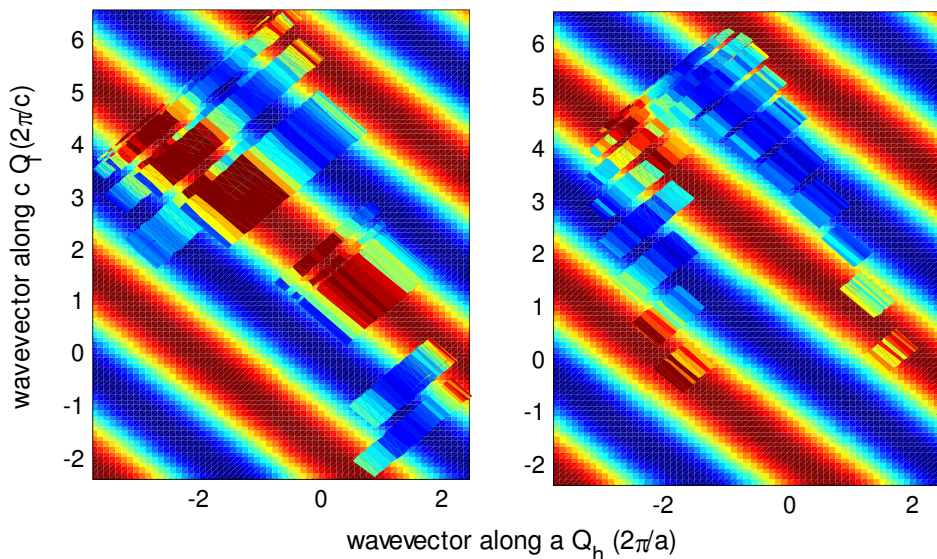


Figure 7.10: Comparison between the dimer structure factor calculation with the data in the h - l scattering plane. The left panel displays the data obtained for measurements without a magnet in the experimental set-up and the right panel data with magnet. The interdimer vector for the calculation has to be varied to $a=0.234$ and $c=0.27$ to establish an agreement.

Comparing the data with the simulation an over-estimation of the intensity for higher Q wavevectors is apparent (compare Figure 7.8) leading to a closer investigation of the intensity distribution in the a^* - c^* scattering plane. The intensity distribution in the scattering plane is obtained by performing scans with different rotation angle φ covering various wavevector combinations, Q_h and Q_l , in the h and l reciprocal plane. The data are extracted for the one-magnon signal by conducting an energy integration over the one-magnon region of $E=0.3$ to 0.6 meV. This can be directly compared with a calcula-

tion of the dimer structure factor in this plane provided by $S^{+-} = (1 - \cos(a \cdot Q_k + c \cdot Q_l))$ with the a and c presenting the coefficients of the intradimer vector ρ .

Figure 7.10 displays the comparison between the measured data and the simulation with the data overlaying the simulation. By altering the intradimer coefficients the steepness and the location of the intensity stripes for the simulation can be varied until an agreement with the data is reached.

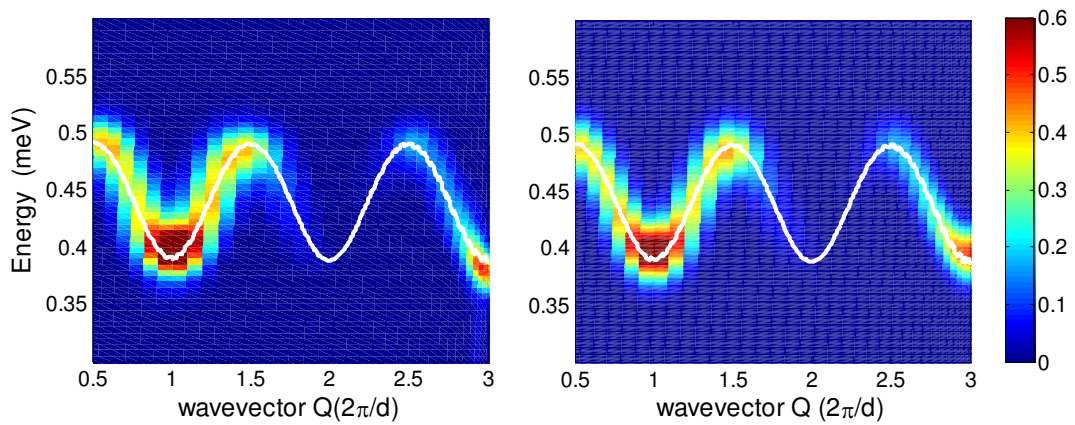


Figure 7.11: Color plot of one-magnon signal. Left panel: magnetic background subtracted data. Right panel: one-magnon simulation with newly obtained interdimer vector.

The left part of the figure represents the data obtained for an experimental set-up without a magnet and the right set of the data for the measurements including the magnet. Both sets are used for the comparison to ensure an exact determination of the dimer spacing. The best agreement is reached for values: $a = 0.234$ and $c = 0.270$ as shown in Figure 7.10. Each data strip is obtained by a different rotation angle φ and covers a different projected orientation of the dimer in the scattering plane (different Q_h and Q_l) allowing a more detailed intensity distribution in the h - l plane.

Overall a very good agreement between the data and the calculation with the new interdimer coefficients is apparent. The difference in the values for the intradimer vector can be explained by a mistaken identification of the dimer position as proposed

in Figure 7.4. Our analysis leads to the conclusion that the dimer is formed between the neighboring spins with the larger separation, i.e. spins 1 and 7 as illustrated in Figure 7.4, and the weaker inter-dimer coupling between spins 7 and 8 identified as the main coupling by Morosin *et al* [10]. Comparing with the crystallographic data provided for copper nitrate the intradimer vector for this new dimer position leads to values of $a = 0.247$ and $c = 0.273$ for room temperature. Considering the decrease in lattice parameter between low-temperature ($T = 3$ K) and room temperature could explain the lower value for the a and c coefficients of the intradimer vector as found by our analysis. Additional discrepancies can possibly be interpreted by an insufficient accuracy of the sample alignment during the experiment for the various rotation angles φ .

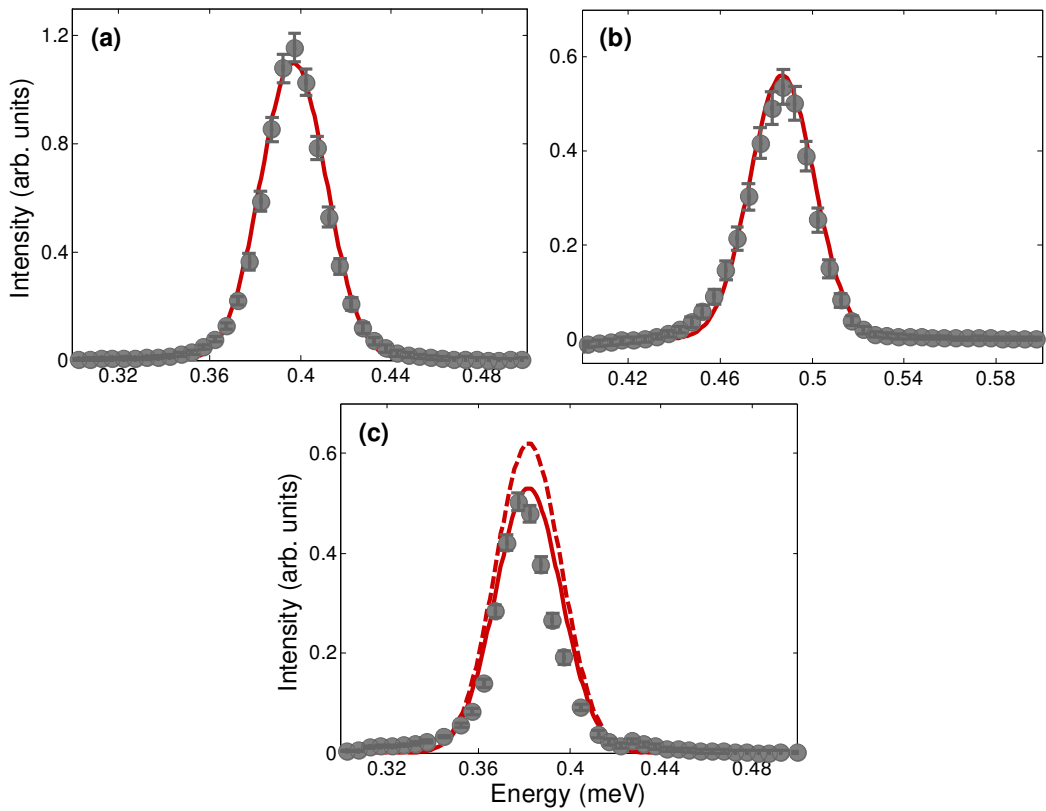


Figure 7.12: Constant wavevector cut: (a) at energy minimum at $Q = 1.0 \pm 0.05$ and (b) at energy maximum at $Q = 1.5 \pm 0.05$ and (c) at $Q = 3.0 \pm 0.05$. The red solid curve is the same cut as performed for the simulation with the newly obtained interdimer vector and the dashed line in part (c) is the same cut through the calculation with the previous interdimer vector.

As apparent from Figure 7.11 the intensity distribution for the higher wavevector regions for the calculation with the newly obtained interdimer vector matches the intensity of the one-magnon data quite well. This feature is more apparent when comparing the constant wavevector cuts as provided in Figure 7.12. Part (a) displays the wavevector cut through the dispersion minimum for $Q = 1.0 \pm 0.05$ and part (b) the cut through the energy maximum at $Q = 1.5 \pm 0.05$. The red curve is the same cut as performed through the simulation illustrating a very good agreement between the data and the simulation. This improvement of the new interdimer position is demonstrated for a constant wavevector cut for a higher value of $Q = 3.0 \pm 0.05$ in part (c). The solid red line is the same cut realized for the calculation with the new interdimer coefficients and the dashed curve presents the previous interdimer position. The intensity discrepancy between the data and the calculation with the previous interdimer vector has not been noticed in the previously performed experiments [1] because of a limited wavevector coverage of only up to $Q \sim 2.5$.

7.6.5 Two-Magnon Scattering

For the calculation of the two-magnon intensity an analytical solution based on the 1D perturbation theory as described by Barnes *et al* [3] is used. The integrated intensity of the two-magnon continuum is composed of a sum of the scattering from the continuum and the bound mode with an expression obtained by the perturbative analysis. The two-magnon continuum contribution is based on the calculation of the wavefunction to the order $O(\alpha)$ and with the help of a large number of spins the neutron scattering matrix element can be calculated analytically. For certain wavevector regions located at the nodes of the continuum the bound mode exists and also contributes to the integrated intensity accessible as also confirmed by numerical calculations to higher order in α [1]. For simplicity the calculation is performed with the interdimer coupling only

and does not include the weak interchain couplings, but is corrected for the estimated instrumental resolution and the mosaic spread of the sample. The comparison between the calculation and the two-magnon data is displayed in Figure 7.13 with the left panel illustrating the background subtracted data including the outline of the calculated continuum based on dimer and interdimer coupling as white dashed curves. The calculation based on the newly obtained interdimer vector is presented in the right panel with the continuum (dashed curves) included. Overall a good agreement can be found, although there are small discrepancies in the intensity distribution especially for higher wavevectors where an overestimate of the intensity in the calculation is apparent despite the use of the new improved dimer position. A possible explanation is an insufficient analytical solution due to only considering wavefunctions up to the order of $O(\alpha)$ and higher order will affect the two-magnon stronger than the one-magnon case due to the already weak signal leading to a mismatch between data and calculation.

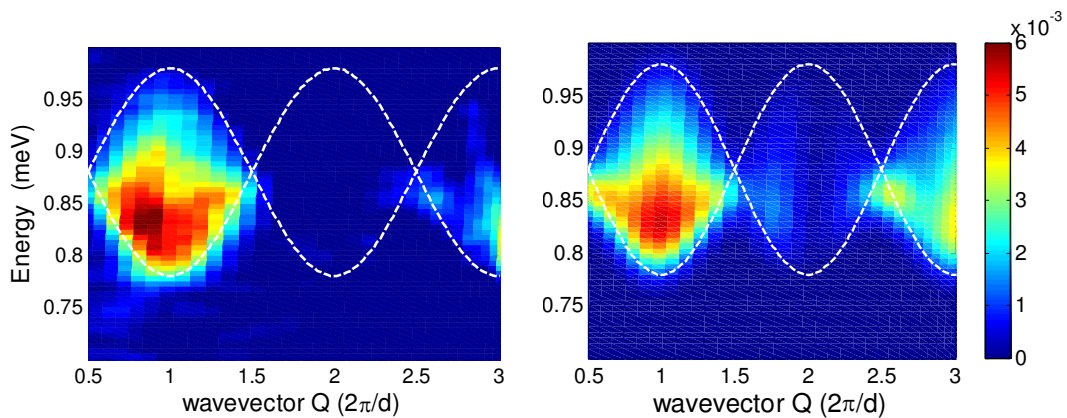


Figure 7.13: Color plot of the two-magnon scattering. (a) Background subtracted data with the theoretically determined two-magnon continuum indicated by the dashed lines. (b) Simulated two-magnon continuum with the boundary indicated by the dashed lines.

For a more detailed comparison constant wavevector cuts at the maximum width and intensity of the two-magnon continuum located at a wavevector of $Q = 1.0$ and at the minimum width of the continuum and prediction of the bound mode at $Q = 1.5$ are provided. Figure 7.14 (a) shows the experimental data points for the wavevector cut

$0.95 < Q < 1.05$ (gray points) and the red curve presents the same cut performed for the two-magnon simulation; additionally a wavevector cut at $1.45 < Q < 1.55$ is illustrated in part (b) of the figure. It is evident from the figure that the theoretical calculation appears to be quantitatively very similar to the data for these wavevectors. One of the most interesting aspects of the multi-particle states is the existence of the bound mode below the two-magnon continuum at certain wavevectors (compare Figure 7.3).

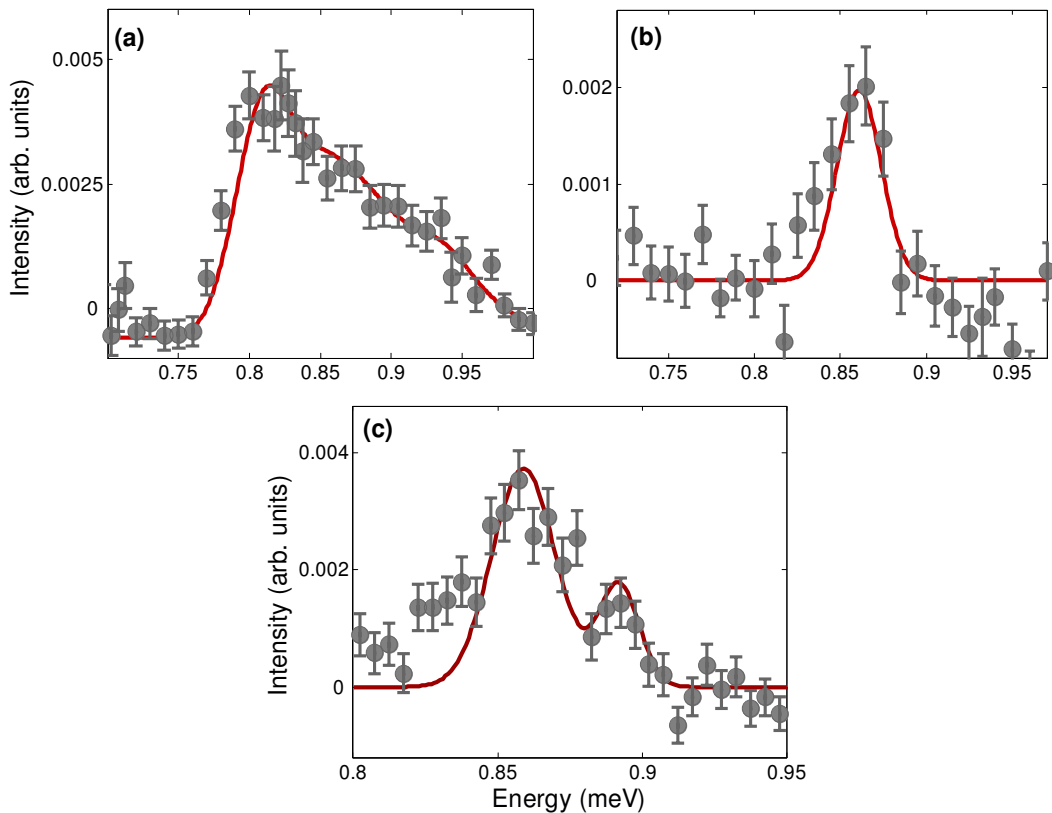


Figure 7.14: Constant wavevector cuts the for two-magnon data: (a) at $Q = 1$ with the red curve indicating the same cut performed through the simulation. (b) At the bound mode at $Q = 1.5$ included cut performed through the simulated data as the red curve. (c) Bound mode for a different rotation angle φ with the solid line presenting two fitted Gaussians.

This bound mode is predicted to be most prominent around $Q = 1.5$ [1] due to the formation of a node of the two-magnon continuum resulting in the appearance of the bound mode and the intensity of the bound mode is discovered strongest for $Q = 1.5$

due to the structure factor given as [3]:

$$S^{+-}(\mathbf{Q}) = \left(\frac{\alpha}{4}\right)^2 \left[1 - 4 \cos^2(Qd/2)\right] \times \{\sin[\mathbf{Q} \cdot (\rho + \mathbf{d})/2] + 3[\mathbf{Q} \cdot (\rho - \mathbf{d})/2]\}^2 \quad (7.5)$$

Performing the cut at $Q = 1.5$ a peak can be resolved as seen in Figure 7.14 (b). Fitting this peak reveals an energy of $E_{bound} = 0.860 \pm 0.006$ meV for the bound mode in excellent agreement with the calculated energy of the bound mode of 0.864 meV for our coupling constants by using the dispersion of the bound mode determined from the perturbative analysis [3]:

$$\omega_{BS} = 2J - \frac{\alpha J}{4} \left[4 \cos^2(Q/2 \cdot \rho) + 1\right] \quad (7.6)$$

Comparing the data with the same cut performed through the simulation dominated by the existence of the bound mode shows a very good agreement both in intensity and position illustrated by the red solid curve in Figure 7.14 (b). The binding energy defined as the difference between the energy of the bound mode and the calculated two-magnon continuum is predicted for the alternating chain to be $E_{binding} = J(\frac{1}{4}\alpha - \frac{13}{32}\alpha^2) = 0.0159$ meV. This agrees with the calculated value for the node of the two-magnon continuum at $Q=1.5$ found at an energy of $E=0.878$ meV.

Choosing a different offset angle φ it is possible to tune into the wavevector region around $Q=1.5$ establishing the possibility of separating the bound mode from the two-magnon continuum. The same wavevector cut for an offset angle of $\varphi=44$ is displayed in Figure 7.14 (c) illustrating two resolved peaks. The peak at the lower energy and the more intense one is found at $E = 0.859$ meV representing the bound mode. The other peak located at $E = 0.892$ meV is agreeing well with the calculated energy of the two-magnon continuum with an onset at $E=0.878$ meV. The shift to a higher energy should result from the rotation angle φ and also the contribution of the resolution over the continuum. The solid line through the data is two fitted Gaussians for the extraction of the peak positions. A comparison with our perturbative theory for the continuum peak

resolution is not possible, as higher order approximations in α need to be considered for the calculation of the continuum intensity at the specific wavevector location of the node.

7.7 Magnetic Field

7.7.1 Overview

Applying a magnetic field to the system will split the three-fold degenerate one-magnon band according to the Zeeman energy $g\mu_B S^z B$. Selecting the field properly the system can be driven through two different phase transitions: condensation of magnons into the ground state at $H_{c,1}$ and spin saturation at $H_{c,2}$. An overview of this process is displayed in Figure 7.15 covering a range of applied magnetic fields from $B = 0$ to 6 T. The intensity scale is kept constant throughout the color plots allowing a direct comparison between the various fields. The one-magnon background consists of the incoherent scattering due to a small amount of hydrogen in the system and is handled as described in the zero field section. Additionally contributing to the non-magnetic background is the incoherent nuclear scattering centered at zero energy especially interfering with the lower Zeeman split band close to the critical fields. However this could be precisely obtained from the zero field measurement.

The first color plot of Figure 7.15 illustrates the system at zero field displaying the familiar one-magnon band discussed previously. The characteristic magnon spin quantum numbers, $S^z = 1, 0, -1$, lead to the splitting of the one-magnon band when applying magnetic field as shown in the second color plot for a field of $B = 1.5$ T. The difference in intensity between the lower ($S^z = -1$) and upper ($S^z = 1$) contribution compared to the middle band ($S^z = 0$) results from the different components contributing to the correlation function. While the middle curve presenting the S^{zz} value is perpendicular to

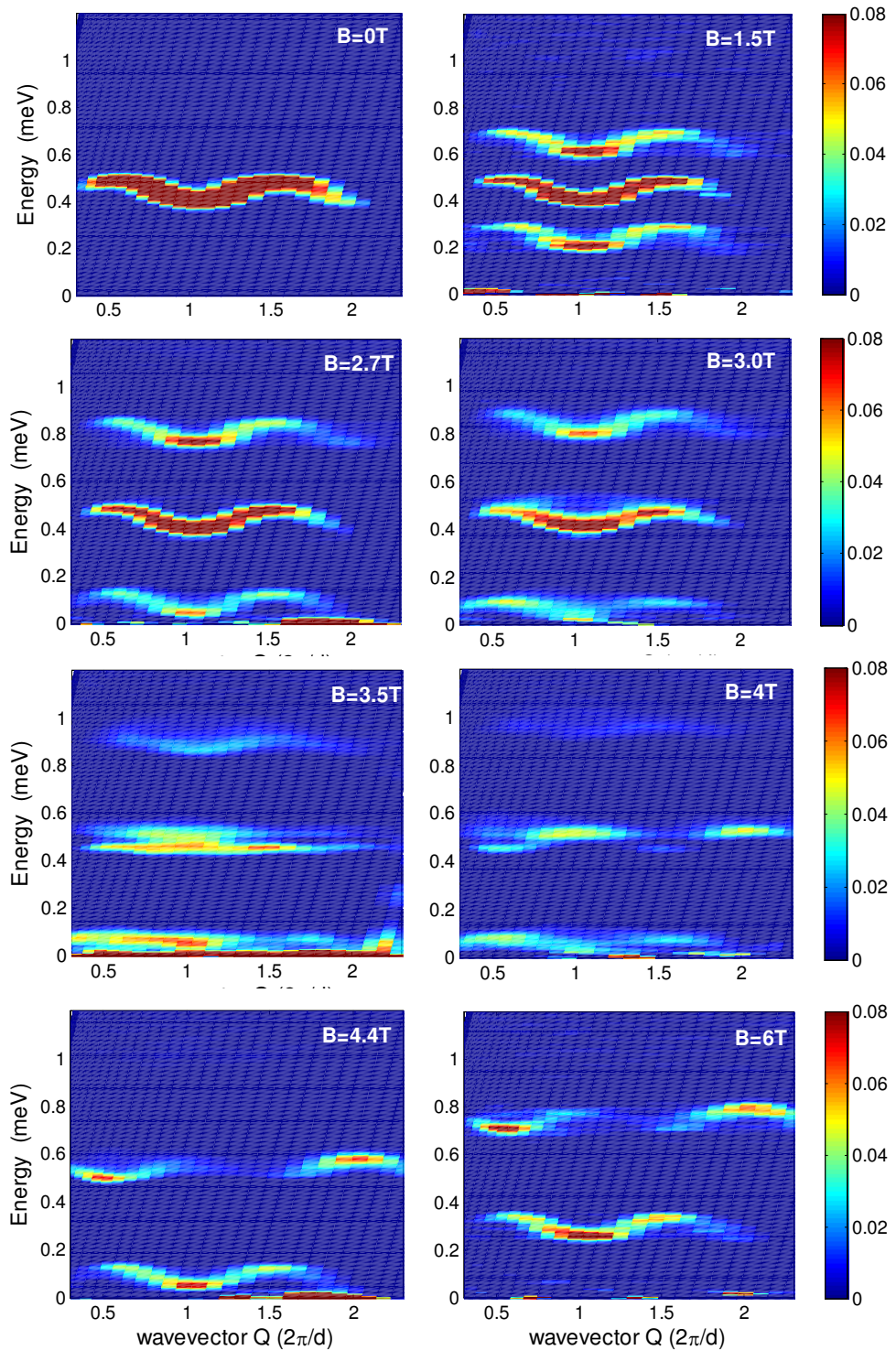


Figure 7.15: Color plots displaying the field evolution and band splitting according to the Zeeman energy with reaching the two critical fields of condensation of magnons into the ground state at $B \sim 3.0\text{ T}$ and saturation at $B \sim 4.4\text{ T}$. Above the second critical field a clear change in the excitation modes is apparent with the behavior consistent with a dimerized ferromagnet.

the beam direction leading to a full contribution to the correlation function, the upper and lower curve embodying the S^{+-} and S^{-+} contributions are composed of an in-plane perpendicular to Q and an in-plane parallel to Q contribution resulting in half the beam intensity. The color plot at a field of $B = 2.7$ T reveals the system in the vicinity of the first critical field with the condensation of magnons into the ground state apparent at a field of $B = 3.0$ T as displayed in the next color plot and showing a quantum phase transition resulting in a change of the excitation spectrum. Forcing the magnons to condense into the ground state changes its characteristics to a Luttinger Liquid (LL) type behavior characterized by quantum fluctuations dominating the ground state. This causes a decoherence of the magnons resulting in an existence of fractional particles in the excitation spectrum comparable to the spinons of the 1D antiferromagnetic Heisenberg spin 1/2 chain (HAFC). In quantum mechanics changes in the angular momentum are only allowed in integer units resulting in the creation of multiple particles during the scattering process of a LL causing the formation of the continuum. At the critical field $H_{c,1}$ a crossover from the magnon type excitation to the fractional particles (v.v. for $H_{c,2}$) is found. This is apparent in the data at $B = 3.0$ T displaying a formation of a continuum with the exact behavior investigated in section 7.7.4 by performing constant cuts at characteristic wavevectors and comparing it to the behavior and line shapes of a LL. The next color plot shows the excitation spectrum at $B = 3.5$ T representing the region in between the two critical fields characterized by a cross-over regime between the different excitation spectra below $H_{c,1}$ and above $H_{c,2}$. The characteristic scattering for the saturation critical field is shown in the following two color plots for fields at $B = 4.0$ T and $B = 4.4$ T. At saturation all the spins are aligned up resulting in an excitation spectrum similar to a ferromagnet. The scattering process to the upper $S^z = 1$ band vanishes due to the neutron scattering selection rule of $\Delta S = 1$. Applying a field of $B = 4.0$ T the continuum of the upper band is still apparent showing that full saturation

has not been reached, but is achieved in the next color plot of $B = 4.4$ T. The last color plot is well above the saturation field at $B = 6.0$ T characterized by the gap reappearance of the lower mode. The excitation modes at the fields above saturation can be modeled using spin wave theory presented in Section 7.7.3 with the simulation of the data included.

7.7.2 Determination of the Critical Fields

This section illustrates the determination of the two critical fields $H_{c,1}$ and $H_{c,2}$ by using the energy splitting of the one-magnon band. The first critical field $H_{c,1}$ is reached upon condensation of magnons into the ground state illustrated in the disappearance of the energy gap of the lower band (compare Figure 7.15), while a gap reappearance marks the transition through the second critical field $H_{c,2}$ when reaching full saturation. Following the lower band with its energy gap (by taking constant energy cuts at $Q = 1.0$) will lead to an exact determination of the critical fields. Due to the difficulty in following the gap close to the critical fields constant wavevector cuts at $Q = 0.5$, the zone boundary, are additionally considered. Once the critical field $H_{c,1}$ is reached the zone boundary will remain at a constant energy indicating the gap closure until an applied field of $H_{c,2}$.

Figure 7.16 shows the gap energy as a function of the magnetic field where the red data points are obtained by the cut at $Q = 1.0$ while the gray data points illustrate the cut at $Q = 0.5$ for the determination of the zone boundary. The solid lines present the fitted lines through the data points with both consisting of the same slope and the intersection of the band gap energy with the magnetic field axis marks the reaching of the two critical fields found at $H_{c,1} = 3.04$ T and $H_{c,2} = 4.03$ T. These values have to be corrected for the interchain coupling. The size of this coupling is evaluated by the difference between the experimentally determined one-magnon gap (in this case

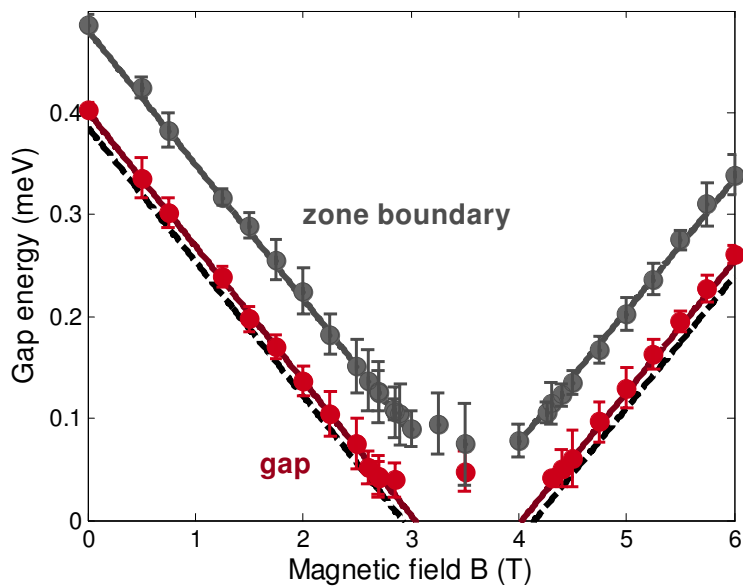


Figure 7.16: Determination of the critical fields by taking constant wavevector cuts to follow the gap (cuts at $Q = 1.0$) and zone boundary (cuts at $Q = 0.5$) evolution for various fields. The intersection of the gap curve with field axis reveals the critical fields and the correction for the interchain coupling is presented by the black dashed lines.

$\Delta = 0.403$ meV) and the gap as calculated by the coupling constants ($\Delta = 0.387$ meV) leading to the corrected critical fields of $H_{c,1} = 2.92$ T and $H_{c,2} = 4.14$ T.

7.7.3 Excitation Spectrum above Saturation

Above the second critical field the excitation spectrum changes its appearance as can be seen for fields above $B = 4.14$ T in Figure 7.15 and also in the left part of Figure 7.17 illustrating the data obtained slightly above the second phase transition at a field of $B = 4.26$ T. Above this second critical field $H_{c,2}$ saturation is reached and thus all the spins are aligned in the same direction transforming the system into a dimerized ferromagnetic chain. This system and its corresponding excitation spectrum can be calculated using a spin wave theory approach. The ground state consists of a product of these ferromagnetic dimers and the first excited state can be expressed as a superposition of spin flips occurring at the left spin of a dimer (spin m_- in Figure 7.2) and spin

flips at the right spin (spin $m, +$) of the same dimer. These spin flips can be expressed by applying the spin annihilation operator S^- representing the spin deviation operator of the spin wave theory as introduced in Section 2.2.1. Diagonalizing the Hamiltonian (7.1) the dispersion relation and the intensities can be extracted with the exact calculation demonstrated in Appendix D. This diagonalization leads to two dispersion relations given by:

$$\omega_Q^- = g\mu_B B - \frac{J\alpha}{2}(1 + \cos(Q \cdot d)) \quad \text{and} \quad \omega_Q^+ = g\mu_B B - \frac{J\alpha}{2}(1 - \cos(Q \cdot d)) - J \quad (7.7)$$

with ω_Q^- presenting the lower mode and ω_Q^+ the upper mode. The intensity distribution is provided by the eigenfunctions of the diagonalized Hamiltonian leading to the following expression for the correlation function for the high field modes:

$$S^{+-}(\mathbf{Q}, \omega) = \frac{N}{2} \left| 1 - \exp(iQ \cdot \rho) \sqrt{\frac{1 + \alpha \exp(-iQ \cdot d)}{1 + \alpha \exp(iQ \cdot d)}} \right|^2 \delta(\omega - \omega_Q^+) \\ + \frac{N}{2} \left| 1 + \exp(iQ \cdot \rho) \sqrt{\frac{1 + \alpha \exp(-iQ \cdot d)}{1 + \alpha \exp(iQ \cdot d)}} \right|^2 \delta(\omega - \omega_Q^-) \quad (7.8)$$

with N the number of dimers. Using equations 7.7 and 7.8 the data can be simulated with the result illustrated in the right part of Figure 7.17 with the instrumental resolution and the isotropic Cu^{2+} form factor also included.

The existence of two modes can be explained in analog to the occurrence of the two modes for the dispersion of a 1D lattice with two ions per unit cell embodying the dimerized structure in our case. In the atomic case the dispersion splits into an optical and an acoustical mode transferable to our case with the optical mode presented by the upper mode. It can be thought of the two neighboring spins rotating in the same direction creating an energy cost for an excitation in analog to a ferromagnet and the dispersion is proportional to the characteristic $(1 - \cos(Q \cdot d))$ intensity behavior of a ferromagnet. The lower mode embodies the acoustical mode and can be visualized

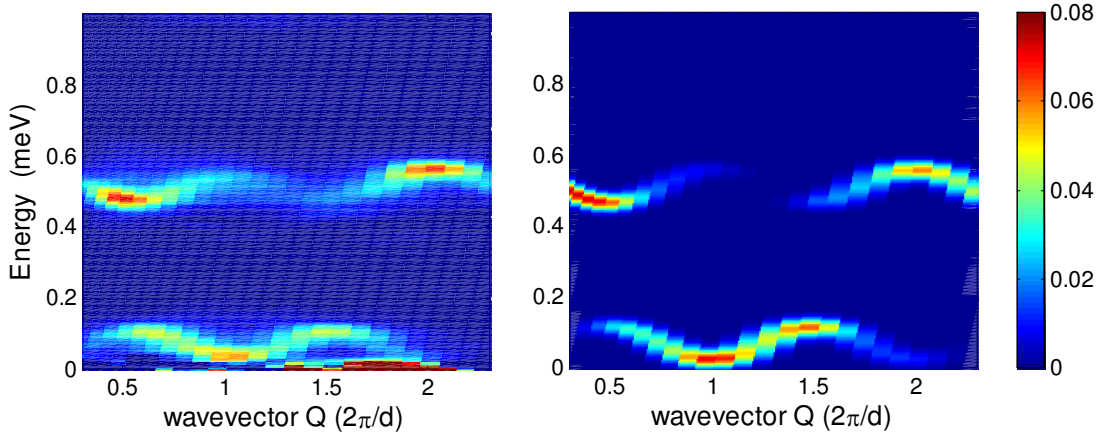


Figure 7.17: Excitation spectrum for the modes above $H_{c,2}$: (a) background subtracted data at $B = 4.26$ T just above saturation. (b) Simulation obtained from spin wave theory including the instrumental resolution.

as two spin rotating in opposite direction resembling an antiferromagnetic state with a gapless excitation proportional to $(1 + \cos(Q \cdot d))$.

Overall a very good agreement between the data and the simulation is apparent confirming the existence of a theoretical description for the excitation spectrum below the first critical field $H_{c,1}$ (shown in section 7.6) and above the second critical field $H_{c,2}$ and also the extracted coupling constants. The regime at the critical field $H_{c,1}$ is investigated in the following section.

7.7.4 Investigation of the Critical Field Regime

This section focuses on the behavior of the first critical field $H_{c,1}$ where a LL-type excitation is expected for the gapless lower band ($S^z = -1$ contribution). A theoretical prediction for the contribution of the other bands does not exist and the characteristic scattering is introduced by investigating the middle band ($S^z = 0$ contribution) due to the stronger intensity distribution. Figure 7.18 displays the lower band contribution by performing characteristic wavevector cuts at the dispersion minimum $Q = 1.0$ (upper set of cuts) and the maximum $Q = 0.5$ (lower set of cuts) for a field below $H_{c,1}$ at

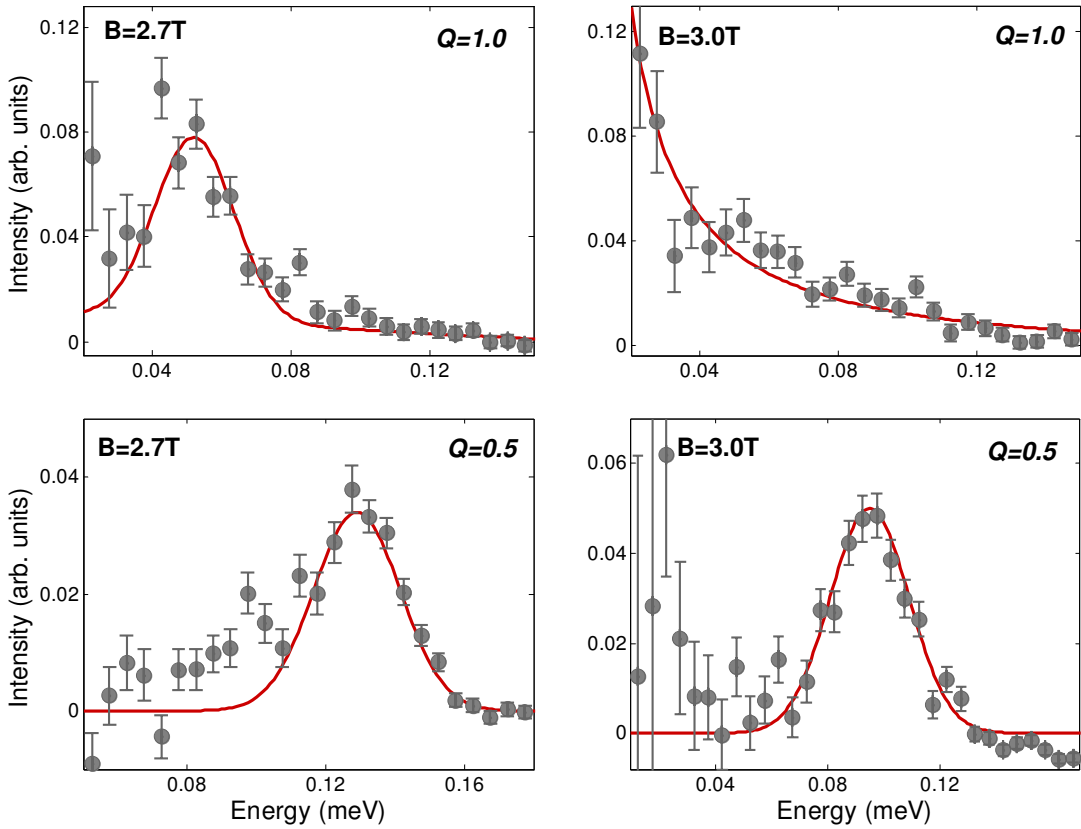


Figure 7.18: Constant wavevector cuts for the lower band presenting the expected LL type behavior. Upper set of cuts performed at $Q = 1.0$ for a field below $H_{c,1}$ ($B = 2.7$ T) and at $H_{c,1}$ ($B = 3.0$ T) displaying the continuum fall-off. Lower set of cuts at $Q = 0.5$ for $B = 2.7$ T and $B = 3.0$ T.

$B = 2.7$ T and at $H_{c,1}$ ($B = 3.0$ T). Extracting a clean measurement of this data set involves some difficulties in the background subtraction due to the appearance of the incoherent scattering centered at zero energy illustrated by larger error bars in the cuts. Below the first critical field (at $B = 2.7$ T) the excitation spectrum for the cuts is composed of a single peak presenting the magnon band as expected and described by theory introduced in the zero field section. This single peak can be fitted by a Gaussian with the width determined by the resolution and is included as the red curve. At $H_{c,1}$ the $Q = 1.0$ cut displays the characteristic continuum fall-off of a LL modeled by a power law indicated by the red curve providing the power law with an exponent of $p = 1.22 \pm 0.3$ [16]. The large error bar on the exponent results from a rather large uncertainty in the

data close to zero energy based on the difficulty in the background subtraction. The excitation cannot be explained by magnons anymore but has to be composed of fractional particles with a strongly correlated ground state. This behavior is confirmed by the $Q = 0.5$ cut at $B = 3.0$ T displaying the single peak marking the lower band of the continuum as characteristic for the LL (compare HAFC) presented by a single Gaussian fit (red curve).

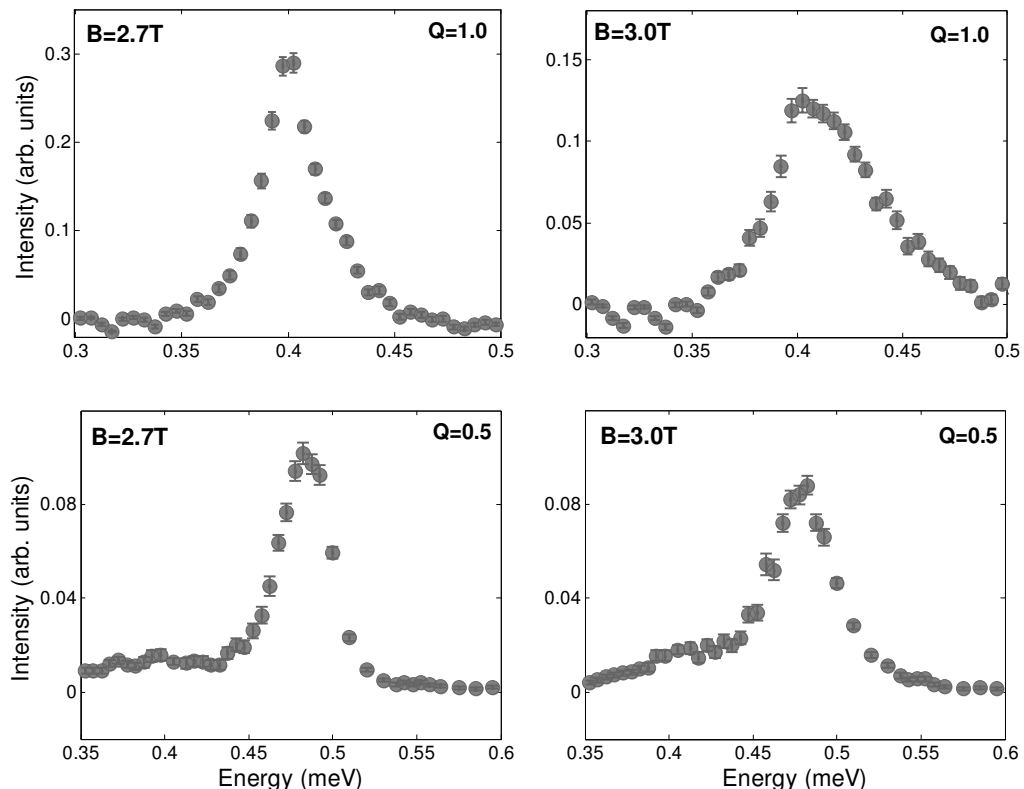


Figure 7.19: Constant wavevector cuts for the middle band at a field below $H_{c,1}$ ($B = 2.7$ T) and at $H_{c,1}$ ($B = 3.0$ T) for wavevector at the dispersion minimum at $Q = 1.0$ (upper set of cuts) and at dispersion maximum $Q = 0.5$ (lower cuts).

Figure 7.19 shows the same wavevector cuts for the middle band contribution. Just as for the lower band, a single peak is apparent for fields below the first critical field, but a clear asymmetric lineshape appears for the dispersion minimum at $H_{c,1}$ indicating the formation of a continuum which is also visible in the color plot of Figure 7.15. The cut performed at the former dispersion maximum $Q = 0.5$ shows a single peak at the

same energy as below the critical field confirming a continuum formation just as the LL based on fractional particles. For the exact lineshape of the asymmetric cut theoretical considerations are necessary and in progress [17].

7.8 Conclusion

This investigation of the excitation spectrum of the dimerized chain material Cu(NO₃)₂·2.5D₂O establishes for the first time a detailed description of the two-magnon continuum and also confirms the existence of the $S = 1$ bound mode. Additionally the one-magnon scattering and its corresponding dispersion relation determine the exact coupling constants of the system to be $J = 0.443 \pm 0.002$ meV, $\alpha = 0.227 \pm 0.005$, $J_{a_{inter}} = 0.006 \pm 0.003$ meV and $J_{c_{inter}} = 0.0018 \pm 0.005$ including a corrected dimer position. A theoretical description of both the one-and the two-magnon scattering is available providing an excellent agreement with the data. This description is also valid when applying magnetic field until reaching the first critical field presented by a condensation of the lower Zeeman split band into the ground state. The data occurring at and above the second critical field (saturation) can be modeled via spin wave theory resulting in an excellent description of the data. At the first critical field the lower band behaves according to a LL with the formation of the continuum based on the existence of fractional particles. A similar behavior is also seen for the middle band contribution with an asymmetric lineshape at the dispersion minimum confirming the existence of a continuum. For a detailed investigation of the lineshape further theoretical consideration are necessary.

References

- [1] D. A. Tennant, C. Broholm, D. H. Reich, S. E. Nagler, G. E. Granroth, T. Barnes, K. Damle, G. Xu, Y. Chen, and B. C. Sales, *Phys. Rev. B* **67**, 054414 (2003).

- [2] H.-J. Mikeska, and C. Luckmann, *Phys. Rev. B* **73**, 184426 (2006).
- [3] T. Barnes, J. Riera, and D. A. Tennant, *Phys. Rev. B* **59**, 11384 (1999).
- [4] A. Brookes-Harris, *Phys. Rev. B* **7**, 3166 (1973).
- [5] S. Sachdev, *Quantum Phase Transitions*, Cambridge University Press, Cambridge (1999).
- [6] J. Villain, *Physica B* **79**, 1 (1975).
- [7] G. Xu, *Spin Correlations and Impurities in 1-D Gapped Spin Systems*, Ph.D. thesis, The John Hopkins University (2001).
- [8] L. Gmelin, *Handbuch der Organischen Chemie*, Verlag Chemie, GMBH, Weinheim/Bergstrasse (1972).
- [9] J. Garaj, *Acta. Chem. Scand.* **22**, 1710 (1968).
- [10] B. Morosin, *Acta. Crystallogr. Sect. B: Struct. Crystallogr. Cryst. Chem.* **26**, 1203 (1970).
- [11] G. Xu, C. Broholm, D. H. Reich, and M. A. Adams, *Phys. Rev. Lett.* **84**, 4465 (2000).
- [12] J. Eckert, D. E. Cox, G. Shirane, S. A. Friedberg, and H. Kobayashi, *Phys. Rev. B* **19**, 420 (1979).
- [13] K. M. Diederix, H. W. J. Blöte, J. P. Groen, T. O. Klaassen, and N. J. Poulis, *Phys. Rev. B* **19**, 420 (1979).
- [14] J. C. Bonner, S. A. Friedberg, H. Kobayashi, D. L. Meier, and H. W. J. Blöte, *Phys. Rev. B* **27**, 248 (1983).
- [15] S. Shamoto, M. Sato, J.M. Tranquada, B. J. Sternlieb, and G. Shirane, *Phys. Rev. B* **48**, 138417 (1993).
- [16] D. A. Tennant and H.-J. Mikeska, *private communications* (2007).
- [17] F. H. L. Essler, *private communications* (2007).

Chapter 8

Temperature Effects of Copper Nitrate

8.1 Motivation

After studying the quantum fluctuations of copper nitrate in the previous chapter, an investigation of the temperature effects on the system is provided in this chapter. The quantum effects have been explored at very low temperatures by tuning the system into criticality where the magnetic field has been used to close the energy gap to the one-magnon band causing a condensation of magnons into the ground state. This changes the composition of the ground state leading to the excitations being based on fractional particles resulting in a continuum excitation spectrum. Temperature of the order of the gap energy introduces a similar process causing the one-magnon band to thermally populate. While this causes thermally excited magnons to enter the ground state, the one-magnon gap still remains unlike for the in-field measurements. This gives rise to several interesting questions regarding the composition of the ground state, the quasi-particles, i.e. magnons or fractional particles, and the statistics of the system where a comparison with the field measurements is included to provide further insight. Additionally copper nitrate embodies a system ideal for studying the interplay between quantum and thermal effects by applying both magnetic field and temperature. Due to the possibility of investigating each effect separately, the implication of the combination can be identified. So far the experimental techniques of such a study have been

missing but our data should provide a possible physical picture for one of the simplest systems to study strong correlations in depth closing the bridge to a future complete analytical treatment and a verification of the physics suggested. The data for this study is provided in the second part of this chapter and available for a comparison with theory once established.

8.2 Temperature Effects without Applied Field

8.2.1 Theory Background

The temperature effects for the alternating chain are investigated for base temperature $T = 120 \text{ mK}$, 2, 4 and 6 K. In addition to studying the effects on the one-magnon dispersion and the two-magnon continuum, the intraband scattering can also be followed. A theoretical comparison based on the numerical evaluation of the thermal averages for all eigenfunctions and eigenvalues for up to 16 spins (8 dimers) based on full exact diagonalization [1] is provided. The Lanczos method allowing the treatment of reasonably large systems (up to 36 spins), however only produces a few low-lying energy levels, so is insufficient for temperature studies due to the existence of thermally excited magnons in higher energy levels.

Whether numerical computations are sufficient to capture the data in detail is unclear, but should be able to provide a considerable guidance of the main features such as lineshapes and energy wavevector dependencies. For finite temperature the general expression for the spin correlation function is (compare with equation 3.10):

$$S^{\alpha\alpha}(\mathbf{Q}, \omega) = \sum_{\lambda} \frac{e^{-\beta E_{\lambda}}}{Z} \sum_{\lambda'} \left| \langle \Psi_{\lambda'} | S_{\mathbf{Q}}^{\alpha} | \Psi_{\lambda} \rangle \right|^2 \delta(\omega - (\omega_{\lambda'} - \omega_{\lambda})) \quad (8.1)$$

and as mentioned in the previous chapter the simplification of only the diagonal components contributing and them being equivalent, $S^{xx}(\mathbf{Q}, \omega) = S^{yy}(\mathbf{Q}, \omega) = S^{zz}(\mathbf{Q}, \omega)$, can

be used due to the isotropic Hamiltonian at *zero* field.

The limit of non-interacting dimers ($\alpha=0$) serves as a starting point where an exact calculation of the dynamical structure factor is possible. This structure factor has two contributions: one centered at $\omega = \pm J$ presenting the one-magnon excitation with the only Q dependence being the dimer structure factor ($1 + \cos(Q \cdot d)$) and a contribution centered at $\omega = 0$ arising from the transition within the excited dimer triplet -the intra-band scattering. Including a finite coupling, α , effects the contributions at $\omega = \pm J$ and $\omega = 0$ by adding a finite width resulting in a dispersion relation and enabling multi-magnon excitations through vacuum fluctuations centered at $\omega \sim nJ$ (n being an integer) [1]. The structure factor is still dominated by the dimer structure factor, but higher order contributions in α exist contributing $\sim 2\%$ for the two-magnon as introduced in Section 7.6.3.

8.2.2 One-Magnon

The effect of applying temperature to the one-magnon dispersion is illustrated in Figure 8.1 with temperatures ranging from $T = 0.12$ K to $T = 6$ K. The intensity scale is constant throughout the color plots allowing a direct intensity comparison among the different temperatures. A drastic intensity decrease from base temperature to the $T = 6$ K data is apparent along with an increase of the one-magnon band width. The base temperature is an order of magnitude smaller than the gap energy previously determined at $\Delta = 0.388$ meV in Section 7.6.2 ensuring the quantum ground state to be free of thermally excited magnons [2]. The temperature of $T = 2$ K is still smaller than the one-magnon gap but enhances the occurrence of thermally excited magnons illustrated in the color plot by an increase in the width of the one-magnon band. This increase is drastically aggravated for the $T = 4$ K data, a temperature of the order of the gap energy, resulting in the mixture of thermally excited magnons into the ground state. The

outcome is illustrated in the color plot by a possible continuum-type formation at this temperature. This is further confirmed by the $T = 6$ K data as seen in the last color plot where the extent and form of the continuum is apparent.

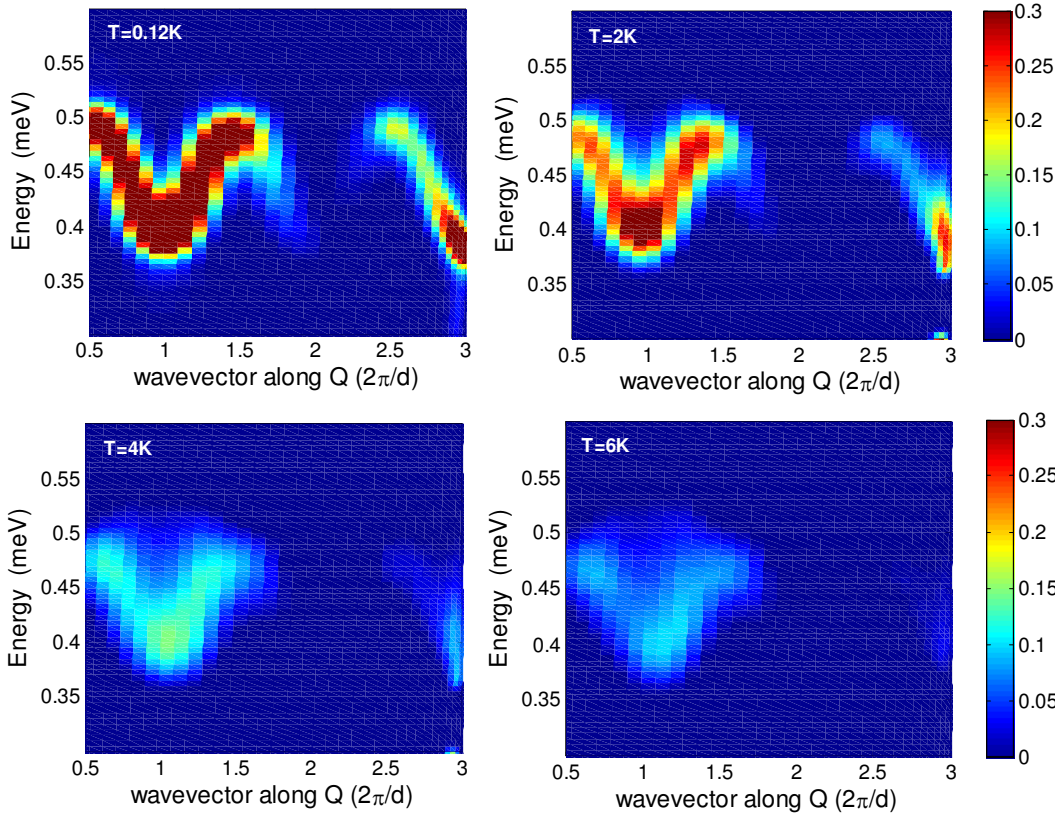


Figure 8.1: Color plot of the one-magnon signal with the non-magnetic signal subtracted displaying the temperature evolution. The intensity scale is kept constant throughout the color plots.

For a more detailed insight into the development of the one-magnon dispersion under applied temperature, constant wavevector cuts at characteristic locations, the energy maximum of the one-magnon band at $Q = 0.5$ and the energy minimum at $Q = 1.0$, are performed. These wavevector cuts are shown in Figure 8.2 and are directly compared to the results provided by the numerical calculation of the diagonalization of the 16 spins included as the red solid curves in the figure. The intensity scaling factor for the calculation is used consistently through the cuts allowing a direct comparison be-

tween the data and the calculation among the various temperatures and the two different wavevectors. Overall the figure illustrates a good agreement between the data and the calculation, as the calculation captures the main features of the data such as intensity and width distribution additionally to peak positions.

The left panel of Figure 8.2 displays the temperature effect for a constant wavevector cut of $Q = 0.5$ while the right panel focuses on the wavevector cuts at $Q = 1.0$. The intensity range is varied throughout the plots allowing an illustration of all the main features including the intensity decrease for increasing temperatures. The majority of the intensity gets redistributed to the intraband scattering with the remaining intensity decrease being based on an redistribution within the band causing the width increase of the magnon band as seen in the figure and also in the color plots of Figure 8.1. While for the cuts at $Q = 0.5$ the intensity moves to lower energies (tail to the left side of the energy peak position), a pronounced shift to higher energies (tail to the right side) is seen for the $Q = 1.0$ cuts in the form of an asymmetrical lineshape for both wavevectors. The reason for this continuum-type excitation spectrum is not well understood, but is a characteristic of a strongly correlated system [3]. So far the temperature effects for thermally excited gapped magnon systems have been assumed to consist of lifetime broadening modeled by a Lorentzian lineshape (e.g. [4, 5]) and this was also claimed to be true in copper nitrate by Xu *et al* [6], but cannot be confirmed by our results. A possible explanation for the formation of the continuum-type scattering could result from a process similar to the two-magnon continuum based on a magnon-type scattering. The two-magnon continuum is based on a neutron scattering off two excited neighboring dimers forming a total $S = 0$ state. When considering the situation of applying temperature of the order of the gap energy, a neutron can then scatter off a dimer neighboring a thermally excited dimer leading to an interference process in analog to the two-magnon scattering and illustrated in the formation of the continuum. Although

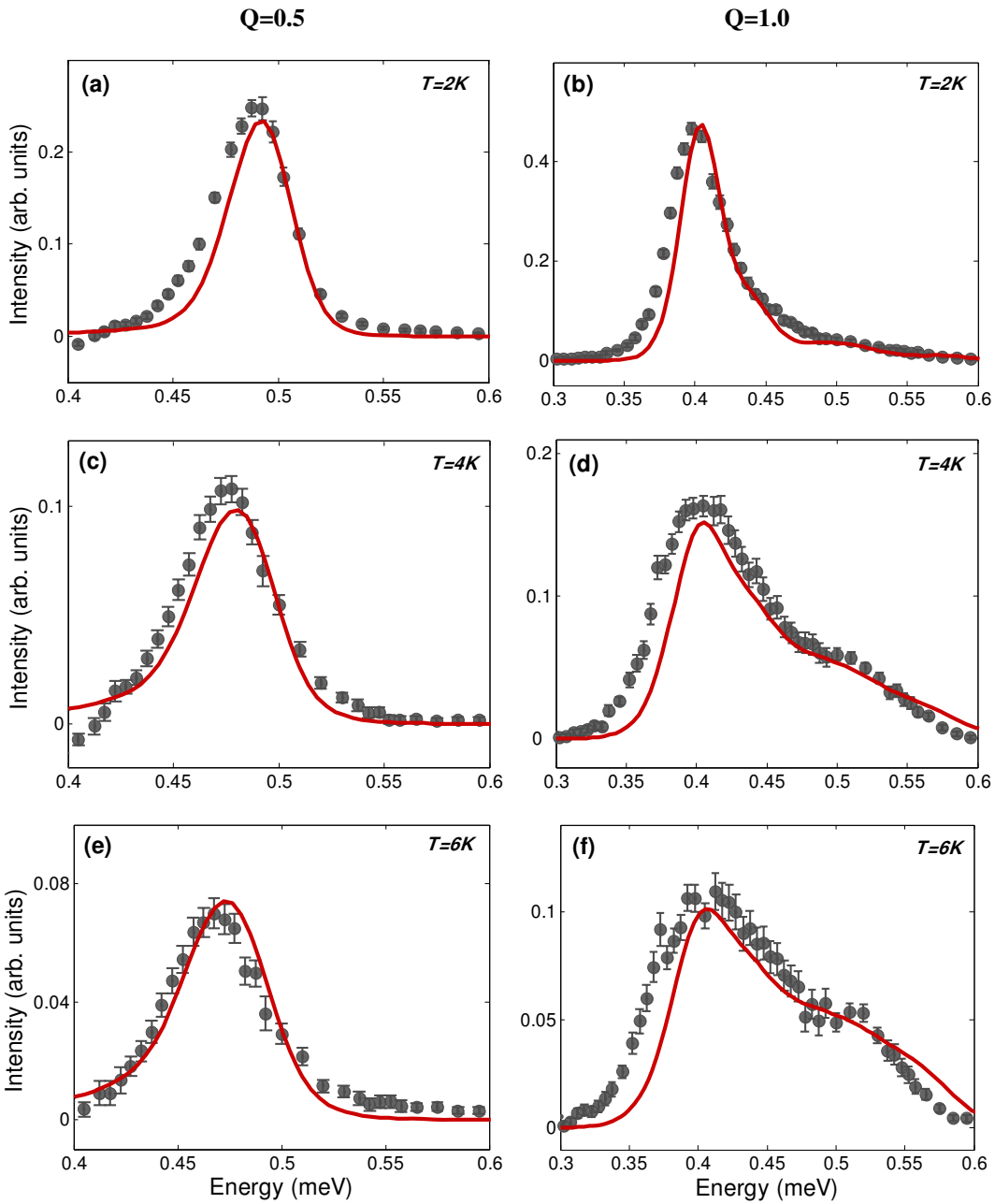


Figure 8.2: Constant wavevector cuts for different temperatures. In the left panel the cuts are performed around the dispersion maximum $Q = 0.5$ and the the right panel at the minimum of $Q = 1$. Part (a) and (b) display the $T = 2\text{ K}$ data, part (c) and (d) the $T = 4\text{ K}$ data, and part (e) and (f) the $T = 6\text{ K}$ data. The red solid lines present the calculated curves based on numerical evaluations of thermal averages for a chain of 16 spins.

the existence of the continuum can be found for both contributions of either thermally exciting magnons or condensed magnons into the ground state, there is assumed to be a

vital difference between the two processes. Applying temperature to the system ensures the existence of the one-magnon gap keeping the distinguishability of the magnons, in contrast to the field measurements with the gap closure causing a change in statistics to a LL type behavior with the existence of fractional particles. However this issue has not been fully addressed yet and the form of the scattering particles, as either magnons or fractional particles, has not been established. A direct comparison with the line shapes of the field measurements should help to provide further insight into this question.

The comparison between the continuum formation under applied field and for temperature is displayed in Figure 8.3. This figure displays the excitation of a gapped magnon from the ground state with a magnon population for applied temperature (upper set of cuts) and magnetic field (lower set of cuts). The chosen temperature is $T = 6\text{ K}$, well above the one-magnon gap, and the magnetic field is $B = 3\text{ T}$ and $T = 0.12\text{ K}$ for the $S^z = 0$ contribution to ensure the gapped phase. For the comparison constant wavevector cuts are performed at $Q = 0.5$ at the node of the continuum (former maximum of the one-magnon dispersion relation) and at $Q = 1.0$ at the maximum of the continuum (former minimum of the one-magnon dispersion). While both sets of cuts capture the asymmetrical lineshape at the one-magnon dispersion minimum $Q = 1.0$, the cuts at $Q = 0.5$ display different behavior. The temperature cuts at $Q = 0.5$ show the asymmetrical lineshape with the intensity allocated to lower energies, absent in the applied field case. Additionally apparent is a shift of the peak position to lower energies for the temperature cuts at $Q = 0.5$ (also compare with Figure 8.2) indicating the characteristic scattering for a formation of a magnon system as also seen in Section 7.6.5 for the two-magnon continuum.

These differences lead to the suggestion that the formation of the continuum is based on different scattering processes. While the formation of the temperature continuum seems to be based on the existence of magnons, the continuum associated with field

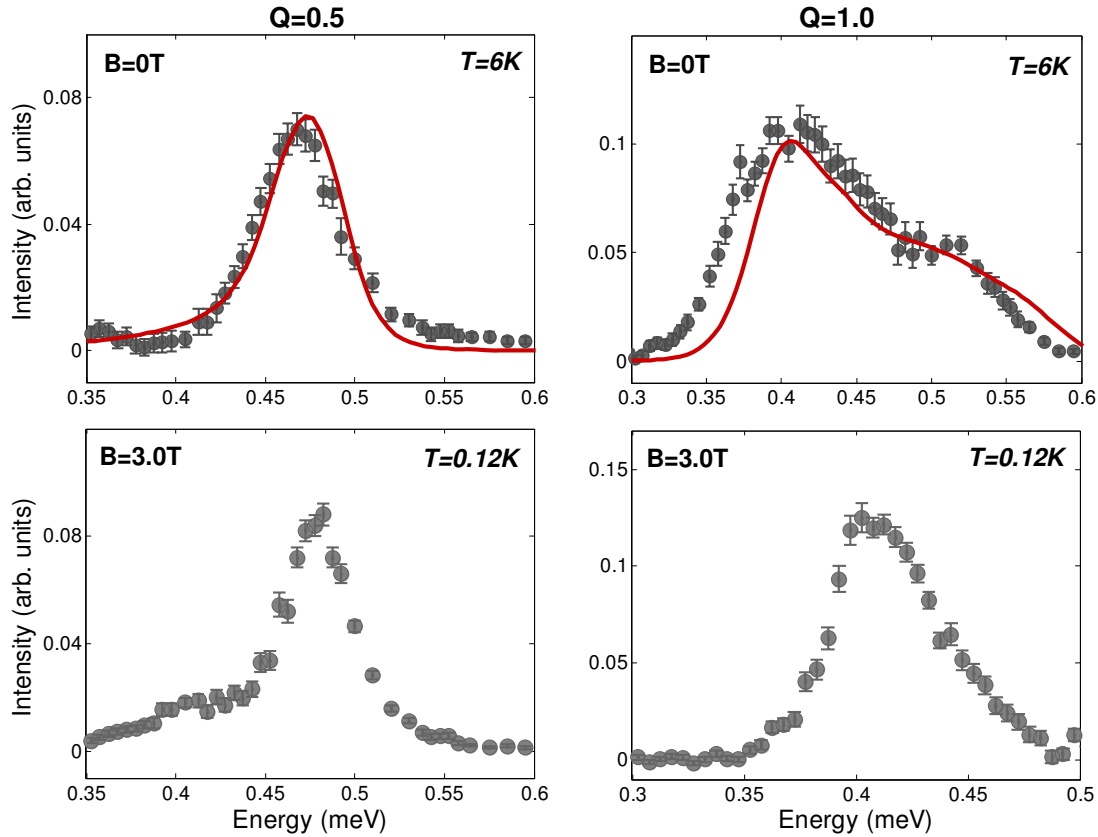


Figure 8.3: Constant wavevector cuts: Upper panel: for a temperature of $T = 6\text{ K}$, well above the one-magnon gap. Lower panel: for a critical field of $B = 3\text{ T}$ and $T = 0.12\text{ K}$ for the $S^z = 0$ contribution representing the gapped populated one-magnon continuum. Left set of cuts performed for $Q = 0.5$ and right set of cuts for $Q = 1.0$.

occurs because of the decomposition of fractional particles. A theoretical description is being prepared [3] confirming the results and should provide a more complete physical picture of the effects of temperature on strongly correlated systems.

8.2.3 Two-Magnon

The evolution of the two-magnon scattering up to a temperature of $T = 4\text{ K}$ is presented in the color plots of Figure 8.4 providing an overview of the changes in the two-magnon scattering when applying temperature. The intensity scale is varied throughout the color plots ensuring a detailed presentation of the features. Part (a) presents the two-magnon continuum at base temperature discussed in depth in the previous chapter; part (b)

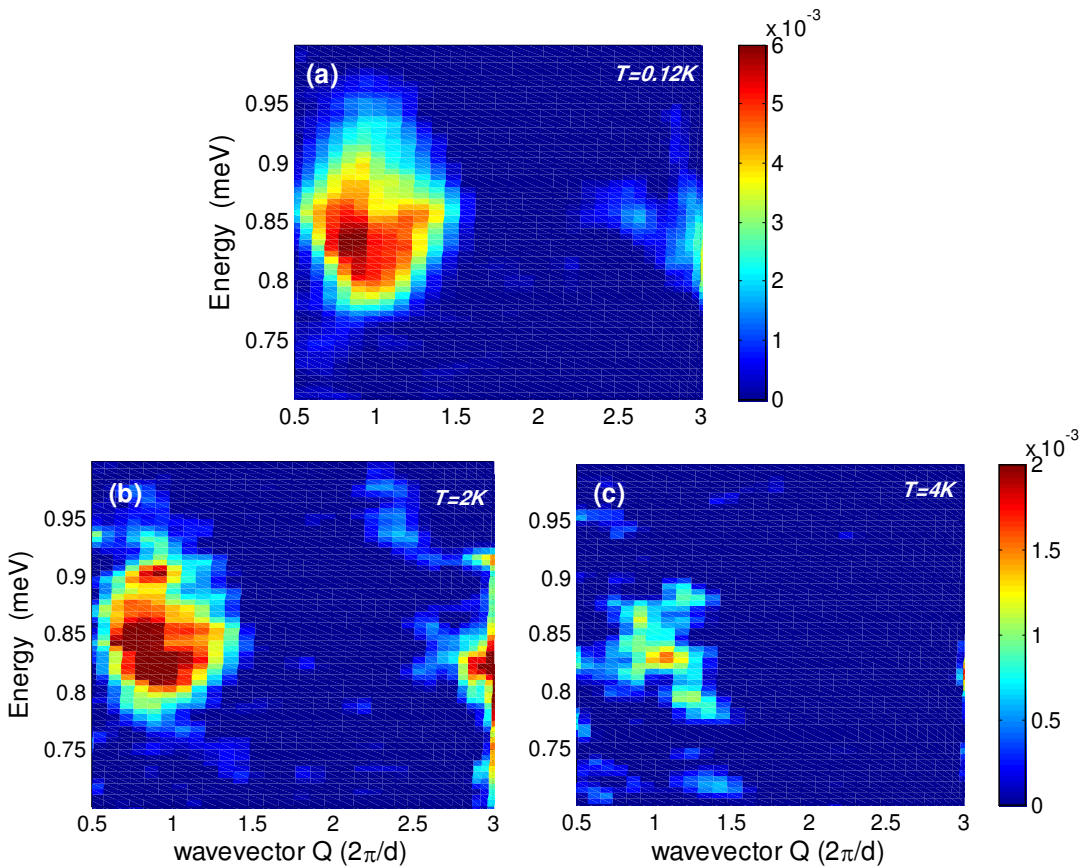


Figure 8.4: Color plot of the two-magnon scattering with the non-magnetic signal subtracted off for different temperatures. (a) Base temperature of $T = 0.12\text{ K}$. (b) $T = 2\text{ K}$ and (c) $T = 4\text{ K}$.

shows the two-magnon scattering at $T = 2\text{ K}$, a temperature below the occurrence of thermally excited magnons mixed into the ground state. And the excitation spectrum with this new ground state composition is illustrated in part (c) at $T = 4\text{ K}$. The scattering for the $T = 2\text{ K}$ shares the same characteristics as the base temperature seen in the formation of a continuum with the maximum weight located at $Q = 1.0$, a similar intensity distribution although an intensity decrease of $\sim 50\%$ is apparent (compare color bar!) and a similar outline of the continuum. The $T = 4\text{ K}$ data displays significant decrease in intensity with the continuum no longer well defined. This is even more apparent in the $T = 6\text{ K}$ data which is too weak to be displayed.

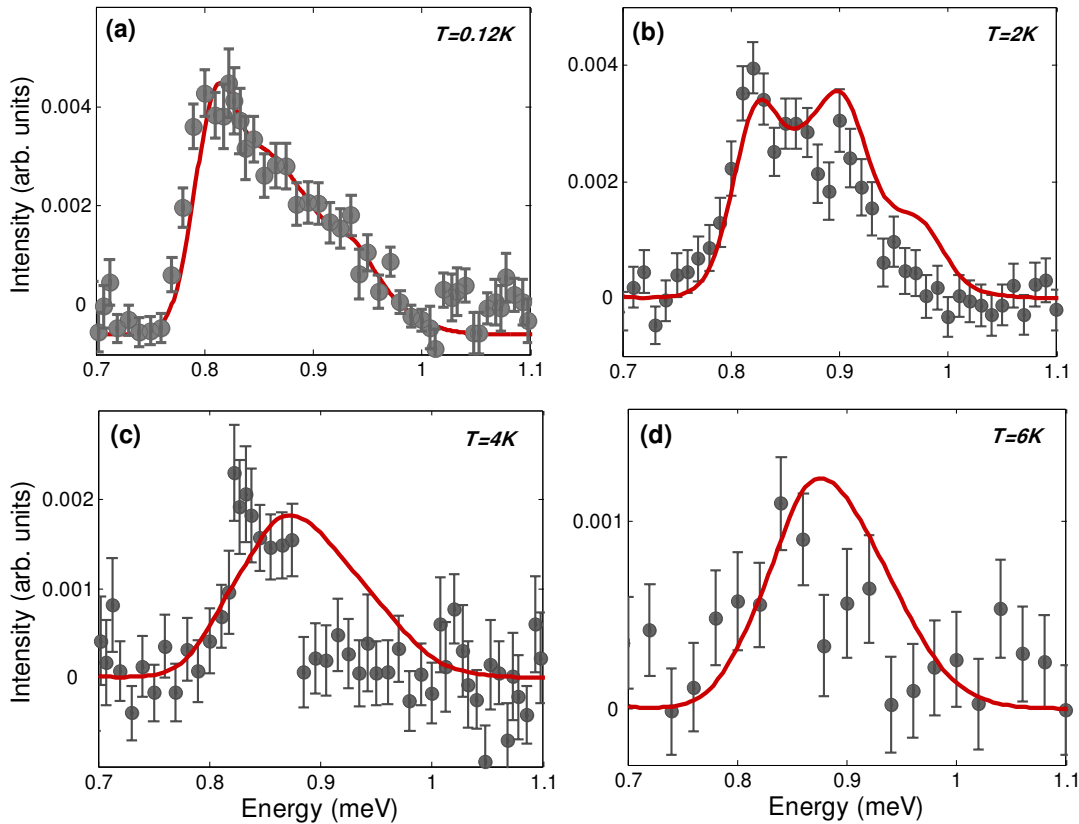


Figure 8.5: Constant wavevector cuts for the two-magnon signal around the maximum width of the continuum for different temperatures: (a) for base temperature of $T = 0.12\text{ K}$, (b) for $T = 2\text{ K}$, (c) for $T = 4\text{ K}$ and (d) for $T = 6\text{ K}$.

Consistent with the one-magnon data a distinct difference for the scattering above a temperature featuring the population of thermally excited magnons into the ground state can be found. For a more in depth analysis constant wavevector cuts analogous to the one-magnon analysis are performed and compared for the different temperatures. Figure 8.5 displays these wavevector cuts around the continuum maximum at $Q = 1.0$ ranging from the base temperature of $T = 0.12\text{ K}$ (part (a)) to the maximum temperature of $T = 6\text{ K}$ in part (d). Unfortunately the very interesting aspect of the evolution of the bound mode presented by cuts at $Q = 1.5$ for the various temperatures cannot be followed due to the extremely weak intensity distribution. The red solid curve in the temperature cuts, parts (b)-(d), presents the numerical calculation based on the exact

diagonalization of 16 spins. Part (a) shows the typical cut for the two-magnon continuum at base temperature with the asymmetrical lineshape and the red solid curve presenting the same cut performed for the calculation based on the 1D perturbation approach as discussed in the previous chapter. The maximum intensity can be found at the lower boundary of the two-magnon continuum presenting the weighted center-of scattering at $E = 0.813$ meV determined by constant wavevector cuts across the two-magnon continuum. In part (b) the same cut performed at a temperature of $T = 2$ K is displayed and although appearing similar, distinctive differences are apparent. The maximum intensity of the data is found at the same wavevector as for the base temperature and the asymmetrical lineshape is also apparent, but a second peak at higher energy of $E \sim 0.9$ meV emerges. The origin of the second peak is not understood, but could be an indication of a change in ground state due to the existence of thermally excited magnons. The red solid curve captures the two peaks well; however a small discrepancy in the intensity and width distribution is obvious. More difficult to analyze are the higher temperature runs due to the little intensity and the difference between the calculated curve and the data. While the data suggests the survival of the two peak structure even for higher temperatures, the calculation predicts the formation of only one peak with a center at the higher energy of the second peak position. For the higher temperature of $T = 6$ K the width of the predicted peak decreases and in both cases the asymmetrical lineshape seems to vanish confirming the assumption of a change in the composition of the continuum after reaching a temperature corresponding to the one-magnon gap energy. For a more quantitative analysis higher statistics for the high temperature data is necessary.

It is interesting to note that the two-magnon intensity remains finite when applying temperature and does not vanish. The two-magnon ($2J$) transition occurs from a pair in the ground state ($|GG\rangle$) via its vacuum fluctuations (proportional to $\alpha \{ |00\rangle + |1\bar{1}\rangle + |\bar{1}1\rangle \}$).

The occupation probability of this lowest energy pair state is:

$$n_{2mag} = \frac{1}{1 + 6e^{-J/kT} + 9e^{-2J/kT}} \quad (8.2)$$

The scattering matrix element to $2J$ states remains valid at all temperatures and is of order $\alpha^2/4$ [7], and so $I(T) \sim n_{2mag}I(T = 0)$ leading to an intensity decrease of the zero temperature two-magnon intensity to a factor of 1/16 for infinite temperatures, but remaining at a finite value.

8.2.4 Intraband Scattering

One very interesting feature when applying temperature to the system is the intraband scattering occurring due to thermally excited magnons populating the one-magnon band. An incoming neutron can scatter off these magnons and move them along the one-magnon band resulting in a continuum centered around zero energy (see Figure 7.3 and first plot of Figure 8.6) and comparable to the Villain mode in soliton system [8], but measured for the first time in a gapped magnon system.

Constant wavevector cuts around the maximum width of the continuum at $Q = 0.5$ are provided in Figure 8.6 for the various temperatures to study the interplay of the thermally excited magnons within the one-magnon band with the red solid curve presenting the results of the exact diagonalization method. The data in Figure 8.6 displays the expected intensity increase with higher temperatures seen in the intensity scale change throughout the cuts to illustrate the exact features and lineshape of the cuts. The increase in intensity results from a higher population of thermally excited magnons in the one-magnon band leading to a higher probability of intraband scattering.

The difficulty in detecting this intraband scattering is due to the incoherent background centered at zero energy and subtracted by using the low temperature data

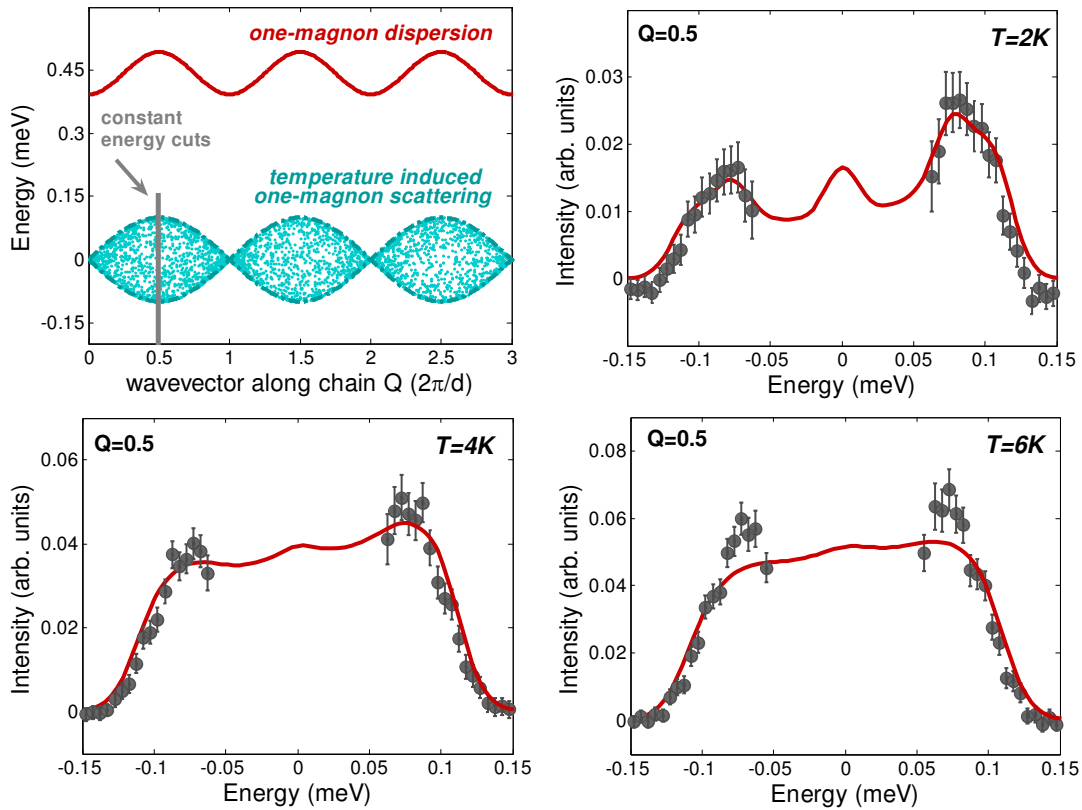


Figure 8.6: Constant wavevector cuts for the maximum width of the continuum at $Q=0.5$ for the temperature induced one-magnon intraband scattering for temperatures of: $T=2$ K, $T=4$ K, and $T=6$ K. The negative data is obtained by using the detailed balance theorem.

($T = 120$ mK) composed of no thermally excited magnons. This background subtraction explains the lack of data below $E = 0.04$ meV, but a clear difference in the intensity distribution as compared to the asymmetrical lineshape of the two-magnon continuum is apparent. The width of the intraband scattering is expected to match the width of the one-magnon band confirmed by the intensity drop-off at $E \sim 0.12$ meV consistent throughout the cuts and providing a proof for the fitted alternation parameter α . The negative data points are obtained by using the detailed balance relationship.

A very good agreement between the data and the calculation is found with the calculation validating the width and the lineshape of the intraband scattering. Note that the intensity of the calculation has to be increased by a factor of 2 for this agreement

consolidated in the geometry of copper nitrate [10]. Very interesting is the $T = 2\text{ K}$ data displaying the expected singularity at the outline of the continuum ($Q \sim \pm 0.1$) in excellent agreement with the calculation (red curve). This singularity presents the scattering from the one-magnon dispersion minimum to the maximum with a singularity forming due to the narrow band width. The existence of the singularity is a signature of fairly well-defined magnons surviving during the scattering process. This effect was just recently detected in the spin-1/2 Heisenberg-Ising (XXZ) chain material CsBoBr_3 [9], but our results show the first realization in a dimerized spin-1/2 Heisenberg chain.

8.3 Outlook: Field Dependence

This section provides an outlook for a detailed investigation of the interplay between magnetic field and temperature effects by supplying the data for an ideal system presented by copper nitrate. Due to the fact that theory is not available yet, only a quantitative description of the data can be established. Once theory input is present the interesting and important questions of the consistency of the ground state and the nature of the excitations can be answered.

An overview for the interplay between field and temperature is displayed in Figure 8.7 for a range of fields from $B = 2.7\text{ T}$ to $B = 4.4\text{ T}$ including the two critical fields $H_{c,1}$ and $H_{c,2}$. The applied temperature chosen is $T = 4\text{ K}$ being of the order of the one-magnon gap and most representative for the thermal effects. The difficulty in obtaining the data consists of the manifold background due to the different contributions composed of band splitting and energy gap closure due to the magnetic field application and the interference with the intraband scattering from applying temperature in addition to the existence of the incoherent scattering. The best background subtraction consists of the zero field for each temperature (in this case $T = 4\text{ K}$) correcting for the

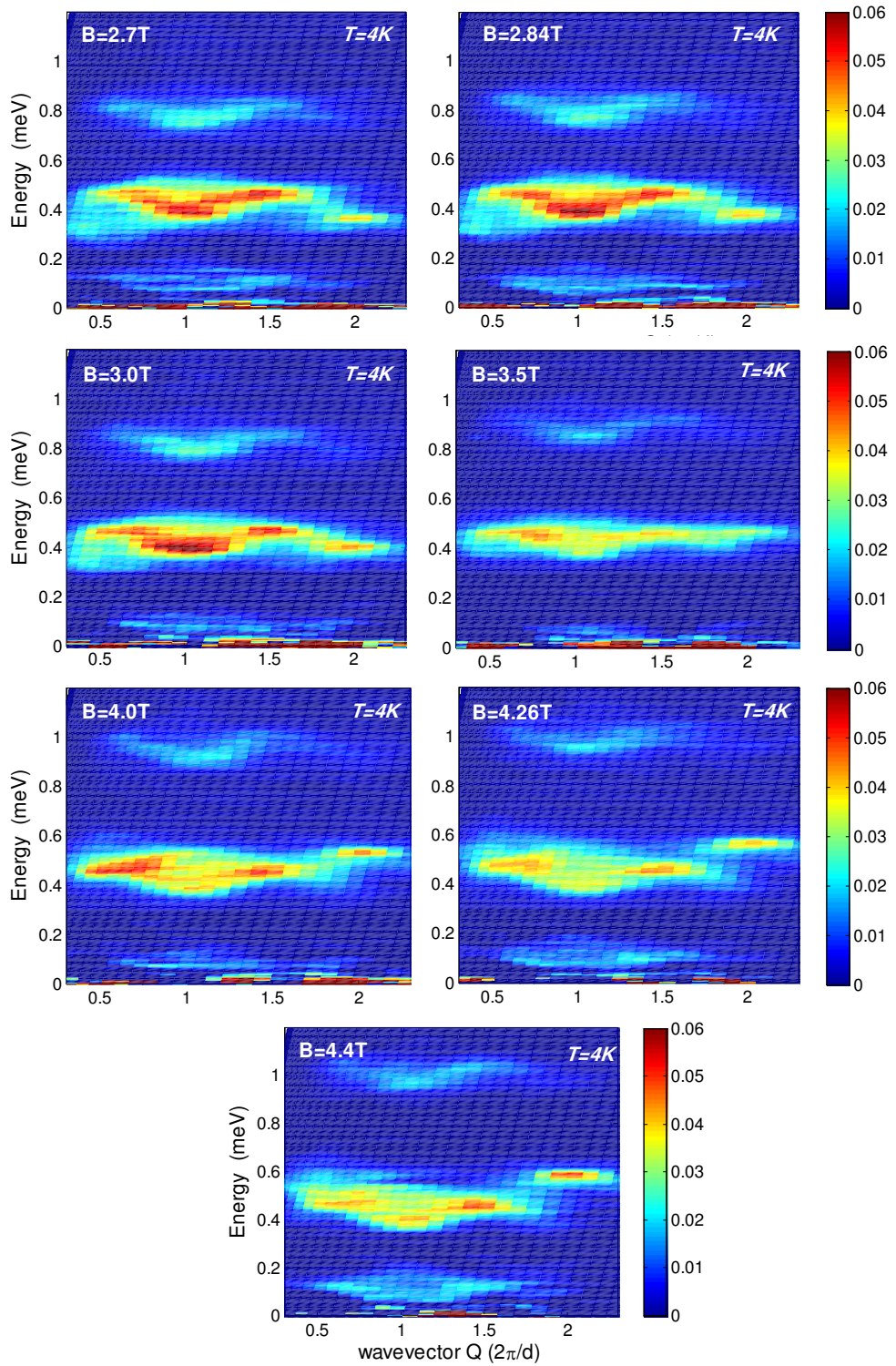


Figure 8.7: Color plot displaying the effect of applying various magnetic fields enclosing the two critical fields for a temperature allowing the thermal population of the one-magnon band.

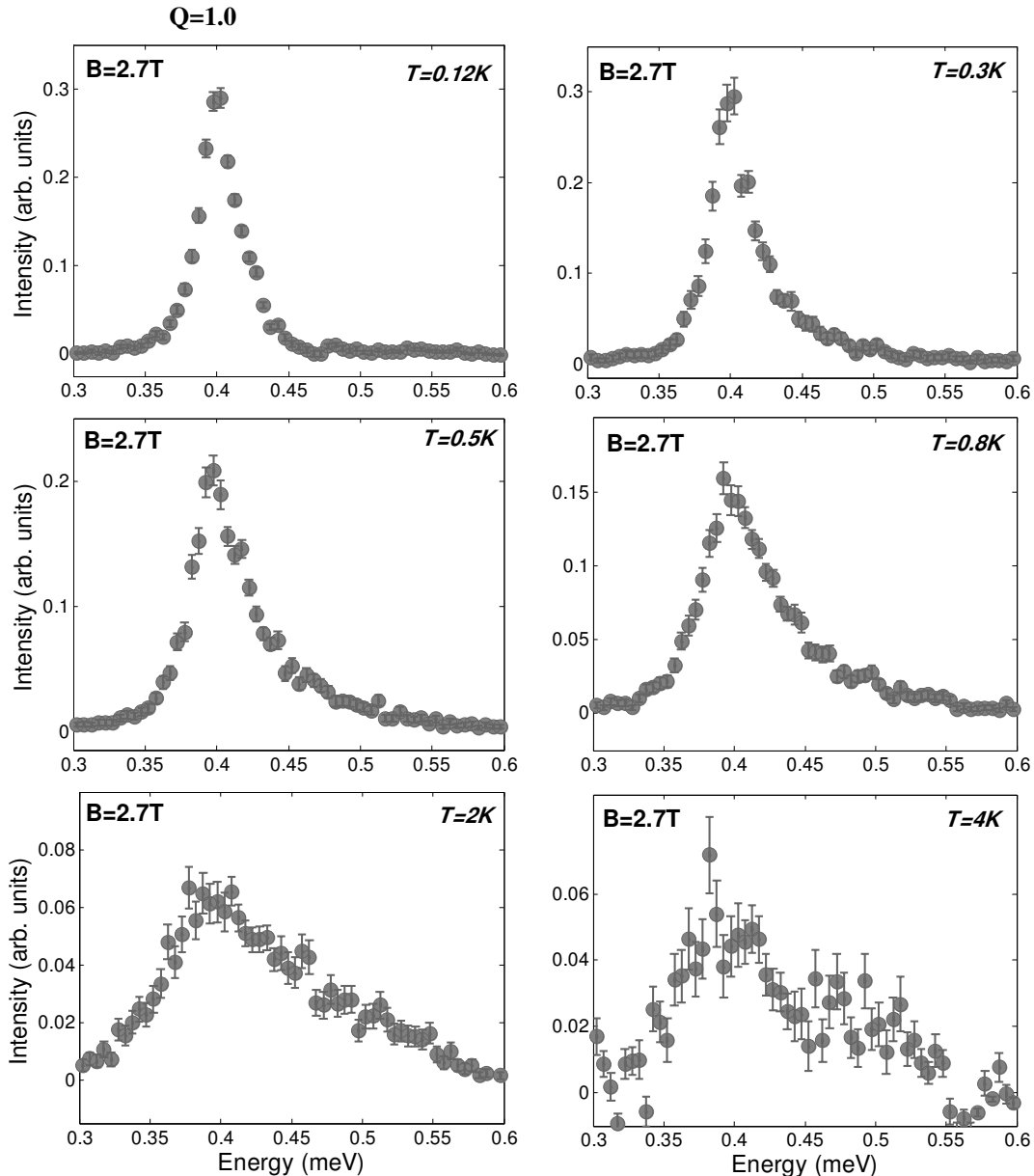


Figure 8.8: Constant wavevector cuts for a field of $B = 2.7 \text{ T}$ for various temperatures up to $T = 4 \text{ K}$ performed at $Q = 1.0$ for the $S^z = 0$ contribution (middle band).

incoherent hydrogen scattering as well as the incoherent and intraband scattering centered at zero energy with the results of the background subtraction and the one-magnon signal shown in Figure 8.7.

Comparing this figure with Figure 7.15 of the previous chapter presenting the equivalent zero temperature data reveals several differences. A strong width increase in the

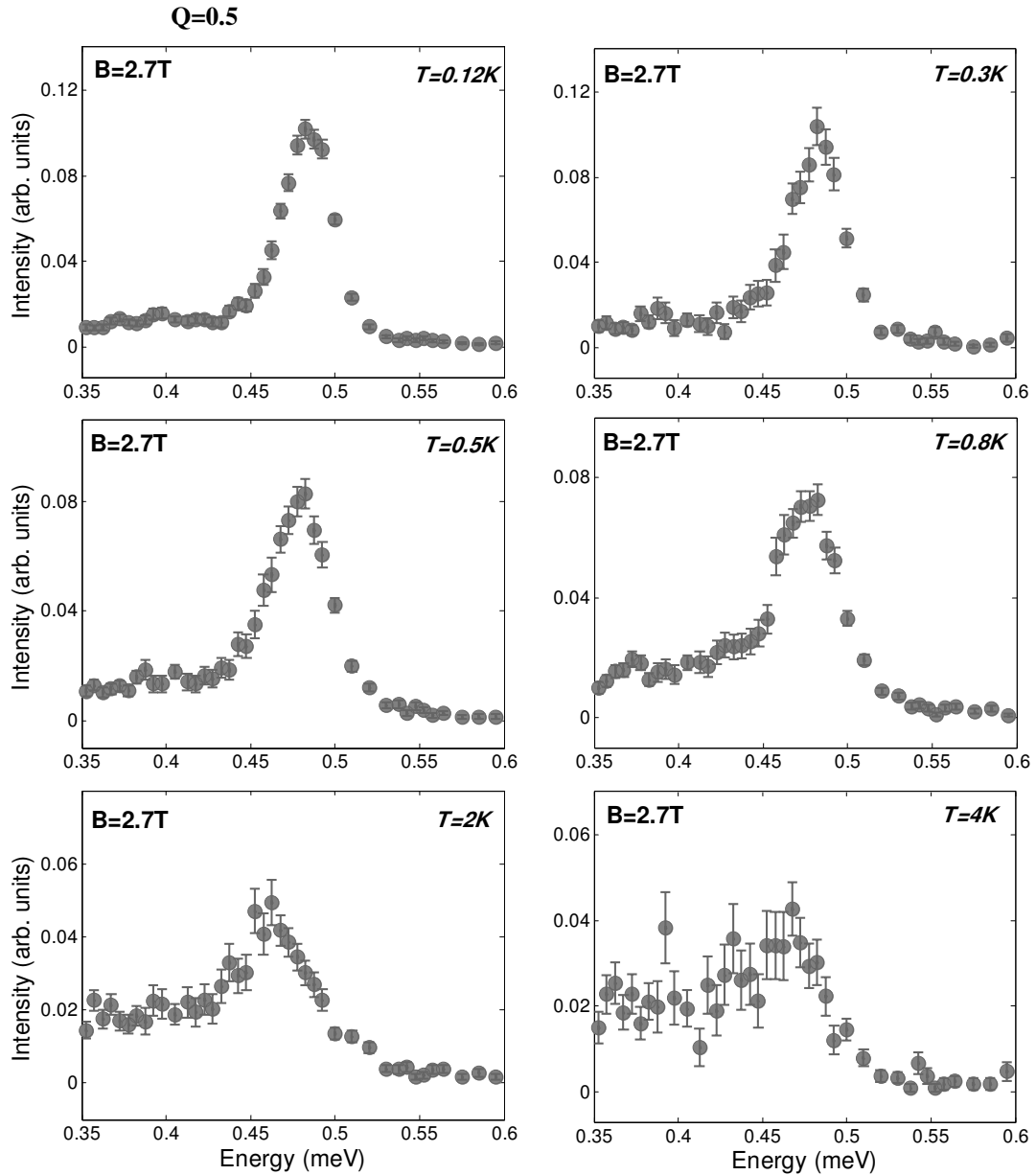


Figure 8.9: Constant wavevector cuts for a field of $B = 2.7\text{ T}$ for various temperatures up to $T = 4\text{ K}$ performed at $Q = 0.5$ for the $S^z = 0$ contribution (middle band).

one-magnon band is apparent illustrating the formation of the temperature-induced continuum scattering which still exists above the second critical field $H_{c,2}$ along with the appearance of the higher field mode (optical mode) as described in Section 7.7.3. The most pronounced difference, however, is the existence of the upper band ($S^z = 1$ contribution) above the second critical field due to the occurrence of thermally excited

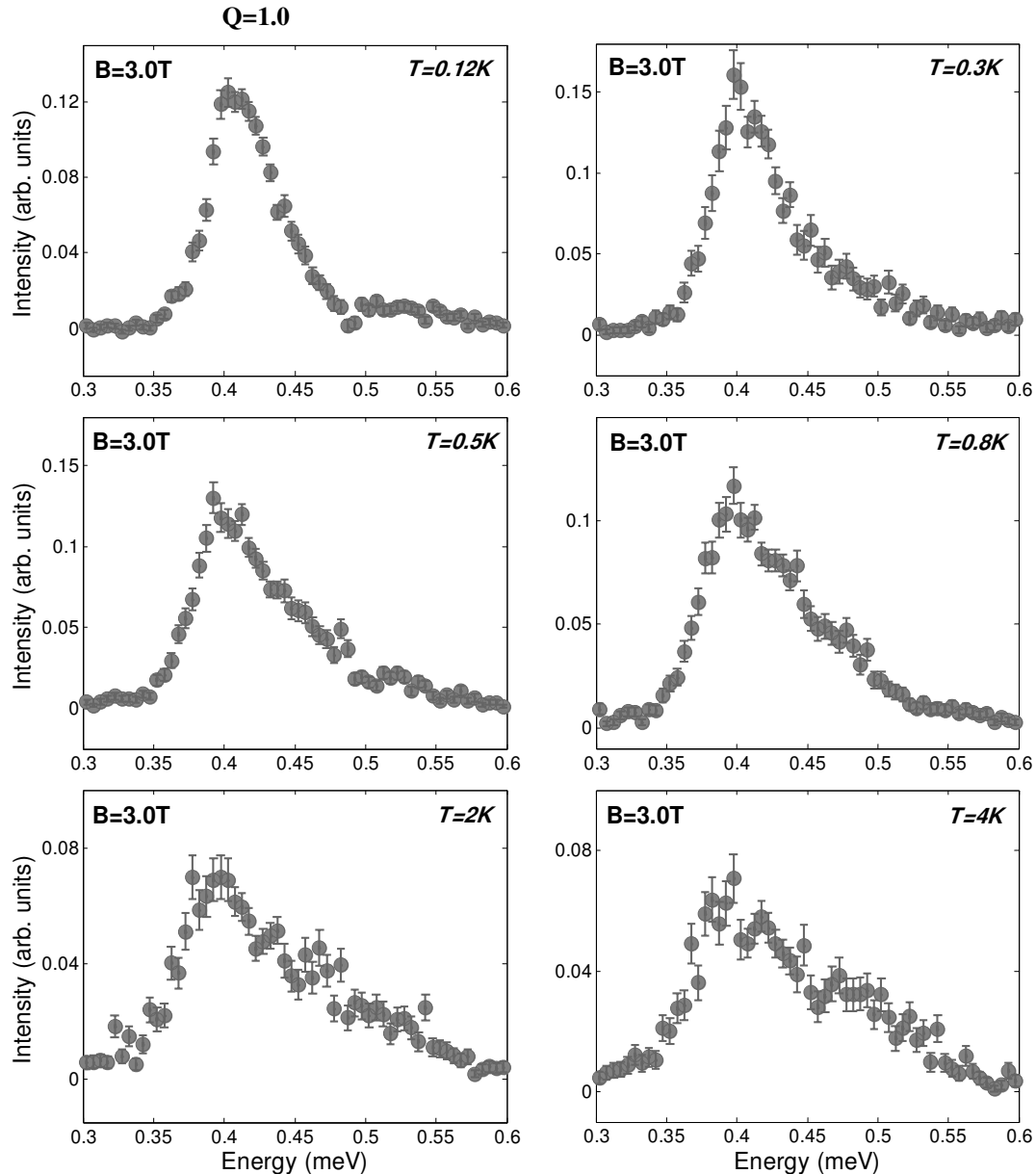


Figure 8.10: Constant wavevector cuts for a field of $B = 3.0\text{ T}$ for various temperatures up to $T = 4\text{ K}$ performed at $Q = 1.0$ for the $S^z = 0$ contribution (middle band).

magnons in the middle band ($S^z = 0$ contribution) allowing the access of the upper band previously prohibited by the neutron scattering selection rule $\Delta S = 1$.

A more detailed study of the interplay is provided by performing constant wavevector cuts at $Q = 0.5$ and $Q = 1.0$ for fields of $B = 2.7\text{ T}$ and $B = 3.0\text{ T}$ for the $S^z = 0$ contribution (middle band) directly comparable to the pure magnetic field effects (Figure 7.19

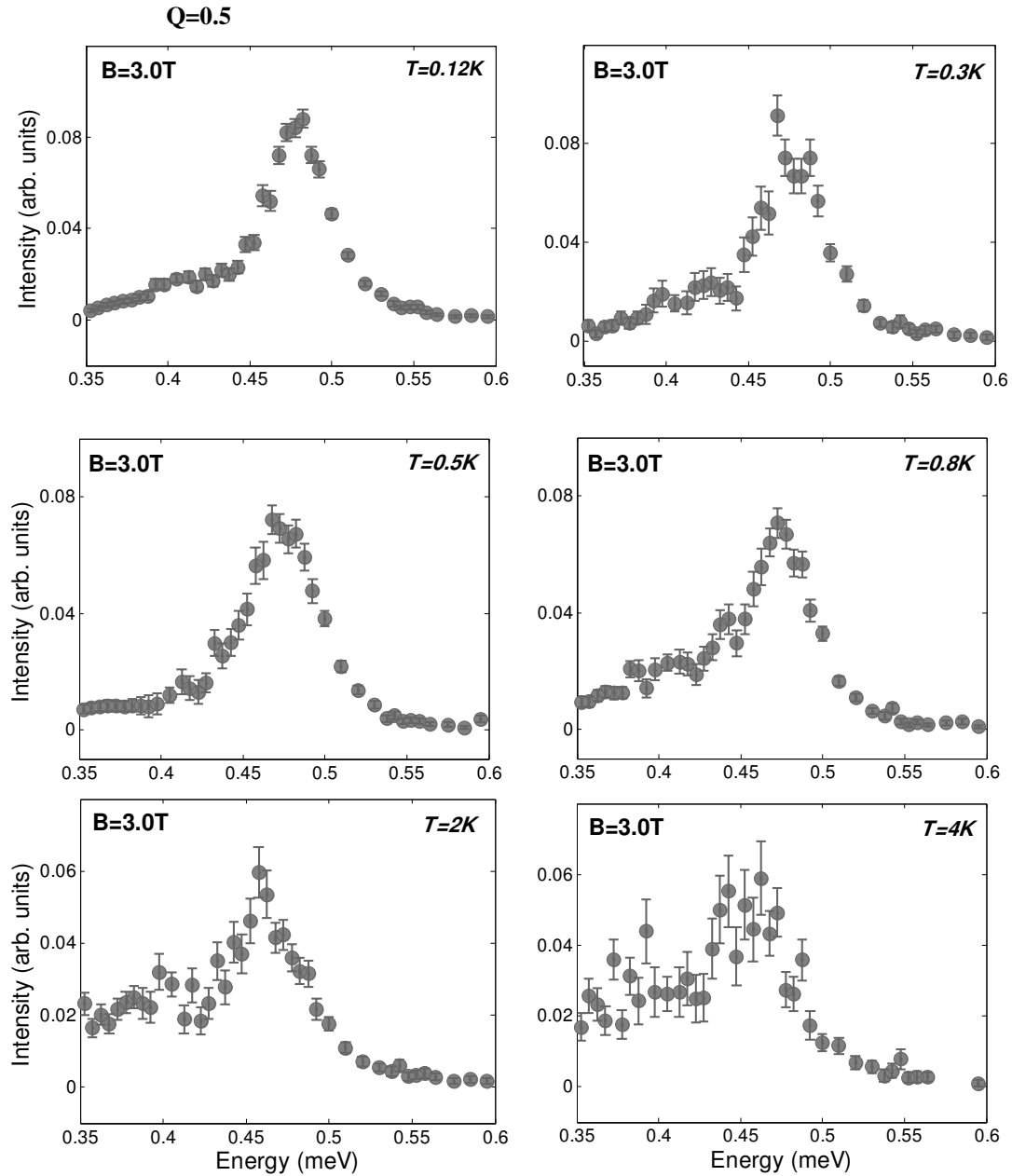


Figure 8.11: Constant wavevector cuts for a field of $B = 3.0\text{ T}$ for various temperatures up to $T = 4\text{ K}$ performed at $Q = 0.5$ for the $S^z = 0$ contribution (middle band).

from the previous chapter) and the pure temperature effects as shown in Figure 8.2. Figure 8.8 displays the constant wavevector cut at $Q = 1.0$ with the lineshape at low temperature as expected from the analysis of the previous chapter (Section 7.7.3 and compare Figure 7.19) and including the asymmetric lineshape for higher energies as

expected for the application of temperature. The characteristic features of the temperature effects are also apparent in the cuts at $Q=0.5$ displayed in Figure 8.9 illustrating the asymmetric tail to lower energies -the clear indication of temperature. A confirmation of the existence of fractional particles can be seen in Figure 8.10 presenting the cuts at $Q=1.0$ with the asymmetric lineshape at low temperature and a stronger broadening through all temperatures obvious when comparing Figures 8.8 and 8.10, while the cuts at $Q=0.5$ again present the asymmetrical lineshape to lower energies as shown in Figure 8.11 indicating the existence of thermal magnons.

Summarizing the observations reveal lineshapes characteristic for both features of applying temperature and magnetic field raising the question of the composition of the ground state and even stronger the nature of the excitations. For a convincing answer theoretical input is crucial and necessary.

8.4 Conclusion

In this chapter the temperature effects on the dimerized chain material copper nitrate are investigated for the one-magnon, the two-magnon and for the first time the intra-band scattering occurring due to thermally excited magnons being moved along the one-magnon dispersion during the neutron scattering process. Applying temperature to the one-magnon dispersion reveals a formation of a continuum. A direct comparison to the continuum appearance for applied magnetic field indicates a different scattering process due to a different behavior in the wavevector cut at the ‘former’ dispersion maximum with an asymmetric tail to lower energies forming for the temperature contribution in contradiction to a simple broadening effect for the field case. This leads to the assumption of the magnons surviving when applying temperature in confirmation with the different statistics of the system due to the remaining of the one-magnon

energy gap apparent in the temperature case. Very importantly the asymmetric line-shape provides an indication of strong correlation in the temperature case which cannot be modeled by a simple damping phenomenon based on a Lorentzian broadening and further theoretical investigations are in progress.

The data for the intraband scattering reveals the expected continuum centered at zero energy with a singularity at the edge of the continuum suggesting the existence of well-defined magnons. A theoretical description is provided for all different processes based on the exact diagonalization of 16 spins presenting a very good overall agreement with the data.

The second part of the chapter introduces the data for the investigation of the interplay between thermal and quantum effects by studying the changes of the system when applying temperature of the order of the one-magnon gap energy and magnetic field. The main issues are established by a comparison with the pure quantum effects as introduced in the Chapter 7 and the pure thermal effects as discussed in this chapter. While a quantitative analysis could be provided, theoretical input is necessary to fully understand the composition of the ground state and the excitation spectrum.

References

- [1] H.-J. Mikeska, and C. Luckmann, *Phys. Rev. B* **73**, 184426 (2006).
- [2] D. A. Tennant, C. Broholm, D. H. Reich, S. E. Nagler, G. E. Granroth, T. Barnes, K. Damle, G. Xu, Y. Chen, and B. C. Sales, *Phys. Rev. B* **67**, 054414 (2003).
- [3] F. H. L. Essler, *unpublished* (2007).
- [4] J. G. Houman, M. Chapellier, A. R. Mackintosh, P. Bak, O. D. McMaster and K. A. Geschneider, Jr *Phys. Rev. Lett.* **34**, 587 (1974).
- [5] S. Sachdev and K. Damle, *Phys. Rev. Lett.* **78**, 943 (1997).
- [6] G. Xu, C. Broholm, D. H. Reich, and M. A. Adams, *Phys. Rev. Lett.* **84**, 4464 (2000).

- [7] T. Barnes, J. Riera, and D. A. Tennant, *Phys. Rev. B* **59**, 11384 (1999).
- [8] J. Villain, *Physica B* **79**, 1 (1975).
- [9] H.-J. Braun, J. Kulda, B. Roessli, D. Visser, K. W. Krämer, H.-U. Güdel, and P. Böni, *Nature Physics* **1**, 159 (2005).
- [10] H.-J. Mikeska. *private communications*, (2007).

Chapter 9

Conclusion

The focus of this thesis has been on the experimental work of the spin dynamics of spin chains and ladders investigated by INS measurements. The study can be separated into two parts with the concentration of the first part on the spin-chain and ladder structures of the copper oxide family $\text{Sr}_{14}\text{Cu}_{24}\text{O}_{41}$ upon charge doping discussed in Chapters 4-6. The second part consists of the investigation of the alternating chain material copper nitrate when applying magnetic field (Chapter 7) and temperature (Chapter 8). In Chapter 4 the excitation spectrum of the low holed-doped edge-sharing chain $\text{La}_4\text{Sr}_{10}\text{Cu}_{24}\text{O}_{41}$ can be modeled by a strong ferromagnetic nearest neighbor coupling, a weak antiferromagnetic next-nearest neighbor coupling and a charge density wave describing the effects of the holes with the new finding consisting of the large ferromagnetic coupling constant and the nature of the hole. Chapter 5 investigates the spin-ladder structure of the same material establishing the coupling constants including a cyclic exchange, for the first time by a direct theoretical comparison of the one- and the two-magnon spectra. In Chapter 6 the hole doped version of the ladder realized by $\text{Ca}_{2.5}\text{Sr}_{11.5}\text{Cu}_{24}\text{O}_{41}$ is studied by a direct comparison of the spectra of the undoped ladder and the charge scattering calculated by the Independent Electron Model. Chapter 7 describes the excitations in $\text{Cu}(\text{NO}_3)_2 \cdot 2.5\text{D}_2\text{O}$ consisting of a gapped one-magnon dis-

persion, a two-magnon continuum and a corresponding bound mode. Also investigated are the magnetic field effects with the high field modes after saturation modeled by spin wave theory and a quantitative description of the established Luttinger Liquid phase is provided. In Chapter 8 the temperature effects in copper nitrate consisting of the one- and two-magnon spectra and additionally of the intraband scattering are compared to a theory based on the exact diagonalization of 16 spins. The data for a complete study of the thermal and quantum effects are provided.

Some possible future projects arise from this work where a follow-up or intensification of the investigation would be interesting. In the case of the edge-sharing chain one-band Hubbard model calculations would enable a link between the size of the gaps in the dispersion and the periodic potential arising from the presence of the holes. For a confirmation of our model and a comparison to theory a high statistic experiment and further measurements of different hole-doping conditions would be beneficial. For a complete understanding of the nature of the holes in the doped ladder material $\text{Ca}_{2.5}\text{Sr}_{11.5}\text{Cu}_{24}\text{O}_{41}$ further work consisting of a measurement of the incommensuration of the subgap scattering and higher statistics for the high energy modes are necessary to provide a complete experimental description serving as a basis for the development of theory. Additionally it would be interesting to perform pressure INS measurements when the system is in its superconducting state providing further insight into the question of high- T_c superconductivity. In the case of copper nitrate a theory describing the Luttinger Liquid region between the two critical fields for the middle band is important in developing an understanding of the ground state composition and the mechanism of the excitations. Additionally the interplay between thermal and quantum effects needs theoretical input for a comprehension of all effects in the system. Bulk measurements (ongoing, but beyond the scope of this thesis) will help to establish the critical components in the system for a complete investigation.

Appendix A

Parity conservation

A.1 Hamiltonian

This section confirms the parity conservation for our spin-ladder system by applying the Hamiltonian onto a plaquette serving as the basic unit of the ladder (compare Figure A.1) and allowing a generalization of the results. The Hamiltonian can be divided into several parts:

$$H = H_{\text{rung}} + H_{\text{leg}} + H_{\text{cyc}} \quad (\text{A.1})$$

where

$$H_{\text{rung}} = J_{\text{rung}} (\mathbf{S}_{1,l} \cdot \mathbf{S}_{2,l}) \quad (\text{A.2})$$

$$H_{\text{leg}} = J_{\text{leg}} (\mathbf{S}_{1,l} \cdot \mathbf{S}_{1,l+1}) \quad (\text{A.3})$$

$$H_{\text{cyc}} = J_{\text{cyc}} [(\vec{\mathbf{S}}_{1,l} \cdot \mathbf{S}_{1,l+1})(\mathbf{S}_{2,l} \cdot \mathbf{S}_{2,l+1}) \quad (\text{A.4})$$

$$+(\vec{\mathbf{S}}_{1,l} \cdot \mathbf{S}_{2,l})(\mathbf{S}_{1,l+1} \cdot \mathbf{S}_{2,l+1}) - (\vec{\mathbf{S}}_{1,l} \cdot \mathbf{S}_{2,l+1})(\mathbf{S}_{1,l+1} \cdot \mathbf{S}_{2,l})]$$

H_{rung} couples two spins into a dimer (rung), H_{leg} connects two dimers into a plaquette and H_{cyc} describes the spin permutation within a plaquette necessary to include in cuprate systems due to the small t/U ratio as introduced in Section 2.1.3.

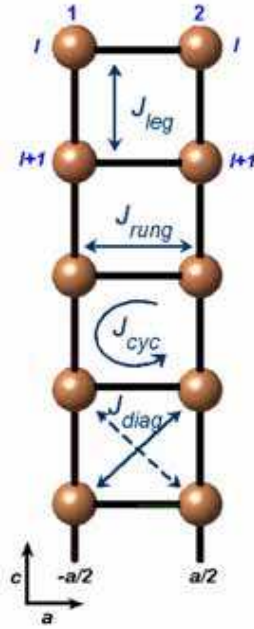


Figure A.1: Arrangement of the ladder in the a^* - c^* plane. The position of each copper spin is indicated by leg 1 at $-a/2$ and leg 2 at $a/2$ in the a^* direction and by $l, l+1, \dots$ in the c^* direction.

As a starting point for this calculation the strong coupling limit with $J_{rung} \gg J_{leg}$ is assumed where the plaquette can be illustrated as a product of two dimers. Applying H_{leg} it can be shown that the parity is conserved, i.e. even (odd) dimer state couple with even (odd) dimers. Afterwards the structure factor for both the one-and two-magnon excitation for the general case of a plaquette is calculated.

A.2 Plaquette

The dimer serving as a basic unit for the plaquette and therefore as well for the ladder consists of a singlet ground state and a triplet excited state with the ground state given by:

$$|\rho\rangle = |G\rangle = \frac{1}{\sqrt{2}} [|\uparrow\downarrow\rangle - |\downarrow\uparrow\rangle] \quad (\text{A.5})$$

and the excited state:

$$|\sigma(m)\rangle = \begin{bmatrix} |1\rangle = |\uparrow\uparrow\rangle & m = 1 \\ |0\rangle = \frac{1}{\sqrt{2}}|\uparrow\downarrow\rangle + |\downarrow\uparrow\rangle & m = 0 \\ |\bar{1}\rangle = |\downarrow\downarrow\rangle & m = -1 \end{bmatrix} \quad (\text{A.6})$$

The plaquette consists of two dimers coupled together with the possible states consisting of states with no, one and two excited dimers found by combining equations A.5 and A.6.

No excited dimer :

$$\begin{aligned} |G_l G_{l+1}\rangle &= |GG\rangle = \frac{1}{\sqrt{2}} [|\uparrow\downarrow\rangle_l - |\downarrow\uparrow\rangle_l] \otimes \frac{1}{\sqrt{2}} [|\uparrow\downarrow\rangle_{l+1} - |\downarrow\uparrow\rangle_{l+1}] \\ &= \frac{1}{2} [|(\uparrow\downarrow)_l(\uparrow\downarrow)_{l+1}\rangle - |(\uparrow\downarrow)_l(\downarrow\uparrow)_{l+1}\rangle - |(\downarrow\uparrow)_l(\uparrow\downarrow)_{l+1}\rangle + |(\downarrow\uparrow)_l(\downarrow\uparrow)_{l+1}\rangle] \end{aligned} \quad (\text{A.7})$$

One excited dimer :

$$\begin{aligned} |G1\rangle &= \frac{1}{\sqrt{2}} [|(\uparrow\downarrow)_l(\uparrow\uparrow)_{l+1}\rangle - |(\downarrow\uparrow)_l(\uparrow\uparrow)_{l+1}\rangle] \\ |G0\rangle &= \frac{1}{2} [|(\uparrow\downarrow)_l(\uparrow\downarrow)_{l+1}\rangle + |(\uparrow\downarrow)_l(\downarrow\uparrow)_{l+1}\rangle - |(\downarrow\uparrow)_l(\uparrow\downarrow)_{l+1}\rangle - |(\downarrow\uparrow)_l(\downarrow\uparrow)_{l+1}\rangle] \\ |G\bar{1}\rangle &= \frac{1}{\sqrt{2}} [|(\uparrow\downarrow)_l(\downarrow\downarrow)_{l+1}\rangle - |(\downarrow\uparrow)_l(\downarrow\downarrow)_{l+1}\rangle] \end{aligned} \quad (\text{A.8})$$

Two excited dimers:

$$\begin{aligned} |11\rangle &= |(\uparrow\uparrow)_l(\uparrow\uparrow)_{l+1}\rangle \\ |00\rangle &= \frac{1}{2} [|(\uparrow\downarrow)_l(\uparrow\downarrow)_{l+1}\rangle + |(\uparrow\downarrow)_l(\downarrow\uparrow)_{l+1}\rangle + |(\downarrow\uparrow)_l(\uparrow\downarrow)_{l+1}\rangle + |(\downarrow\uparrow)_l(\downarrow\uparrow)_{l+1}\rangle] \\ |\bar{1}\bar{1}\rangle &= |(\downarrow\downarrow)_l(\downarrow\downarrow)_{l+1}\rangle \\ |1\bar{1}\rangle &= |(\uparrow\uparrow)_l(\downarrow\downarrow)_{l+1}\rangle \\ |01\rangle &= \frac{1}{\sqrt{2}} [|(\uparrow\downarrow)_l(\uparrow\uparrow)_{l+1}\rangle + |(\downarrow\uparrow)_l(\uparrow\uparrow)_{l+1}\rangle] \\ |0\bar{1}\rangle &= \frac{1}{\sqrt{2}} [|(\uparrow\downarrow)_l(\downarrow\downarrow)_{l+1}\rangle + |(\downarrow\uparrow)_l(\downarrow\downarrow)_{l+1}\rangle] \end{aligned} \quad (\text{A.9})$$

And similar for the commutative states not listed here.

A.3 Hamiltonian H_{leg}

By applying the leg Hamiltonian H_{leg} provided in equation A.3 to the different combination of excited dimer states the parity conservation can be confirmed. Starting with the no excited dimer state of equation A.7 reveals:

$$\begin{aligned} H_{leg}|GG\rangle &= \vec{S}_{1,l} \cdot \vec{S}_{1,l+1} |GG\rangle \\ &= [S_{1,l}^z S_{1,l+1}^z + S_{2,l}^z S_{2,l+1}^z + \frac{1}{2} (S_{1,l}^+ S_{1,l+1}^- + S_{1,l}^- S_{1,l+1}^+) \\ &\quad + \frac{1}{2} (S_{2,l}^+ S_{2,l+1}^- + S_{2,l}^- S_{2,l+1}^+)] |GG\rangle \end{aligned}$$

$$\begin{aligned} S_{1,l}^z S_{1,l+1}^z |GG\rangle &= \frac{1}{2} [\frac{1}{4} |(\uparrow\downarrow)_l (\uparrow\downarrow)_{l+1}\rangle + \frac{1}{4} |(\downarrow\uparrow)_l (\uparrow\downarrow)_{l+1}\rangle \\ &\quad + \frac{1}{4} |(\uparrow\downarrow)_l (\downarrow\uparrow)_{l+1}\rangle + \frac{1}{4} |(\downarrow\uparrow)_l (\downarrow\uparrow)_{l+1}\rangle] = \frac{1}{4} |00\rangle \\ S_{2,l}^z S_{2,l+1}^z |GG\rangle &= \frac{1}{4} |00\rangle \\ \frac{1}{2} S_{1,l}^+ S_{1,l+1}^- |GG\rangle &= \frac{1}{4} [-|(\uparrow\uparrow)_l (\downarrow\downarrow)_{l+1}\rangle] = -\frac{1}{4} |1\bar{1}\rangle \\ \frac{1}{2} S_{1,l}^- S_{1,l+1}^+ |GG\rangle &= -\frac{1}{4} |\bar{1}1\rangle \\ \frac{1}{2} S_{2,l}^+ S_{2,l+1}^- |GG\rangle &= -\frac{1}{4} |1\bar{1}\rangle \\ \frac{1}{2} S_{2,l}^- S_{2,l+1}^+ |GG\rangle &= -\frac{1}{4} |\bar{1}1\rangle \end{aligned}$$

Combining these results:

$$H_{leg}|GG\rangle = \frac{1}{2} |00\rangle - \frac{1}{2} |1\bar{1}\rangle - \frac{1}{2} |\bar{1}1\rangle \quad (\text{A.10})$$

shows the ground state (even number of dimers) couples to a state with two excited dimers. For a confirmation this parity conservation has to be checked for all the other possible dimer states. The leg Hamiltonian H_{leg} applied to the even dimer states gives :

$$\begin{aligned} H_{leg}|11\rangle &= \frac{1}{2} |11\rangle \\ H_{leg}|00\rangle &= \frac{1}{2} |GG\rangle + \frac{1}{2} |1\bar{1}\rangle + \frac{1}{2} |\bar{1}1\rangle \\ H_{leg}|\bar{1}\bar{1}\rangle &= \frac{1}{2} |\bar{1}\bar{1}\rangle \end{aligned}$$

$$\begin{aligned} H_{leg}|1\bar{1}\rangle &= -\frac{1}{2}|1\bar{1}\rangle - \frac{1}{2}|GG\rangle - \frac{1}{2}|00\rangle \\ H_{leg}|01\rangle &= \frac{1}{2}|10\rangle \end{aligned} \quad (\text{A.11})$$

and calculating the effect on the odd dimer states :

$$\begin{aligned} H_{leg}|G0\rangle &= \frac{1}{2}|0G\rangle \\ H_{leg}|G1\rangle &= \frac{1}{2}|1G\rangle \\ H_{leg}|G\bar{1}\rangle &= \frac{1}{2}|\bar{1}G\rangle \end{aligned} \quad (\text{A.12})$$

(and their commutator states not listed here) reveals no inter-channel coupling.

A.4 Structure factor

For the calculation of the structure factor the simple considerations of the strong coupling limit are insufficient and an evaluation of the ground and excited states of the plaquette including the other Hamiltonian contribution is necessary. The two dimers are combined to form states with definite total spin and symmetry evaluated by expressing them as a Clebsch-Gordon series. Only the $S = 0$ and the $S = 1$ are of interest due to the neutron scattering selection rule of $\Delta S = 1$.

The ground state is formed by $S = 0$ states consisting of the no excited dimer state, $|GG\rangle$, and a contribution of two excited dimer states forming a $S = 0$ leading to:

$$|S = 0\rangle = \begin{bmatrix} |\sigma\sigma\rangle_0 \\ |\rho\rho\rangle \end{bmatrix} \quad (\text{A.13})$$

where

$$\begin{aligned} |\rho\rho\rangle &= |GG\rangle \\ |\sigma\sigma\rangle_0 &= \frac{1}{\sqrt{3}}(|1\bar{1}\rangle - |00\rangle + |\bar{1}1\rangle) \end{aligned} \quad (\text{A.14})$$

The $S = 1$ is composed of states with one excited dimer consisting of a symmetric or antisymmetric combination (one-magnon excitation), $|\rho\sigma\rangle_S$ and $|\rho\sigma\rangle_A$ respectively, and states with two excited dimers coupled antisymmetric (two-magnon excitation) $|\sigma\sigma\rangle_1$ [1].

$$|S = 1\rangle = \begin{bmatrix} |\sigma\sigma\rangle_1 \\ |\rho\sigma\rangle_S \\ |\rho\sigma\rangle_A \end{bmatrix} \quad (\text{A.15})$$

with

$$|\rho\sigma\rangle_A = \begin{bmatrix} \frac{1}{\sqrt{2}} [|1G\rangle - |G1\rangle] \\ \frac{1}{\sqrt{2}} [|0G\rangle - |G0\rangle] \\ \frac{1}{\sqrt{2}} [|\bar{1}G\rangle - |G\bar{1}\rangle] \end{bmatrix} \quad (\text{A.16})$$

$$|\rho\sigma\rangle_S = \begin{bmatrix} \frac{1}{\sqrt{2}} [|1G\rangle + |G1\rangle] \\ \frac{1}{\sqrt{2}} [|0G\rangle + |G0\rangle] \\ \frac{1}{\sqrt{2}} [|\bar{1}G\rangle + |G\bar{1}\rangle] \end{bmatrix} \quad (\text{A.17})$$

and

$$|\sigma\sigma\rangle_1 = \begin{bmatrix} \frac{1}{\sqrt{2}} [|10\rangle - |01\rangle] \\ \frac{1}{\sqrt{2}} [|\bar{1}0\rangle - |0\bar{1}\rangle] \\ \frac{1}{\sqrt{2}} [|\bar{1}\bar{1}\rangle - |1\bar{1}\rangle] \\ \frac{1}{\sqrt{2}} [|1\bar{1}\rangle - |\bar{1}1\rangle] \end{bmatrix} \quad (\text{A.18})$$

A.4.1 One-magnon

The structure factor for the one-magnon scattering can be obtained by applying the $S_{\mathbf{Q}}^{\alpha}$ spin creation operator to the ground state. The spin operator is defined in equation 3.11 in Section 3.2 as:

$$S_{\mathbf{Q}}^{\alpha} = \sum_i \exp(-i\mathbf{Q} \cdot \mathbf{R}_i) S_i^{\alpha} \quad (\text{A.19})$$

Starting with considering the upper dimer- dimer1- and applying the z component of the spin creation operator on the ground state of this dimer with spin 1 at position $-a_l/2$ (left spin) and spin 2 at $a_l/2$ (right spin) (compare Figure A.1).

$$\begin{aligned}
 S_{\mathbf{Q}}^z |GG\rangle &= e^{iQa_l/2} S_{1,l}^z |GG\rangle + e^{-iQa_l/2} S_{2,l}^z |GG\rangle \\
 &= \frac{1}{4} [e^{iQa_l/2} (|(\uparrow\downarrow)_l (\uparrow\downarrow)_{l+1}\rangle - |(\uparrow\downarrow)_l (\downarrow\uparrow)_{l+1}\rangle \\
 &\quad + |(\downarrow\uparrow)_l (\uparrow\downarrow)_{l+1}\rangle - |(\downarrow\uparrow)_l (\downarrow\uparrow)_{l+1}\rangle) \\
 &\quad + e^{-iQa_l/2} (-|(\uparrow\downarrow)_l (\uparrow\downarrow)_{l+1}\rangle + |(\uparrow\downarrow)_l (\downarrow\uparrow)_{l+1}\rangle \\
 &\quad - |(\downarrow\uparrow)_l (\uparrow\downarrow)_{l+1}\rangle + |(\downarrow\uparrow)_l (\downarrow\uparrow)_{l+1}\rangle)] \\
 \Rightarrow S_{\mathbf{Q}}^z |GG\rangle &= \frac{1}{4} (e^{iQa_l/2} - e^{-iQa_l/2}) |0G\rangle
 \end{aligned} \tag{A.20}$$

Repeating this process for the second dimer at position a_{l+1} finds:

$$\begin{aligned}
 S_{\mathbf{Q}}^z |GG\rangle &= e^{iQa_{l+1}/2} S_{1,l+1}^z |GG\rangle + e^{-iQa_{l+1}/2} S_{2,l+1}^z |GG\rangle \\
 &= \frac{1}{4} (e^{iQa_{l+1}/2} - e^{-iQa_{l+1}/2}) |G0\rangle
 \end{aligned} \tag{A.21}$$

Combining equations A.20 and A.21 the matrix element of the spin transition operator $S_{\mathbf{Q}}^\alpha$ can be calculated:

$$\begin{aligned}
 {}_S \langle \rho \sigma(0) | S_{\mathbf{Q}}^\alpha | \rho \rho \rangle &= \frac{1}{2\sqrt{2}} [e^{iQa_l/2} - e^{-iQa_l/2} + e^{iQa_{l+1}/2} - e^{-iQa_{l+1}/2}] \\
 {}_A \langle \rho \sigma(0) | S_{\mathbf{Q}}^\alpha | \rho \rho \rangle &= \frac{1}{2\sqrt{2}} [e^{iQa_l/2} - e^{-iQa_l/2} - e^{iQa_{l+1}/2} + e^{-iQa_{l+1}/2}]
 \end{aligned} \tag{A.22}$$

The structure factor is proportional to the square of this matrix element and the evaluation confirms the cosinusoidal dependence:

$$\begin{aligned}
 S(\mathbf{Q}, \omega) &\propto |{}_S \langle \rho \sigma(0) | S_{\mathbf{Q}}^\alpha | \rho \rho \rangle|^2 \\
 &= [(1 - \cos(Q \cdot a_l)) + (1 - \cos(Q \cdot a_{l+1}))]
 \end{aligned}$$

However the $(1 - \cos(Q \cdot a_{l+1}))$ part can be separated into a Q_a and a Q_c contribution [2] because a_{l+1} can be translated into a_l and a Q_c difference (compare Figure A.1).

$$|_S \langle \rho\sigma(0) | S_Q^\alpha | \rho\rho \rangle|^2 = \frac{1}{4} (1 - \cos(Q \cdot a_l)) (1 + Q_c \text{ dependence})$$

Confirming the matrix element to be proportional to the expected cosine:

$$|_S \langle \rho\sigma(0) | S_Q^\alpha | \rho\rho \rangle|^2 \propto (1 - \cos(Q_a \cdot a)) = |_A \langle \rho\sigma(0) | S_Q^\alpha | \rho\rho \rangle|^2 \quad (\text{A.23})$$

Now applying the x and the y component onto the ground state and using

$S_Q^x = \frac{1}{2}(S^+ + S^-)$ and $S_Q^y = \frac{1}{2i}(S^+ - S^-)$ leads to:

$$\begin{aligned} S_Q^x |GG\rangle_{\text{1st dimer}} &= \frac{1}{2\sqrt{2}} (e^{iQa_l/2} + e^{-iQa_l/2}) (|1G\rangle - |\bar{1}G\rangle) \\ S_Q^x |GG\rangle_{\text{2nd dimer}} &= \frac{1}{2\sqrt{2}} (e^{iQa_{l+1}/2} + e^{-iQa_{l+1}/2}) (|G\bar{1}\rangle - |G1\rangle) \\ S_Q^y |GG\rangle_{\text{1st dimer}} &= -\frac{1}{2i\sqrt{2}} (e^{iQa_l/2} + e^{-iQa_l/2}) (|1G\rangle - |\bar{1}G\rangle) \\ S_Q^y |GG\rangle_{\text{2nd dimer}} &= -\frac{1}{2i\sqrt{2}} (e^{iQa_{l+1}/2} + e^{-iQa_{l+1}/2}) (|G1\rangle - |G\bar{1}\rangle) \end{aligned}$$

Combining these results with equation A.15 is consistent with the sinusoidal dependence of equation A.23:

$$|_{S,A} \langle \rho\sigma(m) | S_Q^\alpha | \rho\rho \rangle|^2 \propto (1 - \cos(Q_a \cdot a)) \quad (\text{A.24})$$

Applying the z component onto the $|\sigma\sigma\rangle$ state and using equation A.14 reveals a contribution of $|00\rangle$ also to the one-magnon structure factor through a coupling to the one excited dimer states ($|0G\rangle - |G0\rangle$) and shows following matrix elements:

$$\begin{aligned} s \langle \rho\sigma(m) | S_Q^\alpha | 00 \rangle &= -\frac{1}{2\sqrt{6}} [e^{iQa_l/2} - e^{-iQa_l/2} + e^{iQa_{l+1}/2} - e^{-iQa_{l+1}/2}] \\ {}_A \langle \rho\sigma(m) | S_Q^\alpha | 00 \rangle &= -\frac{1}{2\sqrt{6}} [e^{iQa_l/2} - e^{-iQa_l/2} - e^{iQa_{l+1}/2} + e^{-iQa_{l+1}/2}] \end{aligned}$$

This confirms the square of the matrix element being proportional to $(1 - \cos(Q_a \cdot a))$ in agreement with the previous finding.

For the ladder an additional leg direction dependence Q_c has to be included different for each of the states and provided by the one-and two-magnon dispersion relations as introduced in Section 5.5.3, but does not change the $(1 - \cos(Q_a \cdot a))$ modulation for the rung direction.

A.4.2 Two-magnon

The same procedure can be applied for the calculation of the two-magnon structure factor. Applying the S_Q^α and calculating the matrix element ${}_1\langle \sigma\sigma | S_Q^\alpha | \sigma\sigma_0 \rangle$ where the x and y components of $|00\rangle$ and all components of $(|1\bar{1}\rangle - |\bar{1}1\rangle)$ contribute, reveals for the matrix element:

$${}_1\langle \sigma\sigma | S_Q^\alpha | \sigma\sigma_0 \rangle = \frac{1}{\sqrt{6}}(e^{iQa_l/2} + e^{-iQa_l/2} - e^{iQa_{l+1}/2} - e^{-iQa_{l+1}/2})$$

leading to a structure factor of:

$$\begin{aligned} {}_1|\langle \sigma\sigma | S_Q^\alpha | \sigma\sigma_0 \rangle|^2 &= \frac{1}{3}[(1 + \cos(Q \cdot a)) - (1 + \cos(Q \cdot a_{l+1}))] \\ &\propto \frac{1}{3}(1 + \cos(Q_a \cdot a))(1 + Q_c \text{ dependence}) \end{aligned} \quad (\text{A.25})$$

This shows the two-magnon structure factor being proportional to $(1 + \cos(Q_a \cdot a))$ and therefore in antiphase compared to the one-magnon structure factor. Since the plaquette is the basic unit for the ladder, these results can be generalized to the geometry of the ladder [3].

A.5 Other Hamiltonian

Using the same methodology as in section A.3 for the different contributions of the Hamiltonian such as H_{cyc} and even a diagonal coupling connecting spins $1, l$ with $2, l+1$ and spins $2, l$ with $1, l+1$ (very small in our case and thus neglected) also confirms the parity conservation. However if one would consider only one diagonal coupling the

symmetry argument would be disturbed leading to an invalidation of the separation into one- and two-magnon channel.

Summarizing the Hamiltonian of equation A.2 describing the spin-ladder validates the symmetry argument with a separation of the wavevector dependence of $(1 - \cos(Q_a \cdot a))$ for the one-magnon and a $(1 + \cos(Q_a \cdot a))$ for the two-magnon scattering.

References

- [1] J. T. Haraldsen, T. Barnes, and J. T. Musfled, *Phys. Rev. B* **71**, 064403 (2005).
- [2] D. A. Tennant, C. Broholm, D. H. Reich, S. E. Nagler, G. E. Granroth, T. Barnes, K. Damle, G. Xu, Y. Chen, and B. C. Sales, *Phys. Rev. B* **67**, 064414 (2003).
- [3] K. P. Schmidt, and G. S. Uhrig, *Mod. Phys. Lett. B* **19**, 1179 (2005).

Appendix B

Band Structure Calculation

B.1 Calculation of the Dispersion Relation

For the calculation of the ladder dispersion relation for the band structure as provided in equation 6.4 the free electron Hamiltonian H_0 introduced in Section 2.1.3 serves as a starting point:

$$H_0 = -t_{para} \sum_{j,l,\sigma} (c_{j,l,\sigma}^+ c_{j+1,l,\sigma}^- + c_{j,l,\sigma}^- c_{j+1,l,\sigma}^+) - t_{perp} \sum_{j,\sigma} (c_{j,1,\sigma}^+ c_{j,2,\sigma}^- + c_{j,1,\sigma}^- c_{j,2,\sigma}^+) \quad (\text{B.1})$$

where c describes the hopping matrix element and is given by:

$$c_\sigma(\mathbf{k}) \equiv \frac{1}{\sqrt{2N}} \sum_{j,l} e^{-i(k_{para} j + k_{perp} l)} c_{j,l,\sigma} \quad (\text{B.2})$$

and σ denotes the spin state \uparrow or \downarrow , N represents the number of sites on each leg and the factor of 2 results from the number of legs. The momentum \mathbf{k} is defined as $\mathbf{k} = (k_{para}, k_{perp})$ with k_{perp} taking the possible values of 0 or π (0 for bonding and π antibonding). To simplify the calculation the lattice spacing for both the leg and the rung direction is set to unity.

Applying the Fourier transform onto $c_\sigma(\mathbf{k})$ leads to:

$$c_{j,l,\sigma} \equiv \frac{1}{\sqrt{2N}} \sum_{j,l} e^{i(k_{para,j} + k_{perp,l})} c_\sigma(\mathbf{k}) \quad (\text{B.3})$$

and using equations B.3 along with the Fermion anticommutation relation

$$c_\sigma^\dagger(\mathbf{k}) c_\sigma(\mathbf{k}) = 1 \quad (\text{B.4})$$

the first part of the first sum of H_0 (from equation B.1 given by $H_0 = -t_{para} \sum_{j,l,\sigma} c_{j,l,\sigma}^+ c_{j+1,l,\sigma}^-$) can be written as:

$$\begin{aligned} \sum_{j,l,\sigma} c_{j,l,\sigma}^+ c_{j+1,l,\sigma}^- &= \sum_{j,l,\sigma} \sum_{\mathbf{k}} \sum_{\mathbf{k}'} \frac{1}{2N} e^{i(k_{para,j} + k_{perp,l})} c_\sigma^\dagger(\mathbf{k}) e^{-i(k'_{para}(j+1) + k'_{perp,l})} c_\sigma(\mathbf{k}') \\ &= \sum_{l,\sigma} \sum_{\mathbf{k}, \mathbf{k}'} \left(\sum_j e^{i(k_{para} - k'_{para})j} e^{ik_{para}} \right) \frac{1}{2N} e^{i(k_{perp} - k'_{perp})l} c_\sigma^\dagger(\mathbf{k}) c_\sigma(\mathbf{k}') \end{aligned}$$

This can be simplified taking into account the existence of only two possible values for $k_{perp} - k'_{perp}$ after summing over l (since l is either 1 or 2):

$$1. \ k_{perp} - k'_{perp} = \pi \Rightarrow e^{i\pi} + e^{i\pi^2} = 0$$

$$2. \ k_{perp} - k'_{perp} = 0 \Rightarrow e^{i0} + e^{i0} = 2$$

which results in the simplified realtion for the sum over l :

$$\sum_l e^{i(k_{perp} - k'_{perp})l} = 2 \delta_{k_{perp}, k'_{perp}} \quad (\text{B.5})$$

Similar is true for the sum dependend on $k_{para} - k'_{para}$ but running over i leads to N possible values for the rung in contradiction to the only two values for the leg:

$$\sum_j e^{i(k_{para} - k'_{para})j} = N \delta_{k_{para}, k'_{para}} \quad (\text{B.6})$$

Using equations B.5 and B.6 the first part of the sum of H_0 can be rewritten as:

$$\sum_{j,l,\sigma} c_{j,l,\sigma}^+ c_{j+1,l,\sigma}^- = \sum_\sigma \sum_{\mathbf{k}} e^{ik_{para}} c_\sigma^\dagger(\mathbf{k}) c_\sigma(\mathbf{k}) \quad (\text{B.7})$$

where it is only necessary to sum over \mathbf{k} taking the results of equations B.5 and B.6 into account. In analog the second part of the sum for t_{para} in H_0 provided by the hermitian conjugate of equation B.7 can be evaluated as:

$$\sum_{j,l,\sigma} c_{j,l,\sigma}^- c_{j+1,l,\sigma}^+ = \sum_{\sigma} \sum_k e^{-ik_{para}} c_{\sigma}(\mathbf{k}) c_{\sigma}^\dagger(\mathbf{k}) \quad (\text{B.8})$$

Using this result and equation B.7 the complete first sum of H_0 for t_{para} can be expressed as:

$$-t_{para} \sum_{j,l,\sigma} c_{j,l,\sigma}^+ c_{j+1,l,\sigma}^- + c_{j,l,\sigma}^- c_{j+1,l,\sigma}^+ = -2 t_{para} \sum_{\mathbf{k}, \sigma} \cos(k_{para}) c_{\sigma}^\dagger(\mathbf{k}) c_{\sigma}(\mathbf{k}) \quad (\text{B.9})$$

For the calculation of the second sum of H_0 (equation B.1) describing the perpendicular component of t (t_{perp}) the same procedure is applied with the first part of the sum given by:

$$\begin{aligned} \sum_{j,\sigma} c_{j,1,\sigma}^+ c_{j,2,\sigma}^- &= \sum_{j,\sigma} \sum_{\mathbf{k}} \sum_{\mathbf{k}'} \frac{1}{2N} e^{i(k_{para}j+k_{perp})} c_{\sigma}^\dagger(\mathbf{k}) e^{-i(k_{para}j+2k_{perp})} c_{\sigma}(\mathbf{k}') \\ &= \sum_{\sigma} \sum_{\mathbf{k}, \mathbf{k}'} \left(\sum_j e^{i(k_{para}-k'_{para})j} \right) \frac{1}{2N} e^{i(k_{perp}-2k'_{perp})} c_{\sigma}^\dagger(\mathbf{k}) c_{\sigma}(\mathbf{k}') \end{aligned}$$

The second sum of H_0 does not include the summing over l because the electron hopping along the rung is considered fixing the value of l and thus providing a simplification for the $k_{perp}-k'_{perp}$ component:

$$e^{ik_{perp}-2ik'_{perp}} = e^{-ik_{perp}} \delta_{k_{perp}, k'_{perp}} \quad (\text{B.10})$$

The parallel component $k_{para}-k'_{para}$ follows the results as found in equation B.6:

$$\sum_j e^{i(k_{para}-k'_{para})j} = N \delta_{k_{para}, k'_{para}} \quad (\text{B.11})$$

Combining equations B.10 and B.11 the first part of the sum can be calculated:

$$\sum_{j,\sigma} c_{j,1,\sigma}^+ c_{j,2,\sigma}^- = \sum_{\sigma} \sum_{\mathbf{k}} \frac{1}{2} e^{-ik_{perp}} c_{\sigma}^\dagger(\mathbf{k}) c_{\sigma}(\mathbf{k}) \quad (\text{B.12})$$

Using the hermitian conjugate for the second part of the sum involving the perpendicular component of t as introduced in equation B.1:

$$\begin{aligned} H_0 &= \sum_{\mathbf{k}, \sigma} (-2t_{para} \cos(k_{para}) - t_{perp} \cos(k_{perp})) c_{\sigma}^{\dagger}(\mathbf{k}) c_{\sigma}(\mathbf{k}) \\ &= \sum_{\mathbf{k}, \sigma} \epsilon(\mathbf{k}) c_{\sigma}^{\dagger}(\mathbf{k}) c_{\sigma}(\mathbf{k}) \end{aligned} \quad (\text{B.13})$$

where $\epsilon(\mathbf{k}) = -2t_{para} \cos(k_{para}) - t_{perp} \cos(k_{perp})$ is the disperison relation.

B.2 Calculation of Fermi wavevector

The determination of the Fermi wavevectors is important for the calculation of the boundaries of the charge scattering as introduced in Section 6.5.3 and important for the doped ladder, as doping shifts the Fermi level by δ (as seen in Figure 6.6) and thus translates the Fermi wavevectors from their half-filling position. The doped Fermi wavevector for the lower band $\pm k_{F,0}^d$ gets shifted by $|\delta_0|$ along the wavevector k and the Fermi wavevector of the upper band $\pm k_{F,\pi}^d$ by $|\delta_\pi|$. It is possible to express the Fermi wavevectors in terms of only the hopping parameters, t_{perp} and t_{para} , and the doping δ by utilizing the connection of the doped Fermi wavevector via the following two conditions:

$$k_{F,0}^d + k_{F,\pi}^d + \delta = \pi \quad (\text{B.14})$$

$$\epsilon(k_{F,0}^d) = \epsilon(k_{F,\pi}^d) \quad (\text{B.15})$$

Using the dispersion relation as calculated in the previous section and equation B.15:

$$-2t_{para} \cos(k_{F,0}^d) - t_{perp} = -2t_{para} \cos(k_{F,\pi}^d) + t_{perp} \quad (\text{B.16})$$

and B.14 leads to following condition between t_{para} and t_{perp} :

$$-2t_{para} \cos(k_{F,0}^d) - t_{perp} = -2t_{para} \cos(\pi - \delta - k_{F,0}^d) + t_{perp}$$

$$\begin{aligned}
-\frac{t_{perp}}{t_{para}} &= \cos(k_{F,0}^d) - \cos(\pi - \delta - k_{F,0}^d) \\
-\frac{t_{perp}}{t_{para}} &= -2 \sin\left(\frac{k_{F,0}^d - \pi + \delta + k_{F,0}^d}{2}\right) \sin\left(\frac{k_{F,0}^d + \pi - \delta - k_{F,0}^d}{2}\right) \\
-\frac{t_{perp}}{t_{para}} &= \sin\left(\frac{2k_{F,0}^d - \pi + \delta}{2}\right) \cos\left(\frac{\delta}{2}\right)
\end{aligned}$$

Now $k_{F,0}^d$ and $k_{F,\pi}^d$ can be described in terms of only t_{perp} , t_{para} and δ :

$$\begin{aligned}
k_{k,0}^d &= \frac{\pi}{2} \left(1 - \frac{\delta}{\pi}\right) + \arcsin\left(\frac{t_{perp}}{2t_{para} \cos(\delta/2)}\right) \\
k_{k,\pi}^d &= \frac{\pi}{2} \left(1 - \frac{\delta}{\pi}\right) - \arcsin\left(\frac{t_{perp}}{2t_{para} \cos(\delta/2)}\right)
\end{aligned}$$

With the definition of $\lambda = \arcsin\left(\frac{t_{perp}}{2t_{para} \cos(\delta/2)}\right)$ equations B.17 and B.17 become:

$$k_{k,0}^d = \frac{\pi}{2} \left(1 - \frac{\delta}{\pi}\right) + \lambda \quad (\text{B.17})$$

$$k_{k,\pi}^d = \frac{\pi}{2} \left(1 - \frac{\delta}{\pi}\right) - \lambda \quad (\text{B.18})$$

These Fermi wavevectors are used in Section 6.5.3 to calculate the boundaries of the charge scattering determining the possible hybridization between spin and charge spectra.

Appendix C

Parity Breaking for Hole Doping

For the demonstration of the parity breaking for a single localized hole on the ladder an arrangement of five spins and one hole is considered as shown in Figure C.1. The two dimers located on rung l and rung $l+2$ are connected through a single spin on rung $l+1$ and leg 1 with the opposite position on rung $l+1$ and leg 2 necessary for a dimer formation being occupied by a hole leading to an interruption of the leg coupling J_{leg} . To confirm the parity breaking for this segment it is sufficient to consider the case of applying the leg Hamiltonian H_{leg} onto the arrangement of one excited dimer with the dimer on rung l chosen in the singlet ground state $|G\rangle$, the single spin residing as an up spin \uparrow on leg 1, rung $l+1$ and the dimer on rung $l+2$ presenting the excited dimer in the state $|1\rangle$. The ground and excited states are given as introduced in Appendix A.

Ground state:

$$|\rho\rangle = |G\rangle = \frac{1}{\sqrt{2}} [|\uparrow\downarrow\rangle - |\downarrow\uparrow\rangle] \quad (\text{C.1})$$

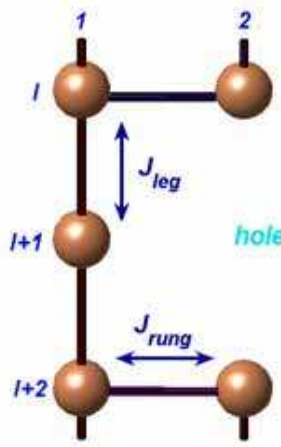


Figure C.1: Arrangement for a segment of the ladder including a single localized hole and five spins; the two dimers are located on rungs l and $l+2$, the single spin at $l+1$ and the hole on leg 2 at the rung $l+1$.

Excited state:

$$|\sigma(m)\rangle = \begin{bmatrix} |1\rangle = |\uparrow\uparrow\rangle & m = 1 \\ |0\rangle = \frac{1}{\sqrt{2}}|\uparrow\downarrow\rangle + |\downarrow\uparrow\rangle & m = 0 \\ |\bar{1}\rangle = |\downarrow\downarrow\rangle & m = -1 \end{bmatrix} \quad (\text{C.2})$$

Our chosen configuration for this five-spin system can be described using the ground and the excited state for the dimer given in equations C.1 and C.2.

$$\begin{aligned} |G_l \uparrow_{l+1} 1_{l+2}\rangle &= \frac{1}{\sqrt{2}} [|\uparrow\downarrow\rangle_l - |\downarrow\uparrow\rangle_l] \otimes \uparrow_{l+1} \otimes |\uparrow\uparrow\rangle_{l+2} \\ &= \frac{1}{\sqrt{2}} [|(\uparrow\downarrow)_l \uparrow_{l+1} (\uparrow\uparrow)_{l+2}\rangle - |(\downarrow\uparrow)_l \uparrow_{l+1} (\uparrow\uparrow)_{l+2}\rangle] \end{aligned} \quad (\text{C.3})$$

Due to the single, localized hole breaking the leg coupling a violation of the symmetry requirement of H_{leg} is assumed and for confirmation this Hamiltonian has to be applied to our chosen arrangement. H_{leg} can be formulated for our system as:

$$H_{leg} = J_{leg} (\mathbf{S}_{1,l} \cdot \mathbf{S}_{1,l+1} + \mathbf{S}_{1,l+1} \cdot \mathbf{S}_{1,l+2}) \quad (\text{C.4})$$

Applying this Hamiltonian onto our segment described in equation C.3 reveals:

$$\begin{aligned}
H_{leg}|G\uparrow 1\rangle &= \mathbf{S}_{1,l} \cdot \mathbf{S}_{1,l+1} |G\uparrow 1\rangle + \mathbf{S}_{1,l+1} \cdot \mathbf{S}_{1,l+2} |G\uparrow 1\rangle \\
&= [S_{1,l}^z S_{1,l+1}^z + \frac{1}{2} (S_{1,l}^+ S_{1,l+1}^- + S_{1,l}^- S_{1,l+1}^+) \\
&\quad + S_{1,l+1}^z S_{1,l+2}^z + \frac{1}{2} (S_{1,l+1}^+ S_{1,l+2}^- + S_{1,l+1}^- S_{1,l+2}^+)] |G\uparrow 1\rangle \\
S_{1,l}^z S_{1,l+1}^z |G\uparrow 1\rangle &= \frac{1}{\sqrt{2}} [|(\uparrow\downarrow)_l \uparrow_{l+1} (\uparrow\uparrow)_{l+2} \rangle] \\
S_{1,l}^+ S_{1,l+1}^- |G\uparrow 1\rangle &= -\frac{1}{\sqrt{2}} |(\uparrow\uparrow)_l \downarrow_{l+1} (\uparrow\uparrow)_{l+2} \rangle \\
S_{1,l}^- S_{1,l+1}^+ |G\uparrow 1\rangle &= 0 \\
S_{1,l+1}^z S_{1,l+2}^z |G\uparrow 1\rangle &= \frac{1}{\sqrt{2}} [|(\uparrow\downarrow)_l \uparrow_{l+1} (\uparrow\uparrow)_{l+2} \rangle - |(\downarrow\uparrow)_l \uparrow_{l+1} (\uparrow\uparrow)_{l+2} \rangle] \\
S_{1,l+1}^+ S_{1,l+2}^- |G\uparrow 1\rangle &= 0 \\
S_{1,l+1}^- S_{1,l+2}^+ |G\uparrow 1\rangle &= 0
\end{aligned}$$

Combining these results:

$$H_{leg}|G\uparrow 1\rangle = \frac{1}{2} |0\uparrow 1\rangle + |G\uparrow 1\rangle - \frac{1}{2} |1\downarrow 1\rangle \quad (\text{C.5})$$

which couples the state with one excited dimer $|G\uparrow 1\rangle$ to states with one, $|G\uparrow 1\rangle$, and two excited dimers, $|0\uparrow 1\rangle$ and $|1\downarrow 1\rangle$ leading to interchannel coupling and therefore confirming the parity breaking for a segment including a single localized hole which can be generalized to the ladder arrangement.

Appendix D

High Field Excitations in Copper Nitrate

D.1 Dispersion Relations

For the evaluation of the two modes in copper nitrate appearing after reaching the second critical field $H_{c,2}$ as introduced in Section 7.7.3 and compare Figure 7.15, spin wave theory can be used to calculate the dispersion relation. The excitations can be found by applying the spin deviation operator (compare Section 2.2.1) to the ground state consisting of a ferromagnetic alignment of the spins due to the saturation condition and diagonalizing this Hamiltonian results in the normal modes of the system.

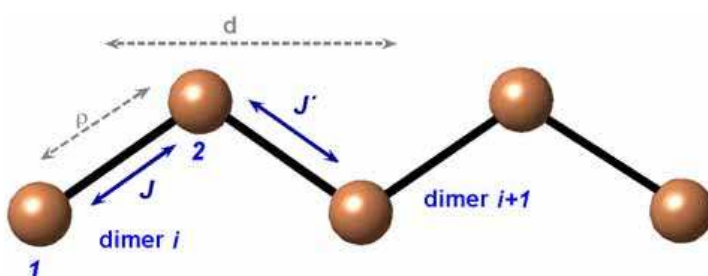


Figure D.1: Arrangement of the dimerized chain with an intradimer coupling labeled by J consisting of dimer i with spins 1 and 2 and an interdimer coupling by J' . The distance within dimer is given by ρ and between dimers i and $i+1$ by \mathbf{d} .

The system can be described by N dimers each consisting of spins 1 and 2 with spin 1 localized at $\mathbf{r}_{i,1} = \mathbf{d}_i - \rho/2$ and spin 2 at $\mathbf{r}_{i,2} = \mathbf{d}_i + \rho/2$, the coupling within dimers is

labeled by J and between dimers by J' as shown in Figure D.1. The Hamiltonian of the system is given by:

$$\begin{aligned} H &= J \mathbf{S}_{i,1} \cdot \mathbf{S}_{i,2} + J' \mathbf{S}_{i,2} \cdot \mathbf{S}_{i+1,1} + g\mu_B B S^z \\ &= J (S_{i,1}^z S_{i,2}^z + \frac{1}{2} (S_{i,1}^+ S_{i,2}^- + S_{i,1}^- S_{i,2}^+)) \\ &\quad + J' (S_{i,2}^z S_{i+1,2}^z + \frac{1}{2} (S_{i,2}^+ S_{i+1,2}^- + S_{i,2}^- S_{i+1,2}^+)) + g\mu_B B S^z \end{aligned} \quad (\text{D.1})$$

The ground state consists of an ferromagnetic arrangement (all spins aligned in one direction), in our case the up direction is assumed:

$$|\Psi_G\rangle = |\cdots \uparrow\uparrow\uparrow\uparrow\uparrow\cdots\rangle \quad (\text{D.2})$$

and the first excited state is assembled by a superposition of states with one spin flip $\Delta S^z = -1$ either occurring at site 1 with wavefunction $|\Psi_{Q,1}\rangle$ or at site 2 with $|\Psi_{Q,2}\rangle$ provided by:

$$\begin{aligned} |\Psi_{Q,1}\rangle &= \frac{1}{\sqrt{N}} \sum_{i=1}^N e^{i Q \cdot d} S_{i,1}^- |\Psi_G\rangle \\ |\Psi_{Q,2}\rangle &= \frac{1}{\sqrt{N}} \sum_{i=1}^N e^{i Q \cdot d} S_{i,2}^- |\Psi_G\rangle \end{aligned} \quad (\text{D.3})$$

where the wavefunctions $|\Psi_{Q,1}\rangle$ and $|\Psi_{Q,2}\rangle$ can be viewed as:

$$|\Psi_{Q,1}\rangle = |\cdots \uparrow\uparrow\downarrow\uparrow\uparrow\cdots\rangle$$

$$|\Psi_{Q,2}\rangle = |\cdots \uparrow\uparrow\uparrow\downarrow\uparrow\cdots\rangle$$

and $S_{i,1}^-$ is the spin deviation operator creating the spin flip.

For the diagonalization it is necessary to find the action of the Hamiltonian (equation D.1) onto the first excited state as provided in equation D.3, but to be able to express this action in terms of the effects on the ground state (provided in equation D.2), the application of the Hamiltonian onto the ground state where only the z components contribute is considered first:

$$H |\Psi_G\rangle = H |\cdots \uparrow\uparrow\uparrow\uparrow\uparrow\cdots\rangle = \left[\frac{N}{4} (J + J') - 2Ng\mu_B SB \right] |\cdots \uparrow\uparrow\uparrow\uparrow\uparrow\cdots\rangle$$

The effect of the Hamiltonian onto the first excited state is given as:

$$\begin{aligned} H|\Psi_{Q,1}\rangle &= H|\cdots \uparrow\uparrow\downarrow\uparrow\uparrow\cdots\rangle \\ &= \left[(N-1) \frac{1}{4} (J+J') - 2(N-1)g\mu_B SB - \frac{J'}{4} - \frac{J}{4} \right] |\cdots \uparrow\uparrow\downarrow\uparrow\uparrow\cdots\rangle \\ &\quad + \frac{J'}{2} |\cdots \uparrow\downarrow\uparrow\uparrow\uparrow\cdots\rangle + \frac{J}{2} |\cdots \uparrow\uparrow\downarrow\uparrow\uparrow\cdots\rangle \end{aligned}$$

and now expressing relative to the ground state:

$$\begin{aligned} H|\Psi_{Q,1}\rangle &= -\frac{J+J'}{2} + g\mu_B B |\cdots \uparrow\uparrow\downarrow\uparrow\uparrow\cdots\rangle \\ &\quad + \frac{J'}{2} |\cdots \uparrow\downarrow\uparrow\uparrow\uparrow\cdots\rangle + \frac{J}{2} |\cdots \uparrow\uparrow\downarrow\uparrow\uparrow\cdots\rangle \\ &= \left[-\frac{J+J'}{2} + g\mu_B B \right] |\Psi_{Q,1}\rangle + \frac{J'}{2} e^{iQ \cdot d} |\Psi_{Q,2}\rangle + \frac{J}{2} |\Psi_{Q,2}\rangle \end{aligned}$$

and similar for the wavefunction of spin 2:

$$H|\Psi_{Q,2}\rangle = \left[-\frac{J+J'}{2} + g\mu_B B \right] |\Psi_{Q,2}\rangle + \frac{J'}{2} e^{-iQ \cdot d} |\Psi_{Q,1}\rangle + \frac{J}{2} |\Psi_{Q,1}\rangle$$

leading to a matrix representation of:

$$H = \begin{bmatrix} A_Q & B_Q \\ B_Q^* & A_Q \end{bmatrix} \begin{bmatrix} \alpha_Q \\ \beta_Q \end{bmatrix}$$

where $\Psi = \alpha_Q \Psi_{Q,1} + \beta_Q \Psi_{Q,2}$ and

$$\begin{aligned} A_Q &= -\frac{(J+J')}{2} + g\mu_B B \\ B_Q &= \frac{J}{2} + \frac{J'}{2} e^{iQ \cdot d} \end{aligned}$$

The eigenstates are:

$$\begin{vmatrix} A_Q - \omega_Q & B_Q \\ B_Q^* & A_Q - \omega_Q \end{vmatrix} = 0$$

where $(A_Q - \omega_Q)^2 = |B_Q|^2 \Rightarrow \omega_Q^\pm = A_Q \pm |B_Q|$

The absolute value of B_Q can be evaluated as:

$$\begin{aligned} |B_Q| &= \sqrt{B_Q B_Q^*} = \sqrt{\frac{J^2}{4} + \frac{J'^2}{4} + \frac{JJ'}{4} (e^{iQ \cdot d} + e^{-iQ \cdot d})} \\ &= \sqrt{\frac{J^2 + J'^2}{4} + \frac{JJ'}{2} \cos(Q \cdot d)} \end{aligned}$$

leading to following dispersion relation:

$$\omega_Q^\pm = -\frac{(J + J')}{2} + g\mu_B B \pm \sqrt{\frac{J^2 + J'^2}{4} + \frac{JJ'}{2} \cos(Q \cdot d)}$$

Defining $\alpha = J'/J$ finds for the upper and lower mode of dispersion ω_Q^+ and ω_Q^- respectively:

$$\begin{aligned} \omega_Q^+ &= g\mu_B B - J \left(-\frac{(1+\alpha)}{2} + \sqrt{\frac{(1+\alpha)^2}{4} + \frac{\alpha}{2} \cos(Q \cdot d)} \right) \\ \omega_Q^- &= g\mu_B B - J \left(-\frac{(1+\alpha)}{2} - \sqrt{\frac{(1+\alpha)^2}{4} + \frac{\alpha}{2} \cos(Q \cdot d)} \right) \end{aligned}$$

Using the simplification that $\alpha \ll 1$ establishes the dispersion relations for the higher field modes as introduced in Section 7.7.3 in equation 7.7:

$$\begin{aligned} \omega_Q^+ &\cong g\mu_B B - \frac{J(1+\alpha)}{2} + \frac{J}{2} (1 + \alpha^2 + 2\alpha \cos(Q \cdot d))^{1/2} \\ &= g\mu_B B - \frac{J(1+\alpha)}{2} + \frac{J}{2} (1 + \alpha \cos(Q \cdot d) + \dots) \\ &= g\mu_B B - \frac{J\alpha}{2} (1 - \cos(Q \cdot d)) \end{aligned} \tag{D.4}$$

and similar for the lower mode:

$$\omega_Q^- = g\mu_B B - \frac{J\alpha}{2} (1 + \cos(Q \cdot d)) - J \tag{D.5}$$

D.2 Intensity Distribution

For the determination of the intensity distribution for the two high field modes in copper nitrate the scattering cross-section proportional to the dynamical correlation function have to be found. The results for the correlation function are already introduced in equation 7.8 with the detailed derivation provided in this section. The dynamical correlation function for the two modes is given by considering the definition in equation 3.9:

$$S^{+-}(\mathbf{Q}, \omega) = |\langle \Psi^+ | S^-(\mathbf{Q}) | \Psi_G \rangle|^2 \delta(\omega - \omega_Q^+) + |\langle \Psi^- | S^-(\mathbf{Q}) | \Psi_G \rangle|^2 \delta(\omega - \omega_Q^-) \quad (\text{D.6})$$

where $S^-(\mathbf{Q})$ is the Fourier transform of the spin annihilation operator and according to equation 3.11 given by:

$$\begin{aligned} S^-(\mathbf{Q}) &= \sum_i e^{i\mathbf{Q} \cdot \mathbf{d}} (e^{-i\rho/2 \cdot \mathbf{Q}} S_{i,1}^- + e^{i\rho/2 \cdot \mathbf{Q}} S_{i,2}^-) \\ &= e^{-i\rho/2 \cdot \mathbf{Q}} \underbrace{\sum_i e^{i\mathbf{Q} \cdot \mathbf{d}} S_{i,1}^-}_{\sqrt{N} |\Psi_{Q,1}\rangle} + e^{i\rho/2 \cdot \mathbf{Q}} \underbrace{\sum_i e^{i\mathbf{Q} \cdot \mathbf{d}} S_{i,2}^-}_{\sqrt{N} |\Psi_{Q,2}\rangle} \end{aligned}$$

leading to:

$$S^-(\mathbf{Q}) = |\Psi_G\rangle = \sqrt{N} (e^{-i\rho/2 \cdot \mathbf{Q}} |\Psi_{Q,1}\rangle + e^{i\rho/2 \cdot \mathbf{Q}} |\Psi_{Q,2}\rangle)$$

Using the definition of Ψ^\pm introduced in the previous section $\Psi^\pm = \alpha_Q^\pm \Psi_{Q,1} + \beta_Q^\pm \Psi_{Q,2}$ the square of the matrix element of equation D.6 becomes:

$$|\langle \Psi^\pm | S^-(\mathbf{Q}) | \Psi_G \rangle|^2 = N |\alpha_Q^\pm e^{-i\rho/2 \cdot \mathbf{Q}} + \beta_Q^\pm e^{i\rho/2 \cdot \mathbf{Q}}|^2$$

leading to a correlation function of:

$$\begin{aligned} S^{+-}(\mathbf{Q}, \omega) &= N |\alpha_Q^+ e^{-i\rho/2 \cdot \mathbf{Q}} + \beta_Q^+ e^{i\rho/2 \cdot \mathbf{Q}}|^2 \delta(\omega - \omega_Q^+) \\ &\quad + N |\alpha_Q^- e^{-i\rho/2 \cdot \mathbf{Q}} + \beta_Q^- e^{i\rho/2 \cdot \mathbf{Q}}|^2 \delta(\omega - \omega_Q^-) \end{aligned} \quad (\text{D.7})$$

For the determination of α^\pm and β^\pm the eigenfunctions have to be taken into account:

$$\begin{bmatrix} A_Q & B_Q \\ B_Q^* & A_Q \end{bmatrix} \begin{bmatrix} \alpha_Q^\pm \\ \beta_Q^\pm \end{bmatrix} = \omega_Q^\pm \begin{bmatrix} \alpha_Q^\pm \\ \beta_Q^\pm \end{bmatrix}$$

With the fact $\omega_Q^\pm = A_Q \pm |B_Q|$ from the determination of the eigenstates in the previous section, section D.1, the eigenfunctions are given by:

$$A_Q \alpha^\pm + B_Q \beta^\pm = (A_Q \pm |B_Q|) \alpha_Q^\pm$$

So

$$\begin{aligned} B_Q \beta_Q^\pm &= \pm |B_Q| \alpha_Q^\pm \\ \beta^\pm &= \pm \sqrt{\frac{B_Q B_Q^*}{B_Q^2}} \alpha_Q^\pm \end{aligned}$$

From the definition of the wavefunction a relation between α_Q^\pm and β_Q^\pm can be established:

$$\begin{aligned} |\Psi|^2 &= |\alpha_Q^\pm|^2 + |\beta_Q^\pm|^2 = 1 \\ \Rightarrow |\beta^\pm|^2 &= |\alpha_Q^\pm|^2 = \frac{1}{2} \end{aligned}$$

By absorbing the overall phase vector in $\alpha_Q^\pm = \frac{1}{\sqrt{2}}, \beta_Q^\pm$ can be determined as:

$$\beta_Q^\pm = \pm \frac{1}{\sqrt{2}} \sqrt{\frac{B_Q^*}{B_Q}} = \pm \frac{1}{\sqrt{2}} \sqrt{\frac{J + J' e^{-iQ \cdot d}}{J + J' e^{iQ \cdot d}}}$$

Combining this result with equation D.7 finds the expression for the correlation function as introduced in equation 7.8 in Section 7.7.3:

$$\begin{aligned} S^{+-}(\mathbf{Q}, \omega) &= \frac{N}{2} \left| 1 - \exp(iQ \cdot \rho) \sqrt{\frac{1 + \alpha \exp(-iQ \cdot d)}{1 + \alpha \exp(iQ \cdot d)}} \right|^2 \delta(\omega - \omega_Q^+) \\ &+ \frac{N}{2} \left| 1 + \exp(iQ \cdot \rho) \sqrt{\frac{1 + \alpha \exp(-iQ \cdot d)}{1 + \alpha \exp(iQ \cdot d)}} \right|^2 \delta(\omega - \omega_Q^-) \quad (\text{D.8}) \end{aligned}$$

which is the expression used to calculate the intensity distribution of Figure 7.17 in Section 7.7.3.